COMPUTATIONAL AND EXPERIMENTAL PORE-SCALE STUDIES OF CARBONATE ROCK SAMPLES FOR THE BRAZILIAN PRE-SALT SCENARIO

William Godoy de Azevedo Lopes da Silva

Tese de Doutorado apresentada ao Programa de Pós-graduação em Engenharia Civil, COPPE, da Universidade Federal do Rio de Janeiro, como parte dos requisitos necessários à obtenção do título de Doutor em Engenharia Civil.

Orientadores: Paulo Couto

Elizabeth May Braga Dulley

Pontedeiro

Rio de Janeiro

Julho de 2019

COMPUTATIONAL AND EXPERIMENTAL PORE-SCALE STUDIES OF CARBONATE ROCK SAMPLES FOR THE BRAZILIAN PRE-SALT SCENARIO

William Godoy de Azevedo Lopes da Silva

TESE SUBMETIDA AO CORPO DOCENTE DO INSTITUTO ALBERTO LUIZ COIMBRA DE PÓS-GRADUAÇÃO E PESQUISA DE ENGENHARIA (COPPE) DA UNIVERSIDADE FEDERAL DO RIO DE JANEIRO COMO PARTE DOS REQUISITOS NECESSÁRIOS PARA A OBTENÇÃO DO GRAU DE DOUTOR EM CIÊNCIAS EM ENGENHARIA CIVIL.

Examinada por:

_____

Prof. Paulo Couto, D.Eng.

_____

Dr. Elizabeth May Braga Dulley Pontedeiro, D.Sc.

_____

Prof. José Antonio Fontes Santiago, D.Sc.

_____

Prof. José Luis Drummond Alves, D.Sc.

_____

Prof. Martinus Theodorus van Genuchten, Ph.D.

_____

Prof. Amir Raoof, Ph.D.

RIO DE JANEIRO, RJ-BRASIL
JULHO DE 2019

Silva, William Godoy de Azevedo Lopes da

Computational and experimental Pore-scale studies of carbonate rock samples for the Brazilian Pre-Salt scenario/ William Godoy de Azevedo Lopes da Silva. – Rio de Janeiro: UFRJ/COPPE, 2019.

XXVI, 179 p.: il.; 29,7 cm.

Orientador(es): Paulo Couto

Elizabeth May Braga Dulley Pontedeiro

Tese (doutorado) – UFRJ/ COPPE/ Programa de Engenharia Civil, 2019.

Referências Bibliográficas: p. 164-178.

1. Simulação numérica. 2. Pore network model. 3. Microtomografia. 4. Permeabilidade. 5. Reservatórios carbonáticos. I. Couto, Paulo *et al*. II. Universidade Federal do Rio de Janeiro, COPPE, Programa de Engenharia Civil. III. Título.

I dedicate this work to my parents Luiz Carlos and Valéria,

with love, respect and gratitude,

to my wife Andiara

who shares her life with me in this small pale blue dot lost “in the vastness of space and the immensity of time”,

and to my nephew Bernardo

“(...) A proclivity for science is embedded deeply within us, in all times, places, and cultures. It has been the means for our survival. It is our birthright. When, through indifference, inattention, incompetence, or fear of skepticism, we discourage children from science, we are disenfranchising them, taking from them the tools needed to manage their future.”

– Carl Sagan, The Demon-Haunted World: Science as a Candle in the Dark (1995)

ACKNOWLEDGEMENT

"Knowledge is in the end based on acknowledgement."

– Ludwig Wittgenstein, On Certainty (1969)

First of all, I would like to thank my family: grandparents, parents, brothers, sisters-in-law, uncles, aunts, cousins. They are my foundation. I have no words to thank them all for their support and love throughout these years.

I would like to thank my advisors, Paulo Couto, and Betty May. When I started a few years ago, Paulo gave the opportunity to develop my master's studies focusing on heterogeneous carbonate rocks, both experimental and numerical. It was a turning point for me. Thank you very much Paulo, for your friendship and support. Betty May met me during my PhD studies, in a moment of uncertanties. Thanks to her guidance and friendship, we could define the better approach, and this work could be done. It was, again, a unforgetable turning point in my life. Thank you so much Betty, for everything.

I would like to thank my PhD committee from COPPE. Thank you very much Prof. José Santiago, for your support and fruitful discussions, since the early days, during Continuum Mechanics classes. This work is also yours. Thank you prof. José Drummond Alves, for our great discussions involving numerical simulation, data analysis, and for your friendship since the beginning of my post-graduation.

Now, I would like to thank my PhD committe from Utrecht University. Thank you Rien, it has been a great journey since our first talk. I'll never forget that a small contribution can be a giant step to a further worthy goal. Thank you Amir. Since our first meeting, some years ago, your contribution and support for the numerical approach changed everything. Thank you very much for sharing with us your knowledge and your energy.

I would like to thank Prof. Leonardo Borghi, from LAGESED, for his support and great discussion involving carbonate rocks. Since my BSc studies, I have a special gratitude and respect for your shared passion for geology. Special acknowledgment to Prof. Ricardo Tadeu, from LIN, who gave us the opportunity to use the μCT equipment.

Regarding LIN, I have no words to thank you Olga Oliveira and Alessandra Machado, for your help with the μCT acquisition. Your support started everything.

Special acknowledgment to Dr. Xiaoguang Yin, for the early discussion involving the PNM Kabs code. Your support was the basis of the Kabs calibration procedure.

My gratitude goes to Dr. André Compan and Felipe Eller from CENPES, Petrobras, for their support during the centrifuge method analysis. I also thank Dr. Paulo Frederico from LRAP, for all his help during the primary drainage studies.

During my PhD studies I could talk to several researchers and professors worldwide. I would like to thank Prof. Majid Hassanizadeh, Prof. Ruud Schotting, Dr. Hamed Aslannejad, from Utrecht University, Dr. Tom Bultreys, Prof. Veerle Cnudde, from Gent University, Prof. Martin Blunt, Prof. Branko Bijeljic, Dr Ali Raeini, Dr. Kamaljit Singh, from Imperial College London, Dr. Ying Guo, Dr. Jan Ludivig, and Widuramina from IRIS (NORCE), and Prof. Ingebret Fjelde from NORCE and Stavanger University.

During my thesis development I was lucky enough to meet incredible people: Tatiana Lipovetsky, Alex Gomes, Lucas Cruz, Edmilson Rios, Nathália Dias, Felipe Adrião, Paulo Moreira, Felippe Pardini, Claudio Salinas, David Caetano, Daniela Costa, Mônica Sant'anna, Rodrigo Bayão, Denise Nunes, Adriano Rocha and Austin Boyd.

Special acknowledgement to Bruno Valle, Bruno Santos, Marcelo Mendes, Thiago Carelli, Lucas Rocha, and all of the LAGESED team.

I would like to thank LIEP/LTEP group: Alessandro de Lima, Alex Sabino, Paulo Victor, Luciano Martins, Daniel Rodrigues, Adão Gonçalves (also for SEM-EDS measurements), Sérgio Lira, and Fábio Galvão.

My gratitude also goes to Dr. Frances Abbotts, and Moisés Silva, from Shell, for all their support during the PhD studies. I would like to thank Shell for the financial support.

Special acknowledgement to CAPES for their financial support.

Luiz Friãens, for all our great coffee time discussions regarding several topics; Mateus Ramirez and Rafael Bastos, without your friendship and help I could not have finished this work; Elton Lima and Ana Jerdy, no words to describe how thankful I am to you both; to Enno de Vries and Laura Martínez, in Utrecht or in Rio, for the excellent time with you too. Thiago Saraiva, Thaís Silveira, Santiago Drexler, Fernanda Hoerlle, and Maira Lima, for all support and frienship since the beginning of this journey. Thank you all.

Finally, I would like to thank my wife Andiara, for all her suppport and love througout this journey. You have been with me since the beginning, sharing good and difficult times. Thank you Andi, for everything.

Resumo da Tese apresentada à COPPE/UFRJ como parte dos requisitos necessários para a obtenção do grau de Doutor em Ciências (D.Sc.).

ESTUDOS COMPUTACIONAIS E EXPERIMENTAIS EM ESCALA DE POROS DE ROCHAS CARBONÁTICAS PARA O CENÁRIO DO PRÉ-SAL BRASILEIRO

William Godoy de Azevedo Lopes da Silva

Julho/2019

Orientadores: Paulo Couto
Elizabeth May Braga Dulley Pontedeiro

Programa: Engenharia Civil

Coquinas, rochas reservatórios em alguns campos do pré-sal na Bacia de Santos, na costa sudeste do Brasil, são exemplos de rochas carbonáticas onde muita atenção tem sido focada na caracterização adequada de suas propriedades de fluxo multifásico e petrofísico. Plugues de coquina foram coletados de um afloramento em uma pedreira no nordeste do Brasil e um conjunto abrangente de análises foi realizado. Isso incluiu Microscopia Eletrônica de Varredura (MEV), Espectroscopia de Raios-X de Energia Dispersiva (EDS), Difração de Raios-X (DRX), Ressonância Magnética Nuclear (RMN), aquisição de imagens por microtomografia micro-computadorizada (μCT) usando uma série de tamanhos de pixel, medições de permeabilidade / porosidade diretas absolutas e método de centrifugação para medições de pressões capilares. Os resultados incluíram a composição de rocha carbonática e sistemas de poros em diferentes escalas, permitindo a reconstrução e modelagem de porosidade e permeabilidade absoluta para amostras de coquina usando reconstruções digitais 3D e simulações numéricas usando modelos de rede de poros (PNMs). Os resultados forneceram informações críticas sobre o sistema de poros de amostras de coquinas, incluindo métodos aperfeiçoados para prever o fluxo monofásico e bifásico através das redes de poros.

Abstract of Thesis presented to COPPE/UFRJ as a partial fulfillment of the requirements for the degree of Doctor of Science (D.Sc.)

COMPUTATIONAL AND EXPERIMENTAL PORE-SCALE STUDIES OF CARBONATE ROCK SAMPLES FOR THE BRAZILIAN PRE-SALT SCENARIO

William Godoy de Azevedo Lopes da Silva

July/2019

Advisor: Paulo Couto
Elizabeth May Braga Dulley Pontedeiro

Department: Civil Engineering

Coquinas, from the pre-salt reservoirs in the Santos Basin off the southeast coast of Brazil, are examples of carbonate rocks where much attention has focused on proper characterization of its petrophysical and multiphase flow properties. Since it is very difficult to obtain rock samples from these very deep reservoirs, analogues from north-eastern Brazil are often used because of very similar geological age and petrophysical properties. Coquina plugs were collected from an outcrop in a quarry in northeast Brazil and a comprehensive set of analysis were performed. This included Scanning Electron Microscopy (SEM), Energy-Dispersive X-ray Spectroscopy (EDS), X-ray Diffraction (XRD), Nuclear Magnetic Resonance (NMR), micro-computed tomography (μCT) image acquisition using a series of pixel sizes, direct absolute permeability/porosity measurements, and centrifuge methods for capillary pressure measurements. Results included the carbonate rock composition and pore systems at different scales, thus allowing the reconstruction and modelling of porosity and absolute permeability of coquina samples based on 3D digital reconstruction and numerical simulations using pore network models (PNMs). The results provided critical information about the pore system of the coquina carbonate rock, and improved methods for predicting single- and two-phase flow through the pore networks.

CONTENTS

List of Figures xiii

List of Tables xx

List of Symbols and Abbreviations xxii

1 INTRODUCTION 1

1.1 Context and Motivation 1

1.2 Objectives 3

1.3 Text Organization 3

2 THEORETICAL FRAMEWORK 5

2.1 Main Definitions 5

2.1.1 Porosity 5

2.1.2 Permeability 8

2.1.2.1 Relative Permeability 10

2.1.3 Wettability 11

2.1.3.1 Contact Angle 13

2.1.3.2 Interfacial Tension 14

2.1.4 Capillary Pressure 17

2.1.5 Representative Elementary Volume (REV) 20

2.2 Contextualization of the Samples Studied 22

2.2.1 Carbonate Rocks 22

2.2.2 The Pre-Salt Cluster 23

2.2.3 Carbonate Rocks Analogous to Pre-Salt Reservoirs 26

2.2.4 Sergipe-Alagoas Basin 27

2.2.5 Morro do Chaves 28

2.2.6 Coquinas 29

2.3 Techniques 30
2.3.1 X-Ray Computed Microtomography 30
2.3.2 Nuclear Magnetic Resonance (NMR) 34
2.3.3 Three-Dimensional Digital Rock Reconstruction 38
2.3.4 Segmentation 38
2.3.4.1 Non-Automated Methods 39
2.3.4.2 Automated Methods 40
2.4 Pore-Network Modeling 42
2.4.1 Numerical Simulation 44
2.4.1.1 Single-phase Flow 45
2.4.1.2 Two-phase Flow 47
3 MATERIALS AND METHODS 55
3.1 Workflow 55
3.1.1 Geological and Morphological Characterization / Petrography 58
3.1.2 Porosity and Permeability Experimental Measurements 62
3.1.3 X-Ray Computerized Microtomography 63
3.1.4 NMR, XRD, SEM and EDS Analyses 66
3.1.4.1 NMR signal post-processing 68
3.1.5 Segmentation 70
3.1.5.1 NMR-based Segmentation 70
3.1.5.2 Automated Segmentation – Algorithms 74
3.1.6 Digital Reconstruction – Pore System 74
3.1.7 Porosity Estimation 75
3.1.8 Pore-Network Modeling (PNM) 76
3.1.8.1 Single-phase Flow Numerical Simulation 77
3.1.8.2 Absolute permeability as a PNM calibration parameter 78
3.1.9 Analysis of sub-resolution porosity 79

3.1.10 Two-phase Flow Numerical Simulation 83
3.1.11 Parameters definition for Two-phase Flow simulation 86
3.1.11.1 Centrifuge Method 89
3.1.12 Optimized Simulation for Primary Drainage 92
4 RESULTS AND DISCUSSIONS 95
4.1 Experimental Results 95
4.1.1 Porosity and Absolute Permeability Measurements 95
4.1.2 Thin Section Analysis 96
4.1.3 SEM-EDS Analysis 100
4.1.4 XRD Analysis 106
4.1.5 NMR Analysis 107
4.1.6 Fluids Analysis 111
4.1.7 Contact Angle Measurements 113
4.1.8 Interfacial Tension Measurements 115
4.2 Digital and Numerical Results 116
4.2.1 X-ray Computed Microtomography 116
4.2.2 Segmentation 118
4.2.2.1 NMR-based Segmentation 119
4.2.2.2 Automated Segmentation – Algorithms 121
4.2.3 Coquina Rock Slabs Modeling 122
4.2.4 Coquina Plug Modeling 133
4.2.5 Sub-resolution Porosity Analysis 143
4.2.6 Primary Drainage Studies 150
5 CONCLUSIONS 161
5.1.1 Further Studies 162
6 BIBLIOGRAPHY 164

APPENDIX A: EVALUATION AND CLASSIFICATION OF AUTOMATED SEGMENTATION METHODS ACCORDING TO SEZGIN & SANKUR (2004) 179

LIST OF FIGURES

Figure 2-1. Relative Permeability Curve as a function of wetting fluid saturation (AHMED, 2010). 11
Figure 2-2. Example of pores of a water-wettable rock (WW) and an oil-wettable rock (OW). (Source: modified by RADKE *et al.*, 1993).....13
Figure 2-3. Example of contact angles on a solid water-wettable surface and an oil-wetted solid surface. The contact angle is measured between the solid surface and the tangent line passing through the point of contact between the droplet and the solid surface. This angle is, by definition, directed toward the region having the aqueous phase. (Source: modified from http://www.petrowiki.com/). 14
Figure 2-4. Example of the tensions acting on the interfaces of a drop of water resting on a solid surface surrounded by oil (Source: DONALDSON & ALAM, 2008).....15
Figure 2-5. Scheme with lateral view involving the interfacial tensions and the contact angle of a drop of water on a solid surface surrounded by oil. (Source: modified from RAZA *et al.*, 1968).....16
Figure 2-6. Scheme of the experiment of LEACH *et al.* (1962), to obtain the contact angles in the advance and retreat of the water in the presence of an oil drop (in green) as the lower plate moves parallel to the top plate. (Source: modified from CRAIG, 1971). 16
Figure 2-7. Definition of the effective radius of the interface r used in the equation to calculate the capillary pressure C_p. (Source: http://www.pucrs.br/). 17
Figure 2-8. Definition of the R_1 and R_2 radii used in the equation for calculating capillary pressure C_p. (Source: http://www.pucrs.br/). 18
Figure 2-9. Example of capillary pressure curves C_p (P^c or P_c) in drainage and imbibition processes. (Source: http://www.perminc.com/). 19
Figure 2-10 – Characterization of REV in a sample. From the volume V3 the porosity value becomes stable (Source: SILVA *et al.*, 2018) 21
Figure 2-11 – Geographical location of the Brazilian Pre-salt. 25
Figure 2-12 – Location map of the Sergipe-Alagoas Basin. (Source: modified from NOGUEIRA *et al.*, 2003).....27
Figure 2-13 – Stratification and heterogeneities present in the lacustrine carbonates of the Morro do Chaves Formation. (Source: CORBETT & BORGHI, 2013). 28
Figure 2-14 – Schematic diagram of the main components of the microtomographic equipment. (Source: Modified from CNUDDE & BOONE, 2013).....32
Figure 2-15 – Obtaining the porosity estimation from the T_2 distribution. (Source: modified by Coates *et al.*, 1999). 36
Figure 2-16 – Distribution of different relaxation times and the relationship with the distribution of different pore sizes. (Source: BEHROOZMAND *et al.*, 2014).....37
Figure 2-17 – Example of a pixel window, highlighting a pixel of coordinates i, j used in the Bernsen method (Local_Bernsen). (Source: Adapted from BIENIECKI & GRABOWSKI, 2005) 42

Figure 3-1 – Overview of the proposed workflow for obtaining petrophysical parameters of coquinas from basic and digital petrophysical techniques. 56
Figure 3-2 – Main techniques selected during execution of this work: (a) geological characterization of a region of interest; (b) selection and morphological evaluation of coquina plugs; (c) preparation and analysis of thin sections using (d) optical microscopy; (e) μCT images acquisition; (f) porosity and absolute permeability measurements; (g) NMR data acquisition; (h) SEM/EDS analysis; (i) XRD analysis; (j) drop shape analysis (DSA); (k) viscosity measurements; and (l) the centrifuge system for capillary pressure measurements. 57
Figure 3-3 – Location of the Sergipe-Alagoas Basin, in the northeast region of Brazil, identifying the constituent sub-basins and the location of the quarry called Mina São Sebastião (in the city of São Miguel dos Campos), where the Morro do Chaves Formation is located. 58
Figure 3-4 – (a) Image of the Morro do Chaves Formation in the Mina São Sebastião quarry of the city of São Miguel dos Campos; (b) identification of a layer (called Bed 2B) highlighted by red points where the samples (named 1-4, 1-19B, 1-20B, and 1-34A) were taken; (c) image of the plug showing some vugular porosity in the sample; (d) thin section obtained from the cut of one end of the sample during the flattening process; (e) rock slab prepared from the thin section, with the red square showing the region that was analyzed using SEM-EDS, XRD, and μCT with higher resolution 59
Figure 3-5 – Plugs used and evaluated in the present work using the proposed workflow and techniques studied. 60
Figure 3-6 – Red squares indicate the regions from where the rock slabs were extracted for SEM-EDS analysis and μCT imaging with higher resolution. 61
Figure 3-7 – Detail of the *Zeiss Imager M2m* optical microscope used to evaluate the thin sections of the selected samples. 61
Figure 3-8 – Detail of the DV-4000 porosimeter and permeameter used to obtain the measurements of effective porosity and absolute permeability of the samples studied 62
Figure 3-9 – Photograph of X-ray microtomography of *Bruker* model *Skyscan 117*3 used to acquire images with different resolutions 63
Figure 3-10 – (a) NMR equipment (model MQC from Oxford Instruments), (b) SEM equipment (TM3030 from Hitachi) using a EDS Bruker XFlash MIN SVE detector, and (c) XRD equipment (Bruker D8 Advanced diffractometer) 67
Figura 3-11 – Example of Pore Size Distribution (PSD) curves obtained from T_2 measurements converted to radii (r) for 10 different samples. 70
Figure 3-12 – NMR porosity partitioned in ϕ_1, $\phi_{2,\text{ and }}\phi_3$, according to 25 and 50μm cut-offs. The total porosity shall be the sum of the three areas, which will correspond to the cumulative porosity. The red and blue arrows indicate the cumulative porosity of each range of radii (separated at 25 and 50μm) 71
Figure 3-13 – Proposed scheme of carbonate rock pore space partitioning used in this work for the NMR-based segmentation procedure. 73
Figure 3-14 – NMR porosity partitioned in ϕ1, ϕ2, ϕ3, and ϕ4. Considering a 3D pore system model reconstructed from μCT images with 20μm pixel size, the porosity calculated from pores with radii smaller than 10μm cannot be detectable. This information is used for segmentation purposes. 74

Figure 3-15 – Images obtained from the *Avizo® 9.5* program showing (a) the digital reconstruction of the plug, (b) digital reconstruction of the plug and the effectively connected pore system associated with this plug after setting the threshold value, and (c) reconstruction of the pore system effectively connected in isolation for purposes of porosity estimation and comparison of results. 75
Figure 3-16 – View of a pore system obtained using PNM technique, (a) with the dimensions associated with the radii of the pore bodies and the throats connecting these pores bodies; (b) showing the region subjected to the higher pressure (input boundaries), and the region subjected to the low pressure (output boundaries), in red, which are specified in the code. Scale in m. 77
Figure 3-17 – Schematic of the adopted network generation: (a) real connections (pore throats in black) and generated connections (pore throats in red) in the pore network; (b) first iteration with the definition of the first level (pore bodies generated and connected to previously existing networks); (c) second iteration, with redundant pore throats being discarded; (d) last iteration, given the non-existence of connections from pore 7, and determination of the final network. 80
Figure 3-18 – The image in (a) shows the porous system saturated with the wetting fluid (in red), with a non-wetting fluid inlet region (in blue) on the right, (b), (c), (d), and (e) show the advance of the wetting fluid, from the right of each image, considering the occurrence of snap-off. The last images in the lower right corner show the saturations of the pore bodies and the orientation of the primary drainage process. 85
Figure 3-19 – Scheme illustrating the Contact Angle (CA) measurement procedure using Kruss/Eurotechnica DSA. Contact angles were measured every 30 seconds during 24 hours. 87
Figure 3-20 – (a) DSS Kruss Goniometer for contact angle and interfacial tension measurements, (b) Anton Paar model M302 rheometer for fluid viscosities measurements, and (c) centrifuge system (model A-200 from Core Lab Instruments) for capillary pressure measurements. 89
Figure 4-1 – Identification of Bed 2B (a) regions from which the samples were collected and (b) characterization of three distinct regions as a function of their permo-porous properties. 96
Figure 4-2 – Images obtained from the analysis of thin sections, aiming the analysis of the pore system, for the samples (a) 1-4, (b) 1-19B, (c) 1-20B and (d) 1-34A. All images were obtained with the optical microscope *Zeiss Imager M2m*. 97
Figure 4-3 – Scanned images of sample 1-34A obtained with optical microscopy showing (a) blue epoxy resin filling the pores of the thin section, (b) highlighted in red the contours of bivalve shells, and (c) highlighted in yellow the size of the bivalve shells. 100
Figure 4-4 – SEM images of a rock slab of sample 1-34A obtained with an increase of (a) 50; (b) 150; (c) 300; (d) 800; (e) 1200, and (f) 2000 times the selected region of the rock slab. Fig. 5a shows the presence of two large pores of a few millimeter each (A and B). 101
Figure 4-5 – SEM images of a rock slab of sample 1-20B obtained with an increase of (a) 50; (b) 150; (c) 300; (d) 800; (e) 1200, and (f) 2000 times the selected region of the rock slab. Fig. 5a shows the presence of a large pore (A) of a few millimeter and a small pore with few micron (B). 101
Figure 4-6 – (a) EDS image of the analyzed area, identifying three well-defined regions (A, a well-defined pore, B, a pore-centered region with dark grey level around it, and C, a dark grey level region similar to B but with no obvious pore boundary), (b) visual evaluation (colors) of the different components of the

sample; (c) abundant presence of calcium, (d) presence of silicon in a small region (white dots), (e) oxygen, and (f) carbon distributed around the sample. 102
Figure 4-7 – (a) EDS image of a ROI from a rock slab of sample 1-19B, identifying three well-defined regions (A, a well-defined pore, B, a grain-centered region with light grey level), (b) visual evaluation (colors) of the different components of the sample; (c) abundant presence of calcium, and (d) presence of sulphur and iron in a small region (white dots), identified as pirite (FeS_2). 103
Figure 4-8 – Spectrum of the main elements identified in the image of Figure 4-7 (a) from EDS analysis. It is possible to verify large amount of calcium, oxygen and carbon, mainly related to calcite ($CaCO_3$). There is also a presence of sulphur and iron, identifying pirite in specific regions of the sample. Small quantities of magnesium and silicon occurs also. The large amount of beryllium identified at the first peak is related to the stabilization of the equipment during the first stages of the analysis with no direct correlation to the sample. Accelarating voltage was 15 keV. 104
Figure 4-9 – Spectrum obtained from EDS analysis of the main elements of a ROI of each rock slab (a) 1-4; (b) 1-20B; and (c) 1-34A. It is possible to verify large amounts of calcium, oxygen and carbon, mainly related to calcite ($CaCO_3$). The presence of sulphur and iron, indicates pirite in specific regions of the sample, while silicon, indicates presence of quartz. The large amount of beryllium and chloride identified at the first peak is related to the stabilization of the equipment during the first stages of the analysis with no direct correlation to the sample. Accelarating voltage of 15 keV. 105
Figure 4-10 – (a) PSD curve obtained from the NMR data, and (b) cumulative porosity for sample 1-4. 108
Figure 4-11 – (a) PSD curve obtained from NMR data, and (b) cumulative porosity for sample 1-19B. 109
Figure 4-12 – (a) PSD curve obtained from NMR data, and (b) cumulative porosity for sample 1-20B. 110
Figure 4-13 – (a) PSD curve obtained from NMR data, and (b) cumulative porosity for sample 1-34A. 111
Figure 4-14 – Density measurements of Oil B at 60ºC using Anton Paar DMA HPM densitometer with a thermostatic bath at different pressures. 112
Figure 4-15 – Density measurements of Brine B at 60ºC using Anton Paar DMA HPM densitometer with a thermostatic bath at different pressures. 112
Figure 4-16 – Main step related to the noise reduction of (a) an original μCT image using (b) non-local filter from Avizo® 9.5. It is possible to verifiy that the image after the filter application is sharper and presents less salt-and-pepper noise. 118
Figure 4-17 – (a) PSD curve of plug 1-34A obtained from NMR data showing the area under the curve that corresponds to the sub-resolution porosity which cannot be reconstructed from μCT images with 9.97 μm pixel size (in red); and (b) percentage of the porosity (identified by the red arrow) that is not detectable during the segmentation procedure. 120
Figure 4-18 – (a) Image of the selected area for μCT, indicating with a red arrow the presence of vugular porosity; (b) 3D volume reconstruction of the region using 6.77μm pixel size μCT images, with the red and yellow arrows highlighting the same vugs as in (b); (c) 3D segmentation and reconstruction of the pore region of the sample, showing red and yellow circles identifying connected ROI from the 6.77μm pixel size μCT images; (d) same from the 9.97μm images, altough the circles do not show connected ROI due to the resolution limitation: pore diameters between 6.77 and 9.97μm are responsible for this connection. 123

Figure 4-19 – PNMs of the reconstructed slab (a) from the 6.77μm pixel size μCT images, highlighting two ROI defined by the red and yellow circles, showing the distributions of pore body and pore throat radii, and (b) from the 9.97μm images. The red circles presents a ROI connected from higher resolution reconstructed model (a), which is not detectable from the lower resolution model (b). The yellow circles from both models show a not connected region, independently of the resolution. Scales are in m. 124
Figure 4-20 – Pore size frequency distributions (equivalent diameters) of the digital pore system of the rock slab 1-20B obtained using (a) 6.77 μm and (b) from 9.97 μm μCT images. Notice a much larger number of spherical elements in the reconstructed model using the higher resolution. 125
Figure 4-21 – (a) Digital reconstruction of the ROI from the rock slab 1-20B from the 6.77μm pixel size μCT images showing different clusters (different colors), and (b) the PNM showing the dimensions of pore bodies (radii) and pore throats (diameters). Scales are in m. 126
Figure 4-22 – (a) Digital reconstruction of the ROI from the rock slab 1-20B from the 9.97μm pixel size μCT images showing different clusters (different colors), and (b) the PNM showing the dimensions of pore bodies (radii) and pore throats (diameters). It is possible to verify a large number of disconnected clusters. Scales are in m. 127
Figure 4-23 – PNMs of the reconstructed slab (a) from the 6.77μm pixel size μCT images, highlighting two ROI defined by the red and yellow circles, showing the distributions of pore body and pore throat radii, and (b) from the 9.97μm images. The red and yellow circles presents ROI connected from higher resolution reconstructed model (a), which are not detectable from the lower resolution model (b), leading to different Kabs estimates. Scales are in m. 129
Figure 4-24 – (a) Image of the selected area for μCT, indicating with a red arrow the presence of vugular porosity; (b) 3D volume reconstruction of the region using 6.77μm pixel size μCT images, with the red arrow highlighting the same vug as in Fig.6a; (c) 3D segmentation and reconstruction of the pore region of the sample, with the right upper extremity being the assimilated vug and a central region with lower porosity showing well-defined bivalve contours from the 6.77μm pixel size μCT images; (d) same from the 9.97μm images (e) selection of the largest pores from the 6.77μm μCT images; (f) same from the 9.97μm images; (g) PNM generated with the largest pores from the 6.77μm pixel size μCT images; and (h) same from the 9.97μm images. 130
Figure 4-25 – Pore size frequency distributions (equivalent diameters) of the digital pore system of the rock slab obtained using (a) 6.77 μm and (b) from 9.97 μm μCT images. Notice a much larger number of spherical elements in the reconstructed model using the higher resolution. 131
Figure 4-26 – PNMs of the reconstructed slab (a) from the 6.77μm pixel size μCT images, and (b) from the 9.97μm images, showing the distributions of pore radii and pore lengths. PNMs of the regions with greater pressure differentials between pore bodies following numerical simulation of fluid flow, as well as of the diameters of the pore throats in these regions, using (c) 6.77μm pixel size μCT images and (d) 9.97μm images. The length and pressure units are m and Pa, respectively. 132
Figure 4-27 – Frequency distributions of the equivalent diameters (Eq Diam) of the pore bodies and pore throats of the digital pore system of the plug obtained using (a) 9.97μm, (b) 18.16μm, and (c) 24.95μm μCT images; and the range of pore throat radii (scale in m) found with the models generated using (d) 9.97μm, (e) 18.16μm, and (f) 24.95μm μCT images. 134

Figure 4-28 – PNM results for plug 1-34A based on 18.16μm μCT images presenting: (a) input (white region) and output (red region) boundaries for the fluid flow numerical simulations, and ranges of (b) pore body radii, (c) pore throat radii, and (d) pore throat lengths. Scales are in m. 136
Figure 4-29 – (a) Image of plug 1-34A, and PNM results of the pressure field based on (b) 24.95 μm, (c) 18.16 μm, and (d) 9.97μm pixel size μCT images (pressure scales are in Pa). 137
Figure 4-30 – (a) PNM of plug 1-19B based on 18.87μm pixel size images (pore throats based on geometric average) with 2% input and output boundaries (white and red zones, respectively), (b) 5%, and (c) 8%; (d) PNM results of the pressure field based on 2%, (e) 5%, and (f) 8% input/ouput boundaries. Pressure scales are in Pa. 139
Figure 4-31 – (a) Pore body size distribution from the PNM of plug 1-19B based on 18.87μm pixel size images; (b) Pore throat size distribution based on harmonic average, (c) geometric average, and (c) arithmetic average. Scales in m. 140
Figure 4-32 – (a) Image of plug 1-19B, and PNM results of the pressure field based on (b) 24.95μm, (c) 18.16μm, and (d) 9.97μm pixel size μCT images, considering 2% of input/output boundaries. Pressure scales are in Pa. 142
Figure 4-33 – (a) Image of plug 1-4, and digital reconstruction of the porosity system based on (b) 24.95μm, (c) 18.16μm, and (d) 9.97μm pixel size μCT images. It is possible to verify different number of connected clusters from each model. 144
Figure 4-34 – (a) Result of the pressure field based on 18.53μm pixel size μCT images PNM for Case 3, (b) pore bodies radii, (c), pressure of pore bodies, showing in lighter colours the connected region, and (d) zoom in of this region. Pressure scales in Pa, dimension in m. 146
Figure 4-35 – PNM of sample 1-4 based on 9.97μm pixel size μCT images showing, (a) 10% input/output boundaries; (b) pore bodies and pore throat radii; (c), size of pore bodies; and (d) pressure field for the studied PNM. Pressure scales in Pa, dimension in m. 148
Figure 4-36 – (a) PNM of sample 1-4 based on 18.53μm pixel size μCT images with 10% input/output boundaries; (b) pressure field for this PNM; (c) PNM of sample 1-4 based on 9.97μm pixel size μCT images with 10% input/output boundaries; and (d) pressure field for this second studied PNM. Pressure scales in Pa. 150
Figure 4-37 – Capillary pressure curves obtained from the centrifuge method for samples 1-19B, 1-20B, and 1-34A. 152
Figure 4-38 – Comparison of capillary pressure curves obtained with the centrifuge method and PNM numerical simulations for sample 1-19B at laboratory condition. 153
Figure 4-39 – Comparison of capillary pressure curves obtained from the centrifuge method and numerical simulation for sample 1-20B at laboratory condition. 154
Figure 4-40 – Comparison of capillary pressure curves obtained from the centrifuge method and numerical simulations for sample 1-34A at laboratory condition. 154
Figure 4-41 – (a) PNM of sample 1-19B based on 18.87μm pixel size μCT images with input/output boundaries selected by PoreFlow; (b) the input/output boundaries considered few points; (c) pore bodies and pore throats radii; and (d) saturation: blue is the wetting phase and red is the non-wetting phase. ... 155

Figure 4-42 – (a) PNM of sample 1-20B based on 17.81μm pixel size μCT images with input/output boundaries selected by PoreFlow; (b) the input/output boundaries considered few points; (c) pore bodies and pore throats radii; and (d) saturation: blue is the wetting phase and red is the non-wetting phase. ... 155
Figure 4-43 – (a) PNM of sample 1-34A based on 18.17μm pixel size μCT images with input/output boundaries selected by PoreFlow; (b) the input/output selection considered few points; (c) pore bodies and pore throats radii; and (d) saturation: blue is the wetting phase and red is the non-wetting phase. 156
Figure 4-44 – (a) Saturation map of sample 1-19B based on 24.95μm pixel size μCT images; (b) 18.87μm; and (c) 9.97μm. Saturation map: blue is the wetting phase and red is the non-wetting phase..... 158
Figure 4-45 – Comparison of capillary pressure curves obtained from the centrifuge method and numerical simulations for sample 1-19B in a oil-wet semi-reservoir scenario of pre-salt. 159

LIST OF TABLES

Table 2-1 – Classification of wettability as a function of contact angle values according to ANDERSON (1986). 14
Table 2-2 – Classification of the methods studied in the present work from the classification proposed by SEZGIN & SANKUR (2004) based on 40 evaluated methods. 40
Table 3-1 – Parameters related to the acquisition and reconstruction of data of the plugs studied using a *Bruker* X-ray microtomograph model *Skyscan 1173*. 65
Table 3-2 – Parameters related to the acquisition and reconstruction of rock slab data studied using the *Bruker* X-ray microtomograph model *Skyscan 1173*. 66
Table 3-3 – Parameters related to NMR data acquisition with the *Oxford Instruments MQC* model. 68
Tabela 3-4 – Pixel size from μCT images and maximum pore radius that can be identified from the NMR data 72
Table 3-5. Total dissolved solids TDS, pH, viscosity, and density (ρ) for Model Brine and Model Oil A used for the contact angle measurements 86
Table 3-6. Main parameters of Oil A used in this work during the primary drainage based on the centrifuge method. 91
Table 3-7. Total dissolved solids TDS, pH, viscosity, and density (ρ) for the Brine B used in this work for the contact angle measurements and simulation purposes 93
Table 3-8 – SARA analysis, acid and basic numbers (TAN and TBN), viscosity and API for the Oil B used in this work for contact angle measurements and simulation purposes 93
Table 4-1 – Basic petrophysical properties of four samples. 95
Table 4-2 – Identified porosity types based on thin section analysis 99
Table 4-3 – EDS quantitative analysis (%wt) for the main elements of a ROI selected from the rock slab 1-19B. 104
Table 4-4 – XRD quantitative analysis (%wt) of the coquina samples. 106
Tabela 4-5 – Saturation Index (SI) for each studied sample. 107
Table 4-6 – Porosity values obtained with the Permeameter and NMR techniques. 108
Table 4-7. Viscosity (cP) and density(g/cm^3) estimates for Model Brine, Model Oil A, Brine B, and Oil B from measurements and simulations using *OLI Studio 9.6*® software 113
Table 4-8. Contact Angle (CA) measurements involving the coquina rock slabs and the interaction between selected fluids at 60ºC and 1,000 psi. 114
Table 4-9. Contact Angle (CA) measurements at different pressures involving the coquina rock slab from sample 1-19B and the interaction between selected fluids. 115
Table 4-10. Interfacial Tension (IFT) measurements involving the combination of selected fluids. 115
Table 4-11. Acquisition time (h), number of slices, reconstruction time (h), obtained pixel size (μm), and file size (GB) for the studied coquina samples μCT images 117
Table 4-12. Sub-resolution and detectable porosities from each reconstructed digital pore systems obtained from each coquina plug. 119

Table 4-13. Calculated and detectable porosities from reconstructed digital pore systems obtained from each coquina plug. 120
Table 4-14. Threshold values (Th) of 8-bit μCT images from the NMR-based segmentation and automated procedures according to the methods of Kittler & Illingworth, Otsu, Ridler & Calvard, Niblack, and Bernsen. 121
Table 4-15. Statistical analysis for threshold values (Th) evaluation of 8-bit μCT images from automated procedures according to the methods of Kittler & Illingworth (K&I), Otsu (Ot), Ridler & Calvard (R&C), Niblack (Ni), and Bernsen (Be). 122
Table 4-16. Porosity (ϕ) and absolute permeability (Kabs) estimated from the reconstructed coquina rock slab from samples 1-20B and 1-34A obtained with two different pixel sizes. 127
Table 4-17. Porosity (ϕ) and absolute permeability (Kabs) of the reconstructed coquina plugs 1-19B and 1-34A using PNM based on 2% input/output boundaries. 133
Table 4-18. Absolute permeability (Kabs) of the reconstructed coquina plug 1-19B using PNM based on different input/output boundaries (%). 138
Table 4-19. Computational time for filtering, PNM generation, and numerical simulation to estimate Kabs based on different pixel size μCT images for sample 1-19B. 142
Table 4-20. Kabs estimates based on PNM generated from 18.53μm pixel size μCT images for sample 1-4 considering 2% of input/output boundaries and geometric average for pore throats generation. 145
Table 4-21. Kabs estimates based on PNM generated from 18.53μm pixel size μCT images for sample 1-4 considering geometric average for pore throats generation for Case 3 using different input/output boundaries. 146
Table 4-22. Kabs estimates based on PNM generated from 9.97 μm and 18.53μm pixel size μCT images for sample 1-4 considering 10% of input/output boundaries and three average for pore throats generation. 147
Table 4-23 – Saturation Index (SI) for primary drainage studies. 151
Tabela 4-24 – Centrifuge Method results for samples 1-19B, 1-20B, and 1-34A. 153

List of Symbols and Abbreviations

A	-	Flow cross-sectional area
B_0	-	Static magnetic field
C	-	Pore conductance
C_p	-	Capillary pressure
$C(i,j)$	-	Contrast function
c_1, c_2	-	Parameters associated to the F generating function
d	-	Distance from the center of the lens to the image
E	-	Measurement of dissimilarity between known values
F	-	Active contours generation function
$\mathbf{F}$	-	Field of volumetric forces of diverse origins
f	-	Focal distance
f_L	-	Larmor natural frequency
$f(s_i^w)$	-	Saturation function of the wetting phase
g	-	Gravity acceleration
g_{ij}	-	Conductance of the pore throat between bodies *i* and *j*
g	-	Luminance value of an image
G	-	Limit value of luminance
h	-	Distance
he	-	Hydraulic head
$h(g)$	-	Probability mass function
h_1, h_2	-	Height relative to a reference
i	-	Hydraulic gradient
I	-	Intensity of the X-ray beam
I_0	-	Intensity of the non-attenuated X-ray beam
k	-	Hydraulic conductivity
K	-	Specific or absolute permeability
$\boldsymbol{K}$	-	Permeability tensor
k_{ij}^{α}	-	Equivalent conductivity of phase α in throat *ij*
K_e	-	Effective permeability
K_r	-	Relative permeability

K_{ri}	-	Relative permeability of phase *i*
$K_{r\alpha}$	-	Relative permeability of phase α
K_{ro}	-	Relative permeability of oil phase
K_{rw}	-	Relative permeability of water phase
K_{xx}	-	Permeability on the *x* direction
K_{yy}	-	Permeability on the *y* direction
K_{zz}	-	Permeability on the *z* direction
L	-	Length of path through which flow passes
M_0	-	Equilibrium magnetization
$M_Z(t)$	-	Magnetization on time *t*
N_i	-	Coordination number of pore *i*
N_{Eff}	-	Number of voxels in the effectively connected 3D pore model
N_{Mod}	-	Number of voxels in 3D pore model
N_{Total}	-	Number of total voxels in 3D model
o	-	Distance from object to center of lens
p	-	Pressure
P_c	-	Capillary pressure
P^c	-	Capillary pressure
$p(g)$	-	Probability mass function
$p_b(g)$	-	Probability mass function of background
$p_f(g)$	-	Probability mass function of foreground
$\overline{p}_i$	-	Mean pressure in pore *i*
p_i^c	-	Capillary pressure in pore *i*
p_i^n	-	Non-wetting phase pressure in pore *i*
p_i^w	-	Wetting phase pressure in pore *i*
Q	-	Volumetric flow rate
Q_{ij}	-	Volumetric flow rate inside the pore throat
q^α	-	Total volumetric flow rate of phase α
Q_{ij}^n	-	Non-wetting fluid volumetric flow rate between pores *i* and *j*
Q_{ij}^w	-	Wetting fluid volumetric flow rate between pores *i* and *j*
Q_{tot}	-	Total volumetric flow rate throughout the pore network
r	-	Effective radius of interface between fluids
r_1	-	Local coordinate of a streamline

R	-	Resistance force against fluid flow within the pore
R1	-	Radius of curvature used in the Young-Laplace equation
R2	-	Radius of curvature used in the Young-Laplace equation
R_{ij}	-	Radius of the pore throat which connects pores *i* and *j*
R_s	-	Resistance force against fluid flow within the pore in the *s* direction
s_i^α	-	Saturation of phase α in the body *i*
s_i^n	-	Non-wetting phase saturation in the pore *i*
s_i^w	-	Wetting phase saturation in the pore *i*
S_W	-	Wetting fluid saturation
S_{wir}	-	Irreducible water saturation
t	-	Time
T	-	Threshold value
T1	-	Longitudinal relaxation time
T2	-	Transverse relaxation time
T_B	-	Threshold value obtained by Bernsen Method
Tc	-	Threshold value obtained by Active Contour Method
Th	-	Threshold value obtained by Histogram Method
T_K	-	Threshold value obtained by Kittler Method
T_N	-	Threshold value obtained by Niblack Method
To	-	Threshold value obtained by Otsu Method
Tr	-	Threshold value obtained by Ridler and Calvard Method
u_0	-	Image obtained from the technique of X-ray microtomography
v	-	Velocity vector
V_τ	-	Volume of phase τ
V_f	-	Total volume of the liquid phase within the pore network
Vp	-	Pore volume
v_s	-	Fluid velocity in an arbitrary direction *s*
Vs	-	Solids total volume
Vt	-	Rock total volume
v_x	-	Component of velocity vector in *x* direction
v_y	-	Component of velocity vector in *y* direction
v_z	-	Component of velocity vector in *z* direction
$\overline{v}$	-	Average velocity of a fluid in the pore

x	-	Position in the orthogonal axis x of the Cartesian coordinate system in three-dimensional space
y	-	Position in the orthogonal axis y of the Cartesian coordinate system in three-dimensional space
z	-	Position in the orthogonal axis z of the Cartesian coordinate system in three-dimensional space

GREEK SYMBOLS

α	-	Phase (wetting or non-wetting)
β	-	Shape factor
γ	-	Gyromagnetic ratio of hydrogen nuclei
γ_w	-	Specific mass of fluid
ε	-	Measurement of dissimilarity between unknown values
ε_τ	-	Volumetric fraction of phase τ
η	-	Dynamic viscosity of fluid
θ	-	Contact angle
ϑ	-	Linear attenuation coefficient
λ_1, λ_2	-	Parameters associated to the *F* generating function
μ	-	Dynamic viscosity of fluid
μ^n	-	Dynamic viscosity of non-wetting phase
μ^w	-	Dynamic viscosity of wetting phase
ξ_τ	-	Indicator function of phase τ
ρ	-	Density of fluid
σ	-	Interfacial tension
σ^2	-	Variance of an image
σ_b	-	Standard deviation of the background
σ_f	-	Standard deviation of the object
σ^{nw}	-	Interfacial tension between wetting and non-wetting fluid
σ_{os}	-	Interfacial tension between oil and surface
σ_{ow}	-	Interfacial tension between oil and water
σ_{ws}	-	Interfacial tension between water and surface
τ	-	Phase of interest

ϕ	-	Porosity
ϕ_e	-	Effective porosity
ϕ_r	-	Residual porosity
χ	-	Value of petrophysical property of interest
$\overline{\chi}$	-	Average of the values of a petrophysical property of interest
ψ	-	Magnitude to be measured
ψ_τ	-	Magnitude of the phase τ to be measured
Ω	-	Pore medium domain
ω_L	-	Larmor angular frequency

ABBREVIATIONS

CT	-	X-ray Computed Tomography
DIA	-	Digital Image Analysis
FID	-	Free Induction Decay
FZI	-	Flow Zone Indicator
GHE	-	Global Hydraulic Elements
HFU	-	Hydraulic Flow Unit
HU	-	Hydraulic Unit
IFT	-	Interfacial Tension
MCT	-	X-ray Micro-Computed Tomography
MTF	-	Modulation Transfer Function
NDT	-	Non-Destructive Tests
OW	-	Oil-wet
PNM	-	Pore-Network Modelling
RAM	-	Rapid Access Memory
REV	-	Representative Elementary Volume
RMN	-	Nuclear Magnetic Resonance
ROI	-	Region of Interest
SEM	-	Scanning Electron Microscopy
SI	-	International System of Units
WW	-	Water-wet

1 INTRODUCTION

1.1 Context and Motivation

Carbonate reservoirs present several challenges regarding their exploration and production of oil and natural gas. About 50% of the world's reserves of hydrocarbons are in formations of this nature, according to VIK *et al.* (2013a). In Brazil, pre-salt carbonate reservoirs accounted for 31.5% of total national oil production in 2015, accounting for about 50% of total hydrocarbons produced in Brazil in 2017 (ANP, 2018).

Although the average production of pre-salt wells reached 1.3 million barrels per day in 2017 (ANP, 2018), many studies are still needed to obtain a satisfactory understanding of the fluid flow dynamics in the porous systems of these carbonate rocks, thus potentially providing an even more significant increase in production.

The first major challenge when studying the pre-salt reservoir's carbonate rocks is the difficulty of obtaining samples for study and geological, sedimentological and petrophysical characterization purposes. An approach used to overcome this difficulty is the use of geologically analogue samples to the pre-salt reservoir rocks.

These analogous rocks are lacustrine carbonate rocks, such as coquinas and microbialites. The coquinas can be defined as rocks formed by the accumulation of shells (CAMARA, 2013), being denominated autochthonous when the deposition of shells and/or their fragments occurs *in situ* or with little movement, without influence of a transport agent, or allochthonous, characterized as concentrations of shells and/or fragments deposited by some transport agent (PETTIJOHN, 1957; KRUBEIN & SLOSS, 1963, apud CAMARA, 2013). In the present work, samples of allochthonous coquinas were selected whose outcrops are found in the Sergipe-Alagoas Basin, specifically in the Morro do Chaves Formation. Samples (plugs) of Layer named 2B were selected.

A number of data acquisitions were carried out, after the selection of samples from layer 2B, through the use of permeameter / porosimeter, Nuclear Magnetic Resonance (NMR), Scanning Electron Microscopy (SEM), X-ray spectroscopy (XRS), X-ray diffraction (XRD), analysis of thn sections and X-ray computed microtomography (with different resolutions), corresponding to the one defined in the present work as basic petrophysics. A second stage, characterized by the digital reconstruction of the porous systems of the samples and simulation of the flow of fluids in these systems, with the help of programs and computer codes, was also performed, being defined as digital

petrophysics. A workflow has been proposed and developed with the purpose of optimizing the data flow and optimizing the results obtained.

With the aid of digital petrophysics, one can estimate petrophysical parameters associated to the single-phase and two-phase flow. All the simulations are optimized by taking into account the data obtained experimentally: contact angle between the wetting fluid and the rock, through a goniometer, interfacial tension between wetting and non-wetting fluids, fluid viscosities and obtaining capillary pressures through the centrifugation method. In addition, during the data acquisition steps through X-ray microtomography, limitations on the resolutions used to obtain images, the question of porosity in sub-resolution, and the selection and definition of the threshold value for segmentation of the images are discussed, and, when possible, also optimized.

The simulations to obtain the intrinsic or absolute permeability must be performed in a Representative Elementary Volume (REV) based on the absolute permeability values, since the porosity-based REV may not be sufficient for the understanding of fluid flow in pore systems of heterogeneous carbonate rocks (SILVA *et al.*, 2018). In this case, the numerical simulations must be performed in the total volume of the plug, thus avoiding results that are not representative when working in volumes below the REV.

Absolute permeabilities calculated for the total volume of each sample, as well as relative permeabilities, were obtained through the PNM method, using quasi-static simulations. Experimental data such as porosity, absolute permeability, contact angle, viscosity measurements, interfacial tension and capillary pressure measurements are used for comparison, optimization and calibration of computational models and comparison of results.

The characterization of the porous system of these coquinas, as well as the interaction of these with different fluids, are not completely understood. The acquisition of data and obtaining and evaluation of models that help the geology and the engineering of reservoirs for the exploration and production of hydrocarbons in these challenging carbonate reservoirs motivated the creation of this workflow. It involves a brief geological assessment, basic petrophysics, digital petrophysics and computational simulation that can provide valuable and reliable information for the creation of a database that can aid in the simulation of flow and production of field scale hydrocarbon reservoirs.

1.2 Objectives

The present work addresses several topics related to basic and advanced petrophysics, including a proposed workflow to perform and evaluate computational and experimental pore-scale studies in highly complex heterogenous carbonate rock samples from the Brazilian Pre-salt scenario.

Specific objectives of this study are to generate and study pore-scale models of real coquina plugs using experimental and digital data, and to perform numerical single and two-phase flow simulations using pore-network modeling (PNM) from X-ray microtomography images obtained under different pixel sizes.

Some other important objectives are:

i) Generation of the modeled pore networks using absolute permeability numerical simulation estimates and real measurements as the main calibration parameters;

ii) Use of nuclear magnetic resonance (NMR) data for segmentation purposes and to identify the porosity that is not detected from 3D reconstructed models from those microtomography images, which can be understood as sub-resolution porosity;

iii) Modeling of sub-resolution porosity in order to predict fluid flow through low-permeability samples;

iv) Verify the feasibility of the proposed workflow based on several experimental techniques such as scanning electron microscopy (SEM), energy-dispersive X-ray spectroscopy (EDS), energy-dispersive X-ray diffraction (XRD), drop shape analysis (DSA), and centrifuge method (for cappilary pressure measurements);

The ultimate goal of this research is to gain basic knowledge about the modeling of heterogeneous carbonate rock pore systems, using experimental data to calibrate these networks, and the state-of-art in digital petrophysics. This study therefore aims to provide reliable results to aid in the development of representative reservoir models.

1.3 Text Organization

Chapter 2 presents a contextualization of the study, containing the main topics related to the definition of petrophysical parameters evaluated in this work, as well as

characterization of the sample and its collection site, the data acquisition stage with the X-ray microtomograph, steps for digital reconstruction of the sample, presentation of nuclear magnetic resonance techniques and scanning electron microscopy, through segmentation methods studied, digital image analysis, the generation of three-dimensional models for subsequent numerical simulation of fluid flow in porous media through two different techniques.

Chapter 3 presents the workflow developed and the proposed methods, highlighting each of the steps described above, specifying each point considered important and crucial for the development of the studies.

Chapter 4 presents results of the execution of the steps presented in the proposed workflow, as well as relevant discussions.

Chapter 5 presents conclusions of this study, also showing ideas for future work.

Finally, Chapter 6 features bibliographical references, while Chapter 7 presents appendices to the present work.

2 THEORETICAL FRAMEWORK

In order to contextualize and support the present work, it is necessary to approach the main topics addressed and discussed during the execution of the proposed studies.

2.1 Main Definitions

Initially it becomes necessary to present a theoretical basis of the main terms discussed in the present work.

2.1.1 Porosity

Porosity can be defined in general as the ratio of pore volume to total rock volume, expressed as a fraction. According to AHR (2008), the reservoir rocks are composed of solid material and interstitial porous spaces that may or may not be connected, leading to the following equation:

$$\phi = \left(\frac{Vp}{Vt}\right).100 \tag{2.1}$$

where porosity is represented by ϕ, Vp represents the volume of the pores and Vt the total volume of the rock, being calculated as:

$$Vt = Vp + Vs \tag{2.2}$$

where Vs is the volume of total solids.

It should be noted that an important definition is that of effective porosity (ϕ_e), which refers to the fraction of total porosity that is interconnected and capable of transmitting fluids, being calculated as the ratio of the volume of interconnected pores and the total volume of the rock. According to AHR (2008), measurements made in the laboratory to obtain the pore volume (Vp) actually calculate the effective porosity of the sample. It is defined the residual porosity (ϕ_r) in such a way that:

$$\phi = \phi_e + \phi_r \tag{2.3}$$

The main types of porosity can be separated according to SELLEY (2000) in:

i) Primary or depositional porosity: it is the porosity that by definition is associated with the deposition of the sediments themselves and, consequently, of the particles that compose them, and can be subdivided into:
   a. Intergranular or interparticle: occurs in the spaces between the grains or debris that form the frame or framework of a sediment;
   b. Intragranular or intraparticle: type of porosity present within the grains or debris that compose a sediment, especially if it is of carbonate origin associated with skeletal remains;

ii) Secondary or post-depositional: It is, by definition, the porosity formed after the deposition of a sediment. It is more easily found in carbonate rocks due to the great mobility of carbonate minerals in the subsurface and can be subdivided into:
   a. Intercrystalline porosity: occurs between the individual crystals of a crystalline rock. It is characteristic of carbonates that have undergone crystallization;
   b. Fenestral porosity: resulting from openings in the structure of larger and wider rocks than interstices supported by grains and to a large extent can be attributed to digging organisms or to gas escape routes;
   c. Moldic porosity: formed by the dissolution of grains from deposition usually after some type of cementation and is associated with individual particles;
   d. Vugular porosity: Second type of porosity formed by dissolution typically found in carbonates and with larger pores when compared to the moldic pores. With the increase in vugs size there is also the denomination of cave-type porosity;
   e. Fracture porosity: formed by fractures, this porosity characterizes rocks that are strongly lithified and is formed later to the other types of porosity;

Other porosity types found in the literature (Scholle & Ulmer-Scholle, 2003) are: (i) shelter porosity: it is a type of interparticular porosity created by the shelter of large

sedimentary particles in such a way that filling the porous space under them is prevented; (ii) breccia porosity: also of the interparticular type that occurs in breccias easily found in carbonate rocks; (iii) channel-type porosity: the porous system is in an elongated shape such that there is continuity of the latter in one or two dimensions; (iv) porosity of organic constructions (*Growth-framework*): primary porosity created from the *in situ* growth of structures in the framework of the carbonate rocks; (v) borings or burrows: they are openings created by different organisms by means of drilling and excavation, respectively, of these in rocks and other carbonate materials, and (vi) shrinkage porosity: porosity produced by the contraction of the sediment.

The previously presented classifications described in the works of SELLEY (2000) and SCHOLLE & ULMER-SCHOLLE (2003) are in fact based on the types of porosity defined according to CHOQUETTE & PRAY (1970), whose classification is simple and is based on the separation in three groups: selective frames, non-selective frames and selective frames or not. It is interesting to note that, as described by AHR (2008), CHOQUETTE & PRAY (1970) classification is a useful method to describe porosity in carbonates, but it was not designed to aid in the determination of the spatial distribution of porous types and has little usefulness in determining the relationships between the rocks and their petrophysical properties, since it focuses on the selectivity of the frames.

Another important classification refers to the work of LUCIA (1983). One of the objectives of this classification is to provide a practical method for visual description of porosity in carbonate samples, one of its main attributes being the importance given by this characterization to the emphasis on the petrophysical meanings of the separated and connected vugs. By definition given by the author, vugs are pores larger in size than the grains in the surrounding framework. According to LUCIA (1983), the pore types are separated into two central categories: vugulares and interparticles. As reported by AHR (2008), this classification provides a separation more focused on objectivity than on genetic characteristics, thus providing no information about the characteristics of rocks and pores, however, but it provides an excellent practical method focused mainly on the relationship between the rocks and their petrophysical properties.

2.1.2 Permeability

The experiments carried out by Henry Philibert Gaspard Darcy (1803-1858) and Charles Ritter (1793-1864) (apud AHR, 2008) had as their main objective to establish the laws governing the flow of a fluid, in their case water, through a mixture of sand and gravel contained in a well-packed column so that they could obtain the flow rate of pure water flowing through the mixture under atmospheric pressure conditions. According to AHR (2008), the main variables involved were associated with the textural characteristics of the sand and gravels used in the experiments, which operated with small flow rates and pressure differentials as compared to hydrocarbon reservoir conditions. The experiments conducted by Darcy were carried out in a homogeneous and isotropic porous medium in such a way that the flow through this medium had a constant velocity, presenting a laminar regime in its flow.

The expression originally described and published in 1856, with some modifications in relation to the original work in the letters representing the parameters and measures used, is given by:

$$\frac{Q}{A} = -k \left(\frac{h_1 - h_2}{L}\right) \tag{2.4}$$

where, in the International System (SI), Q is flow rate in m^3/s, A is the cross-sectional area of the flow in m^2, k is the hydraulic conductivity in m/s, ($h_1 - h_2$) is the hydraulic load in m and L is the length of the trajectory through which the flow passes in m Eq. 2.4 is widely known as *Darcy's Law*.

A reduced version of this equation used in the literature (ROSA *et al.*, 2006) is given by:

$$Q = -k \,.\, i \,.\, A \tag{2.5}$$

in which i is a dimensionless parameter representing the hydraulic gradient, given by:

$$i = \frac{dhe}{dx} \tag{2.6}$$

with the term dhe/dx represents the hydraulic head loss per unit length in the direction of flow. The negative sign in equations 2.4 and 2.5 indicates that flow occurs in the direction opposite the hydraulic gradient.

The intrinsic permeability (K) of a porous medium is directly related to the hydraulic conductivity (k) through the following equation (NARSILIO *et al.*, 2009):

$$K = k \,.\left(\frac{\eta}{\rho.\, g}\right) \tag{2.7}$$

where, in SI units, η is the dynamic viscosity of the fluid given in Pa.s (kg/m.s) that is flowing through the porous medium, ρ is the density of the same fluid in kg/m^3 and g is the acceleration of gravity given in m/s^2.

In the expression above, K represents the absolute or specific permeability coefficient, a geometric factor that defines characteristics of fluid transmission in a porous medium, having area dimension (m^2 in IS).

By definition, 1 *Darcy* is the permeability of a rock when a fluid with unit viscosity (1 Pa.s) flows through an area with a cross section of 1 cm^2 with a flow rate of 1 cm^3/s and pressure differential of 1 atm/cm. This value of 1 Darcy, represented by 1 D, corresponds to 9,869 x 10^{-13} m^2 in the International System of Units (approximately 1 μm^2). In carbonate hydrocarbon reservoirs, for example, absolute permeability may range from values below 0.1 mD (1 milidarcy equals 1 x 10^{-3} darcy) to values greater than 10 D, according to AHR (2008).

The permeability can be expressed according to the following classification:

i) Specific or Absolute Permeability (K): is the permeability of a given rock or porous medium related to the flow of a single fluid, and can be measured in samples or cores in the laboratory;

ii) Effective Permeability (K_e): is a measure of the permeability of the rock or porous medium to another fluid when this same rock or porous medium is already saturated in such a way that the presence of a wetting fluid prevents partially the entry of the non-wetting fluid into the pores of a given rock and, therefore, its value is lower than that found for absolute permeability;

iii) Relative Permeability(K_r): is the ratio between the effective permeability at a given saturation of a fluid and the absolute permeability at a saturation

of 100% of this same fluid, which can be obtained by the relation $K_r = K_e/K$.

The permeability is dependent not only on the pore size but also on the degree of interconnection between the pores and/or cracks, being related to the porosity, specifically the effective porosity (AHR, 2008).

Originally conceived as a particular constant of the medium, the permeability is actually spatially non-uniform (corresponding to usually heterogeneous porous media), dependent on the direction (being non-isotropic in most cases), dependent on the stress conditions the rocks are in and on the electrolytic composition of the fluids as well as the quantity and respective distribution of the phases of these fluids (BIRD, 1960).

According to BEAR (1972), the permeability $\boldsymbol{K}$ is a tensor that measures the ability of a porous medium to allow the passage of fluids (being originally defined for the flow of Newtonian fluids with low velocities, permanent and isothermal flow in porous media through Darcy's Law).

2.1.2.1 Relative Permeability

The relative permeability to a phase is the ratio of the effective permeability of that phase to the absolute permeability, with the relative permeability being usually identified for a phase i as Kri (Krw for water and Kro for oil, for example).

The relative permeability corresponds to the flowing capacity of each phase in a given porous medium according to the distribution of this phase in the pore volume considered (AHMED, 2010).

The relative permeability curves as a function of wetting fluid saturation, which are widely used in reservoir engineering, can be analyzed by identifying three distinct regions, as shown in Figure 2-1. The first one, represented as region A, shows the saturation values where predominantly oil flows. Regions B and C denote saturations where two-phase flow and mostly water occur, respectively. It is important to emphasize that, in Figure 2-1 that the phase composed by the non-wetting fluid presents higher values of the relative permeability over a greater range of saturations, indicating that there is a lower resistance to the flow of this phase when compared to the wetting fluid.

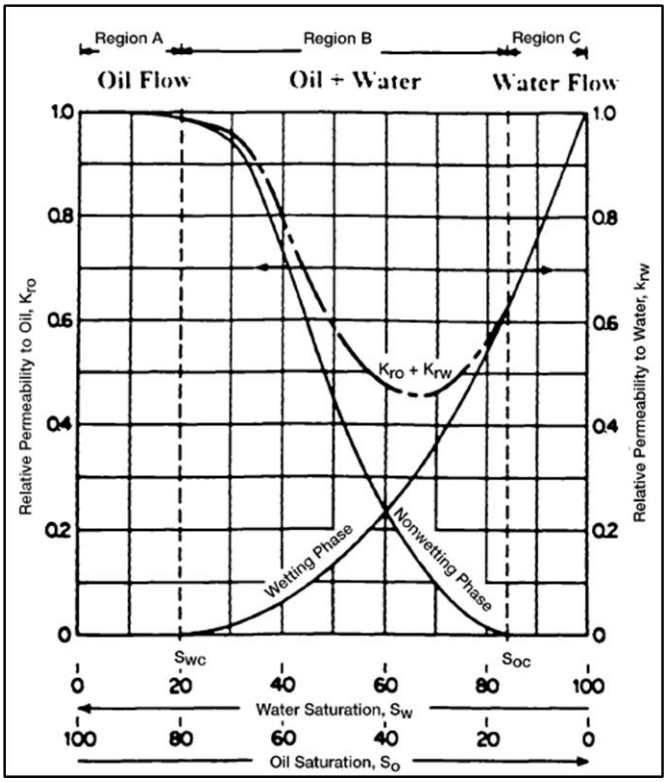


Figure 2-1. Relative Permeability Curve as a function of wetting fluid saturation (AHMED, 2010).

2.1.3 Wettability

The term wettability represents the attraction or repulsion of a fluid to a porous medium in the presence of other immiscible fluids. The difference between the forces of attraction and repulsion determines how the fluids will distribute in this porous medium. Thus, the fluid with greater attractive forces with the rock will maximize the contact between these two phases (HORNAPOUR *et al.*, 1990). On the other hand, the fluid with higher repulsive forces will minimize contact with the rock.

When two immiscible fluids saturate a porous medium, the tendency to adhere to or spread on the surface of the rock is determined by the wettability. According to (DONALDSON & ALAM, 2008), there are four different states of wettability between a fluid and a solid surface:

i) Water wettability: The system is considered when most of the surface is wettable to water. In this case, since the medium has great affinity for water, this phase will be located in the smallest pores maximizing its contact with the solid. In an oil-water-rock system, water will form a film that will extend throughout the porous volume as a continuous phase. On

the other hand, the oil will remain, often as a discontinuous phase, in the largest pores, surrounded by a water film. Due to this tendency, the water will spontaneously soak the rock by displacing the oil present in the porous volume. The spontaneous imbibition of the aqueous phase will continue until the surface and capillary forces equalize. In case the porous medium is saturated with water, the oil phase will not enter the pores spontaneously. A displacement pressure is required to displace the non-aqueous phase in the porous medium, in a process known as drainage;

ii) Fractional wettability: The term was introduced by BROWN & FATT (1956) to classify a porous media in terms of a water-wettable part, and an oil-wettable part. Attributed mainly to rocks whose mineral components on their surface are quite heterogeneous. In this system, water- and oil-wettable surfaces are not defined by pore size (FAERSTEIN, 2010);

iii) Mixed wettability: Term introduced by SALATHIEL (1973), differs from the fractional wettability, because in this case the oil forms a continuous medium preferentially in the larger pores and water in the smaller pores (FAERSTEIN, 2010). This can be explained by the presence of agents in the oil that can adsorb on the surface of the rock, gradually changing the wettability. These systems have been associated with low residual oil saturations, due to the formation of continuous oil paths through the larger pores, which promote the flow of oil in the porous system;

iv) Oil wettability: unlike water wettability, in this case the oil forms a film throughout the porous system, being located mainly in the smaller pores, while the water will be present in the largest pores, surrounded by the oil film. If oil is injected, reducing the saturation of water to very low levels, water present will be forming small droplets inside the oil phase. In these systems, water will not spontaneously soak into the porous medium only through a pressure differential imposed.

There are also solid surfaces that do not have a preference for their wettability: they are said to have neutral wettability (SOARES, 2016). Thus, if the solid is not wetted preferentially by any of the fluids present, the system is defined as neutral or having intermediate wettability (FAERSTEIN, 2010).

According to TREIBER *et al.* (1971), ANDERSON (1986) and OKASHA *et al.* (2007), carbonate rocks are more oil-wet than siliciclastic rocks. In the work of ANDERSON (1986) one can still find the effects of mineralogy on the wettability of some rocks studied.

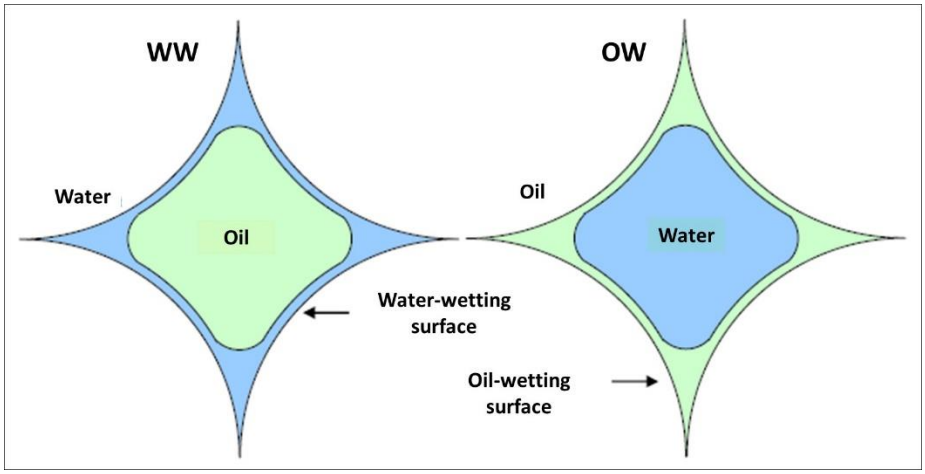


Figure 2-2. Example of pores of a water-wettable rock (WW) and an oil-wettable rock (OW). (Source: modified by RADKE *et al.*, 1993).

Figure 2-2 shows the pore example of a predominantly water-wetted rock (WW) and a predominantly oil-wetted rock (OW). In the case of a WW rock, the water is adhered to the pore walls and the oil is located in the center of the pore. Similarly, in an OW rock the oil is adhered to the pore walls with the water located in the center.

2.1.3.1 Contact Angle

One of the most widely used methods for predicting wettability is measuring the contact angle. This method consists of releasing a drop of liquid under the solid surface such that this drop will adopt a specific equilibrium conformation. According to RAMIASA *et al.* (2014), this conformation is obtained when the interfacial energies of the system, in this case represented by the liquid-solid interface, come into equilibrium, resulting in a specific configuration and angle of contact. Thus, the contact angle can be defined as the angle measured between the solid surface and the tangent that passes through the point of contact between the drop and the solid surface for the region with water, as shown in Figure 2-3. This angle is, by definition, directed toward the region that has the aqueous phase (FAERSTEIN, 2010).

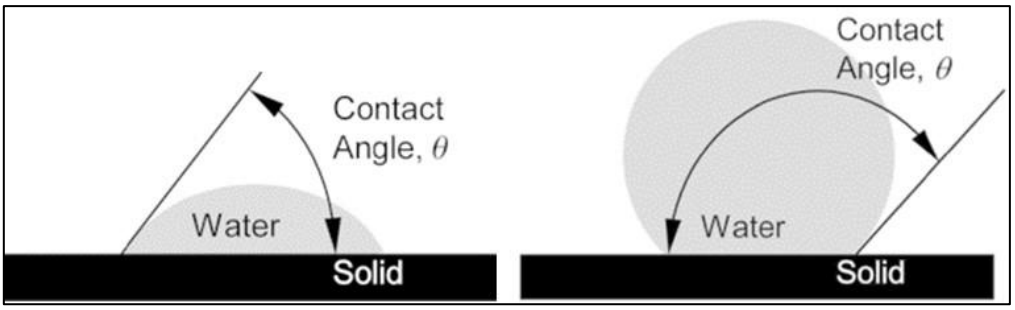


Figure 2-3. Example of contact angles on a solid water-wettable surface and an oil-wetted solid surface. The contact angle is measured between the solid surface and the tangent line passing through the point of contact between the droplet and the solid surface. This angle is, by definition, directed toward the region having the aqueous phase. (Source: modified from http://www.petrowiki.com/).

The experiments performed to obtain the values of the contact angles of an oil-water-rock system find certain difficulties of execution due to the complex geometry of the pores and the chemical complexity of the fluids involved (FAERSTEIN, 2010). However, when properly executed, they help to determine the preference of wettability in rocks (SOARES, 2016).

Table 2-1 – Classification of wettability as a function of contact angle values according to ANDERSON (1986).

Wettability	**Water-wetting**	**Neutral-wetting**	**Oil-wetting**
Minimun contact angle (θ)	0°	60° to 75°	105° to 120°
Maximum contact angle (θ)	60° to 75°	105° to 120°	180°

According to ANDERSON (1986), for contact angles (θ) close to 0º the surface is strongly wettable to water, while at contact angles close to 180º the surface is strongly oil-wetted. Table 2-1 shows values commonly used to define water, oil and neutral wettability, according to ANDERSON (1986).

2.1.3.2 Interfacial Tension

The interfacial tension is a material property of a fluid-fluid interface whose origin is tied to the different intermolecular forces of attraction acting on the two phases of these fluids. The result is an interfacial energy per area that acts to oppose the creation of a new

interface, being equivalent to a linear tension acting in all directions parallel to the interface (BUSH, 2004). The interfacial tension has unit of force/length or equivalent energy/area.

The Young's equation can be used to relate these tensions acting on a drop of water resting on a solid surface surrounded by oil, according to Figure 2-4. The Young equation is given by:

$$\sigma_{OW} \cdot \cos(\theta) = \sigma_{OS} - \sigma_{WS} \qquad (2.8)$$

Where the term σ represents the interfacial tension and θ the contact angle. The indexes *o*, *w* and *s* represent the different phases in the system: oil, water, and solid, respectively.

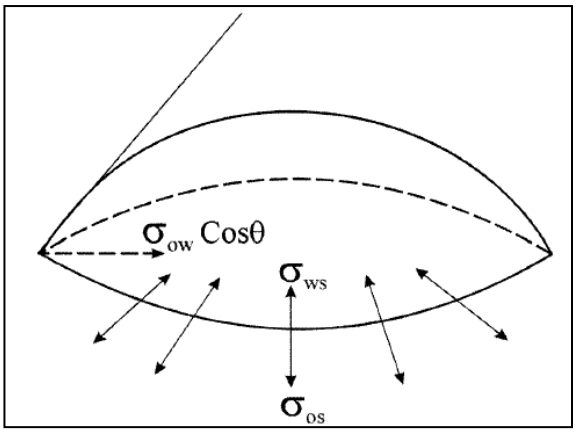


Figure 2-4. Example of the tensions acting on the interfaces of a drop of water resting on a solid surface surrounded by oil (Source: DONALDSON & ALAM, 2008)

In the equation, the contact angle (θ) of this drop of partially wetting water is related to the interfacial tensions of the fluids involved, in this case oil and water, and the solid surface. Figure 2-5 shows a schematic with side view involving the interfacial tensions and the contact angle of the drop shown in Figure 2-5.

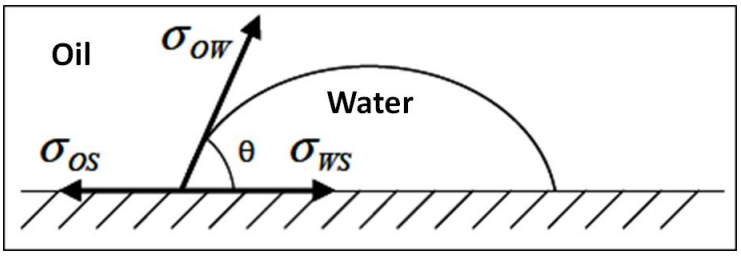


Figure 2-5. Scheme with lateral view involving the interfacial tensions and the contact angle of a drop of water on a solid surface surrounded by oil. (Source: modified from RAZA *et al.*, 1968).

A possible way of measuring the contact angle, presented by LEACH *et al.* (1962), is achieved by positioning a drop of oil, surrounded by water, between two parallel surfaces, moving one of them and measuring the resulting angles, as shown in the scheme presented in Figure 2-6.

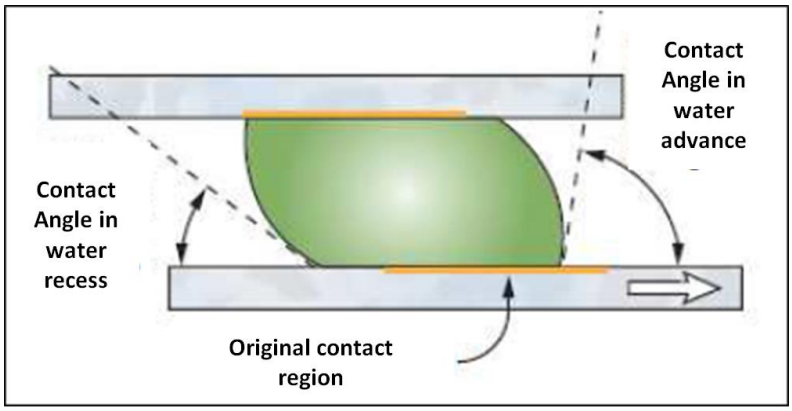


Figure 2-6. Scheme of the experiment of LEACH *et al.* (1962), to obtain the contact angles in the advance and retreat of the water in the presence of an oil drop (in green) as the lower plate moves parallel to the top plate. (Source: modified from CRAIG, 1971).

The contact angles are then obtained in the water receding and advancing process. This method results in angles for the advance and the retreat of the water. The water/rock contact angle at the water retreat, when the oil displaces the water, may be much smaller than the water/rock contact angle at the water advance (in this case the water displaces the oil), as shown in Figure 2-6. In the experiment conducted by LEACH *et al.* (1962) these angles were measured as a function of time, reaching a stabilization time between 1 and 2 days. It is important to highlight that FAERSTEIN (2010) mentioned that this difference between the forward and backward contact angle of water, which can reach 75° (DONALDSON & ALAM, 2008), is the main cause of the observed hysteresis in relative permeability curves and capillary pressure. This is because the aging time, i.e.

the time that the drop of oil remained in contact with the solid surface, changes the wettability according to the phase that first came into contact with the porous medium. The work of TREIBER *et al.* (1971) showed that the aging time is a very important variable during the measurement of the contact angle.

2.1.4 Capillary Pressure

Capillary pressures are generated at the interfaces between two immiscible fluids that exist in the pores (capillaries) of a porous medium. The basic relationship between capillary pressure, interfacial tension, contact angle and effective radius is given by:

$$C_p = \frac{2\sigma \cos(\theta)}{r} \tag{2.9}$$

Where C_p (P_c or P^c) is the capillary pressure, σ is the interfacial tension, θ is the contact angle and r is the effective radius of the interface between the two fluids. This equation is widely used to calculate the pressure in a glass capillary located at the interface between water and oil, according to Figure 2-7.

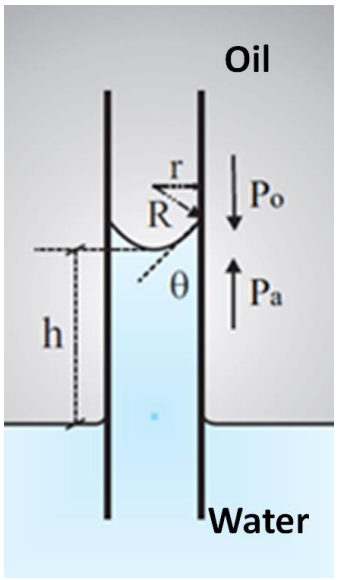


Figure 2-7. Definition of the effective radius of the interface r used in the equation to calculate the capillary pressure C_p. (Source: http://www.pucrs.br/).

Capillary pressure is therefore responsible for the curvature at the interface between two fluids. The Young-Laplace equation defines a pressure differential ΔP,

which is the capillary pressure, as a function of the mean radii of curvature, R_1 and R_2, and the interfacial tension σ between two fluids:

$$\Delta P = C_p = \sigma\left(\frac{1}{R_1} + \frac{1}{R_2}\right) \quad (2.10)$$

This equation shows that the capillary pressure is directly proportional to the interfacial tension between the phases and the smaller the confinement radius, the higher the C_p. Figure 2-9 shows the delimitation of the R_1 and R_2 radii used in the Young-Laplace equation for calculating capillary pressure.

For the displacement of a droplet that is trapped in a pore by the action of capillary forces, the pressure differential must be greater than the capillary pressure. By the equation it is evident that the capillary pressure is higher in small pores, and the pressure required to remove the phase captured by these pores will also be high.

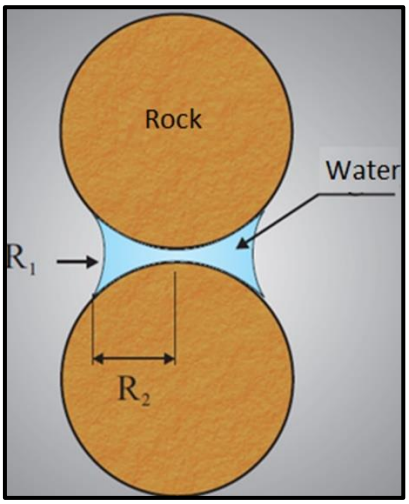


Figure 2-8. Definition of the R_1 and R_2 radii used in the equation for calculating capillary pressure C_p. (Source: http://www.pucrs.br/).

Analyzing equation 2.10 it is possible to conclude that:

a. If $R_1<R_2$ the capillary pressure C_p will be greater than zero ($C_p>0$) and there is a system whose surface is wettable to water;
b. If $R_1>R_2$ the capillary pressure C_p will be less than zero ($C_p<0$) and there is a system whose surface is oil-wettable.

The saturation of water in a system can be defined as the relation between the volume of water and the total volume of fluids in a porous medium. There is an inverse

relationship between saturation and capillary pressure: the lower water saturation in a porous medium the higher the capillary pressure. This inverse tendency is the same when the radius of curvature R1 is reduced, shown in Figure 2-8, and there is an increase in C_p.

The extraction of one phase from the porous medium by another is defined according to the displaced phase (wetting or non-wetting). Two processes can be identified: drainage, in which the non-wetting phase displaces the wetting phase and imbibition, in which the wetting phase displaces the non-wetting phase. In a rock wettable preferably by water, the drainage and inbibition processes can be observed through the graph of Figure 2-9.

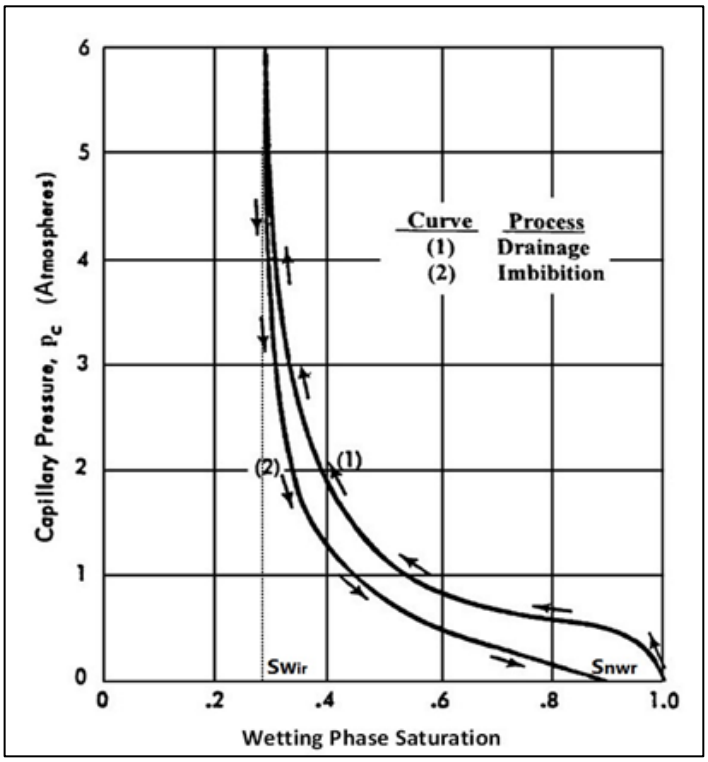


Figure 2-9. Example of capillary pressure curves C_p (P^c or P_c) in drainage and imbibition processes. (Source: http://www.perminc.com/).

Drainage in a water-oil-rock system is characterized by the displacement of water by the oil, whose porous medium is initially completely saturated with water. When irreducible water saturation (S_{wir}) is reached, drainage ceases, regardless of the pressure exerted on the system. During imbibition, the oil is displaced by water. In this case, increasing the water saturation capillary pressure decreases, however, without ever reaching the same saturation values found during the drainage, characterizing, therefore, a hysteresis. It is important to mention that the water saturation always reaches a

maximum value when the capillary pressure cancels, so that at this point the amount of oil present can not be reduced, even with a great change in the capillary pressure, denominated this minimum saturation of oil as residual oil saturation.

2.1.5 Representative Elementary Volume (REV)

The petrophysical parameters used in models and numerical simulators of flow of fluids in reservoirs are usually determined in the laboratory, with the aid of samples taken from the reservoirs themselves, by means of direct experimental measurements, or by their prediction, through numerical simulations using digitally reconstructed rocks ("*Digital Rock Physics*"). However, these measured or calculated parameters depend on samples and representative data, directly related to materials that have dimensions above the heterogeneity scale (VIK *et al.*, 2013a), in such a way that the values of these properties do not vary considerably and can be used .

Representative Elementary Volume (REV) can be defined as the volume of a sample capable of capturing a representative quantity of its heterogeneity (BEAR, 1972). Thus, REV can be considered as the volume at which macroscopic properties (such as hydraulic conductivity or permeability, for example) are relatively insensitive to small volume changes of the sample analyzed (Figure 2-10) or to the location of the region of interest within this same sample (CORBETT *et al.*, 1999; CORBETT, 2009). The REV may differ in size according to the petrophysical property that one wishes to measure (VIK *et al.*, 2013a), so that a suitable representative scale may depend directly on the property being evaluated momentarily. With REV, fluctuations in measurements of the properties studied are non-existent and a representative amount of heterogeneity can be established. Thus, REV can be characterized as the volume of a heterogeneous material that is large enough to be statistically representative and yet small enough to be considered an elementary volume of Continuum Mechanics (OLIVEIRA *et al.*, 2014). The work of KANIT *et al.* (2003) presented a quantitative definition of the REV based on statistical arguments, describing that it must guarantee with great precision the value of some property obtained through spatial averaging over a given domain.

In this way, REV becomes essential for an effective approximation between the values of the data collected and/or calculated in a sample, and the actual values found in a sample of much larger dimensions, or even in the scale of the reservoir, in such a way

that REV is essential for the study, development and implementation of upscaling techniques (LIU *et al.*, 2014; 2016).

As presented by VIK *et al.* (2013a, 2013b), a possible way to calculate the REV is through a change of scale or dimension while analyzing a particular petrophysical property of a sample. When the scale of the measurements does not involve the REV, the values of the measurements obtained show large variations, which indicates, by geostatistical analysis, the existence of samples with insufficient dimensions (CORBETT *et al.*, 1999; VIK *et al.*, 2013a). Thus, with the increase in the sample volume, these variations or fluctuations in the values of a given property are decreasing and there is a tendency of stabilization to a fixed value or threshold: this threshold being considered the REV, equivalent to the optimal volume in which the measure obtained represents, with a high degree of reliability, the measurement found in upper volumes of the same sample.

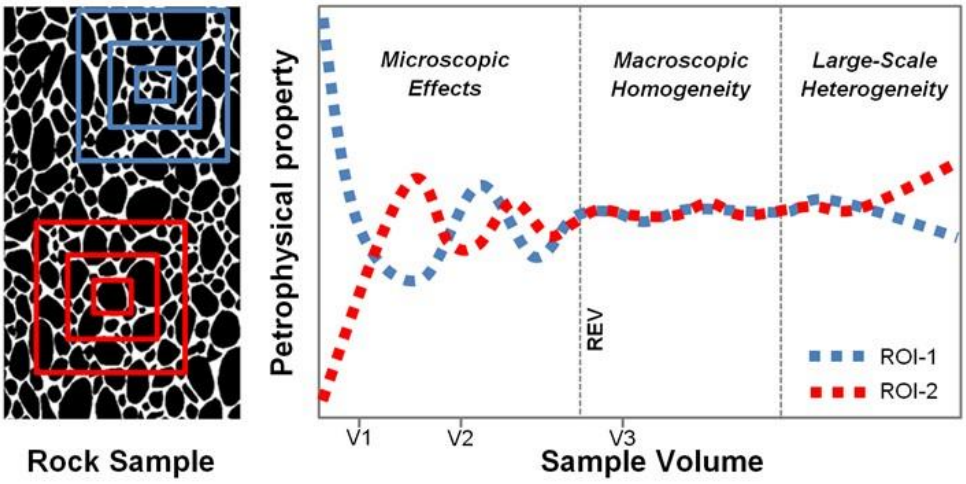


Figure 2-10 – Characterization of REV in a sample. From the volume V3 the porosity value becomes stable (Source: SILVA *et al.*, 2018)

Many studies involving the REV and the influence of sample volumes or dimensions to obtain petrophysical properties are widely available in the literature. GHARAHBAGH & FAKHIMI (2010) studied the determination of REV of rocks through numerical simulations involving hybrid programming between the Finite Element Method (FEM), and the Discrete Element Method. STROEVEN *et al.* (2004), who used the finite element method to investigate the REV of granular materials, ŁYDŻBA & RÓŻAŃSK (2012), which presented a method of evaluation of the minimum REV based only on the morphology of the microstructures, more precisely on the

properties of the geometries of these microstructures. NORDAHL & RINGROSE (2008) characterized the REV from the permeability obtained numerically of digitally reconstructed rocks.

A more accurate definition of REV, which is often considered an intuitive and ill-defined formulation entity including its physical size (SILVEIRA FILHO, 2003), can be analyzed through a mathematically more concise and robust approach. According to this author, REV can be estimated from the intrinsic means for each property of interest (absolute permeability, for example). This evaluation of the REV is a function of the property of interest is fundamental and can lead to very different results when analyzing different petrophysical parameters (SILVA *et al.*, 2018).

2.2 Contextualization of the Samples Studied

A contextualization of the carbonate samples studied in the present work, the presentation of some information necessary for a possible correlation between them and the reservoirs of the Pre-salt of the Santos basin, as well as the geographical location of the sample collection site, are addressed in this topic.

2.2.1 Carbonate Rocks

Carbonate rocks host about 50% of the worldwide hydrocarbon reserves (VIK *et al.*, 2013a). These rocks constitute a type of chemical/biochemical sedimentary rock which originated from the precipitation of minerals present in the water through various chemical or biological processes and, which can be distinguished from siliciclastic sedimentary rocks through their mineralogy, textural characteristics and their own chemical nature, as stated by BOGGS (2006). According to the author, carbonate rocks correspond to 20 to 25% of all sedimentary rocks found in geological records, from Cambrian to Quaternary, and can be divided, based on mineralogy, into limestones and dolomites, and composed mainly of the minerals calcite and dolomite, respectively.

SELLEY (2000) reports that carbonate rocks suffer even more from weathering when compared to terrigenous sediments, being the products of this weathering transported as solutes, and that many of the existing carbonate rocks originate from organic origin, presenting great variability in the size of their particles and chemical instability in the carbonates that constitute them.

AHR (2008) points out three great characteristics of carbonate rocks: First, carbonates form within the basins by biological, chemical or detrital deposition processes; Second, carbonates are strongly associated with biological activities, either by metabolic activities inherent to the organisms or by their movement, through the creation of paths or galleries in the rocky body itself; And third, carbonates are susceptible to rapid dissolution, cementation, recrystallization and relocation depending on the physicochemical conditions found in the various diagenetic environments.

An important difference between siliciclastic and carbonate rocks is porosity: while in the former the porosity is mainly interparticular, in the latter it does not always present such porosity, but may have pores with different sizes, shapes and origins. According to AHR (2008), since porosity and permeability are mutually related and have a good degree of correlation in siliciclastic rocks (sandstones), experimental measurements made on small specimens from these rocks can be considered representative for obtaining data of samples with larger volumes, as long as they are homogeneous, however, for carbonate rocks, which have very heterogeneous pore systems, the permeability values are not always intrinsically related to porosity values, and measurements carried out in small volumes may not be representative of a sample with a larger volume. Similar information is available from VIK *et al.* (2007; 2013a), who also explained that these rocks have great heterogeneity and a wide range of pore classes, which makes them, from the point of view of the characterization of their petrophysical properties and understanding of the flow and recovery mechanisms of fluids, more challenging than most sandstone materials.

2.2.2 The Pre-Salt Cluster

The pre-salt cluster represents a structure that was created about 160 million years ago when the supercontinent Gondwana began to separate, originating the continents of South America and Africa, is located in ultra-deep waters , approximately 290 km from the coast of the state of Rio de Janeiro, southeastern region of Brazil, (FORMIGLI *et al.*, 2009).

BELTRÃO *et al.* (2009) reported that the pre-salt reservoirs are partially dolomitized Cretaceous (Aptian) carbonate rocks and include coquins and other lithologies of the Rift phase below the Sag phase microbial carbonates located directly beneath the salt. FORMIGLI *et al.* (2009) explained that due to severe climate changes

on Earth, salt dissolved in a low-energy marine environment created between the two continents precipitated into a layer that eventually became a perfect seal for the hydrocarbons that migrated into these reservoirs.

DOS SANTOS *et al.* (2013) reaffirmed that the Santos Basin is located on the passive eastern margin of Brazil, exhibiting a complex structural evolution formed during the African-American Split, in the Rift phase. They highlighted some important points about the petroleum system of the Santos Basin:

i) The main source rock is associated with lacustrine deposits, and shales of the Itapema Formation;
ii) The migration occurred in the Paleogene, when a truly effective seal, with up to 2,000 m of an evaporitic section developed, while and there was also the formation of structural traps, which suffered few changes;
iii) The reservoir consists of thick bundle of carbonates.

CARMINNATI *et al.* (2009) have further described the Pre-salt sequence, which can be subdivided into three subunits: a Lower Syn-Rift Sequence, an Upper Syn-Rift Sequence and a Sag Sequence, they indicated some characteristics of its reservoirs:

i) According to drilled wells, which cores produced in analogy to the Campos Basin, indicated that the lower part of the sequence was deposited in a lacustrine environment;
ii) Coquinas were deposited at the top of this sequence and represented a potential exploratory target in the Campos Basin;
iii) A well-delimited separation existed between the Upper Syn-Rift Sequence and the Sag Sequence. This sequence is composed mainly of microbioalites deposited in a saline paleoenvironment and represents the carbonate reservoirs;
iv) Erosive events following this deposition may have played an important role in the preservation or destruction of some sections of these reservoirs.

These events are also cited by JONES & CHAVES (2011), who conclude that the carbonates may have undergone significant changes through diagenetic alterations suffered by the reservoir rock, which eventually altered its petrophysical parameters

(permeability and porosity) and through of rainfall, which gave rise to an additional secondary porosity. These effects were being constructed through a combination of events and time.

Figure 2-11 presents the fields of the area known as Pre-salt, which extends from the Santos Basin to the Campos Basin and is located in ultra-deep waters. In the Santos Basin, the Pre-salt is found at a depth between 1900 and 2400 m, approximately 290 km offshore of the coast of Rio de Janeiro (PINHEIRO *et al.*, 2015).

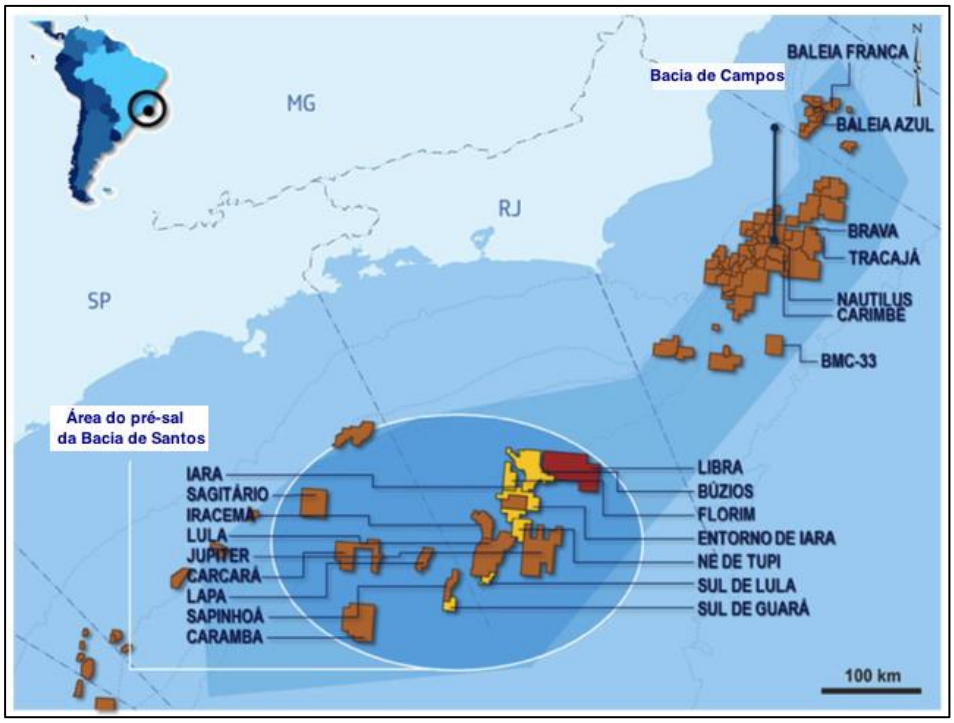


Figure 2-11 – Geographical location of the Brazilian Pre-salt.
(Source: modified from PINHEIRO *et al.*, 2015).

As for the petrophysical parameters, the reservoirs modeled and presented by MELLO *et al.* (2011), based on available data (lithology, temperature, maturity and hydrocarbon discoveries) consistent with knowledge of the Santos basin and its carbonate reservoirs, showed several values of porosity, especially in the Rift and Sag sequences. As a result of the proposed model, the values of this petrophysical property varied from 2% to 15% in Buracica/Piçarras, 2% to 14% in Jiquiá/Itapema and 2.5% to 16% in Alagoas/Sag. However, through high-resolution 3D seismic data obtained from an area of about 4,000 km² during 2011 and 2012, and more than 20 wells drilled in the BMS-9 block, more information from the Pre-salt region was obtained, according to DOS

SANTOS *et al.* (2013). The complemented and essential information about the main reservoir, Barra Velha Formation, are already available: it has a thickness that can reach 500 m with a porous column of up to 300 m, net-pay ranging from 30 to 200 m and an average porosity of 12 %, with associated permeabilities ranging from 50 mD to 1,000 mD. In addition, they reported that this reservoir was deposited in an alkaline lacustrine environment and corresponded to complex deposits with strong associated diagenetic processes.

As for the dynamic properties of these reservoirs, PIZARRO & BRANCO (2012) explained that due to the very heterogeneous nature of carbonate reservoirs, partly due to the great reactivity of the carbonates which usually suffer intense chemical diagenesis, hydrocarbon recovery is strongly controlled by vertical and horizontal connectivities, while regions of high permeability and the presence of fractures and faults can create preferential paths for the flow of fluids in these reservoirs, whether they are injected or produced.

2.2.3 Carbonate Rocks Analogous to Pre-Salt Reservoirs

BELTRÃO *et al.* (2009) stated that microbial carbonates in the predominant Pre-salt reservoirs, are very little known around the world, being the first great challenge to identify and study possible analogues for this type of rocks, considering the heterogeneity and the corresponding dynamic aspects. Their work, however, emphasizes that the continuity of the low and high permeability layers, the role of diagenesis and the role of fractures and faults can be critical in the search for an analogue of these reservoirs, be they outcrops or recent deposits.

VIRGONE *et al.* (2013) have described that the production of important carbonates occurs in lacustrine systems composed predominantly of microbialites/tufas, locally associated with oolites, in hypersaline shallow environments, or coquinas in more moderate salt environments, with the margins of lacustrine carbonate systems composed of overlapping microbial constructions, thus exhibiting different internal morphologies, due to changes in the depositional environment. The authors still argue that the study of analogous outcrops can help in the characterization of the properties of these carbonate deposits mainly with the aid of petrophysics and X-ray computed tomography techniques.

CORBETT & BORGHI (2013) have shown that lacustrine carbonates can develop from chemical and / or biological processes, as affected by a wide range of environmental

factors. They supposed that the carbonates present in the pre-salt reservoirs are similar to many other carbonate rocks exhibiting different types of porosity with a certain complexity and with a great variety of sizes and shapes. Due to this complexity, the authors argue that, for modeling purposes of reservoirs based on these carbonate rocks, careful characterization is necessary. Moreover, they affirm that the samples have several types of rocks, making a statistical characterization of these carbonates a great challenge.

2.2.4 Sergipe-Alagoas Basin

The Sergipe-Alagoas Basin is located in the states of Sergipe, Alagoas and also in a small portion of Pernambuco (Figure 2-12). Its total area is estimated at 44,370 km², of which one third is in the emergent part and the other two thirds in the submerged part. (CÂMARA, 2013).

According to CORBETT *et al.* (2013), the Sergipe-Alagoas Basin is known due to its outcrops that include all sections of the evolution of the Brazilian continental margin.

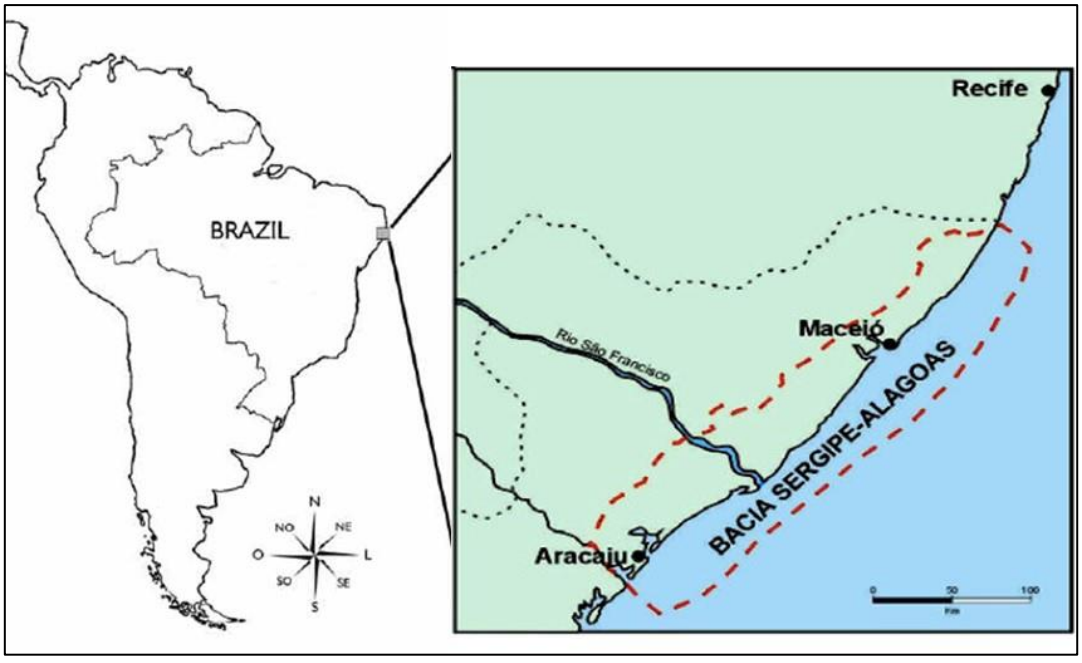


Figure 2-12 – Location map of the Sergipe-Alagoas Basin. (Source: modified from NOGUEIRA *et al.*, 2003).

Sergipe-Alagoas Basin occupies an elongated strip in the SW-NE direction of the Brazilian continental margin, 350 km long and 35 km wide on land (CAMARA, 2013).

The Basin is limited to the south by the Jacuípe Basin, by the Vaza Barris fault system in the ocean portion, and to the north, by the Pernambuco-Paraíba Basin by the Alto de Maragogi. The western boundary, with the crystalline basement dating from the Precambrian, is determined by systems of distensional faults and associated structures (TAVARES, 2014). According to FEIJÓ & PEREIRA (1994), the Sergipe and Alagoas basins were individualized because of important differences in their structural and stratigraphic character.

2.2.5 Morro do Chaves

The Morro do Chaves Formation is defined by AZAMBUJA & ARIENTI (1998) as a carbonate succession that intercalates with siliciclastic rocks of the Coqueiro Seco and Rio Pitanga formations. Located in the municipality of São Miguel dos Campos in the state of Alagoas, it currently corresponds to a quarry of limestone, formerly known as Quarry Atol but currently called the São Sebastião Mine. The quarry is about 60m high and 1km long, where there is an outcrop, a succession dominated by coquinas interspersed with sandstones and shales (CÂMARA, 2013).



Figure 2-13 – Stratification and heterogeneities present in the lacustrine carbonates of the Morro do Chaves Formation. (Source: CORBETT & BORGHI, 2013).

AZAMBUJA & ARIENTI (1998) stated in their work that coquinas from Morro do Chaves Formation are formed by non-marine bivalves and ostracodes with varied terrigenous percentages. The bivalves developed in shallow oxygenated waters, and after their death the shells were reworked and accumulated as coquina bars, washover fans and beaches, having different sizes and degrees of fragmentation (Figure 2-13). The formation and preservation of these thick deposits of coquinas are related to a high productivity of these bivalves, which

can be correlated to environmental and ecological factors, especially in moments of low tectonic activity and low contribution of terrigenous sediments.

2.2.6 Coquinas

The coquinas can be defined as rocks formed exclusively by shells or fragments of shells, mainly shells of bivalves, deposited by the action of some transporting agent (SCHÄFFER, 1972). As reported by CÂMARA (2013) and ESTRELLA (2015), the composition, stratum geometry and distribution of these carbonate rocks are governed by the sedimentation laws.

Coquinas are denominated autochthons when the deposition of shells and/or their fragments occurs *in situ* or with little movement without influence of transporting agents, or allochthons characterized as concentrations of shells and/or their fragments deposited by some transporting agent (KRUBEIN & SLOSS, 1963, *apud* CÂMARA, 2013). The rocks appear in the geological record as layers ranging from a few centimeters to a few meters, associated with terrigenous and/or carbonate deposits (CASTRO, 1988). TEIXEIRA (2012) reported that the rocks were formed by carbonate and siliciclastic constituents, sand to pebble size, deposited by a transporting agent in a lacustrine environment.

According to CASTRO (1988) and TEIXEIRA (2012), the main forms of the coquina layers are related to:

a. High bioclastic production: associated to environments where large variations in temperature, salinity, energy and turbidity occur;
b. Mass mortality: influenced by different factors that allowed colonization of the substrate and subsequent accumulation of bioclasts;
c. Hydraulic selection: associated with the capacity of waves and / or currents to carry shells of greater granulometry;
d. Diagenetic effect: related to the concentration of the shells through several processes that can influence in a greater or lesser degree to carbonation in the layers, depending upon temperature, pressure and pH.

According to ESTRELLA (2015) the bivalves were pulled out of the substrate by the action of currents or waves, and it is difficult to find deposits of shells of bivalves that maintain their position when alive. During transport the shells were subject to

fragmention or bioerosion (action of other organisms/microorganisms), thus weakening them and allowing their reduction to the micrite (carbonate mud), as presented by TEIXEIRA (2012).

The coquinas from Morro do Chaves Formation come from lacustrine environments, where currents and waves were the agents responsible for transporting these shells, being bivalve shells highly resistant to transport and therefore preserved in great quantity (TEIXEIRA, 2012 and ESTRELLA, 2015).

2.3 Techniques

In order to obtain and analyze the pore systems of the selected carbonate samples, it is necessary to summarize some important techniques used in the present work.

2.3.1 X-Ray Computed Microtomography

Computed X-ray microtomography (micro-CT, MCT or μCT), also called high-resolution computed tomography, can be defined as a non-destructive technique that allows the collection and analysis of hundreds of sections or images and enables subsequent reconstruction and three-dimensional visualization of the internal regions of the analyzed samples, as well as automated area and/or volume quantification (NETO *et al.*, 2011).

The most important aspects of the equipment and the computed microtomography technique are summarized below, according to information available in the work of NETO *et al.* (2011):

i) The basic components of a tomograph are: X-ray source, detector and a rotation system (MEES *et al.*, 2003);

ii) X-rays are produced artificially by the source through the acceleration of electrons against a metallic material of high atomic number, resulting in electromagnetic radiation characterized by high frequency, small wavelength and high penetration power;

iii) The smallest amount of any kind of electromagnetic radiation is called a photon, being the set of photons generated by bombardment of electrons of high kinetic energy defined as an X-ray beam;

iv) The attenuation is linked to a reduction of the intensity of a beam, as it crosses the material, leading to absorption of the radiation through the medium, or dispersion of the beam;

v) When an X-ray beam strikes a certain object of thickness x, part of the radiation is absorbed and part is scattered, while a fraction passes without interacting with this object, according to the equation:

$$I = I_0 e^{-\vartheta x} \quad (2.8)$$

where I is the intensity of the X-ray beam passing through the object, I_0 is the intensity that is not attenuated by the object and ϑ is the linear attenuation coefficient that is specific to each constituent phase of the analyzed object (SERVIDONI, 2012);

vi) When X-rays pass through an object, they are attenuated at different intensities, depending on the differences between the linear attenuation coefficients of the phases: being the density and the effective atomic number of the objects are the main factors that determine the degree of X-ray absorption;

vii) The construction of the image on computed tomography basically consists of an analysis of the attenuation suffered by the beam of radiation that crosses a certain object (LOPES *et al.*, 1997);

viii) The greatest limitation of X-ray tomography techniques (including computed microtomography) is the resolution reached (CNUDDE *et al.*, 2006);

ix) The resolution is related to the size of the sample and the distance between it, the X-ray source and the detector (AIRD, 1988);

x) Other important points reported by NETO *et al.* (2011) that affect the quality of the images are X-ray beam geometry, beam rotation around the analyzed sample, the choice of suitable voltage (in quilovolts - kV) and current (in microamperes - μA), which in turn depend mainly on the size and density of the sample, and the degree of X-ray dispersion (depending on the relationship between the tube and the X-ray detector);

xi) A similarity in the attenuation coefficients of the materials can hinder the differentiation between certain parts of the sample, thereby generating noise that affects the capacity of a tomograph to represent exactly the analyzed material (BULTREYS *et al.*, 2016);

xii) For a better data acquisition and reduction of possible noise or errors associated with the technique, several actions can be taken, especially the following: check the alignment between the beam emitting tube and the X-ray detector, consider the use of filters in order to reduce the incidence in the detector of low energy radiation, which does not contribute to the formation of images, an apparatus that reduces the dispersion of the X-ray beams and to perform a good post-processing of the obtained data, using programs and computational routines (TELES, 2016).

CNUDDE & BOONE (2013) described the technique of X-ray microtomography, including the main devices associated with the technique (Figure 2-14), in addition to explaining in detail the advantages and disadvantages of the technique. One of the great advantages of using X-ray microtomography is due to the non-destructive nature of this technique, allowing not only an analysis of valuable samples, without a need to destroy them during the process, but also allowing the monitoring of the microstructure of porous media during changing conditions. One of its disadvantages is the size of the voxel that can be obtained as a function of the sample size being analyzed.

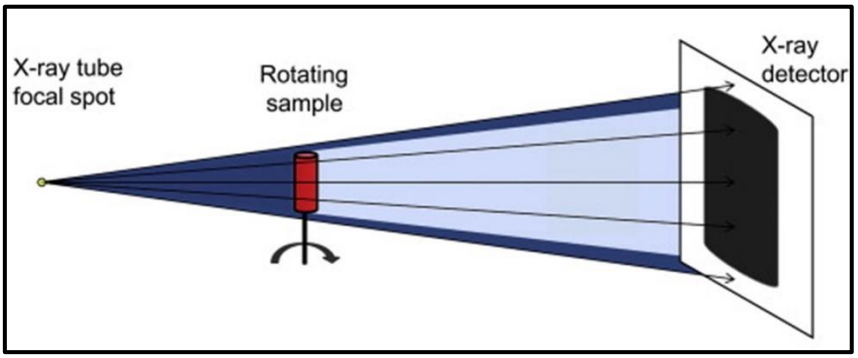


Figure 2-14 – Schematic diagram of the main components of the microtomographic equipment. (Source: Modified from CNUDDE & BOONE, 2013)

In general, the smaller the voxel size the larger the resolution of an image. Voxel (or pixel volume) can be defined as the 3D equivalent of a pixel (being the smallest unit of a digital or graphic image that can be represented in a digital device) in three-

dimensional space. Thus, on the one hand, the smaller the voxel size the larger the resolution of a 3D image reconstructed from the data obtained using microtomography, and on the other hand, the larger the sample the larger the voxel needs to represent it. In this way, it is invariably necessary to use plugs from a larger sample, in order to increase the desired resolution. These plugs or subsamples, however, may not represent the properties of the original sample, particularly where heterogeneity is an important feature of the sample analyzed (CNUDDE & BOONE, 2013). It is worth remembering, however, that the term resolution is constantly used to denote the size of the voxel, or also to represent the number of pixels and voxels in an image, but that its definition is tied to the Modulation Transfer Function (MTF) that is associated with the measurement of the resolution power of an image system (CNUDDE & BOONE, 2013).

Studies involving X-ray tomography applied to geosciences and engineering have been developed for several decades, ranging from works focused on the data acquisition process, such as a study of WITHJACK (1988) who focused on the rotation of the x-ray source during the acquisition of the data, including the detailed investigation of the influence of resolution and noise on the microtomograph data (HOUSTON *et al.*, 2013). WILDENSCHILD & SHEPPARD (2013) in their work focused on micro-CT as a tool for hydrology and hydrocarbon reservoir research.

As for the utilization of microtomography to analyse porous media, many studies involving their characterization of petrophysical properties (DUNSMUIR *et al.*, 1991; WILDENSCHILD *et al.*, 2002; COENEN *et al.*, 2004; ARNS *et al.*, 2005; TOUATI *et al.*, 2009; NETO *et al.*, 2011), utilizing many different types of rocks (YOUSSEF *et al.*, 2007; FERNANDES *et al.*, 2009; KACZMARCZYK *et al.*, 2010a, 2010b), are found on the literature. These studies ranged from the influence of the resolution for the prediction of petrophysical data using the technique of computerized microtomography (AL-ANSI, 2013) to the characterization of the petrophysical parameters of samples (cores) of non-conventional reservoirs (KNACKSTEDT *et al.*, 2012) at different sample scales (ALBERTS *et al.*, 2013).

Many numerical pore-scale simulators used for the prediction of several intrinsic parameters of the rocks, such as permeability, for example, require a precise quantitative description of the microstructures present in a sample (ARNS *et al.*, 2003). Using computed microtomography, it is possible to identify microstructures not only on the micrometer order, but also in nanometers (IZZO JR. *et al.*, 2008), depending upon the

desired resolution, the size of samples, and the tomographic equipment used to acquire the data.

Many researches involving dynamic imaging have been carried out (BULTREYS *et al.*, 2016), highlighting different processes in the geosciences, such as fluid flow in porous media (BERG *et al.*, 2013), carbonation (BOONE *et al.*, 2013) and dissolution (MENKE *et al.*, 2015) processes, dynamic two-phase flow processes (BULTREYS *et al.*, 2015b) and solute transport at the pore scale (BOONE *et al.*, 2015).

2.3.2 Nuclear Magnetic Resonance (NMR)

Nuclear Magnetic Resonance (NMR) is a non-destructive technique based on radio waves in an environment with a constant magnetic field on the atomic nucleus (COATES *et al.*, 1999).

NMR can be defined as a phenomenon that occurs when atomic nuclei that are immersed in a static magnetic field are exposed to a second oscillating magnetic field. Some atomic nuclei that have intrinsic angular momentum, or spin, are susceptible to the NMR phenomenon (COATES *et al.*, 1999).

The most commonly used physical property for NMR applications in laboratory analysis is the spin of hydrogen protons in water molecules. This magnetic spin is an intrinsic property of an atom that has an angular momentum, without physical rotation, and an associated magnetic moment (Behroozman *et al.*, 2014). Hydrogen is used because it has a relatively high magnetic moment due to the presence of only one proton and no neutrons at its core, thus causing the NMR signal induced by an external magnetic field to be large enough to be detected (FIORELLI, 2015), besides having an intrinsic angular momentum.

When the magnetic moments of the hydrogen protons are situated within a static magnetic field (B_0), they preform around the field at a frequency called the Larmor frequency. Thus, when there is no external magnetic field influence, the axes of the spins are randomly distributed and, for the NMR measurement, the nuclei of the atoms must be subjected to a constant external magnetic field, defined as B_0, so that the spins are then distributed neatly and aligned (COATES *et al.*, 1999; FIORELLI, 2015).

With the application of a magnetic field B_0 on the core of a magnetic atomic nucleus, the axis of the spin aligns itself to the axis of B_0, resulting from a torque (μ x

B_0), in such a way that the spin axis will precess in around of the magnetic field axis B_0. The frequency of Larmor, previously defined, can be obtained by the following equation:

$$f_L = \frac{\omega_L}{2\pi} = \frac{-\gamma|B_0|}{2\pi} \quad (2.9)$$

Where $\gamma = 0.2675 \times 10^9$ s^{-1} T^{-1} is the gyromagnetic ratio of the hydrogen nuclei, which is a measure of the strength of nuclear magnetism, being an intrinsic constant of each isotope. For hydrogen, $\gamma/2\pi$ = 42.58 MHz/Tesla, and ω_L represents the angular frequency of Larmor. The frequency of Larmor depends on the strength of the static magnetic field, which can vary many orders of magnitude (Behroozman *et al.*, 2014).

NMR experiment begins when the protons, initially in thermal equilibrium, are disturbed by an energizing pulse associated with the Larmor frequency. If this pulse is applied and then removed, the protons move away from thermal equilibrium and then slowly return to this condition. As the protons relax, they emit a measurable signal. Thus, the first step for the NMR measurement is the alignment of protons as a function of the external magnetic field (B_0). The nuclei are then said to be polarized (COATES *et al.*, 1999). The polarization increases exponentially with the characteristic time T_1 known as the longitudinal relaxation time of the rotation structure, which is represented by the following equation:

$$M_Z(t) = M_0\left(1 - e^{\frac{-t}{T_1}}\right) \quad (2.10)$$

Where $M_Z(t)$ is the magnetization at time t and M_0 is the equilibrium magnetization.

By applying a time-varying energizing magnetic field B_1, oscillating at the Larmor frequency, a change occurs in the direction of the magnetization vector M_0, whose direction becomes transverse to that of the magnetic field B_0. Thus, the magnetic field B_1 is applied perpendicular to B_0, during a short period of time (τ_p), and the resonance condition is established with the same frequency as Larmor (Coates *et al.*, 1999; Behroozman *et al.*, 2014).

Application of the energizing pulse causes a departure from the magnetization vector in the longitudinal direction, which may be associated with the angle with which

the magnetization vector moves away from the z-axis. This angle is variable and depends on the duration and/or intensity of the current with which the energizing pulse is applied. When a single pulse is applied with a 90 ° clearance angle, there is a free induction decay (FID), usually exponential and associated with phase loss of the protons, a process known as nuclear relaxation (Coates *et al.*, 1999, BEHROOZMAND *et al.*, 2014).

Each FID has its own time constant, called the transverse relaxation time (T_2) or spin relaxation time. The following equation represents the transverse relaxation time:

$$M_Z(t) = M_0^{\frac{-t}{T_2}} \qquad (2.11)$$

Where $M_Z(t)$ now represents the signal intensity at time t and M_0 the signal strength at time zero. The advantage of measuring the longitudinal relaxation time (T_1) is that, unlike transverse relaxation time, is unaffected by a lack of homogeneity of the magnetic field (Behrooyzand *et al.*, 2014).

For the analysis of porosity in samples, for example, the NMR equipment responds to the hydrogen index (HI), which is directly proportional to the amount of water in the pores of the saturated samples. If the fluid is different, it will be necessary to adjust the HI to be able to calculate the porosity. This property will be calculated by integrating the area under the T_2 distribution chart, as shown in Figure 2-15. Since the area under the distribution of T_2 is a function of the initial polarization, T_1, is necessary to guarantee the complete polarization of the hydrogen nuclei in order to have a representative and satisfactory measure. Proper determination of the T_2 distribution is a very important step in the processing of NMR data, since it represents the observed magnetization.

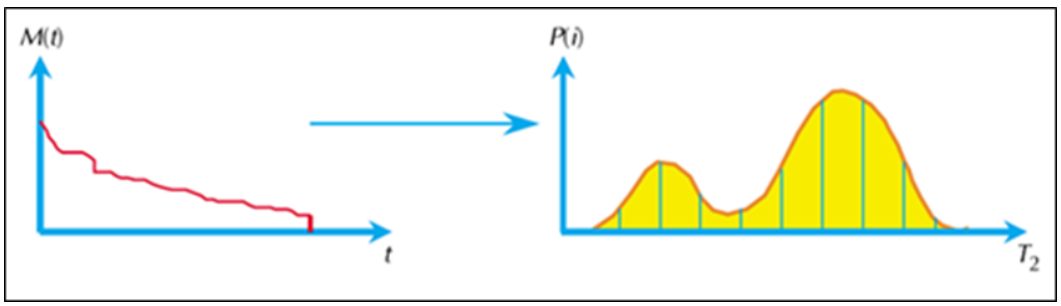


Figure 2-15 – Obtaining the porosity estimation from the T_2 distribution. (Source: modified by Coates *et al.*, 1999).

When the pores have geometric forms, morphological characteristics and/or distinct physicochemical properties, they will present different T_2 values. According to COATES *et al.* (1999) the transverse relaxation time T_2 will be directly proportional to the pore surface-volume ratio, which is a pore size measurement, when the formation is 100% saturated with a single fluid and when the acquisition is performed with the use of a short energizing pulse.

One can relate short relaxation times to relatively small pores and long relaxation times to larger pores. Figure 2-16 shows various relaxation time distributions for uniformly or heterogeneous distributed pore sizes with similar geometric shapes. These correlations are the subject of study in the literature, involving comparisons of the T_1 and/or T_2 distributions with the pore size distributions of various saturated porous media. ARNS (2004) and STRALEY *et al.* (1997) present studies involving these correlations, where the pore size distributions (or grains size distributions) agree the NMR data of arenitic and carbonate samples.

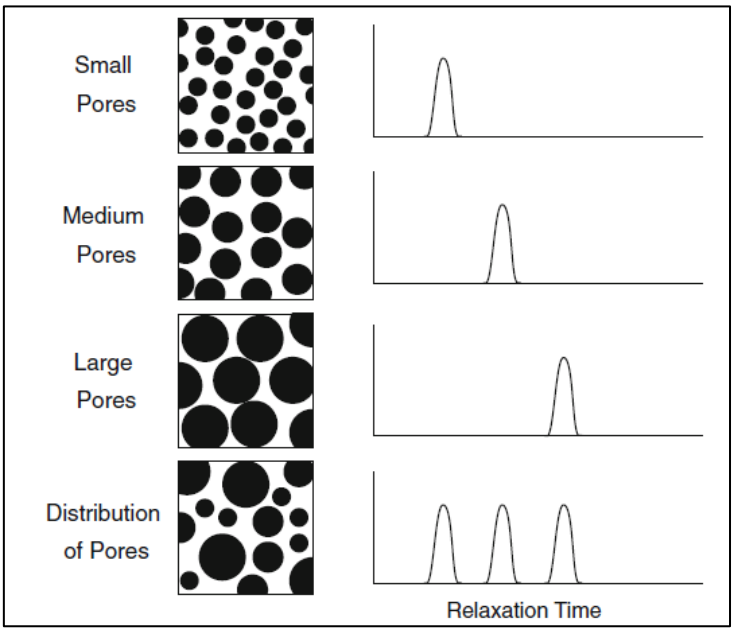


Figure 2-16 – Distribution of different relaxation times and the relationship with the distribution of different pore sizes. (Source: BEHROOZMAND *et al.*, 2014)

More complete theoretical discussions about nuclear magnetic resonance are provided by COATES *et al.* (1999), DUNN *et al.* (2002a, 2002b), LEVITT (2006) and BEHROOZMAND *et al.* (2014).

2.3.3 Three-Dimensional Digital Rock Reconstruction

After acquiring the data using microtomography, a step of 3D reconstruction and visualization of the results from 2D slices that are overlapped to form a set of sections ("*stack*") is necessary. The 2D sections are created from programs developed by microtomographers that use local linear attenuation coefficient (μ) distributions from the original (attenuated) intensity of the X-ray beam traversing the object (in this case the rock sample) and are converted by the detector into information that is later used for the formation of two-dimensional images. The data generated by these programs (*raw data*) can be read or converted by other commercial or open source programs, in digital formats ("*Dicom*", for example), which are supported by most of the programs intended to 3D reconstruction of images.

3D reconstruction, possible for each section, can be done through commercial programs such as *Avizo*® (Visualization Sciences Group, FEI Company), *VGStudio / VGStudio Max*® (Volume Graphics GmbH), *ScanIP*® (Simpleware Ltd.), *MAVI*® (Fraunhofer Institute for Industrial Mathematics ITW), or through free open source programs such as *Fiji / ImageJ* (Wayne Rasband, National Institute of Health, U.S.A.), for example, or even through algorithms developed with the help of *Matlab*® (The Mathworks Inc.) or other platforms that use programming languages like Fortran or C ++, among others.

A number of studies have focused on 3D reconstruction techniques from microtomographies (YEONG & TORQUATO, 1998a; 1998b; BLUNT *et al.*, 2002, OKABE & BLUNT, 2004), as applied to materials ranging from sandstone (NETO *et al.*, 2011) to extremely heterogeneous carbonates with the presence of vugular porosity (OKABE & BLUNT, 2007).

2.3.4 Segmentation

After the steps of data acquisition through the use of μCT and 3D reconstruction of the images using specific programs or well-defined programming routines, one has the stage of image processing and formulating three-dimensional models that can represent the *micro-* and *macro-structures* present in the analyzed rock sample. One of the most important steps during the analysis of reconstructed 3D images is segmentation.

Segmentation can be understood as a process of converting a grayscale, or even a colored image, to a binary image by identifying two populations present in the image

based on the intensity of their values obtained during tomographic acquisition (AL-RAOUSH & WILLSON, 2005). In studies involving the analysis of rocks and their respective pore systems, for example, these two populations refer to the pore phase and to solid phase, which makes it possible to distinguish the pores of solid materials present in a given sample. These two phases are due to different absorption properties of the materials, related to different local attenuation coefficients (μ) as previously explained, generating different values of intensity in the obtained images (WILDENSCHELD *et al.*, 2002). However, each phase has a variety of intensities due to the interactive nature of the X-ray spectrum with the analyzed system (AL-RAOUSH & WILLSON, 2005). The images of the porous media are on a gray scale and, in many cases, show bimodal distributions of the populations, corresponding to the empty space (pores) and the grains (LINDQUIST & VENKATARANGAN, 1999).

These simpler targeting methods are based on the choice of a threshold value obtained from the grayscale distribution histogram from the obtained images. Often computational algorithms are used based on the histogram evaluation to obtain the threshold value, and in some cases the choice of the value obtained is justified by the use of petrographic slides (HAYASHI, 2014; HOERLLE, 2018).

2.3.4.1 Non-Automated Methods

Among the most used non-automated segmentation methods, the analysis of thin sections, a technique which identifies the pores with blue epoxy resin, facilitating the observation of these structures. The concomitant visualization between the thin section and images from the X-ray computed microtomography technique, through the use of different computational programs allows the choice of a threshold value and its segmentation (HOERLLE, 2018). This analysis includes some uncertainties related to the experience of the user during the identification of the pore system, including also the limitation of the optical microscope itself, whose resolution may be lower than that of the μCT images.

Direct analysis using optical microscopy with SEM improves the segmentation procedure (WILDENSCHILD *et al.*, 2002; AL-RAOUSH & WILLSON, 2005). The use of thin sections impregnated with blue epoxy resin helps to more accurately identify pore spaces, especially for detecting the intraparticle porosity of coquina samples. Although the use of visual segmentation methods requires some experience, they often improve the selection of regions where meso- and macro-pores are dominant, among other

applications. The use of SEM as an auxiliary tool also guarantees the possibility of visualizing, with high resolution, regions that may become indistinct in μCT images generated with larger pixel sizes (BLUNT *et al.*, 2013; BULTREYS *et al.*, 2016).

2.3.4.2 Automated Methods

SEZGIN & SANKUR (2004) performed and extensive research on the most varied automated methods of segmentation of images, classifying them according to their similarities and ranking them according to an average coming from the evaluation of five pre-established criteria.

Table 2-2 presents their classification adopted some of the methods that will be explained in this section and can be used for image analysis of carbonate rocks (SILVA, 2015; HOERLLE, 2018).

Table 2-2 – Classification of the methods studied in the present work from the classification proposed by SEZGIN & SANKUR (2004) based on 40 evaluated methods.

Method	Position	Average Rating
Cluster_Kittler	1°	0.256
Cluster_Otsu	6°	0.318
Cluster_Ridler	14°	0.401
Local_Bernsen	24°	0.550
Local_Niblack	33°	0.638

The clustering-based method called *Cluster_Ridler*, also defined as an iterative thresholding method, presented in the paper by RIDLER & CALVARD (1978), also known as *Isodata*, was one of the first iterative models based on two major Gaussian distributions. Basically this method, at a given iteration n, finds a threshold value called T_n, obtained from the mean of the object and background classes, so that the iteration ends when changes in the values of these averages become very small.

The presence of two main peaks a grayscale histogram demonstrates the existence of two distinct luminance regions, one corresponding to the object and one to the background. An important advantage of this method is that by establishing distinct levels for the object and for the background, a processed image always appears as a white object contrasting under a black background. However, the main disadvantage of this method occurs when the histogram is bimodal, with two well defined distinct peaks, which makes it difficult obtain an appropriate level of separation, is.

The clustering-based method called *Cluster_Otsu*, also defined as a clustering thresholding method, presented in the work of OTSU (1979), is based on the minimization of the weighted sum of the variances inherent to each class (that of the object and the background) to establish an optimal threshold. It is important to emphasize that the minimization of the inherent variances of each class is equivalent to the maximization of the data between these classes. In addition, the best results using this method occur when the number of pixels in a class, such as that of the object, for example, approximates the number of pixels in the background.

Some important points related to this method are (OTSU, 1979):

i) The procedure to obtain the threshold (or thresholds, depending on the number of classes) is simple, so that the computational algorithms developed to represent this method only use the zero order and first order accumulated moments of the histogram of gray scales, in their calculations;

ii) An optimal threshold value is selected automatically and presents great stability since the technique is based on integration (that is, on a global property) of the histogram, and not on differentiation (that is, on local properties) of the histogram.

Another clustering-based method, also defined as a minimum error thresholding method, is called *Cluster_Kittler*, presented in the work of KITTLER & ILLINGWORTH (1986). This method is based on the premise that the image can be characterized by a mixed distribution, $p(g)$, of pixels of the object $p_f(g)$ and of the background $p_b(g)$, such that the premise that the variance is the same is discarded, leading essence to a problem of Gaussian minimum error density adjustment.

Local method based on the work of NIBLACK (1986), uses the local variance as the evaluation parameter, based on obtaining the local mean $m(i,j)$ and the standard deviation, $\sigma(i,j)$, calculated for a window of pixels of dimensions $b\ x\ b$, the parameters calculated for a given pixel of coordinates (i,j), its neighborhood will be composed of a window of $b\ x\ b$ pixels.

However, a local method based on the work of BERNSEN (1986), uses as an evaluation parameter of the local contrast, such that the threshold is associated with a mean value, calculated as the average the value of the minimum intensity of the pixel $I_{low}(i,j)$ and the maximum intensity of the pixel $I_{high}(i,j)$ within a window of $b\ x\ b$

pixels (Figure 2-17). This method uses a predefined value for the threshold in its algorithm, so that if the local contrast is greater than or equal to this value, the threshold value is associated with the local gray level value (the mean values of the minimum and maximum gray within the pixel window), and if it is smaller than this, the neighborhood is considered to consist of only one class, object or image, as a function of the obtained $T(i, j)$.

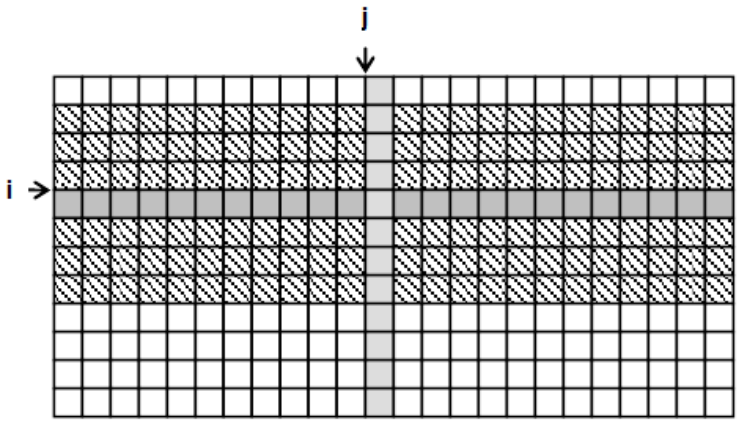


Figure 2-17 – Example of a pixel window, highlighting a pixel of coordinates (i, j) used in the Bernsen method (Local_Bernsen). (Source: Adapted from BIENIECKI & GRABOWSKI, 2005)

2.4 Pore-Network Modeling

Pore-Network Modeling (PNM) considers a porous medium as a system of porous elements composed of bodies (Pore Bodies), which because of their larger dimensions control the porosity of the medium, and throats (Pore Throats), whose reduced dimensions determine the hydraulic conductivity (DE VRIES *et al.*, 2017). The first studies involving the use of PNMs were performed by FATT (1956).

An important feature of the reconstruction of porous systems through the PNM technique is that the generated models are computationally simple, in that reconstructions generate porous body-throat systems, which can be used for numerical simulation purposes involving fluid flow without large computational demand (RAOOF *et al.*, 2013). Moreover, important statistical characteristics of the porous media models generated using this technique can be obtained: pore size distribution, as presented in the works of OREN *et al.* (1998), LINDQUIST *et al.* (2000) and RAOOF *et al.* (2013), and distributions of coordination numbers, as shown by RAOOF & HASSANIZADEH (2009), RAOOF *et al.* (2013) and XIONG *et al.* (2016). The coordination number, which

is a topological property of the network, can be defined as the number of pore throats connected to a given pore body (JOEKAR-NIASAR & HASSANIZADEH, 2011).

It is important to highlight that the bodies and the throats can present different geometries when analyzing a slab of the cross section of these structures. For simulation purposes, for example, the cross-sections can retain the wetting fluid in their corners while allowing other fluids to flow through the same pore (RAOOF *et al.*, 2013), thus configuring a more realistic feature to the model of the porous system obtained.

The reconstruction of a porous medium using PNMs technique from the network extraction in X-ray microtomography images can be performed in two stages: one refers to the separation of the pore space in discrete elements while the second one relates to subsequent measurement of the geometric properties of each element of the pore network, such as radius, volume, length and some shape description parameters for each element of the network. The methods that approach these two steps can be classified as: methods that select and separate the pore space based on a central topology (Topology-central Methods) and methods that do it based on a central morphology (Morphology-central Methods), as presented in the work of BULTREYS *et al.* (2016).

The methods based on the central topology, developed initially by LINDQUIST *et al.* (1996), use the concept of the medial axis, a representation of the porous space through a central skeleton, through which the branching points are considered the centers of the porous bodies. Usually the medial axis is used as a search structure to find the location of the throats, recognized in the form of narrower cross-sections.

These methods, however, present some associated problems, especially when there are small defects/imperfections in the surface of the porous space coming from the image that is used as the basis for the reconstruction and generation. These small imperfections lead to inaccurate identification, according to the existence of incorrect branches originating from the process of separation between the voxels that define the rock and the pore. Techniques of pre- and post-processing of the images can be used to try to correct these deviations. Another problem is the assumption that the pore network junctions are defined as pore bodies, since they often do not necessarily form the geometric pore bodies (BULTREYS *et al.*, 2016). This problem eventually interferes with simulations involving the flow of fluids, because processes such as slow drainage and imbibition are controlled by the pore network geometry. However, the great advantage is

due to the fact that networks, generated using these methods, are directly related to the real geometry coming from the analyzed images.

Methods based on the central morphology, initially developed by ZHAO *et al.* (1994) use a multi-oriented scanning of the digitally reconstructed porous system to identify constrictions in order to obtain a more reliable coordination number, thereby obtaining a better separation between porous bodies and pore throats. However, after checking with a defined number of guidelines, some throats may not be identified or even lost during scans.

Among the methods based on morphology, some are related to the central axis topology method, and are defined as Grain-based Methods. In this case, the individual grains are identified and dilated in such a way that no pore spaces remain. In places where three grains touch, a skeleton forms, while points where four or more grains touch each other become the nodes of the porous network.

A complete description of PNMs and associated simulation techniques can be found in the works of BULTREYS *et al.* (2016), RAOOF *et al.* (2013), RAOOF (2011), JOEKAR-NIASAR (2010) e BLUNT (2001).

2.4.1 Numerical Simulation

From the acquisition of data through computed X-ray microtomography techniques, three-dimensional digital reconstruction (or two-dimensional, depending on the focus of the study), segmentation of the reconstructed image capable of separating the object, i.e. rock, from the background. It is possible to calculate fluid flow parameters related to the flow of different fluids (single or multiphase flow) and different rocks.

The present work opted for simulations of fluid flow at the pore level based on the studies of JOEKAR-NIASAR & HASSANIZADEH (2011) and RAOOF *et al.* (2013), it is possible to estimate the parameters of the meso- and macro-scale from micro-scale information, specifically of the pore system to be reconstructed. Absolute permeability calculations, as previously described, are based on the relation between the resolution of equations for the micro and meso/macroscale. For two-phase oil-water simulation in a porous system, in which one of the fluids is defined as wetting and the other as non-wetting, the numerical simulations are done using PNM technique because it is computationally simpler and allows the estimation and prediction of parameters in samples with larger dimensions.

For PNM simulation of flow of one or more fluids two approaches are used to solve the relevant equations. A first approach assumes a quasi-static flow modeling for estimating the absolute permeability calculation, and a second approach uses dynamic flow modeling for estimating capillary pressures and relative permeabilities as a function of water saturation.

Although the two approaches can be used for two-phase simulation, there are some differences in the use of each (JOEKAR-NIASAR, 2010):

a. Quasi-static modeling is based on the fact that fluid displacement is controlled by the entry capillary pressure of the different pores, thus allowing only simulations of the equilibrium states of the drainage and imbibition processes. In this case, conditions between the states of equilibrium are not modeled, being the modeling necessary near these states.
b. In dynamic modeling, capillary and viscous forces should be included at the pore scale, with fluid invasion at the pore scale determined by the entry capillary pressure of the network elements, and the rate of invasion as determined by capillary and viscous forces. This modelling approach is more robust and complex modeling than quasi-static approach.

2.4.1.1 Single-phase Flow

Fluid flow is established in the network by imposing a pressure differential across network. It is assumed that the laminar flow occurs with each pore throat may as described with the Hagen-Poiseuille equation:

$$Q_{ij} = g_{ij}(p_j - p_i) \tag{2.32}$$

where Q_{ij} is the volumetric flow rate through the pore throat between two adjacent porous bodies, i and j, connected, p_i and p_j are the pressures of these two adjacent bodies and g_{ij} is the conductance of the cylindrical shaped pore throat whose value can be obtained by the following equation:

$$g_{ij} = \frac{\pi R_{ij}^4}{8\mu l_{ij}} \tag{2.33}$$

where R_{ij} is the radius of the pore throat that connects the bodies *i* and *j*, μ is the dynamic viscosity of the fluid and l_{ij} the length of the pore throat.

For a flow considered incompressible, the continuity equation can be applied in the pore connections as follows:

$$\sum_{j=1}^{N_i} Q_{ij} = 0; \qquad i = 1,2,3,\dots,N_i \tag{2.34}$$

where Q_{ij} is the volumetric flow rate within the pore throat going from the pore body *i* to the body *j*, and N_i is the coordination number of pore body *i*.

Equations 2.32-2.34 can be solved through a linear system of equations with a sparse, symmetric and definite positive coefficient matrix, which will be solved to obtain the pressures in the pore bodies. Considering a well-defined volume sample, the average velocity of a fluid in the pore, $\bar{v}$, can be calculated as (RAOOF *et al.*, 2013):

$$\bar{v} = \frac{Q_{tot} L}{V_f} \tag{2.35}$$

where Q_{tot} is the total flow rate through the pore network, which can be determined at the inlet or outlet of the pore network as the sum of all flows, *L* is the length of the pore network and V_f is the total volume of the liquid phase within the pore network.

The absolute permeability *K* of the sample is then calculated using the Darcy equation:

$$K = \frac{\mu Q_{tot} L}{A\Delta \mathrm{P}} \tag{2.36}$$

where μ is the viscosity of the fluid, ΔP is the pressure differential between the inlet and outlet of the pore network and A is the cross-sectional area of the porous network.

The equations described above refer to the calculations required to obtain absolute permeability estimates using the PNM technique. The equations necessary for the simulations involving two-phase flow and obtaining the capillary pressure values and relative permeabilities, as a function of water saturation, will be discussed below.

2.4.1.2 Two-phase Flow

For the simulations involving the flow of two fluids in the porous network, considering the existence of a wetting and non-wetting fluid, the quasi-static modeling approach was adopted, based on the work of JOEKAR-NIASAR (2010) and RAOOF (2011), who described improved, more robust and efficient algorithms for solving the proposed equations. These algorithms are defined for two pressures, that is, when a body is filled with two fluids, each fluid has its own pressure (JOEKAR-NIASAR, 2010). This concept is based on the work of THOMPSON (2002), who defined local capillary pressures and solved the pressure field for the two phases separately. The capillary pressure for body *i* can be defined as:

$$p_i^c = p_i^n - p_i^w = f(s_i^w) \tag{2.37}$$

where p_i^c is the pore capillary pressure *i*, p_i^n is the pressure of the non-wetting phase in the pore *i*, p_i^w is the pressure of the wetting phase, being the shown difference a function of saturation of the wetting phase, $f(s_i^w)$, in the body *i*.

A flow rate Q_{ij}^{α} is associated with the pore throat *ij* for each phase, non-wetting and wetting, separately. Equation 2.34 can then be replaced by the total volume balance for the pore *i*:

$$\sum_{j=1}^{N_i} Q_{ij}^n + Q_{ij}^w = 0 \tag{2.38}$$

In addition, a separate volumetric balance for each phase is applied:

$$V_i \frac{\Delta s_i^\alpha}{\Delta t} = -\sum_{j=1}^{N_i} Q_{ij}^\alpha \; ; \;\; \alpha = w, n \tag{2.39}$$

where V_i is the volume of pore body i, s_i^α is the saturation of phase α in body i and Q_{ij}^α is the volumetric flow rate of phase α in body i. This volumetric flow rate is given by the following equation:

$$Q_i^\alpha = -k_{ij}^\alpha \Delta p_{ij}^\alpha \; ; \qquad \alpha = w, n \tag{2.40}$$

where k_{ij}^α is an equivalent conductivity, which is a function of the pore throat radius, pore throat length, fluid viscosity, and location of the meniscus in the pore throat, and Δp_{ij}^α is the pressure differential between the bodies i and j for each phase. This formulation allows the inclusion in the simulation of mechanisms related to local capillary pressure, such as a snap-off, for example.

Before exposing the other equations, it is necessary to present the main assumptions used in the equation and resolution of the two-pressure algorithm:

a. The volume of the pore throats is considered negligible when compared to the volumes of the bodies, such that the time required to fill a pore throat is not considered for calculation purposes;
b. The hydraulic resistance to fluid flow in bodies is assumed negligible when compared to that of the throats;
c. The fluids are assumed incompressible and immiscible and the solid matrix is defined as rigid;
d. It is assumed that flow in the pore throats has a low Reynolds number, such that the transient effects are neglected in the pore scale;
e. Finally, no effect of gravity is considered in the simulations such that flow occurs only as a function of the pressure differential between the pore network boundaries.

Considering a pore body *i* with radius R_i, saturation of the wetting phase is given by:

$$p_i^c(s_i^w) = \frac{2\sigma^{nw}}{Ri\left(1 - exp(-6{,}83 s_i^w)\right)} \tag{2.41}$$

where s_i^w is the wetting phase saturation and σ^{nw} is the interfacial tension between the wetting and non-wetting fluids.

The minimum saturation of the wetting phase ($s_{i,min}^w$) that must be considered in a pore body depends on the overall pressure difference (p_{global}^c) and is given by the equation:

$$s_{i,min}^w = -\frac{1}{6{,}83} ln\left(1 - \frac{1}{R_i}\frac{2\sigma^{nw}}{p_{global}^c}\right) \tag{2.42}$$

When the inlet capillary pressure in a pore throat invaded by the non-wetting fluid is less than the capillary pressure in the pore body associated with this throat, it will be invaded by the non-wetting fluid such that the inlet capillary pressure is given by (MA *et al.*, 1996):

$$p_{e,ij}^c = \frac{2\sigma^{nw}}{r_{ij}} ln\left(\frac{\theta + cos^2\theta - \frac{\pi}{4} - sin\theta cos\theta}{cos\theta - \sqrt{\frac{\pi}{4} - \theta + sin\theta cos\theta}}\right) \tag{2.43}$$

where r_{ij} is the radius of the cross-section circle of the pore throat connecting the bodies *i* and *j*, and θ is the contact angle between the wetting phase and the pore.

The pore throat conductivity values depend on whether they are occupied by the wetting fluid alone or are being invaded by the non-wetting fluid. In the first case mentioned, based on the work of AZZAM & DULLIEN (1977):

$$k_{ij}^{w} = \frac{2r_{ij}^{2}}{\pi\mu^{w}l_{ij}} \quad ; \quad k_{ij}^{n} = 0 \tag{2.44}$$

where μ^w is the viscosity of the wetting phase and l_{ij} is the length of the pore throat. In case the pore throat is invaded by the non-wetting fluid, based on the work of RANSOHOFF & RADKE (1988):

$$k_{ij}^{w} = \frac{4-\pi}{\beta\mu^{w}l_{ij}}\left(\frac{\sigma^{nw}}{p_{ij}^{c}}\right)^{4} \tag{2.45}$$

$$k_{ij}^{n} = \frac{\pi}{8\mu^{n}l_{ij}}\left(r_{ij}^{eff}\right)^{4} \tag{2.46}$$

$$r_{ij}^{eff} = \frac{1}{2}\left(\sqrt{\frac{r_{ij}^{2} - (4-\pi)\left(\frac{\sigma^{nw}}{p_{ij}^{c}}\right)^{2}}{\pi}} + r_{ij}\right) \tag{2.47}$$

Where μ^n is the viscosity of the non-wetting phase, p_{ij}^{c} is the entry capillary pressure of the pore body located in the immediately anterior region and β is a resistance factor that depends on the geometry, surface roughness and other parameters associated with the cross section. The necessary information on the form factor can be found in the work by ZHOU *et al.* (1997).

For the modeling of the snap-off, which occurs during drainage when the capillary pressure of the pore throat becomes less than a critical value of capillary pressure, the following criterion is used for the verification or not of the occurrence of snap-off:

$$p_{ij}^{c} \leq \frac{\sigma^{nw}}{r_{ij}}(cos\theta - sin\theta) \tag{2.48}$$

At the end of the snap-off, the wetting fluid will complete the entire pore throat and the non-wetting phase will be disconnected, remaining in the pore bodies connected by this throat (JOEKAR-NIASAR, 2010).

The pressures are calculated in order to reduce the computational cost, considering then a mean pressure in pore *i* with associated saturation:

$$\bar{p}_i = s_i^w p_i^w + s_i^n p_i^n \tag{2.49}$$

Knowking that $s_i^w + s_i^n = 1$, there is the following system of equations:

$$p_i^w = \bar{p}_i - s_i^n p_i^c \tag{2.50}$$

$$p_i^n = \bar{p}_i + s_i^w p_i^c \tag{2.51}$$

These equations are used to calculate the pressures of the wetting and non-wetting phases based on the mean pressure previously defined. Finally, replacing equations 2.50 and 2.51 in the equation given by the substitution of equation 2.38 in equation 2.40, there is:

$$\begin{aligned}\sum_{j=1}^{N_i}\left(Q_{ij}^n + Q_{ij}^w\right)\left(\bar{p}_i - \bar{p}_j\right) \\ = -\sum_{j=1}^{N_i}\Big[\left(k_{ij}^n s_i^w - k_{ij}^w(1 - s_i^w)\right)p_i^c \\ + \left(k_{ij}^w\left(1 - s_j^w\right) - k_j^n s_j^w\right)p_j^c\Big]\end{aligned} \tag{2.52}$$

which relates the mean pressures on the bodies *i* and *j* connected by a pore throat.

Thus, after the calculation of the mean pressures, the pressures of each phase are calculated by returning to equations 2.50 and 2.51, as well as the volumetric flow rates of

each phase according to equation 2.40. The volumetric flow rates at a later time can be obtained from the flows calculated in previous times.

Using equation 2.40 for two phases and summing up the terms and rewriting p_i^w in terms of p_i^c and p_i^n there is:

$$Q_{ij}^n + Q_{ij}^w = \left(k_{ij}^n + k_{ij}^w\right)\left(p_i^n - p_j^n\right) - k_{ij}^w\left(p_i^c - p_j^c\right) \tag{2.53}$$

From the previous equation, it is possible to obtain:

$$Q_{ij}^n = k_{ij}^n \frac{\left(Q_{ij}^n + Q_{ij}^w\right)}{\left(k_{ij}^n + k_{ij}^w\right)} - \frac{k_{ij}^w k_{ij}^n}{\left(k_{ij}^n + k_{ij}^w\right)}\left(p_i^c - p_j^c\right) \tag{2.54}$$

Substituting the equation above in equation 2.39 we have:

$$V_i \frac{\Delta s_i^w}{\Delta t} - \sum_{j=1}^{N_i} k_{ij}^n \frac{\left(Q_{ij}^n + Q_{ij}^w\right)}{\left(k_{ij}^n + k_{ij}^w\right)} - \frac{k_{ij}^w k_{ij}^n}{\left(k_{ij}^n + k_{ij}^w\right)}\left(p_i^c - p_j^c\right) = 0 \tag{2.55}$$

The term referring to capillary pressure can be approximated by:

$$\left(p_i^c - p_j^c\right) = \frac{\partial p_{ij}^c}{\partial s_{ij}^w}\left(s_i^w - s_j^w\right) \tag{2.56}$$

where the term $\frac{\partial p_{ij}^c}{\partial s_{ij}^w}$ is calculated with the immediately preceding pore body.

After replacing equation 2.56 in equation 2.55 and reformulating for a linear equation matrix, there is a saturation update after a time step *x*:

$$\left(\frac{V_i}{\Delta t}-\sum_{j=1}^{N_i}\frac{k_{ij}^n k_{ij}^w}{\left(k_{ij}^n+k_{ij}^w\right)}\frac{\partial p_{ij}^c}{\partial s_{ij}^w}\right)(s_i^w)^{x+1}+\left(\sum_{j=1}^{N_i}\frac{k_{ij}^n k_{ij}^w}{\left(k_{ij}^n+k_{ij}^w\right)}\frac{\partial p_{ij}^c}{\partial s_{ij}^w}\right)\left(s_j^w\right)^{x+1} = \frac{V_i}{\Delta t}(s_i^w)^x+\sum_{j=1}^{N_i}\frac{k_{ij}^n}{\left(k_{ij}^n+k_{ij}^w\right)}\left(Q_{ij}^n+Q_{ij}^w\right) \tag{2.57}$$

The time step should then be determined based on the filling time of the pore body by the wetting or non-wetting phase, wherein the saturation of the wetting phase ranges from 1 to a minimum value ($s_{i,min}^w$) of saturation calculated by equation 2.42, when the body is drained. If imbibition occurs in locally in some bodies, the saturation in some bodies can return to the maximum value, 1. Thus, the time will depend on the process.

$$\Delta t_i=\begin{cases}\frac{V_i}{Q_i^n}\left(s_i^w-s_{i,min}^w\right) & para\ drenagem\ local, Q_i^n>0\\ \frac{V_i}{Q_i^n}(1-s_i^w) & para\ embebição\ local, Q_i^n<0\end{cases} \tag{2.58}$$

Thus, the time step will be chosen so that the time Δt_i be minimum.

Finally, for the calculation of absolute permeabilities, the following equation is used (CONSTANTINIDES & PAYATAKES, 1996):

$$\frac{q^\alpha}{A}=-K_{r\alpha}\frac{K}{\mu^\alpha}\frac{\Delta p^\alpha}{L}\ ;\quad \alpha=w,n \tag{2.59}$$

where q^α is the total flow rate for phase α, A is the cross-sectional area of the pore network normal to the direction of flow, $K_{r\alpha}$ is the relative permeability of phase α, K is the absolute permeability of the pore network, μ^α is the viscosity of phase α, L is the pore network length in the flow direction and Δp^α is the pressure drop of phase α, which can be the wetting phase (w) or the non-wetting phase (n).

For calculation of the flow rate q which is used in the previous equation, Poiseuille's equation is used:

$$q_{ij}^{\alpha} = \frac{\pi}{8\mu^{\alpha} l_{ij}} r_{ij}^{4} (p_i - p_j) \tag{2.60}$$

where q_{ij}^{α} is the total flow rate of phase α from body i to body j, p_i and p_j are the pressures in these bodies and l_{ij} is the length of the pore throat between the aforementioned bodies.

The volumetric balance for each body i requires that the following equation be satisfied:

$$\sum_{j=1}^{N_i} q_{ij}^{\alpha} = \frac{\pi}{8\mu^{\alpha}} \sum_{j=1}^{N_i} r_{ij}^{4} \frac{(p_i - p_j)}{l_{ij}} = 0 \tag{2.61}$$

Thus, satisfying the previous equation and calculating q_{ij}^{α}, one can obtain the absolute permeability values for each phase α, wetting (w) or non-wetting (n).

3 MATERIALS AND METHODS

This chapter will discuss each stage of the proposed workflow, including the method, materials and techniques used, studied and developed.

3.1 Workflow

The workflow proposed and presented below aims at an approach to obtain petrophysical data in coquinas involving all the steps necessary to obtain experimental data, such as porosity and absolute permeability, the steps of data acquisition through computed X-ray microtomography and digital reconstruction of the porous systems of the studied rocks, as well as the numerical simulation of the flow of fluids involving Pore-Network Modeling (PNM) and porosity studies in sub-resolution. Figure 3-1 presents an overview of the proposed workflow, contemplating all the steps and techniques necessary to obtain petrophysical parameters in the samples of selected coquinas. The boxes identified by the same colors correspond to steps that are performed and analyzed together, being directly dependent.

Boxes delimited by green color refer to the stages of geological and morphological characterization of the studied samples, including petrography. The gray boxes correspond to the steps of acquisition of experimental data through several techniques, as well as the acquisition of μCT data and treatment of these. The steps in the blue boxes represent the studies of digital reconstruction of 3D pore networks and numerical simulations of single phase flow. The orange color identifies the steps related to the analysis of the representativeness of the results, which must be obtained in the REV of each sample. The yellow boxes identify the steps for obtaining data that are used in the numerical simulation of the two-phase flow.

Although the workflow was motivated by studies of coquina samples, it can be applied *a priori* to a wide range of heterogeneous carbonate samples. In this work, however, only samples of coquinas are considered (i.e. rocks) geologically analogous to the reservoir rocks present in some fields of the Brazilian Pre-salt region in the Santos Basin.

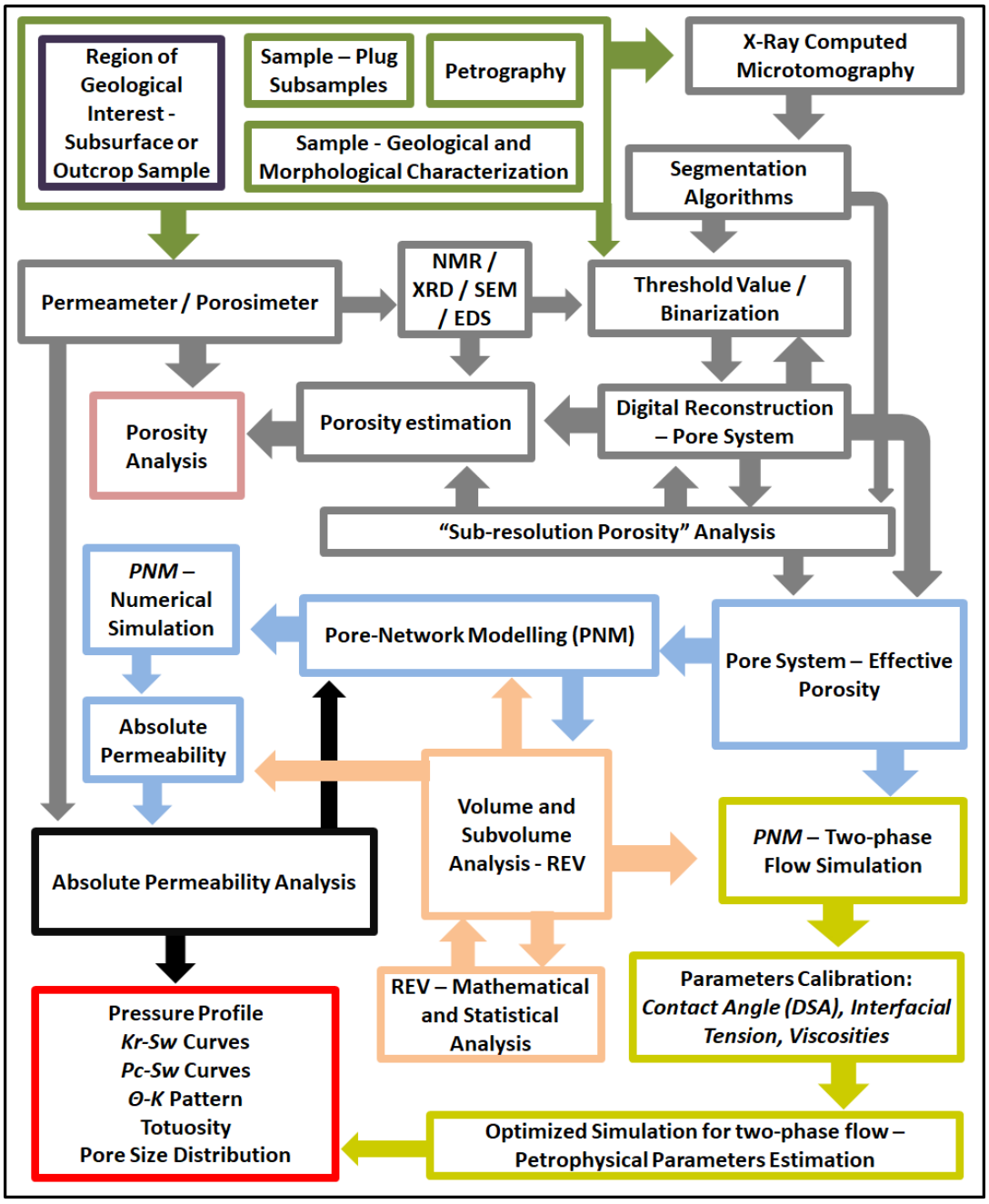


Figure 3-1 – Overview of the proposed workflow for obtaining petrophysical parameters of coquinas from basic and digital petrophysical techniques.

For the identification of each step in Figure 3-1, in order to present a more detailed description of each activity and its associated methods and materials, the materials and methods selected are presented in this section. Figure 3-2 presents the main techniques, by means of various through the images of the equipment used throughout this study.

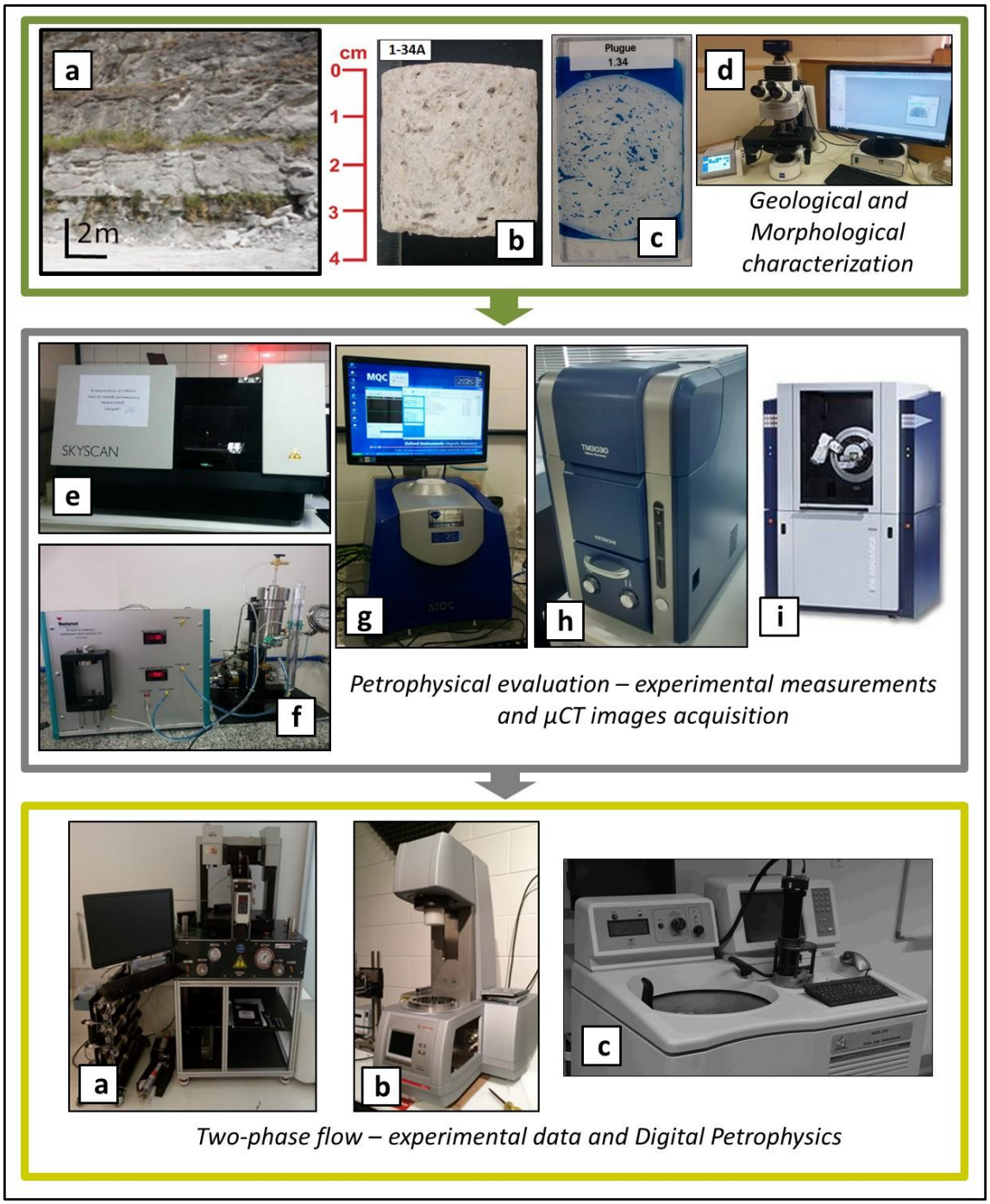


Figure 3-2 – Main techniques selected during execution of this work: (a) geological characterization of a region of interest; (b) selection and morphological evaluation of coquina plugs; (c) preparation and analysis of thin sections using (d) optical microscopy; (e) μCT images acquisition; (f) porosity and absolute permeability measurements; (g) NMR data acquisition; (h) SEM/EDS analysis; (i) XRD analysis; (j) drop shape analysis (DSA); (k) viscosity measurements; and (l) the centrifuge system for capillary pressure measurements.

The following items will generally address the main stages of the workflow described in Figure 3-1, detailing the equipment used and the methodologies followed.

3.1.1 Geological and Morphological Characterization / Petrography

Initially one should select and delimit a region whose geology has some interest. In the present study, the Sergipe-Alagoas Basin was selected, more specifically the Morro do Chaves Formation. Figure 3-3 shows the location of the Morro do Chaves Formation, in the city of São Miguel dos Campos.

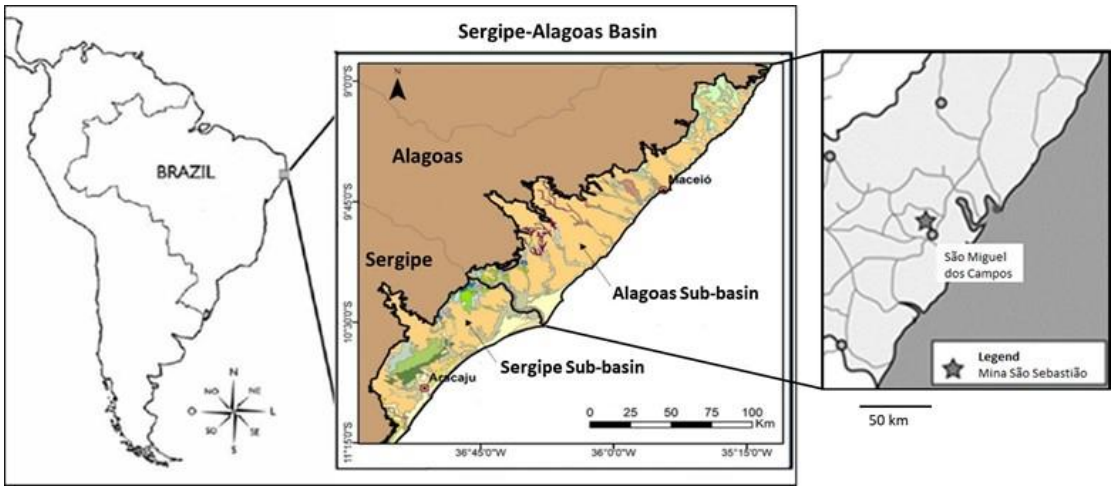


Figure 3-3 – Location of the Sergipe-Alagoas Basin, in the northeast region of Brazil, identifying the constituent sub-basins and the location of the quarry called Mina São Sebastião (in the city of São Miguel dos Campos), where the Morro do Chaves Formation is located.

A layer of interest in the Morro do Chaves Formation (Figure 3-2 (a)), called Bed 2B was selected. CORBETT *et al.* (2016) pointed out that it is possible to use cross-stratification as evidence that the coquinas in this layer were deposited lakewards or lagoonwards as accreting bioclastic bars. Visually, Bed 2B presents a great horizontal variation in the porosity, whose values obtained experimentally demonstrated to have bands with good and moderate porosity, in an intercalated way (TAVARES, 2014; ESTRELLA, 2015).

Bed 2B is about 1 meter tick (vertically) and 10 meters long (horizontally), from where the plugs were collected. According to ESTRELLA (2015), Bed 2B are showed inclined surfaces that suggest non-horizontal time lines of deposition. Figure 3-4 shows the representation of Bed 2B through photographs, indicating the regions from which the plugs were selected, and which dashed lines indicating the time lines of deposition of the coquinas.

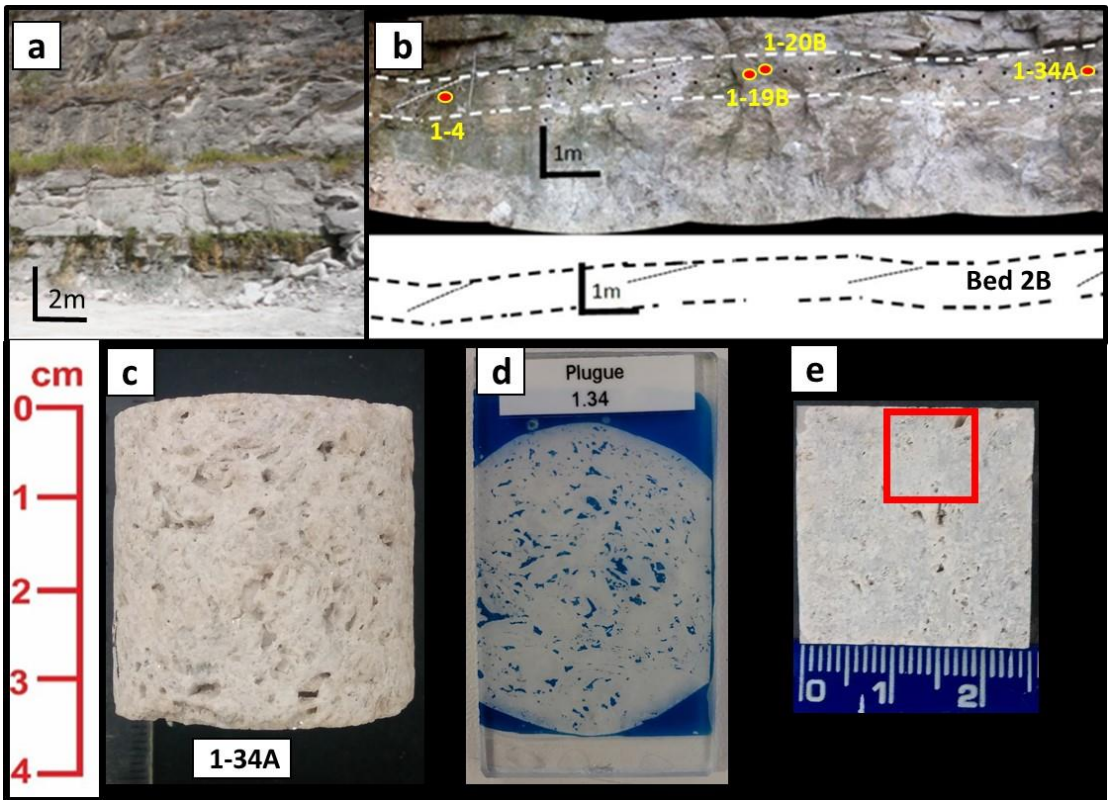


Figure 3-4 – (a) Image of the Morro do Chaves Formation in the Mina São Sebastião quarry of the city of São Miguel dos Campos; (b) identification of a layer (called Bed 2B) highlighted by red points where the samples (named 1-4, 1-19B, 1-20B, and 1-34A) were taken; (c) image of the plug showing some vugular porosity in the sample; (d) thin section obtained from the cut of one end of the sample during the flattening process; (e) rock slab prepared from the thin section, with the red square showing the region that was analyzed using SEM-EDS, XRD, and μCT with higher resolution

Out a total of 35 samples initially collected, it were selected 10 plugs were selected based on the work of ESTRELLA (2015): 1-2A, 1-4, 1-6, 1-14A, 1-18B, 1-19B, 1-20B, 1-28, 1-31B e 1-34A. However, from these ten (10) plugs, three (3) were selected based on the work of HOERLLE (2018) for a more in-depth analysis involving the two-phase simulation steps proposed in this work: 1-19B, 1-20B e 1-34A. The sample 1-4 was also selected for the analysis of the sub-resolution porosity (Figure 3-5).

The plugs were prepared, flattened (top and bottom), cleaned with methanol and toluene, and placed in an oven at 60° C for 24 hours. The cleaning and drying processes were the same as adopted by CORBETT *et al.* (2017), without needing a humidity-controlled drying environment since the carbonate sample did not contain gypsum or solid hydrocarbon-like gilsonite or pyrobitumen. After preparation and cleaning, each plug was approximately 35mm in diameter and about 35mm in length. In addition, small volumes were prepared with the materials from the slices, with a square cross-section of 1.0cm x

1.0cm and 5mm thickness (rock slabs). These subsamples will be used in scanning electron microscopy (SEM/EDS) and computed X-ray microtomography with higher resolutions (red squares in Figure 3-6).

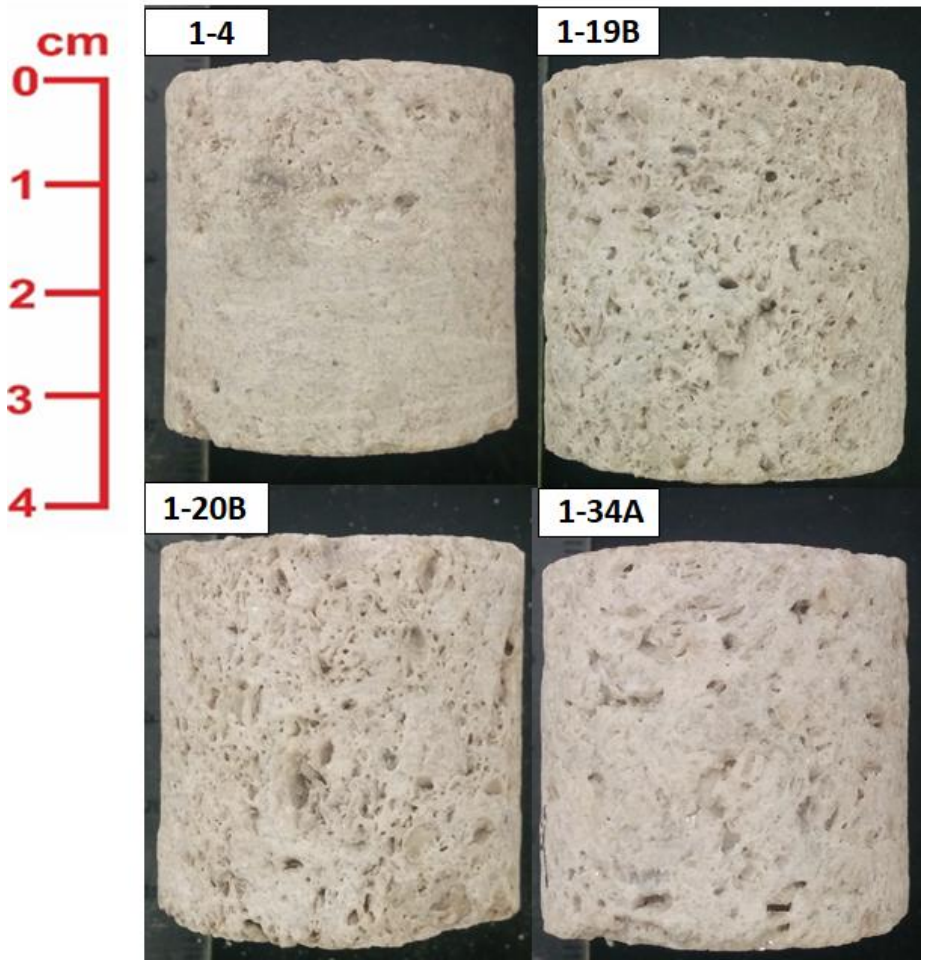


Figure 3-5 – Plugs used and evaluated in the present work using the proposed workflow and techniques studied.

The effects of the physical compaction of the coquinas were evaluated in terms of three characteristics: fractured grains, dense packing and orientation of the shells parallel to the bedding (TAVARES, 2014; HOERLLE 2018). According to TAVARES (2014), the main factor that affects the porosity of the coquinas of the Morro do Chaves Formation (especially Bed 2B, the target in this study) is their diagenesis in that three variables control the final porosity of these rocks: preservation of primary porosity, creation of secondary porosity and porosity obliteration.

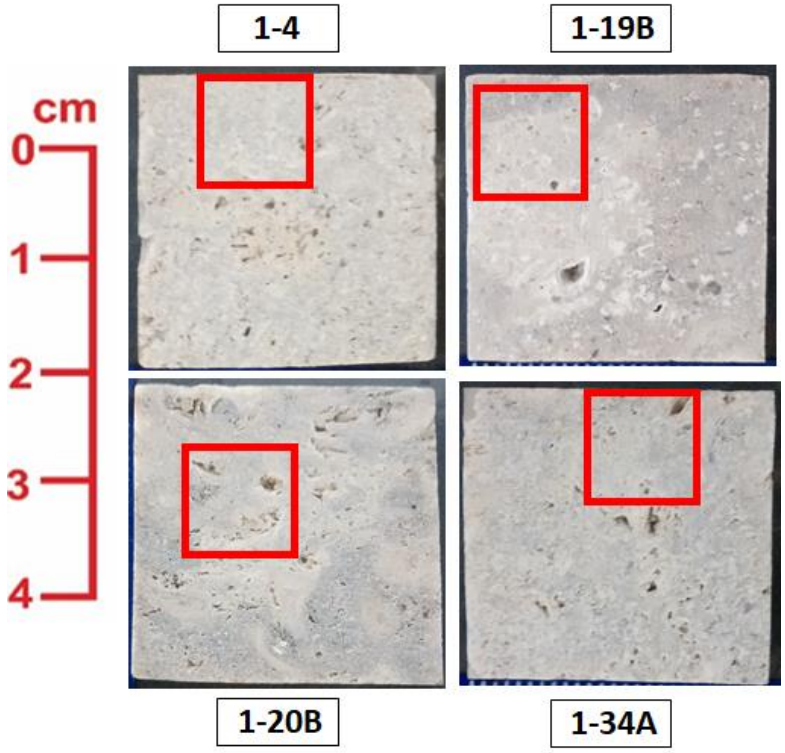


Figure 3-6 – Red squares indicate the regions from where the rock slabs were extracted for SEM-EDS analysis and μCT imaging with higher resolution.

Digital image analysis (DIA) was performed next. For each thin section it was obtained a Scan-type RGB image was obatined. Verification of the pore systems impregnated with blue epoxy resin on the thin section was performed using a Zeiss Imager M2m® optical microscope (Figure 3-7) with an increase of 2.5 times. The scanning was done by capturing images in mosaics, which were automatically joined by the microscope itself, resulting in a panoramic image of the entire thin section.



Figure 3-7 – Detail of the *Zeiss Imager M2m* optical microscope used to evaluate the thin sections of the selected samples.

3.1.2 Porosity and Permeability Experimental Measurements

Quantification of the porosity was done using an Advanced Automated Permeameter-Porosimeter System DV-4000 (*DV-4000 Advanced Automated Permeameter Porosimeter System*) from Weatherford Laboratories. The equipment shown in Figure 3-8 uses the Helium Gas Expansion technique applying Boyle's Law and Charles's Law to yield the effective porosity. According to LUCIA (2007), this is the most accurate method to obtain values of the effective porosity in samples. The helium gas used is directed to a leak-proof calibrated chamber where the rock is located (Matrix Cup or Core Holder), the system gives estimates of grain volume, grain density, pore volume, and porosity ranging from 0.1% to 40%.



Figure 3-8 – Detail of the DV-4000 porosimeter and permeameter used to obtain the measurements of effective porosity and absolute permeability of the samples studied.

The absolute permeability was measured using gas, in this case nitrogen (N_2), using Darcy's law for a permanent flow regime. A constant flow of nitrogen passed through the sample, creating an inlet pressure. The equipment program was automatically computed the flow pressure and the output pressure, leading to estimates of the absolute permeability. The system can accurately measure absolute permeabilities ranging from 0.0001 mD to 40 D. In the present work, estimated and calculated absolute permeability measurements will always be labeled and compared to absolute permeability values found with the aid of the DV-4000 permeameter with the entire plug samples.

The samples were introduced further into a matrix cup to calculate grain volume (Vg), pore volume (Vp), bulk or total volume (Vt) and grain density (Dg). Once these

data were estimated, samples were placed in the Hassler type cell to measure the effective porosity with Helium (He) gas.

3.1.3 X-Ray Computerized Microtomography

The data acquisition step from the X-ray computerized microtomography technique was performed using a *Bruker X-ray microtomographer* model *1173* (Figure 3-9). The equipment is considered a bench (107 cm wide, 72 cm deep, 62.5 cm high and 270 Kg), having a sealed X-ray source, tungsten target and flat detector.

The tungsten filament X-ray tube (Hamammatsu, model L9181) effectively operates between 40kV and 130kV voltages with a maximum current of 200μA, reaching maximum power of 8W and a maximum focal size of 5μm (Hamammatsu Photonics). On the other hand, the detection system (Hamammatsu model C7942SK-05) consists of a *flat-panel* sensor, which operates with a maximum pixel array of 2240x2240.



Figure 3-9 – Photograph of X-ray microtomography of *Bruker* model *Skyscan 117*3 used to acquire images with different resolutions.

Once this sample is correct positioned in the equipment the time to acquire the data depends on some factors such as the sample size itself, the desired resolution and the current and voltage used during the acquisition.

For the microtomography measurements of the samples, some important observations should be highlighted:

i) Due to the large size of samples 1-4, 1-19B, 1-20B and 1-34A, an increase in the size of the obtained pixel (approximately 9.97 μm) was required, eventually reducing the sample resolution. As previously mentioned, the resolution is related to the size of the sample and the distance between it, the X-ray source and the detector (AIRD, 1988);

ii) For the four large samples mentioned above, the microtomographies with different pixel sizes help in understanding the limitation of the reconstruction of the porous system as a function of the resolution itself;

iii) X-ray microtomografies of the rock slabs were performed with a maximum pixel size supported by the equipment, given the size of these samples (pixel size close to 6μm).

To obtain quality μCT images, three aspects are important: noise, resolution in density and spatial resolution according to TELES (2016). The noise level is associated with the degradation level of an image and can be analyzed by the signal-to-noise ratio (SNR), while the density resolution is related to the smallest distinguishable difference between the attenuation coefficients that the system can detect. The third aspect, spatial resolution, is related to the ability to differentiate between two very close structures, as evaluated by the modulation transfer function (MTF), which is influenced by the resolution of the detector and the size of the focal point in the X-ray tube.

After the acquisition and generation of the data, it is necessary to use a specific program of the equipment manufacturer, capable of converting the information from the detector (depending on the analysis of the attenuation suffered by a beam of incoming radiation passing through the sample, in this case, carbonate rock) into data that are interpreted as digital images that can be read by other programs. In this study, the programs of Bruker *NRecon® (v.1.6.9.4)* and *InstaRecon® (v 1.3.9.2)*, were used, capable of saving and converting data to *"Dicom"* and "*bmp"*, extension files. These files are generated and read by various programs (commercial and free) for treatment or reconstruction of images, and allow the correction or treatment of the main image artifacts generated due to the acquisition process, such as beam hardening and ring artifacts.

It is important to mention that the μCT equipment used in this work was the target of several analyses performed by TELES (2016), in terms of both signal-to-noise ratio

and its spatial resolution and density. These analyses were performed for matrices of 2240x2240 pixels, 1120x1120 pixels and 560x560 pixels. The present work used a 2240x2240 pixels matrix, which is the best detection matrix for this equipment.

For the μCT *Bruker Skyscan 1173* used in this work, table 3-1 shows the spatial resolution for different pixel sizes in the 2240x2240 detection matrix. One may conclude (e. g. TELES, 2016) that the spatial resolution of the structures depends not only on the pixel size of the detector but is influenced also by the blur of the pixels due to the dimensions of the X-ray tube focal point. The system becomes then larger in very close structures, which compromises the detectability of the system (ENGELHARDT & BAUMANN, 2006).

Table 3-1 shows the main parameters related to the data acquisition of the plugs of the studied samples, using *Bruker Skyscan 1173* μCT.

Table 3-1 – Parameters related to the acquisition and reconstruction of data of the plugs studied using a *Bruker* X-ray microtomograph model *Skyscan 1173*.

Sample / Pixel Size (μm)	**Source Voltage (kV)**	**Current (μA)**	**Ring Artefact Correction Factor**	**Smoothing Factor**	**Beam Hardening Correction (%)**	**Filter Al / Cu (mm / mm)**
1-4 / 9.97	130	61	5	4	15	0.5/0.5
1-4 / 18.53	130	61	13	5	20	0.5/0.5
1-4 / 24.95	130	61	4	3	20	0.5/0.5
1-19B / 9.97	130	61	10	10	30	0.5/0.5
1-19B / 18.87	130	61	5	7	20	0.5/0.5
1-19B / 24.95	130	61	4	5	30	0.5/0.5
1-20B / 9.97	130	61	3	4	25	0.5/0.5
1-20B / 17.81	130	61	4	5	30	0.5/0.5
1-20B / 24.95	130	61	5	7	20	0.5/0.5
1-34A / 9.97	130	61	1	5	20	0.5/0.5
1-34A / 18.17	130	61	5	3	15	0.5/0.5
1-34A / 24.95	130	61	5	7	15	0.5/0.5

Table 3-2 presents the main parameters related to the acquisition of rock slab data of the studied samples, using *Bruker Skyscan 1173* μCT. Although the voltage and current were changed, its product, which corresponds to the power used by the acquisition system, is approximately the same as that used to obtain the images from the plugs (approximately 8W).

Table 3-2 – Parameters related to the acquisition and reconstruction of rock slab data studied using the *Bruker* X-ray microtomograph model *Skyscan 1173*.

Sample / Pixel Size (µm)	Source Voltage (kV)	Current (µA)	Ring Artefact Correction Factor	Smoothing Factor	Beam Hardening Correction (%)	Filter Al / Cu (mm / mm)
1-4 / 6.07	70	114	4	4	30	0.5/0.5
1-4 / 9.97	70	114	1	1	30	0.5/0.5
1-19B / 6.07	70	114	4	4	30	0.5/0.5
1-19B / 9.97	70	114	6	6	25	0.5/0.5
1-20B / 6.77	70	114	4	5	30	0.5/0.5
1-20B / 9.97	70	114	6	6	25	0.5/0.5
1-34A / 6.77	70	114	4	5	30	0.5/0.5
1-34A / 9.97	70	114	6	6	25	0.5/0.5

The equipment of thi study has been in continuous operation for some years, with natural wear, which contributed to a reduction in the efficiency of the detector. Flat-panel detectors like the one in the equipment that was used, cause a degradation in the quality of the image due to the appearance of dead pixels, as well as a loss of efficiency as a function of time and detector operation (PADGETT & KOTRE, 2004).

In order to carry out the activities proposed at this stage, from acquisition to reconstruction of the images, a computer with the following configurations was chosen:

i) 2 Processing units Intel® Xeon™ E5 2603 v4 1.70 GHz;

ii) Motherboard Intel® Serverboard™ for processors Intel® Xeon™;

iii) 512 GB of RAM DDR4;

iv) Video card Nvidia® Quadro™ P6000 with 24GB of RAM DDR5;

v) Operating system Microsoft® Windows™ 10 Pro of 64 bits;

3.1.4 NMR, XRD, SEM and EDS Analyses

For the estimations of effective porosity of the samples, measurements of T_1 and T_2 were performed with the nuclear magnetic resonance technique, according to information presented in the previous chapter. This step was performed after the computerized X-ray microtomography stage, because the samples needed to be saturated with pre-prepared saline solution. The solution has a concentration of 50,000 ppm sodium chloride (NaCl) and a density of 1.039 g/cm³ at a temperature of 25 ºC (standard lab). The samples were fully saturated by applying isostatic pressure of 2,000 psi.

At the end of the saturation procedure one must calculate the saturation index. This calculation is used to verify the effectiveness of the procedure. Usually, 100%

saturation of the samples is expected, but values between 98% and 102% are considered good (LUNA *et al.*, 2016). The following equations were used to calculate the saturation index (%):

$$V_{brine} = \frac{M_{saturated} - M_{dried}}{\rho_{brine}} \tag{4.1}$$

$$SI = \frac{V_{brine} \cdot 100}{V_p} \tag{4.2}$$

where SI is the saturation index, $M_{saturated}$ is the mass of the sample saturated with brine, M_{dried} is the dry mass of the sample, ρ_{brine} is the brine density, V_{brine} is the volume of the brine filling the pore space of the rock and V_p is the pore volume of the sample.

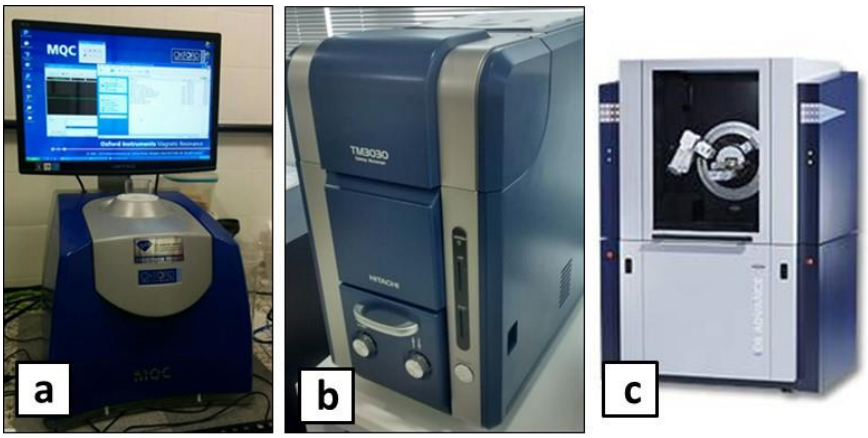


Figure 3-10 – (a) NMR equipment (model MQC from Oxford Instruments), (b) SEM equipment (TM3030 from Hitachi) using a EDS Bruker XFlash MIN SVE detector, and (c) XRD equipment (Bruker D8 Advanced diffractometer).

Equipment of Oxford Instruments model MQC (Figure 3-10) was used. The acquisition parameters of the NMR data are presented in Table 3-3.

The measurements aid not only in comparisons of the effective porosity as measured with the porosimeter, but also in the selection of the segmentation method or the threshold value itself by comparing pore size distribution graphs from the NMR equipment with the digital reconstructions of porous systems. Comparisons of the pore size distribution graphs is an important part of the analysis of the double porosity properties of the plugs.

Table 3-3 – Parameters related to NMR data acquisition with the *Oxford Instruments MQC* model.

Parameters	Values
Echo time	500μs
Number of averages	100
Waiting time between averages	15s
90º pulse width	8.6μs
180º pulse width	17.2μs
Temperature	22ºC

SEM was used to characterize the surface of each rock slab and to visualize the chosen pore spaces, and EDS for qualitative analysis and identification of the main elements composing the surface. SEM was performed using a Hitachi TM3030® Plus low vacuum atmosphere and an acceleration voltage of 1.5 kV with EDS using a Bruker XFlash® MIN SVE detector. The SEM equipment is shown in Figure 3-10 (b).

The remaining material after preparing the rock slab was powdered and taken for analysis using XRD technique. Pulverization was carried out in an agate grinding mill followed by micronization in a McCrone mill. The powdered material weighted around 2.0 grams. XRD analyses were perfoprmed in a Bruker D8® Advanced diffractometer using the following test conditions: Cu tube, 40 kV nominal voltage and 40 mA current, Soller slit 2.5°, primary slit 0.6 mm, secondary slit 5mm, LINXEYE® linear detector with opening of 189 channels, Ni of 0.02mm, step size of 0.02 and speed of 1.1° / min. Qualitative mineralogical analyses were done using Jade 9 software (with PDF-2 database). Quantitative analyses were carried out using the Rietveld Method within the TOPAS software.

3.1.4.1 NMR signal post-processing

After the acquisition of NMR data, post-processing techniques are required for the correlation of T_2 values with pore radii (μm), and for porosity evaluation and pore size distribution of a given sample (COATES *et al.*, 1999).

It is possible to convert the acquired signal of each saturated coquina sample to T_2 distribution using an Inverse Laplace Transformation method, according to the following equation:

$$\frac{1}{T_2} = \frac{1}{T_{2,Bulk}} + \frac{1}{T_{2,Surface}} = \frac{1}{T_{2,Bulk}} + \rho_2 \frac{S}{V} \qquad (4.3)$$

where T_2 is the measured transversal relaxation time from each satured coquina sample, $T_{2,Bulk}$ is the fluid's bulk relaxation time, $T_{2,Surface}$ is the relaxation time due to rock/fluid interaction, S/V is the pore's surface area-to-volume ratio and ρ_2 is the surface relaxitivity parameter, related to rock/fluid interaction. The fluid's bulk relaxation time used in this work is equal to 2.7s, since it is the value for brine. Actually, 2.7s is the value for a 30,000 ppm NaCl concentration brine, having a 1.043 g/cm^3 density at 21.5◦C (LUNA *et al.*, 2016), but it was considered similar to a 50,000 ppm NaCl concentration brine, having a 1.039 g/cm^3 density at 25ºC.

In order to obtain the pore size distribution (PSD) curves based on T_2 data using Eq 4.3, it is necessary to calculate the surface relaxivity parameter (ρ_2), which is correlated to the relaxation phenomenon due to the rock/fluid interaction (rock lithology dependent). This parameter is calculated based on a well-defined experimental procedure (SOUZA *et al.*, 2013). LUNA *et al.* (2016) obtainded the values for five different coquina samples from the same Bed 2B of Morro do Chaves Formation. In this work ρ_2 was calculated based on the arithmetic average (HOERLLE *et al.*, 2018) of the five surface relaxivity parameters ($\rho_{2,average}$ = 35.76 μs).

Based on Eq 4.3, calculating S/V as a function of pore radius, the conversion from a T_2 distribution to pore radius distribution can be done using the following equation

$$r(T_2) = C\ \rho_2\ T_2 \qquad (4.4)$$

where $r(T_2)$ is the calculated radius from a specific measured transversal relaxation time (T_2), C is a geometric factor that represents planar (C = 1), cylindrical (C = 2) or spherical (C = 3) pore shapes (RIOS *et al.*,2015), and ρ2 is the transverse surface relaxivity.

The PSD curves can be obtained using Eq 4.4 for several T_2 measurements, using C = 3 (considering all pore shapes being spherical) and a constant $\rho_{2,average}$ = 35.76 μs. The resulting PSD curves commonly shows radius (μm) versus incremental porosity (%), as presented in Figure 3-11.

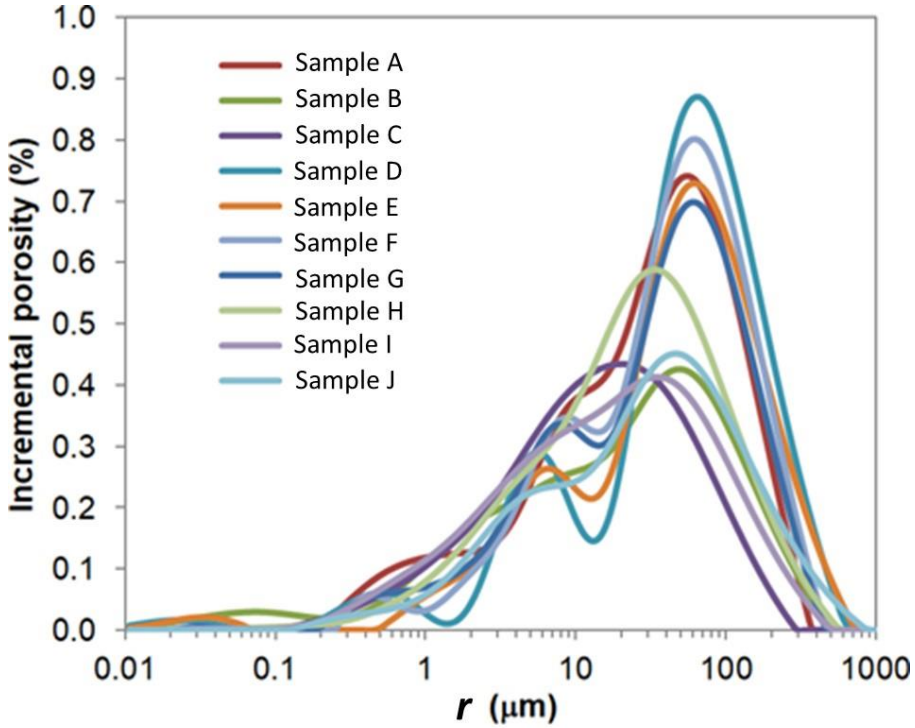


Figura 3-11 – Example of Pore Size Distribution (PSD) curves obtained from T_2 measurements converted to radii (r) for 10 different samples.

3.1.5 Segmentation

As previously mentioned, segmentation is an important step for modeling puposes. The binarization between rock matrix and pore systems can be performed as a non-automated procedure, defined in this work as NMR-based segmentation, and using automated procedures based on predefined well-known algorithms.

After μCT image acquisition, it is also important to postprocess the generated data. This step can be done using one or more filters (e.g., anisotropic diffusion or non-local means filters) to correct and enhance the quality of the images. Non-local means filters (BUADES *et al.*, 2005) are especially popular when working with images of heterogeneous carbonate rocks.

For the execution of the activities proposed in this stage, which includes from the loading of the images to the use of segmentation algorithms and software associated with this step, the same 512 GB RAM workstation was used.

3.1.5.1 NMR-based Segmentation

After the generation of the pore size distribution curves from NMR data, it is possible to use this information for segmentation purposes. The central idea behind this

methodology is based on verification of the digital porosity obtained through the 3D model of the porous network generated through images obtained by μCT for each selected pixel size.

As shown in Figure 3-12, for each ray range one can calculate the area respectively associated with a given value, that corresponds to the porosity of that area (blue, green or pink). Considering the same example, with cut-off at 25 and 50 μm will generate the porosities ϕ_1, ϕ_2 e ϕ_3, denominated as micro, meso and macroporosity, respectively (LØNØY, 2006).

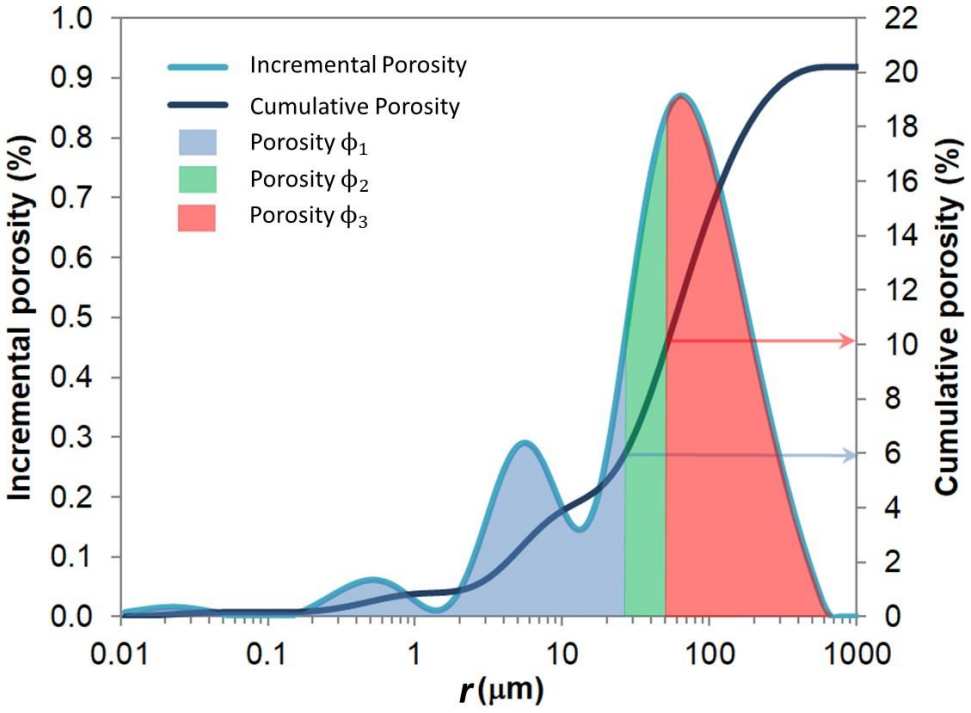


Figure 3-12 – NMR porosity partitioned in ϕ_1, $\phi_{2,\text{ and }}\phi_3$, according to 25 and 50μm cut-offs. The total porosity shall be the sum of the three areas, which will correspond to the cumulative porosity. The red and blue arrows indicate the cumulative porosity of each range of radii (separated at 25 and 50μm)

Assuming that μCT images are acquired with 50μm pixel size, all of the porosity defined by the blue region (ϕ_1) could not be digitally calculated since this part corresponded to a sub-resolution porosity whose largest pores are of the order of 25μm (half the size pixel value) of the reconstructed pore network.

Similarly, all of the porosity defined by the pink area would correspond to the pore network model generated from images with 100μm pixel size (digitally reconstructed pore radii exceeding 50μm, inclusive). In this case, the total area defined by the sum of

the blue and green regions from the NMR data could not be identified from the pore network model as reconstructed from CT images with pixel size equal to 100μm.

This method, although iterative, requires relatively low computational cost. Since it requires the calculation of the digital porosity for each radius range above half of the value of the selected pixel size. The porosity value obtained by the 3D model generated from a selected threshold value can be compared with the value of the porosity obtained by NMR for the range of possible radii to be detected given the pixel size of the μCT images. In case of a porosity difference exceeding a given maximum limit (1%, for example), a threshold value that is immediately lower or higher can be used to reduce this difference.

By taking the selected pixel sizes during the acquisition of the μCT images, according to item 4.1.3, pore radii whose dimensions are presented in Table 3-4 can be identified from the NMR data.

Tabela 3-4 – Pixel size from μCT images and maximum pore radius that can be identified from the NMR data

Pixel Size (μm) from μCT	**Maximum Pore Radius (μm) from NMR**
9.97	4.985
17.81	8.905
18.17	9.085
18.53	9.265
18.89	9.445
24.95	12.475

Taking the images with a pixel size equal to 9.97 μm, one can conclude that pores whose radius are less than 4.905 μm will not be identified, and part of the porosity obtained from pores with a lower radius can not be calculated, the digital models obtained from the μCT images can be used.

The use of NMR is proposed here for purposes of segmentation of μCT images because the limitation imposed by the latter method. It is necessary that the total porosity obtained by NMR is sufficiently close to that measured through the DV-4000 porosimeter, thus making saturation a key factor for the effective use of this segmentation method. In addition, the definition of micro, meso and macroporosity from the NMR data are only indicative, and the definition of sub-resolution porosity is more adequate for the analysis of the results.

Figure 3-13 shows a correlation between the data obtained from NMR and μCT techniques for the use of the segmentation method based on the radius distribution from the NMR technique. The sub-resolution porosity is calculated for each model from the pores whose radius are less than half the pixel size value.

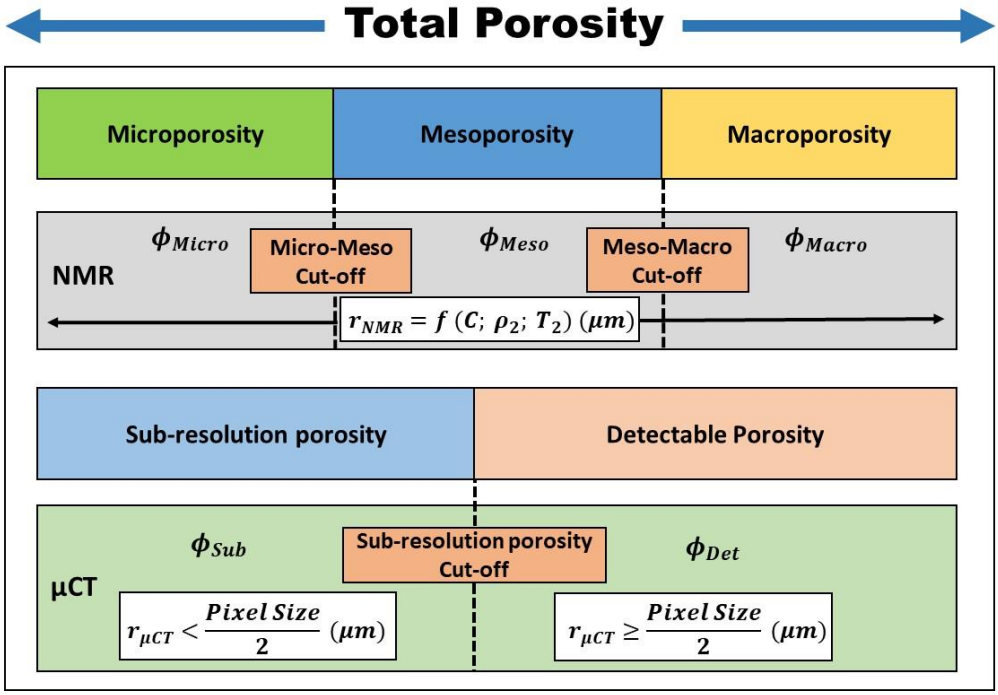


Figure 3-13 – Proposed scheme of carbonate rock pore space partitioning used in this work for the NMR-based segmentation procedure.

Thus, the separation between detectable porosity represented by pores whose radii are greater than or equal to half the pixel size used, and the sub-resolution porosity that can not be identified as a function of the selected resolution, and represented by pores whose radii are less than half the pixel size, can be easily realized.

Considering the pore radius distribution curve obtained from the NMR data, according to Figure 3-14, and μCT images whose pixel size is equal to 20μm, one can identify the region that corresponds to the porosity of sub -resolution (blue region hatched on the graph) that can not be reconstructed and / or calculated from μCT images. In this case, any radius below 10μm is detectable only by the NMR technique, and that portion of the porosity related to these radii are not calculated digitally.

Thus, by digitally calculating the porosity of the detectable region by the μCT technique and comparing with the value obtained by the NMR technique (in the example of Figure 3-14, the regions identified by unhatched blue, green and pink color) , it is

possible to identify the threshold value necessary to obtain the same porosity value, thus performing NMR-based segmentation.

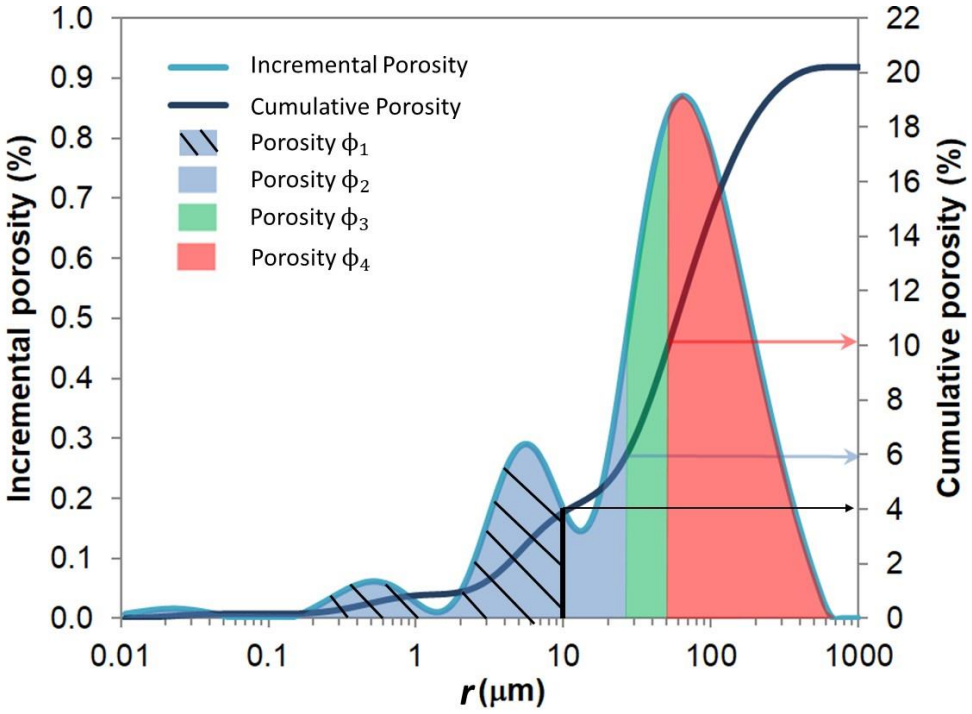


Figure 3-14 – NMR porosity partitioned in ϕ1, ϕ2, ϕ3, and ϕ4. Considering a 3D pore system model reconstructed from μCT images with 20μm pixel size, the porosity calculated from pores with radii smaller than 10μm cannot be detectable. This information is used for segmentation purposes.

Based on the analysis of the same figure, it can be seen that the porosity that can be calculated is equal to the accumulated porosity (equal to 20%), discounting the non-detectable pore portion (cumulative porosity equal to 4%). Thus, the 3D model of the pore network generated from the μCT images has porosity close to 16%, thus allowing one verify the threshold value that allows to obtain a porous system with this value.

3.1.5.2 Automated Segmentation – Algorithms

This study will use algorithms based on the methods described in Chapter 2 of this work (Kittler & Illingworth, Ridler & Calvard, Otsu, Niblack and Bernsen) implemented with the help of *Matlab*® 2015 software.

3.1.6 Digital Reconstruction – Pore System

Although digital reconstruction of the samples is possible using the *Fiji/ImageJ* and *Avizo® 9.5* software is possible, reconstructions of the pore systems of these samples

are only possible after the threshold value has been defined. The same programs mentioned in this item are used to create the models of the total and effective pore systems of the coquina samples of coquinas studied. The same computer will be used since reconstruction of the total pore system of each plug requires a high computational cost, mainly regarding the use of RAM.

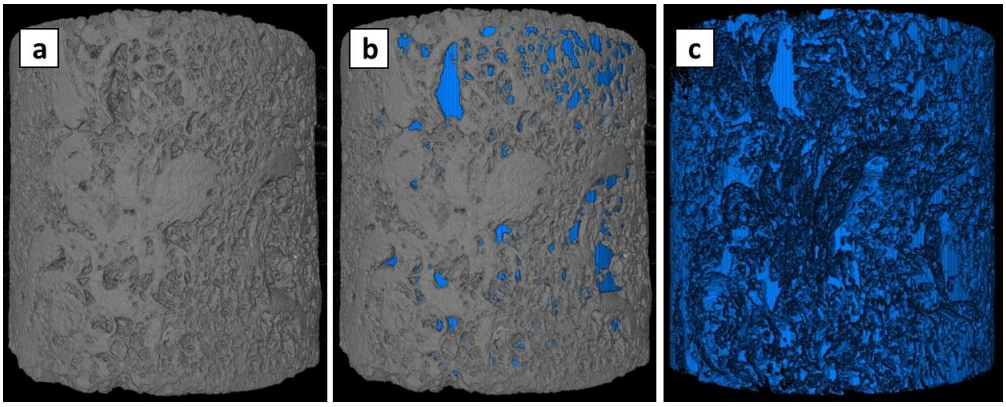


Figure 3-15 – Images obtained from the *Avizo® 9.5* program showing (a) the digital reconstruction of the plug, (b) digital reconstruction of the plug and the effectively connected pore system associated with this plug after setting the threshold value, and (c) reconstruction of the pore system effectively connected in isolation for purposes of porosity estimation and comparison of results.

Figure 3-15 shows an example of a three-dimensional digital reconstruction of the plug, the plug associated with the effectively connected pore system and only the effectively connected pore system. All images were generated and exported from the Avizo® 9.5 program after setting the threshold value found in the previous step. In this example, a threshold value was selected only to show the sequence of generation of the porous system of a plug from the images originating from μCT.

3.1.7 Porosity Estimation

This step corresponds to the calculations and evaluations necessary to obtain the porosity estimates as a function of the digital techniques and the NMR and SEM techniques previously performed. The results obtained here are pre-analyzed, taking into account all the limitations and uncertainties associated to the method itself and the proposed workflow.

The total porosity calculations from the proposed digital technique were performed simply by the ratio of the number of voxels corresponding to the pore media model to the total number of voxels of the sample, excluding the background. For the

pore system effectively connected, it is necessary to replace the number of voxels of the model representing the total pore system by the number of voxels of the model representing the largest pore system effectively connected. Equation 4.5 shows how the calculation of the total and effective porosity is performed:

$$\phi_\alpha = \frac{N_\alpha}{N_{Total}} x100\,; \quad \alpha = Eff, Mod \tag{4.5}$$

where ϕ is the porosity (%) and α may represent the model of the effectively connected pore system (*Eff*) or the total pore system model (*Mod*), with N_α being the number of voxels, of each model α, depending on the selected index, and N_{Total} being the number of total voxels in the three-dimensional sample model.

3.1.8 Pore-Network Modeling (PNM)

After reconstruction of the 3D model of the pore system, based on selection of the appropriate threshold value, it is possible to selected networks based on the size of the clusters (voxel count), since the numerical simulations were carried out assuming connectivity between the top and bottom of the sample (the z-axis), being the direction of flow in this plug. The same procedure was followed for the rock slab models. The Avizo® 9.5 software was used to separate the larger networks and to generate topology information for subsequent reconstruction of the PNM. The pore domains were generated based on topology information provided by the software. Other software such as Matlab® (Mathworks Inc.), Mathematica® 10 (Wolfram Research Inc.), as well as free software *CodeBlocks* 16.01 (The Code::Blocks Team), with a C++ compiler, were also used during this step.

Pore bodies of the pore network were associated with the largest elements present in the network system, with spherical geometry, while pore throats were identified and calculated based on being smaller spherical elements, depending upon their size and topology, as discussed by FOUARD *et al.* (2006). The length of the pore throats was defined by the distance between two connected pore bodies, while their radii were calculated as a function of the mean radii of the spherical elements along the path between the two pore bodies. We calculated the radii of the pore throats using three different averaging methods: harmonic, geometric, and arithmetic, as well as the minimum radius method, which considers the average radius based on the minimum value found on a

defined pore throat. Absolute permeabilities were calculated using the generated pore structure, while saturated fluid flow within the network domain was simulated using PNM algorithms.

In order to verify the dimensions and to have a final verification of the connections in the system of pore throats, it was used the software *Paraview* 5.3.0 (AYACHIT, 2015).

3.1.8.1 Single-phase Flow Numerical Simulation

In order to perform numerical simulations of single-phase flow in the effectively connected pore systems of coquina samples, *Matlab*® program was used as the platform to run the algorithms developed for calculation of the equations in item 2.5.2.1 presented in Chapter 2 of this work, based on the studies of RAOOF *et al.* (2013) and YIN (2018).

An important step before performing the calculations to obtain the permeability estimates is the correct definition of the pore bodies that will define the inlet and outlet limits of the fluid in the pore system as shown in Figure 3-16.

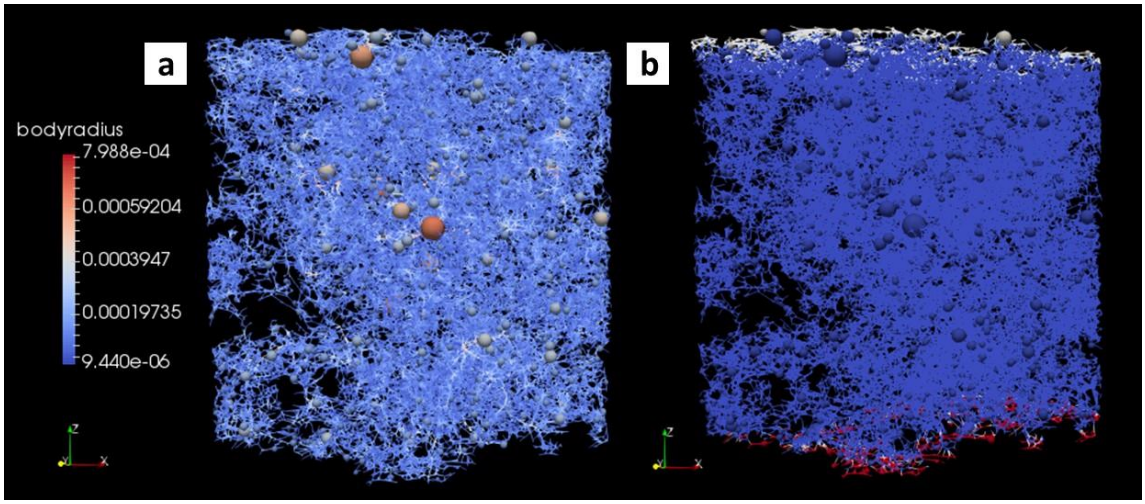


Figure 3-16 – View of a pore system obtained using PNM technique, (a) with the dimensions associated with the radii of the pore bodies and the throats connecting these pores bodies; (b) showing the region subjected to the higher pressure (input boundaries), and the region subjected to the low pressure (output boundaries), in red, which are specified in the code. Scale in m.

The inlet and outlet pressures (Pa) are also defined in this step, directly in the computational algorithm, as well as the initial pressure along the pore network. All other parameters necessary for calculation of the equations described in item 2.5.2.1 are obtained directly from the pores body-pore throat pore system, except for the viscosity of the fluid, which similarly as the pressures, must be inserted directly into the code.

It was imposed a pressure differential of 5.0×10^{-3} Pa was imposed between the upper and lower boundaries of the PNM along the z-axis. This small differential was adopted to guarantee laminar flow (low Reynolds number), an important assumption to solve Equations 2.32 to 2.36.

The analysis of absolute permeability estimates from the numerical simulations performed involves several important considerations:

i) Depending on the inlet and outlet pressures, and even on the domain which represents the pore system, the obtained pressure field must be analyzed, identifying possible inconsistencies in the results obtained through the simulations performed;

ii) Verification is needed of all geometric parameters and those associated with the fluid used in the simulation (e.g. being these the dimensions of the total sample length, the cross-sectional area relative to the fluid outlet, the viscosity and the temperature of the fluid used);

iii) Correct definition of the fluid inlet and outlet limits of the system, specifying in the pore network the regions that correspond to these limits;

iv) Observation of the coherence of the data obtained for the generation of the body-throat systems in the PNM technique, so that during the subsequent steps no important information regarding the reconstruction of the pore system is neglected;

v) Evaluation of absolute permeability calculated in digitally generated volumes for a correct analysis of the ranges of values and orders of magnitude obtained (milidarcies, darcies).

3.1.8.2 Absolute permeability as a PNM calibration parameter

The step of obtaining the absolute permeability (K_{abs}) through numerical simulation is understood, in the present work, as a step of calibrating the real pore system of the coquina samples obtained from digital reconstruction and modeling (PNM) techniques. Thus, the numerical results understood to be a calibration parameter of the network, comparing the value found with that measured experimentally through the DV-4000 equipment.

By recreating the pore systems and evaluating the methods of generating the pore throats, using the data obtained with the permeameter and the NMR techniques to

compare the results, it is possible to verify the quality of the generated networks. The central idea of this step is, therefore, obtaining PNM that is representative and very close to the real porous networks of the studied sample. It is important to consider that the networks are quite representative taking into account the different assumptions and simplifications adopted during the execution of the proposed workflow.

Calculation of the K_{abs} then allows the generation of a network whose geometry is representative from the point of view of fluid flow in pore systems. By observing the PSD curves obtained from the NMR data, it is possible to verify the necessity of insertion of pores from the sub-resolution that reconnect the reconstructed porous system, in order to reach the same value of K_{abs} as measured experimentally. This possibility will be addressed in the next item.

The calibration of pore structures from real coquina samples based on the numerical simulation of single-phase fluid flow is an important step to reliably perform multiphase flow numerical simulation as well as transport within the medium.

3.1.9 Analysis of sub-resolution porosity

It is possible to verify from NMR data the size of pore radii (bodies and throats) that cannot be identified nor reconstructed due to the μCT resolution limitation. The lack of μCT data related to these smaller pore bodies and pore throats can lead to generation of not-connected pore networks. PNM allows the reconnection of these pore systems based on the generation of sub-resolution pore structures.

The methodology used for the generation of porosity in sub-resolution and connection between previously separated pore networks is based on the work of ALVES (2018), DE VRIES *et al.* (2017) e BULTREYS *et al.* (2015c), with some modifications in how to connect the networks through these pores in sub-resolution.

The central idea lies in the insertion of pores and throats with smaller dimensions than those possible to be detected due to the limitation of sample size imposed by the μCT system. As previously discussed, it is possible to verify the pore size distribution by the NMR technique, verifying the porosity that can not be detected as a function of the pixel size in the images from the μCT technique. In many samples, the flow of fluids in their porous systems is made possible by the presence of very small pores, capable of connecting larger systems (some even with the presence of vugs).

The first challenge lies in the way to connect the pore bodies, regardless of whether or not there is overlap between two or more pore throats. Thus, it was decided to

start the connectivity studies using a technique called guided random generation within a limited volume (ALVES; 2018). In this technique, the dissociated neighborhoods (pore networks) are first defined, interspersed by a zone of indetermination in gray scale in microtomography images and with indications of connectivity. It is important to highlight that these selected areas are regions of possible and probable pores in sub-resolution, as a function of the gray scale in the images from the μCT technique.

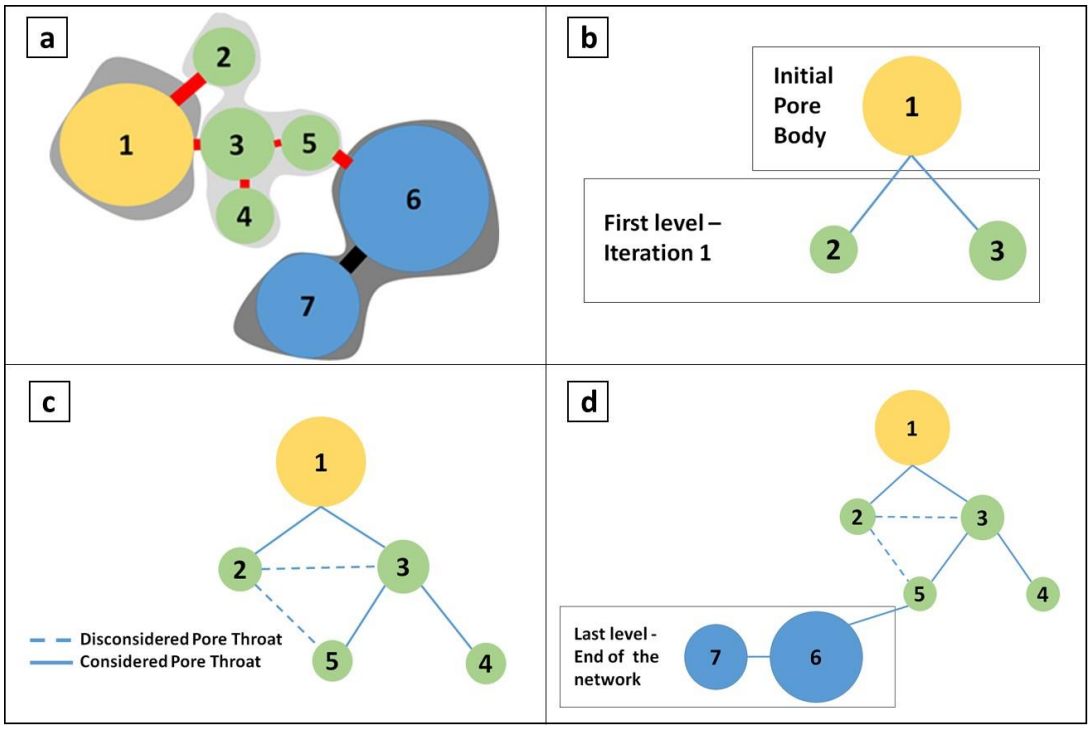


Figure 3-17 – Schematic of the adopted network generation: (a) real connections (pore throats in black) and generated connections (pore throats in red) in the pore network; (b) first iteration with the definition of the first level (pore bodies generated and connected to previously existing networks); (c) second iteration, with redundant pore throats being discarded; (d) last iteration, given the non-existence of connections from pore 7, and determination of the final network.

When using the reconnection algorithm, pairs of pore bodies are defined, one belonging to the neighborhood to be connected and another to the main network, which will be interconnected by the introduced sub-resolution pores. In this approach, before determining which pore pairs are to be connected, it is first necessary to define which disconnected networks are present in the model believed to belong to a larger system. These networks, also called neighborhoods, are a set of pores that interconnect forming a closed system and without communication with the rest of the porous network of the model, also called the main network. The distance between these neighborhoods and the

main network often has pore throat size and the space that separates them is a region of indetermination with great possibility of presenting undetected micropores in the imaging step or neglected in the segmentation stage.

In order to realize these connections, in view of the possibility of lack of previous knowledge about the pore-neighborhood relationship allied with the difficulty of realizing the delimitation described previously, an auxiliary algorithm was developed to supply the necessary information. Its functioning can be seen as the process of going through a decision tree, where each node is a pore body and each branch represents a connection, with all of the pore bodies belonging to a single network. In practice, this procedure discards the connections between two or more pore bodies of the same hierarchical level of the tree, as well as those that have one body in common with the next level.

Figure 3-17 helps to illustrate the above-mentioned algorithm. The main steps and considerations as follows:

i) Initial selection of an arbitrary pore of the set of pairs as the "origin"/"reference": in this example, the pore identified by number 1 was generated from the reconstruction of the porous system as a function of the gray scale of the μCT images, through the PNM technique;

ii) Identification of the pores connected to this origin (pore bodies 2 and 3) and storage of their indices, to avoid repetitions: these pore bodies are generated for regions that are not identified as pores after the segmentation step, as a function of their gray scale;

iii) Definition of each of the pores identified in the previous step (pore bodies 2 and 3) as the new origin;

iv) Identification and storage of the pores connected to at least one of the new origins (pore bodies 4 and 5);

v) Repetition of steps *iii* and *iv* until an iteration occurs in which no new generated pores are generated, indicating therefore the end of the connectivity of a network. In this step, the generated and connected pore bodies connect to pore bodies of the original network (identified by the number 6), which may be previously connected to other pore bodies (in this case by a single one, indicated by the number 7);

vi) All previously identified pores are classified as belonging to a neighborhood since they are interconnected, and the procedure is

restarted from a new arbitrary pore body that does not belong to any known neighborhood;

vii) Execution of the algorithm ends when there are no more non-grouped pores, returning the poro-neighborhood relation. In this example, pore bodies identified by numbers 6 and 7 may be new sources, generating new connections with other neighborhoods, since there are regions whose gray scale delimits areas whose existence of pores in sub-resolution is possible and probable.

As previously mentioned, one can verify that the connections between the pore bodies do not occur through pore throats that have intersections with each other. The problem of intersection of the throats arriving or departing from the same pore is mathematically translated as determining whether the curve generated by the intersection of one cylinder-ball pair intersects the curve generated by another cylinder-ball pair. However, due to the high computational cost involved in this step of verification of intersections of large samples, it was chosen to generate and reconnect the porous systems considering the existence of some overlays in the generated pore throats.

Due to the resolutions adopted during acquisition of μCT data of the selected samples, some assumptions were adopted:

i) The diameter of the new pores generated has, necessarily, as an upper limit the pixel size chosen and used during the μCT stage, since they would have been detected during imaging if they had larger dimensions;

ii) Their lower limit, however, can not be easily estimated geometrically, but since the intention is a system that adequately describes the behavior of the network and not its structure itself, the diameter could not be so small as to compromise its impact on subsequent simulation;

iii) For images with a pixel size of 9.97μm, for example, the estimation for both limits was approximately 2.0μm and 9.1μm, for the maximum and minimum, respectively, which is considered a uniform distribution given the absence of a known distribution. These values correspond respectively to 20% and 98% of the smaller throat diameter value given the selected pixel size;

iv) For images with a pixel size around 18.5μm, the estimates for the minimum and maximum values were 2.0μm and 18.2μm, and for the pixel size of 24.95μm were 2.0μm and 24.5μm, respectively;

v) The lower limits for the pore bodies and pore throats sizes, irrespective of the pixel size of the μCT images, were considered the same and equal to 2.0μm;

vi) The selected distribution chosen was log-normal with the parameters μ and σ selected as a function of the pore size distribution of the analyzed sample;

3.1.10 Two-phase Flow Numerical Simulation

In order to perform numerical simulations of two-phase flow in the effectively connected pore systems of the samples it was used *PoreFlow* code (RAOOF *et al.*, 2013). The platform solves the equations presented in item 2.5.2.2, Chapter 2 of this study.

As already described, drainage in a water-oil-rock system is characterized by the displacement of water by oil, with pore medium initially being completely saturated with water. The two-phase flow simulations performed in this work consider the primary drainage process, where after application of the displacement pressure, oil is forced into the rock to reduce the water saturation. As the capillary pressure is increased, the water saturation continues to be reduced until irreducible water saturation is reached (Swi). A brine-mineral oil system, with the main parameters such as viscosities, contact angle, and interfacial tension obtained experimentally.

In this step, unlike single-phase flow simulation presented in 3.2.1.16, not only the inlet and outlet limits of the fluid in the pore system must be defined, but also the input and output pressures (Pa), as well as important parameters: the viscosities of the fluids, the contact angle between the wetting phase and the boundaries of the body-throat systems, and the interfacial tension between the wetting and non-wetting fluids. All of these parameters can be changed manually in *PoreFlow*.

This study assumes that an angular form of pores is essential for realistic representation of the porous media for two-phase flow purposes. The assumption of pores having a circular cross section causes insufficient connectivity of the wetting phase (RAOOF & HASSANIZADEH, 2012) and as result poor correlation of numerical and measured data (ZHOU *et al.*, 2000). However, for calibration purposes of the pore

network, mainly related to the connectivity and the number of pore bodies and pore throats (which are based on K_{abs} numerical results), a circular cross section of these pores can be considered for single-phase flow simulation.

An important premise adopted at this stage is the conversion of the geometries representing the pore bodies. Differently from the geometry adopted during numerical simulations of single-phase flow (which considers the pore bodies as spheres) for the simulation of the primary drainage the pore bodies are considered to be cubic in shape (in order to generate vertices). The cross sections retain the wetting fluid in their corner and allow two fluids to flow simultaneously through the same pore (RAOOF & HASSANIZADEH, 2012). In order to maintain the properties of the generated pore network approximately constant, each pore body with spherical geometry used to calculate K_{abs} is transformed into a pore body with cubic geometry so that its volume remains the same.

The same approach can be used in the conversion of the geometries of the cross sections of the pore throats, although in this case three possible shapes can be selected: circular, triangular, and rectangular cross section. The shape of angular pore cross section is prescribed in terms of a dimensionless shape factor, G (RAOOF & HASSANIZADEH, 2012) defined as

$$G = \frac{A}{P^2} \tag{4.6}$$

where A and P are the area and the perimeter of the cross section for pore throats, respectively. In the present work the transversal sections of the pore throats were considered as circles. Further details can be found in RAOOF & HASSANIZADEH (2012).

PoreFlow assumes that the hydraulic conductance of pore throats accounts for the resistance to the flow within the two adjacent pore bodies (RAOOF & HASSANIZADEH, 2012). The code assignes an effective conductance to a given pore throat, as a function of its own conductance and those of its two neighboring pore bodies. In the presence of a nonwetting phase, *PoreFlow* considers the conductances of the pore bodies and pore throats a function of saturation. However, it is not necessary to calculate conductances of pore bodies explicitly. A correction term which is a function of

saturation. This term uses the harmonic mean of saturations of two pore bodies adjacent to a pore throat:

$$k_T(S_w) = 2k_{ij}\,\frac{S_w^i S_w^j}{S_w^i + S_w^j} \tag{4.7}$$

where S^i_w and S^j_w are saturations of pore bodies i and j, respectively, corresponding to the imposed capillary pressure, k_{ij} is the conductance of the connecting throat between bodies i and j, and k_T in the total conductance to be assigned to the pore unit, as a function of the saturated pore bodies.

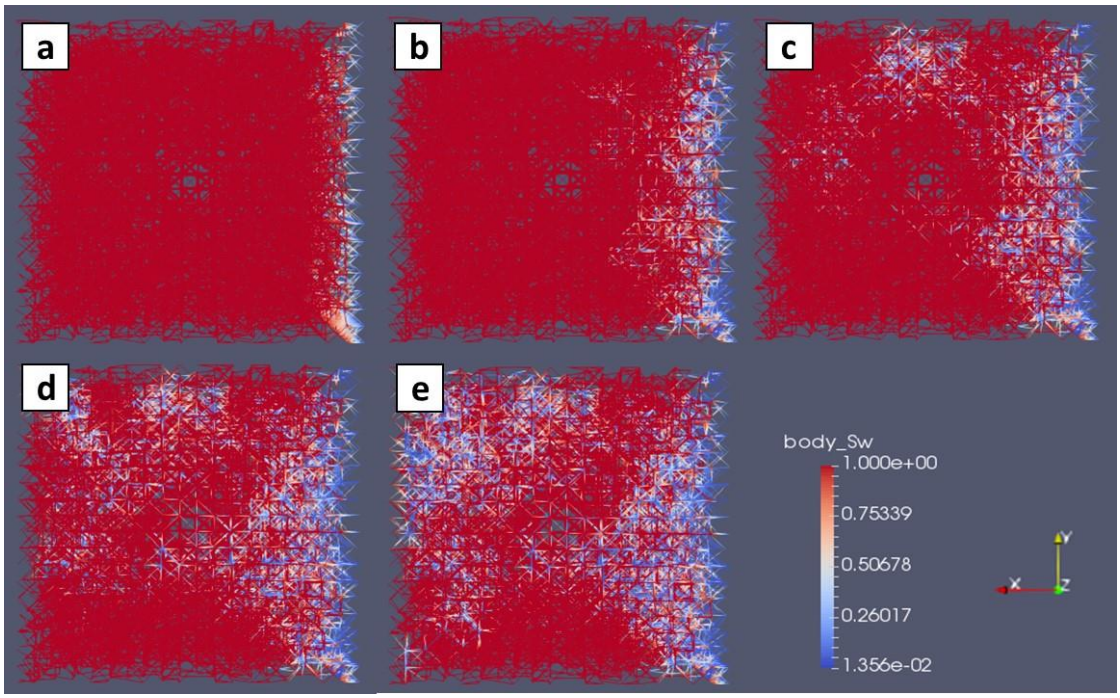


Figure 3-18 – The image in (a) shows the porous system saturated with the wetting fluid (in red), with a non-wetting fluid inlet region (in blue) on the right, (b), (c), (d), and (e) show the advance of the wetting fluid, from the right of each image, considering the occurrence of snap-off. The last images in the lower right corner show the saturations of the pore bodies and the orientation of the primary drainage process.

As previously mentioned, it was used the quasi-static modeling, based on the work of RAOOF *et al.* (2013) was used in such a way that the capillary pressure curves versus the saturation of the wetting fluid (*Pc-Sw*) are obtained. The models generated by *PoreFlow*, after the numerical simulations, can be visualized using the *Paraview* 5.3.0 program, as example given in Figure 3-18, which shows the primary drainage of a body-

throat system whose saturations in the porous bodies constituting the system are displayed.

3.1.11 Parameters definition for Two-phase Flow simulation

As previously mentioned, the parameters used in two-phase flow simulations, such as fluid viscosities, the contact angle between the wetting phase and the boundaries of the body-throat systems, and the interfacial tension between the wetting and non-wetting fluids can be changed easily in *PoreFlow*. In this step, the values of these parameters are obtained experimentally.

For measurements of the contact angle and interfacial tension, a Kruss/Eurotechnica goniometer (Figure 3-20 (a)) was used based on a technique known as Drop Shape Analysis (DSA). The equipment, also called Drop Shape Analyzer, allows the measurement of the contact angle between the surface of the rock slabs and two fluids. The rock slabs are the same as those used in SEM-EDS analysis (Figure 3-6).

Table 3-5. Total dissolved solids TDS, pH, viscosity, and density (ρ) for Model Brine and Model Oil A used for the contact angle measurements

	Model Brine *	**Model Oil A***
TDS (ppm)	35177	-
pH	8.6	-
Viscosity (cP)	0.968	1.96
ρ (g/cm^3)	1.031	0.785

* Measurements at 25°C and 14.7 psi.

The Contact Angle (CA) measurements were conducted using the rock slab and two fluids, an external phase (brine) in which the rock is immersed and a phase contained in the drop deposited on the rock surface (oil). Coquina samples 1-19B and 1-34A were aged for 1 day in Model Brine and 30 days in Model Oil A. Coquina samples 1-4 and 1-20B were aged for 1 day in Brine B and 30 days in Oil B. Model Oil A and Model Brine parameters are shown in Table 3-5. Model Oil A does not contain resins or asphaltenes. Model Brine has salinity close to seawater (approximately 35,000 ppm), low hardness and basic pH.

A complete procedure for aging, brine and oil composition analysis, and CA measurement can be found in FACANHA *et al.* (2016), DREXLER (2018) and DREXLER *et al.* (2018; 2019). Contact angle measurements were carried out at 1,000psi

(6.89 MPa) and 60°C. The aged rock slab was placed in the equipment's chamber, which is filled with brine (either Model Brine or Brine B). A drop of oil (either Model Oil A or Oil B) was injected and images were continuously acquired to obtain both left and right contact angles every 30 seconds. The experiments were continued for 24 hours. Bulk oil cleaning was performed by rinsing the rock slabs with cyclohexane and subsequent centrifugation.

Figure 3-19 shows contact angle measurements (θ) towards the denser phase (Brine B). Greater contact angle value represents more oil-wet behavior and a lower contact angle value indicates water-wet behavior, as presented before in Table 2-1.

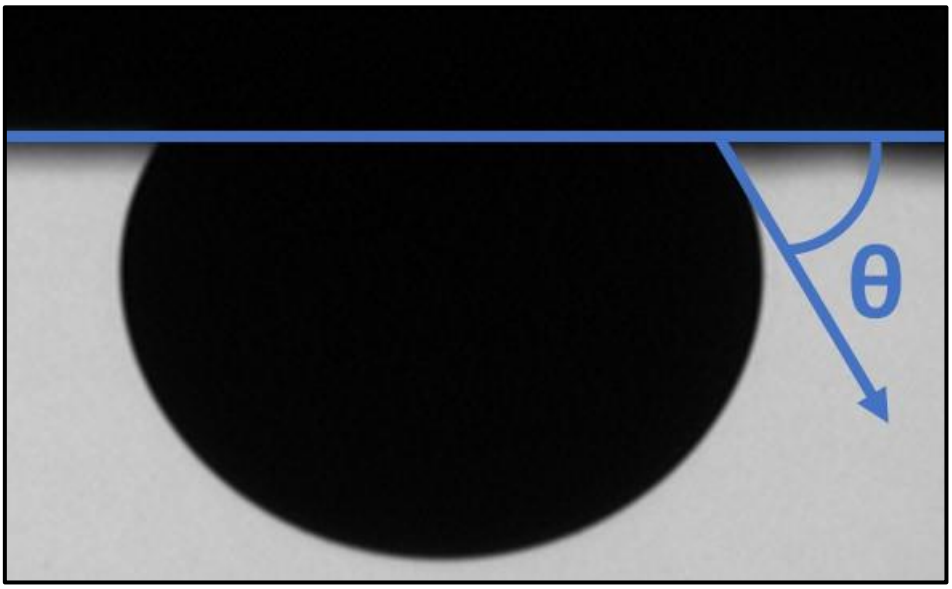


Figure 3-19 – Scheme illustrating the Contact Angle (CA) measurement procedure using Kruss/Eurotechnica DSA. Contact angles were measured every 30 seconds during 24 hours.

Interfacial Tension (IFT) values were measured based on DSA technique. The measurements consists of injecting a pendant drop of oil in the capillary tube from the bottom of the equipment (DSS Kruss/Eurotechnica goniometer). The drop then remains suspended due to the balance between gravity and interfacial forces. Further information can be found at DREXLER (2018). Measurements are performed every 30 seconds for the complete length of the test. During each measurement, the software from the equipment calculates the following output values: IFT, drop volume, drop surface area, drop shape parameter (*B*) and fitting error The IFT is calculated based on the folowing equation:

$$B = b\left(\frac{\Delta\rho g}{\sigma^{nw}}\right)^{0.5} \tag{4.8}$$

where b is the radius of curvature at the apex, $\Delta\rho$ is the density difference between both fluids, g is the acceleration of gravity and σ^{nw} is the interfacial tension. Spherical drop shapes decrease the precision of the measurements, so it is important to avoid B values lower than 0.5 in order to obtain reliable results (HOORFAR *et al.*, 2005). BUTT *et al*. (2006) and YAKHSHI-TAFTI *et al*. (2011) give further information regarding the IFT numerical evaluation.

The software from the equipment solves the force balance derived from the Young-Laplace Equation as follows:

$$\frac{d^2z}{dx^2} + \left[1 + \left(\frac{dz}{dx}\right)^2\right]\frac{1}{x}\frac{dz}{dx} = (2 + \mathrm{Bz})\left[1 + \left(\frac{dz}{dx}\right)^2\right]^{3/2} \tag{4.9}$$

where x and z are the axis coordinates of the drop profile and parameter B given by Equation 4.8.

The DSA tests study the IFT as a function of time for different pressures of the oil-brine systems. The selected procedure used for IFT evaluation was the “Same drop” experiments.

The “Same drop” experiments consist of analyzing the effect of pressure on the IFT for the same drop. After reaching equilibrium, the pressure is increased. To avoid a decreased volume due to compression of the drop, oil is injected to keep the same drop volume for all test pressures. The experiment seeks to evaluate the equilibrium IFT reducing mass transfer diffusion time for the different pressures considered in the test. The experiments were selected to verify the contact angles for different coquina samples, once only one rock slab was generated from each studied plug. A complete procedure for the “same drop” IFT analysis can be found in DREXLER (2018) and DREXLER *et al.* (2018).

In order to calculate the density difference between both fluids, it is necessary to verify each density, separately, as a function of pressure. Measurements were performed using an Anton Paar DMA HPM densitometer with a thermostatic bath. The injection pressure was controlled by using of Quizix pumps. Details can be found at PÉNELOUX *et al.* (1982) and DREXLER (2018). Model Oil A and Brine B density measurements

were obtained experimentally using the same procedures. After the measurements plots of pressure versus can be used to obtain density for each analysed fluid. The trend lines give a clear indication how the density is changing during the test.

Fluid viscosities at atmospheric pressure and different temperatures (25ºC and 60ºC) were measured with an Anton Paar 302 (Figure 3-20 (b)). It was also used the *OLI Studio 9.6*® software to estimate density and viscosity values of all fluids at different temperatures (25°C and 60°C) and different pressures (14.7 psi and 1,000 psi).

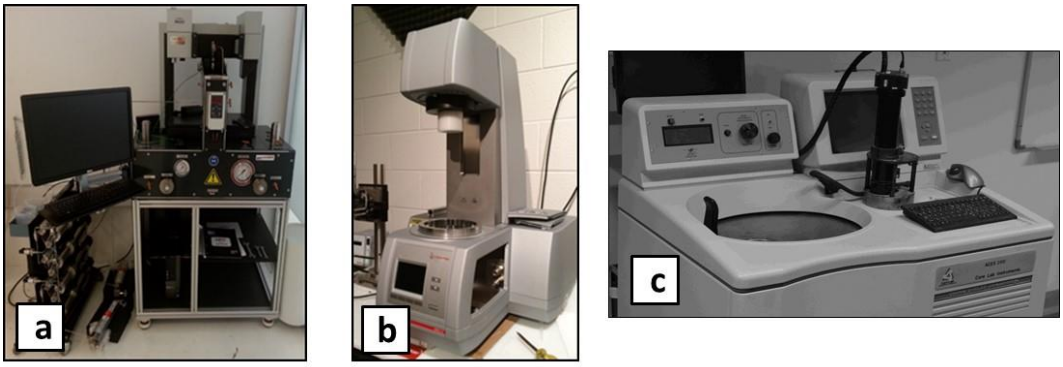


Figure 3-20 – (a) DSS Kruss Goniometer for contact angle and interfacial tension measurements, (b) Anton Paar model M302 rheometer for fluid viscosities measurements, and (c) centrifuge system (model A-200 from Core Lab Instruments) for capillary pressure measurements.

All measurements were used as input data for performing primary drainage simulations based on real parameters. Results of the simulations can be compared with data obtained from the tests performed with the centrifuge method, provided that the same input parameters are used: densities, viscosities, interfacial tensions and contact angles.

Although the first three parameters can be used directly in the simulation, maintaining good correlation with the measured contact angles (through the dependence of the local rock-fluid interaction), it is important to have the a same value for the whole plug, even though the experiments were performed on a rock slab.

3.1.11.1 Centrifuge Method

The centrifuge method is widely used to obtain capillary pressure curves. The primary drainage tests were carried using a centrifuge system model A-200 from Core Lab Instruments (Figure 3-20 (c)). For the oil-brine drainage cycle, brine saturated coquina plugs are immersed in oil, known as Oil A. The selected plugs used during this procedure were 1-19B, 1-20B, and 1-34A.

During the tests, brine was expelled from the plugs at a given rate of rotation. Model Brine, as previously presented. The volumes were measured while the centrifuge is spinning at high velocities. The rate is then increased in stages, with the produced brine volumes being recorded for each rotation speed to give data that will be converted to Pc-Sw curves.

Important aspects to be considered during execution of the centrifuge test:

i) Oil A properties are described in Table 3-6. Oil A is a mineral oil composed of a mixture of paraffinic and naphthenic hydrocarbons obtained from high pressure catalytic hydrogenation of petroleum distillates;

ii) A capillary pressure gradient is applied during the test, which must inevitably give rise to a saturation gradient. This gradient is more exaggerated at low pressures;

iii) Differences in wetting characteristics and oil compositions should be taken into account when applying laboratory data to modeling;

iv) Estimated capillary pressure curves from centrifuge measurements were obtained using inverse non-linear regression method based on Maximum Likelihood Estimation (MLE) using the homographic parameterization as presented by Equation 4.13 and 4.14, following the procedure of ALBUQUERQUE *et al.* (2018);

In order to generate the capillary pressure curves, fundamental equations (HASSLER & BRUNNER, 1945) are solved for primary drainage. The capillary pressure (*Pc*) can be calculated using:

$$Pc = \frac{1}{2}\,\omega^2 \Delta\rho\,(r_1{}^2 - r_2{}^2) \qquad (4.10)$$

where ω is the centrifuge rotation speed, $\Delta\rho$ is the difference in density between the Oil D and Brine B, r_1 and r_2 are the radial distances to the sample extremities (top and bottom in the *z* direction, following the same pattern adopted during absolute permeability measurements with DV-4000®).

Table 3-6. Main parameters of Oil A used in this work during the primary drainage based on the centrifuge method.

Oil A	Viscosity (cP)	Density (g/cm^3)
21ºC and 14.7 psi	23.5	0.844
25ºC and 14.7 psi	19.6	0.843
60ºC and 14.7 psi	5.63	0.818
60ºC and 1,000 psi	14.5	-

Fluid saturation at a given point in the sample subjected to a capillary pressure, *Sw(Pc)* is given by the following equation:

$$\overline{S_w}(P_c) = \frac{\left(1+\sqrt{1-R}\right)}{2}\int_0^1 \frac{S_w(xP_c)}{\sqrt{1-Rx}}dx \tag{4.10}$$

$$S_w = \frac{V_w}{V_p} = \frac{V_w}{V_w + V_o} \tag{4.11}$$

$$R = 1 - \left(\frac{r_1}{r_2}\right)^2 \tag{4.12}$$

where $\overline{S_W}$ is the sample average water saturation, Vw, Vp, and Vo are the water, sample pore, and oil volumes, respectively.

The homographic parameterization proposed by GLOTIN *et al.* (1990) can be defined as:

$$S_w(P_c) = min\left(1, \frac{1+\alpha S_{wi}(P_c - P_d)}{1+\alpha(P_c - P_d)}\right) \tag{4.13}$$

where α, Swi and Pd are parameters that are related to shape, irreducible water saturation, and initial displacement pressure, respectively.

The analytic solution of the saturation equation for this parameterization can be obtained from the following equation:

$$\overline{S_w}(P_c) = \frac{\left(1+\sqrt{1-R}\right)}{2}\left(\int_0^{\frac{Pd}{Pc}} \frac{1}{\sqrt{1-Rx}}dx + \int_{\frac{Pd}{Pc}}^1 \frac{S_w(xP_c)}{\sqrt{1-Rx}}dx\right) \tag{4.14}$$

According to ALBUQUERQUE *et al.* (2018), inverse methods are likely to result in comparable to smaller estimated water saturation errors when compared to pre-smoothed direct methods, such as HASSLER & BRUNNER (1945), and FORBES (1994). These errors are introduced by numerical integration of the saturation equation (Equation 4.14).

3.1.12 Optimized Simulation for Primary Drainage

This step refers to numerical simulations of primary drainage in the samples of selected coquinas. The parameters obtained experimentally are used in the simulations to obtain the capillary pressure versus saturation curves. In this way, each simulation performed will be optimized for the coquina as function of the calibrated parameters, both relative to the rock and the fluids used.

Following the workflow proposed at the beginning of this chapter, the simulations involving two-phase flow are based on data obtained through laboratory assays and tests, as well as simulations involving the software *OLI Studio 9.6*®:

i) Contact angle and interfacial tension measurements from DSA;

ii) Density and viscosity measurements and simulations using different fluids (Model Oil A, Oil A, Oil B, Model Brine, and Brine B);

iii) Absolute permeability-calibrated pore systems (PNM) of different coquina samples reconstructed from X-ray computed μCT images with different pixel sizes;

iv) Capillary pressure measurements from the centrifuge method for final comparison.

At the end of this step, therefore, the estimates of the *Pc-Sw* curves are obtained, and can be compared to the same curves obtained experimentally by the centrifugation method.

As described, for the purposes of calibration of the primary drainage simulation, the parameters of Model Oil A, Oil A and Model Brine were used. The parameters related to Oil B and Brine B were used for the numerical prediction of primary drainage in the pore systems of coquinas using fluids whose properties are similar to the fluids found in the Santos Basin Pre-Salt scenario. Brine B corresponds to formation brine from producing wells in a Pre-Salt field. Brine B parameters are presented in Table 3-7. Dead crude oil samples from Field B, known as Oil B, were supplied by Shell Brasil. Oil B corresponds to lighter crude and its parameters are presented in Table 3-8.

Table 3-7. Total dissolved solids TDS, pH, viscosity, and density (ρ) for the Brine B used in this work for the contact angle measurements and simulation purposes

	Brine B
TDS (ppm)	226,401
pH*	5.7
Viscosity (cP)*	2.135
ρ (g/cm^3)*	1.18

* At 25 °C and 14.7 psi.

Table 3-8 – SARA analysis, acid and basic numbers (TAN and TBN), viscosity and API for the Oil B used in this work for contact angle measurements and simulation purposes

	Oil B
Saturates (%wt)	64.06
Aromatics (%wt)	25.98
Resins (%wt)	8.46
Asphaltenes (%wt)	1.50
TAN (mg KOH/g)	0.37
TBN (mg KOH/g)	4.0
Viscosity (cP)*	14.5
API	26.14

* Measurements carried out at 60 °C, 14.7 psi

Some important assumptions for conducting the simulations of primary drainage and subsequent comparison to data obtained through the centrifuge method are described below:

i) Tests performed in the centrifuge were performed with Oil A and Model Brine;

ii) Tests to obtain the contact angles were performed with a combination of the following fluids: Model Oil A and Model Brine, Brine B and Oil B;

iii) Tests for obtaining the interfacial tensions (IFT) used the same combinations of fluids described as in (*ii*);

iv) Some density and viscosity data were not obtained experimentally, but from the *OLI Studio 9.6*® simulator;

v) For comparison with the Pc-Sw curves obtained by the centrifuge method, numerical simulations of a primary drainage were performed

with the contact angles and IFT obtained with a combination of Model Oil A and Model Brine;

vi) Simulations with Oil B and Brine B, which are typical of some Brazilian Pre-salt fields, were carried out using experimental data with the calibrated PNM as described in this chapter, thus representing pore systems similar similar to these of rocks from the Brazilian Pre-salt.

4 RESULTS AND DISCUSSIONS

This chapter presents the experimental and numerical results of the assays and studies described in Chapter 3 and presented in the workflow.

4.1 Experimental Results

In this section the main results from the experimental tests conducted are presented. Initially, the measurements of porosity and absolute permeability for the studied samples, the analyses of the petrographic thin sections and tests conducted with SEM, EDS, XRD, and the pore size distributions through the NMR technique are presented. Subsequently, results are presented concerning fluid analyses, such as densities and viscosities, as well as measurements related to rock-fluid interaction, such as contact angle, and fluid-fluid, such as interfacial tensions. These analyses are necessary for understanding two-phase flow in the pore systems of the coquinas.

4.1.1 Porosity and Absolute Permeability Measurements

Table 4-1 shows the measurements obtained with the porosimeter/permeameter DV-4000 for samples 1-4, 1-19B, 1-20B and 1-34A.

Table 4-1 – Basic petrophysical properties of four samples.

Sample	Pore Volume (cc)	Porosity He (%)	Permeability N_2 (mD)	Grain Density (g/cc)	Diameter (cm)	Length (cm)	Mass (g)
1-4	5.26	14.7	33.19	2.70	3.63	3.52	82.26
1-19B	6.82	19.8	765.09	2.69	3.50	3.61	74.26
1-20B	6.57	18.7	1,075.01	2.69	3.62	3.61	77.04
1-34A	5.74	16.3	639.08	2.69	3.60	3.53	79.30

Figure 4-1 shows, for the Bed 2B layer, the location of the regions from which the samples studied were taken. From the permoporosity data it was possible to identify three regions that present very distinct characteristics. In order to characterize the samples, three porosity and absolute permeability (K_{abs}) levels were assumed, as follows:

i) For the porosity measurements, values up to 10% were defined as low porosity; intermediate porosity between 10% and 15%; and high porosity above 15%;

ii) For the K_{abs} measurements, values up to 150 mD were defined as low permeability; K_{abs} intermediate values between 150 mD and 650 mD; and high K_{abs} values greater than 650 mD;

Hence, the results of the measurements with the poropermeameter helped to characterize of the 4 selected samples, also shown in Figure 4-1 (b):

i) Sample 1-4: Intermediate porosity and low K_{abs};

ii) Samples 1-19B and 1-20B: High porosity and high K_{abs};

iii) Sample 1-34A: High porosity and intermediate K_{abs};

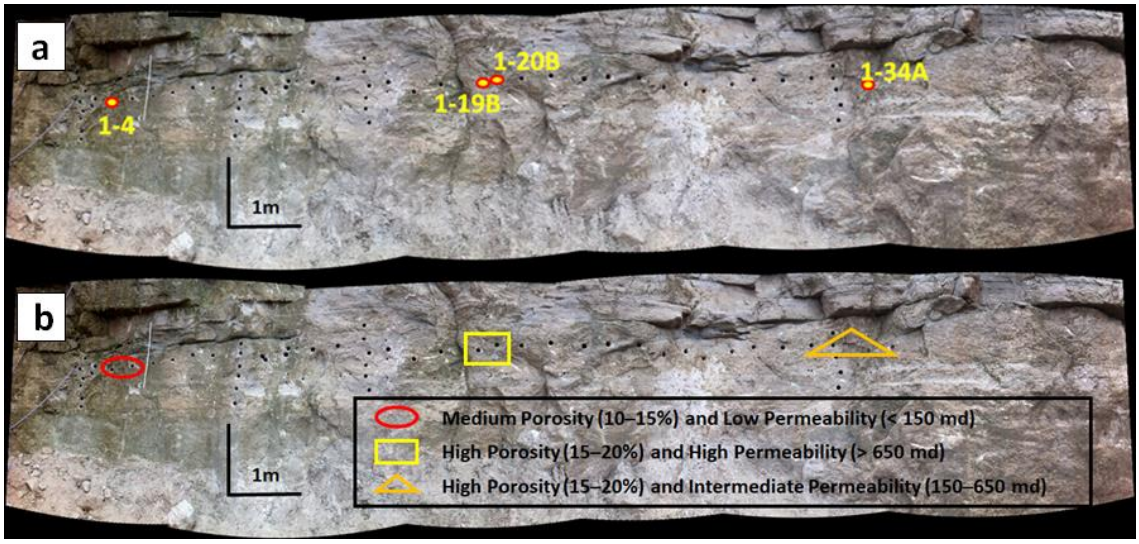


Figure 4-1 – Identification of Bed 2B (a) regions from which the samples were collected and (b) characterization of three distinct regions as a function of their permo-porous properties.

Samples with high and intermediate K_{abs} (1-19B, 1-20B and 1-34A) were then selected for the experimental primary drainage test using the centrifugation method.

4.1.2 Thin Section Analysis

Thin sections were also obtained and analyzed for visual evaluation of the total porosity of the samples. Figure 4-2 presents some regions of interest (ROI) in the images of the analyzed petrographic thin sections.

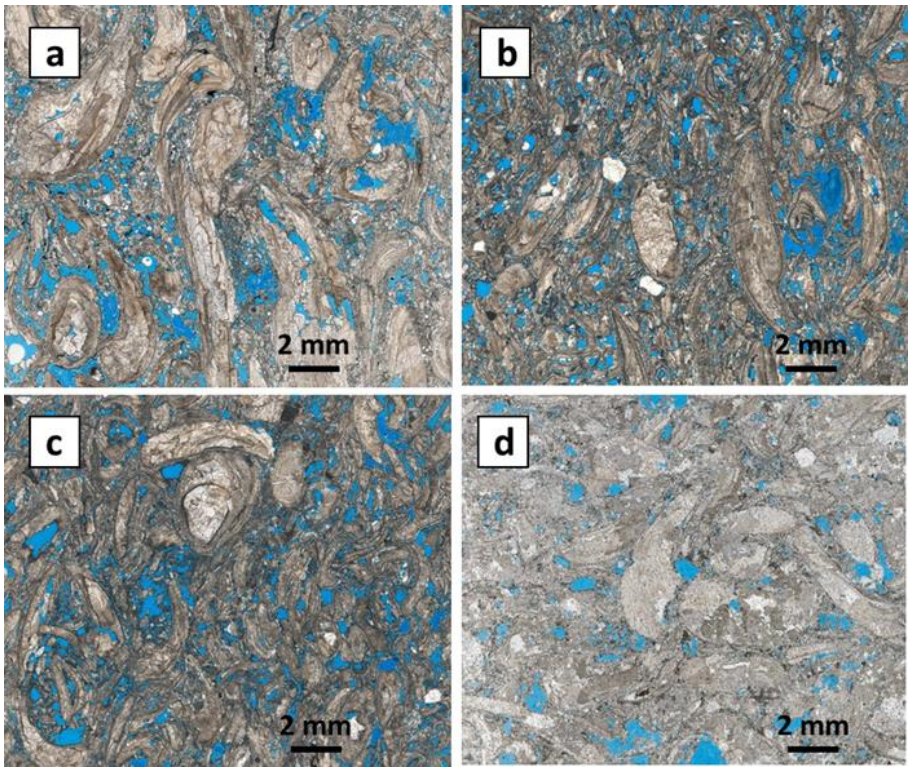


Figure 4-2 – Images obtained from the analysis of thin sections, aiming the analysis of the pore system, for the samples (a) 1-4, (b) 1-19B, (c) 1-20B and (d) 1-34A. All images were obtained with the optical microscope *Zeiss Imager M2m*.

This visual evaluation step assists in the determination of porosity during the segmentation stage, since it is possible to analyze a region of interest (ROI) that allows a correlation between the porous system being visualized and what will be obtained using μCT. Figure 4-2 shows some ROI selected for each sample, in order to observe the pore system in greater detail. The blue color in the images present refer to epoxy blue resin that allows a better contrast between the pores and the rock.

When analyzing the images of thin sections in Figure 4-2, a preliminary evaluation of the samples can be made:

i) Sample 1-4: Rocks consisted of robust, whole and fragmented bivalves, that are well preserved and with a low intensity fragmentation rate. Shell fragments range from approximately 1 mm to 15 mm, with shells larger than 2 mm predominant. Bioclasts are moderately oriented and poorly sorted. There are rare (2%) subangular siliciclastic grains of low sphericity, moderately sorted and of an average size of 0.5 mm. There are traces of opaque minerals, classified as microcrystalline pyrite. The rock is grain-supported with an open framework. Bioclasts present longitudinal and sometimes sutured contact. In this way, they have

dense packing. Several phases of dissolution have generated the current porosity. The types of porosity present are: interparticle, intraparticle, moldic and vugular. Predominance of vugular and interparticle porosity;

ii) Sample 1-19B: Rock formed by fragments of robust and medium shells, with fragments ranging from approximately 0.3 mm to 9 mm. The rock is well sorted, with most bioclasts having a size up to 4 mm. Presence of rare siliciclastic (3%) angular and spherical grains, with an average size of 0.5 mm. There are also rare fragments of disarticulated ostracodes (2%) and traces of microcrystalline pyrite. The rock is grain supported, with an open framework and dense packing. Bioclasts are moderately oriented. The rate of fragmentation of the bioclasts is high. There was mechanical compaction. It is possible to reconstruct some shell fragments, demonstrating that there was fragmentation, but there was no subsequent transport to remove these fragments. The types of porosity present are: intraparticle, interparticle, vugular, moldic, intercrystalline and breccia. Predominance of intraparticle, interparticle and intercrystalline porosities, with the least significant being the moldic porosity;

iii) Sample 1-20B: Rock formed by fragments of shells, rounded, predominantly robust, with size varying from 0.5 mm to 10 mm. It has a medium intensity fragmentation rate. Bioclasts are composed mainly of bivalves, with rare presence of gastropods and ostracodes. Rare angular siliciclastic grains of low sphericity, with an average size of 0.5 mm. The rock is grain supported and with an open framework. Bioclasts, moderately sorted and oriented, have dense packing. The contact between them is predominantly longitudinal, although punctual contact also occurs. There are bioclasts with a thin micrite layer. The rock was cemented at least twice. Several phases of dissolution have generated the current porosity. The types of porosity present are: intraparticle, interparticle, vugular, intercrystalline, breccia, shelter and moldic;

iv) Sample 1-34A: Rock formed by fragments of robust shells. Size of the fragments of the bioclasts vary from 1 mm to 8 mm, which are poorly

sorted and moderately oriented. They have low intensity fragmentation rate with little sign of abrasion. There is a rare presence of siliciclastic grains (2%), sub-rounded, spherical and with an average size of 0.5 mm. The rock is grain supported with open framework. The packing is dense, with contact between the point and longitudinal bioclasts. The interparticular cement is fine. Several phases of dissolution have generated the current porosity. The types of porosity present are: intraparticula, interparticula, vugular and intercrystalline. With predominance of interparticle and vugular porosities and less significance of intraparticle porosities.

It is important to highlight that the analysis of the petrographic thin sections helps to identify the main types of porosity in samples of the sorted coquinas. Table 4-2 shows the main types identified.

Table 4-2 – Identified porosity types based on thin section analysis.

Sample	Porosity Types
1-4	Interparticle, Intraparticle, Moldic, and Vugular
1-19B	Interparticle, Intraparticle, Moldic, Vugular, Intercrystal, and Breccia
1-20B	Interparticle, Intraparticle, Moldic, Vugular, Intercrystal, Shelter and Breccia
1-34A	Interparticle, Intraparticle, Intercrystal, and Vugular

Several dissolution phases generated the current porosity of several of the samples: 1-4, 1-20B, and 1-34A. The measured porosity and absolute permeability values indicate good connectivity between the meso- and macro-pores for samples 1-19B, 1-20B, and 1-34A, which could be evaluated from the this section analysis. Figure 4-3 identifies the contours and sizes of bivalve shells of sample 1-34A, showing interparticle and intraparticle porosity.

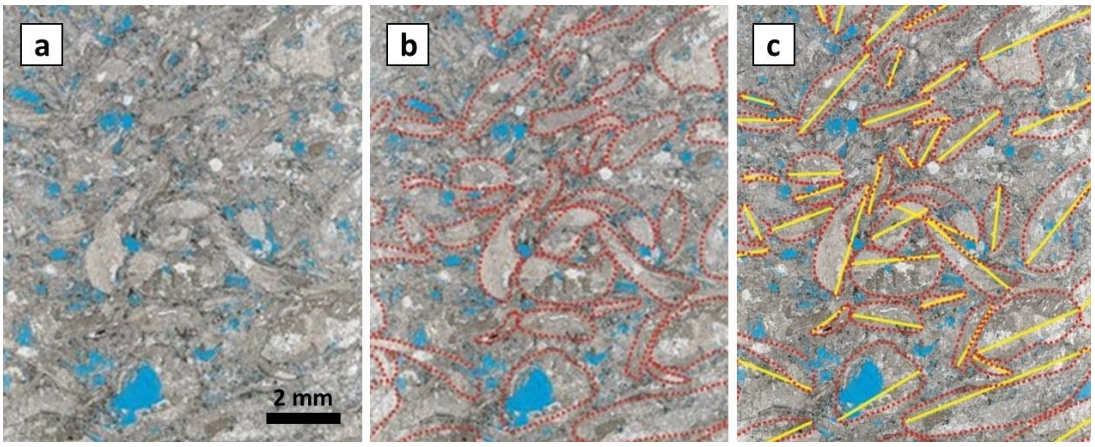


Figure 4-3 – Scanned images of sample 1-34A obtained with optical microscopy showing (a) blue epoxy resin filling the pores of the thin section, (b) highlighted in red the contours of bivalve shells, and (c) highlighted in yellow the size of the bivalve shells.

4.1.3 SEM-EDS Analysis

SEM was used next to analyze the surface of the selected rock slabs in order to evaluate the characteristics and dimensions of different pore structures. Central areas of the cut rock slabs (Figure 3-6) were selected for this purpose.

The images in Figure 5-4 show a gradual zoom of this region, with increases of 50, 150, 300, 800, 1200 and 2000 times the original size for the rock slab of sample 1-34ª, of a region which constituted the inner part of a bivalve shell. Figure 4-4(a) shows the presence of several large pores in the order of a few millimeters, externally to the center of the bivalve, while the largest zoom shows pores larger than 30 μm (Figure 4-4 (f)). These observations suggest that optical microscope analyses of the thin section were consistent since they showed the same patterns: predominance of interparticle and vugular porosities in different regions. These results are important to understand the main aspects related to the pore size distribution and the connectivity of these pore systems.

Figure 4-5 shows the same gradual zoom for a slab rock 1-20B. In this case, the presence of a dense packing of bioclasts and the presence of cementation are observed from the images with the greatest increase. Figure 4-5 (a) shows pores with dimensions from a few microns up to a few millimeters. Although the SEM images show much information about the rock matrix, the permoporosity data indicate a sample with high porosity and high K_{abs}, contrasting with information obtained directly from the SEM. This is one indication of the considerable heterogeneity of this sample, while also suggesting that the rock slab may not be the a proper REV of the sample.

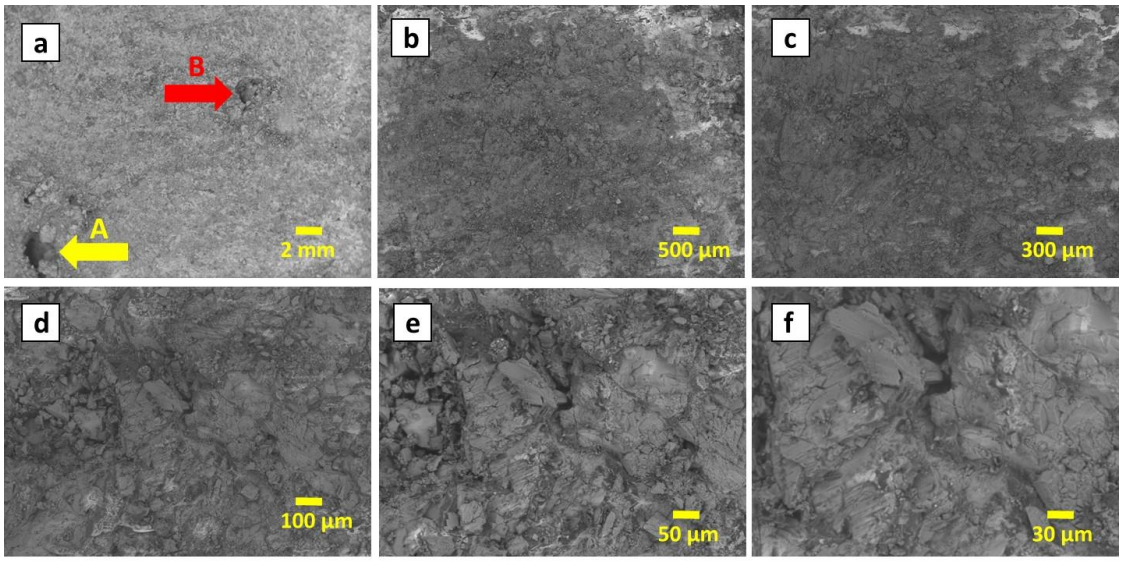


Figure 4-4 – SEM images of a rock slab of sample 1-34A obtained with an increase of (a) 50; (b) 150; (c) 300; (d) 800; (e) 1200, and (f) 2000 times the selected region of the rock slab. Fig. 5a shows the presence of two large pores of a few millimeter each (A and B).

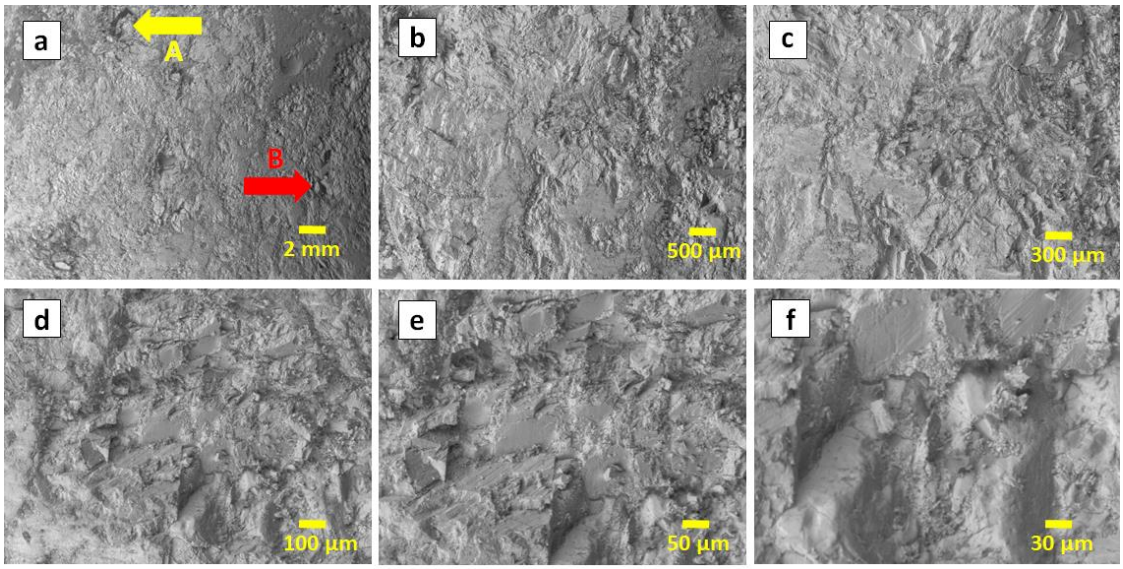


Figure 4-5 – SEM images of a rock slab of sample 1-20B obtained with an increase of (a) 50; (b) 150; (c) 300; (d) 800; (e) 1200, and (f) 2000 times the selected region of the rock slab. Fig. 5a shows the presence of a large pore (A) of a few millimeter and a small pore with few micron (B).

Several regions were particularly challenging for analyzing the pore system and the rock composition of some of the coquina samples. Regarding the sample 1-34A, it was selected a southern region from the cut rock slab was selected to perform an EDS analysis. The analysis was very helpul to evaluate dubious regions, which could be interpreted visually as pores or as material with a lower attenuation coefficient in the µCT

images, as well as providing a qualitative indication of the elements presented in the sample. Figure 4-6 (a) shows three well-identified regions (represented by the letters A, B and C above the arrows, in the image). The yellow arrow (A) indicates a pore that is a few mm wide, while the red arrow (B) points to a well-defined pore (in the center) surrounded by a region that is more poorly defined. That region has a grey-level quite similar to that of the area in blue (C), which clearly does not correspond to a pore. The EDS allowed us to identify the latter region (C) as being composed of siliciclastic material (Figure 4-6 (d)), which was already identified in the thin section.

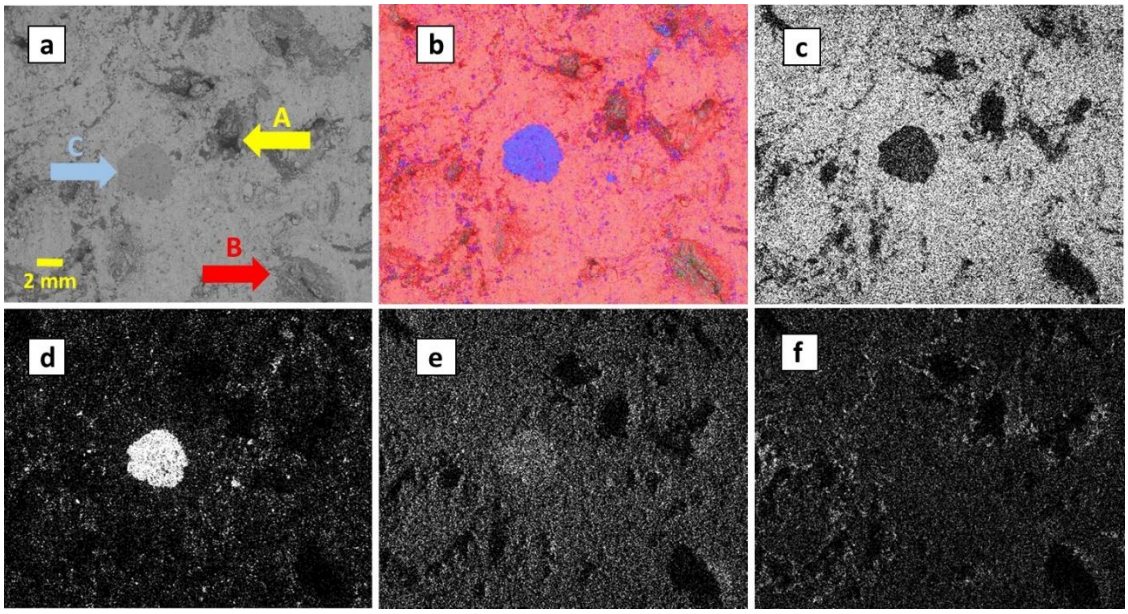


Figure 4-6 – (a) EDS image of the analyzed area, identifying three well-defined regions (A, a well-defined pore, B, a pore-centered region with dark grey level around it, and C, a dark grey level region similar to B but with no obvious pore boundary), (b) visual evaluation (colors) of the different components of the sample; (c) abundant presence of calcium, (d) presence of silicon in a small region (white dots), (e) oxygen, and (f) carbon distributed around the sample.

Rock lithology evaluation is an important step during EDS analysis which will help to establish correlations between the relaxation time T_2 and the pore radius. This then can be done using Eqs 4.3 and 4.4, based on the right selection of the surface relaxivity parameter (ρ_2). As previously mentioned, this parameter is linked to the rock/fluid interaction. The value of ρ_2 equals to 35.76 μs from the work of LUNA *et al.* (2016) while HOERLLE *et al.* (2018) considers the composition of coquina samples from Bed 2B higher than 90% of calcite ($CaCO_3$).

As an example Figure 4-7 presents the analysis of a rock slab area of sample 1-19B with the identification of two regions: a first one referring to a well-defined pore, surrounded by a region with a darker gray scale (region A) and a region defined by well-delimited grains with a lighter color, corresponding to pyrite (FeS_2), according to Figure 4-7 (d). Figures 4-7 (b) and (c) correspond to a region predominantly formed by calcium, the constituent of which is identified as calcite ($CaCO_3$).

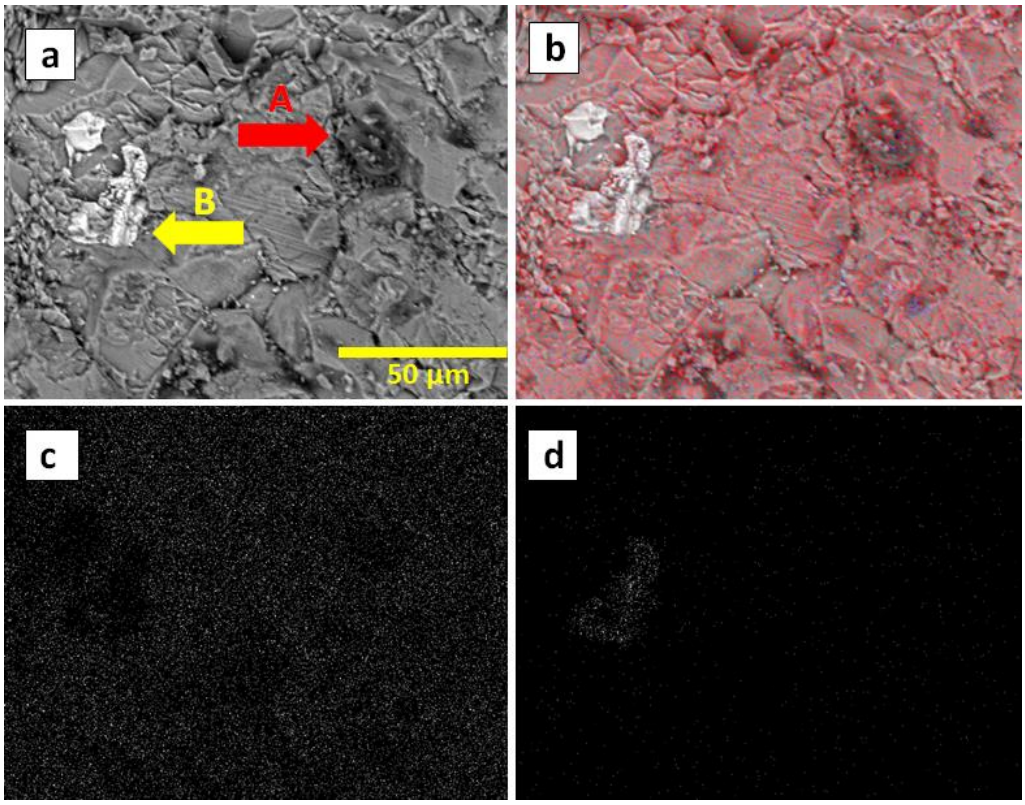


Figure 4-7 – (a) EDS image of a ROI from a rock slab of sample 1-19B, identifying three well-defined regions (A, a well-defined pore, B, a grain-centered region with light grey level), (b) visual evaluation (colors) of the different components of the sample; (c) abundant presence of calcium, and (d) presence of sulphur and iron in a small region (white dots), identified as pirite (FeS_2).

Figure 4-8 shows the spectrum of the main elements identified from the image in Figure 4-7 (a). The presence of large amounts of the calcium, oxygen and carbon, components of calcite can be verified, being identified throughout the sample. The region identified by the yellow arrow (arrow B) corresponds to pyrite whose presence can be verified in the analyzed spectrum. Two smaller peaks, referring to sulfur and iron are also easily visualized. Some remnants also exist of magnesium and silicon, the latter being associated with quartz (SiO_2). The large amount of beryllium observed in the first peak

refers to the stabilization of the equipment during the first stages of the analysis, not specifically corresponding to some material present in the sample.

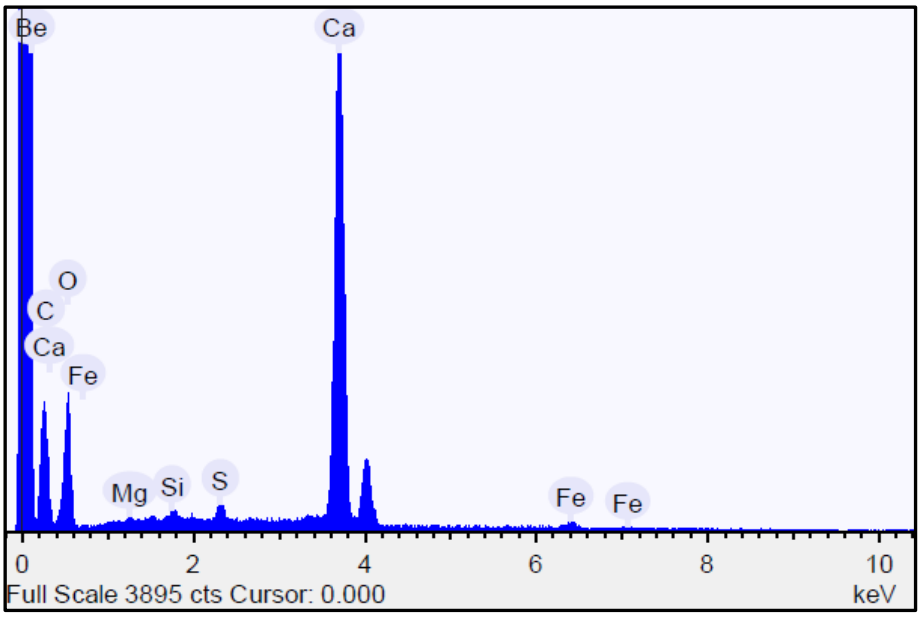


Figure 4-8 – Spectrum of the main elements identified in the image of Figure 4-7 (a) from EDS analysis. It is possible to verify large amount of calcium, oxygen and carbon, mainly related to calcite ($CaCO_3$). There is also a presence of sulphur and iron, identifying pirite in specific regions of the sample. Small quantities of magnesium and silicon occurs also. The large amount of beryllium identified at the first peak is related to the stabilization of the equipment during the first stages of the analysis with no direct correlation to the sample. Accelarating voltage was 15 keV.

Table 4-3 presents a quantitative analysis regarding the area analysis of Figure 4-7 and the spectrum presented in Figure 4-8. This spectrum for the selected area detected around 30% calcium, 53% oxygen, and 15% carbono (%weight), typical of calcite. The results also indicate the presence of iron (around 1.3%), and sulphur (around 0.7%) related to pirite, as previously identified. A small concentration of silicon (around 0.3%) also indicates the presence of quartz.

Table 4-3 – EDS quantitative analysis (%wt) for the main elements of a ROI selected from the rock slab 1-19B.

Sample	Calcium (%wt)	Carbon (%wt)	Oxygen (%wt)	Silicon (%wt)	Sulphur (%wt)	Iron (%wt)
1-19B	30.2	14.6	52.8	0.3	0.7	1.3

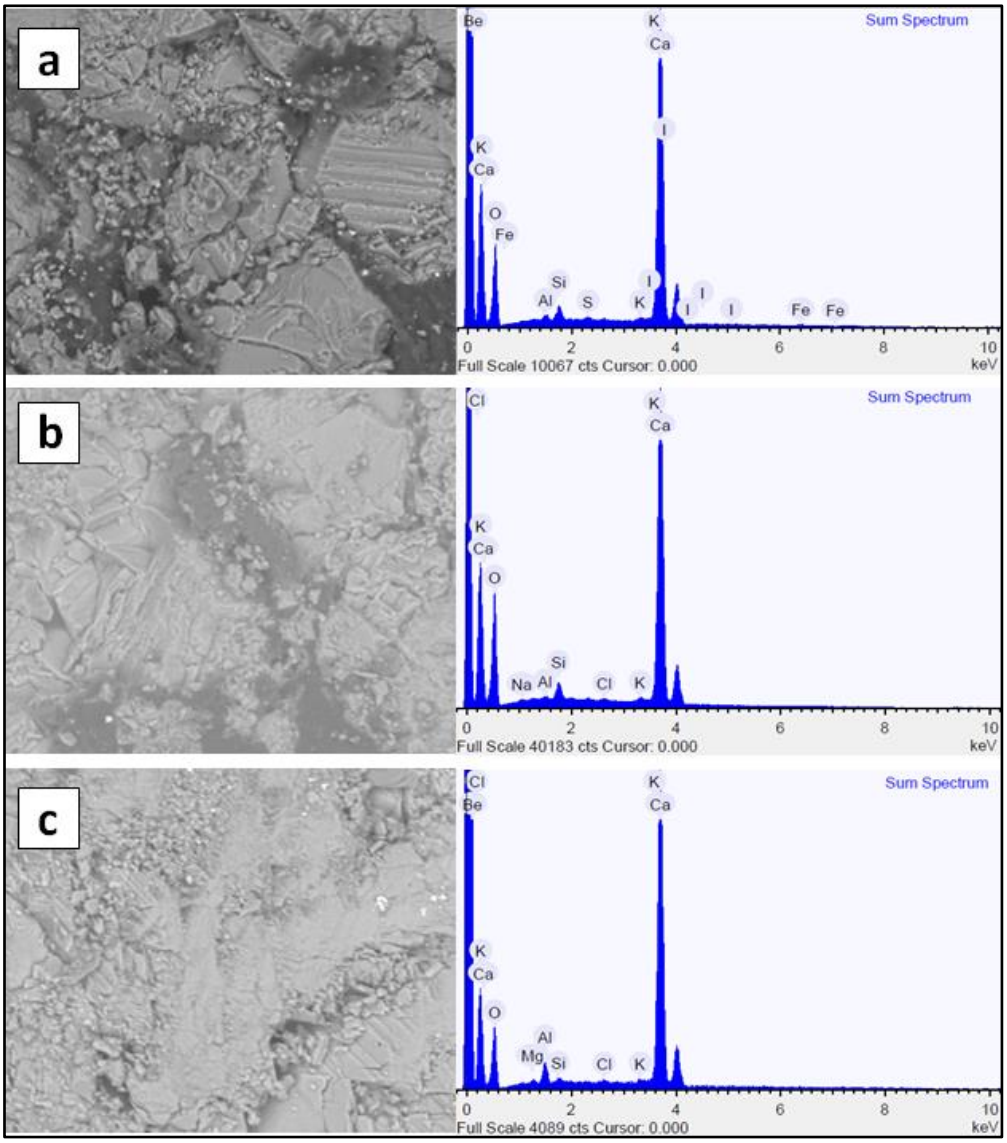


Figure 4-9 – Spectrum obtained from EDS analysis of the main elements of a ROI of each rock slab (a) 1-4; (b) 1-20B; and (c) 1-34A. It is possible to verify large amounts of calcium, oxygen and carbon, mainly related to calcite ($CaCO_3$). The presence of sulphur and iron, indicates pirite in specific regions of the sample, while silicon, indicates presence of quartz. The large amount of beryllium and chloride identified at the first peak is related to the stabilization of the equipment during the first stages of the analysis with no direct correlation to the sample. Accelarating voltage of 15 keV.

Figure 4-9 presents the main elements found during the evaluation of different ROI from different rock slabs: 1-4, 1-20B, and 1-34A. The SEM-EDS images are presented with the spectra related to them. The results clearly indicate the main component of all coquina samples: calcite.

4.1.4 XRD Analysis

XRD results for the studied coquina samples are showed in Table 4-4. As expected, from the SEM-EDS analysis, coquinas are rich in calcite and contain small percentage of quartz and some pyrite (not measureable). It should be considered that the actual surface Ca content of these samples is not known. The SEM-EDS results presented in this chapter showing higher calcium concentrations at the surface is likely correct. Furthermore, being very heterogeneous reservoir rocks, the composition may differ among the different slabs. The analysis could not be performed in a greater number of rock slabs due to limited number of samples.

Table 4-4 – XRD quantitative analysis (%wt) of the coquina samples.

	Sample	Quartz	Pyrite	Calcite	Clays
Coquina	1-4	1	*	99	-
	1-19B	1	*	99	-
	1-20B	1	*	99	-
	1-34A	*	*	100	-

* Presence (i.e. lower than 1%).

The results of the SEM-EDS and XRD analyses indicate that the coquinas contain more than 99% of calcite. This result is important because it provides two important pieces of information:

i) It is possible to consider the surface relaxivity parameter (ρ_2), as previously described, as 35.76 μs. LUNA *et al.* (2016) and HOERLLE *et al.* (2018) consider this value based on the composition of Bed 2B coquinas to be higher than 90% of calcite. This parameter is paramount to correlate relaxation time T_2 and the pore radius, from NMR measurements, accordingly;

ii) The XRD analysis indicates that the samples do not contain any type of clay. This is important to understand the connectivity of the pore systems, since clay could reduce the permeability of the samples;

4.1.5 NMR Analysis

This section addresses the results obtained from the NMR technique to verify pore size distribution (PSD). Prior to saturation, as described in Chapter 3, the samples were microtomographed, and the results will be presented later in this chapter in another section.

Table 4-5 shows the Saturation Indexes (SI) results of the samples. Although the SI values were below 98%, the saturation procedure was considered satisfactory, since as indicated by. LUNA *et al.* (2016), complete saturation due to problems filling vugs present on the surface of the samples with the saturating fluid. These porous structures significantly decrease the effectiveness of the saturation process.

Tabela 4-5 – Saturation Index (SI) for each studied sample.

Sample	Dried Mass (g)	Saturated Mass (g)	Brine Density (g/cm^3)	Pore Volume (cm^3)	SI (%)
1-4	82.21	87.43	1.039	5.26	95.51
1-19B	74.10	80.94	1.039	6.82	96.53
1-20B	76.76	83.29	1.039	6.57	95.66
1-34A	79.10	84.83	1.039	5.74	96.09

Table 4-6 shows a comparison of results of the porosity measurements (obtained using DV-4000 gas permeameter) and porosities obtained using NMR. This is an important calibrator for the construction of PSD curves because inconsistent values between these two techniques would lead to erroneous interpretations of the results.

Like LUNA *et al.* (2016) and HOERLLE *et al.* (2018), the transformation of T_2 into radii assumed spherical shapes for the pores and a surface area factor (S) equal to three (3). For the classification of pore sizes, from an analysis by LØNØY (2006) of the interparticle pores and following HOERLLE *et al.* (2018), the following pore diameter size ranges were considered for classification of the NMR data: micropores below 50 μm, mesopores from 50 to 100 μm, and macropores above 100 μm.

Table 4-6 – Porosity values obtained with the Permeameter and NMR techniques.

Sample	Porosity (Phi) NMR (%)	Porosity (Phi) Porosimeter (%)	Relative Difference (%)
1-4	14.26	14.7	3.0
1-19B	18.36	18.7	1.8
1-20B	19.74	19.8	0.3
1-34A	15.72	16.3	3.6

Figure 4-10 shows the PSD curves and cumulative porosities of sample 1-4. An analysis of the curves indicates that:

i) The PSD curve shows that the pore array with radius below 10 μm represents a significant portion of the porosity, although the peak distribution is between 40 μm and 50 μm. This sample has an average porosity and a low permeability. Thus, according to LØNØY (2006) and HOERLLE *et al.* (2018), sample 1-4 has the majority of pores represented by micropores, according to the classification based on the NMR data;

ii) The cumulative porosity curve indicates that about 20% of the porosity is formed by pores with radii up to 10 μm, representing a significant portion of this petrophysical property;

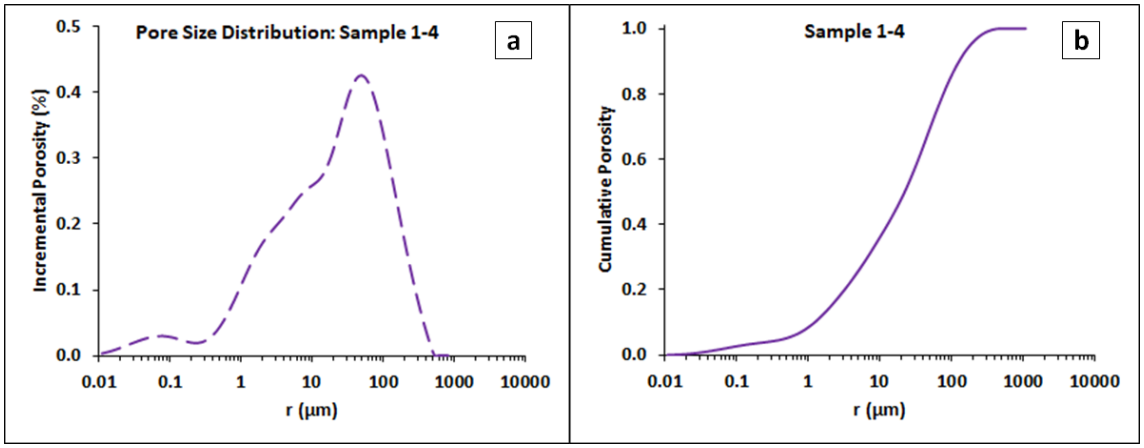


Figure 4-10 – (a) PSD curve obtained from the NMR data, and (b) cumulative porosity for sample 1-4.

The results show that sample 1-4, which has a low Kabs, must have a large part of its effective porosity related to pores with dimensions equal to or less than 10 μm. Figure 4-10 (a) shows a very characteristic secondary peak around 0.1 μm. Notably, the

PSD curve appears to have another peak (intermediate Gaussian) for some value between 1 μm and 10 μm, although this peak is relatively ill defined as a function of the sums of Gaussians that generate the PSD curve.

Figure 4-11 shows the PSD curves and cumulative porosity of sample 1-19B. The curves it can be verified that:

i) Three very distinct peaks in the PSD curve are present: the first around 0.5 μm, the second between 7 μm and 8 μm, and the largest of them between 70 μm and 80 μm. This sample has a relatively high porosity and high permeability. Thus, according to LØNØY (2006) and HOERLLE *et al.* (2018), sample 1-19B has the majority of its pores in the form of meso- and macropores;

ii) By observing the accumulated porosity curve, one can see that about 65% of the porosity of this sample is in the range of meso- and macropores;

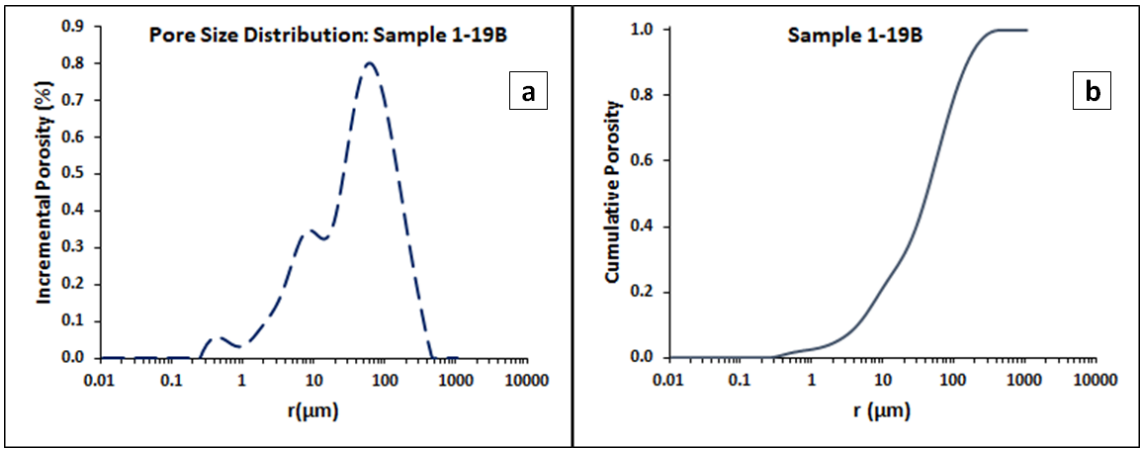


Figure 4-11 – (a) PSD curve obtained from NMR data, and (b) cumulative porosity for sample 1-19B.

Figure 4-12 shows the PSD curves and cumulative porosity for sample 1-20B. The curves indicate that:

i) The PSD curve is slightly different from the PSD curve of sample 1-19B, although the sample 1-20B also has three distinct peaks, the first peak is not as well defined as in the previous sample, although its peak is also around 0.5 μm. The second peak is in the range of 7 μm to 8 μm, and the highest peak is between 70 μm and 80 μm. This sample was described earlier as having high porosity and high permeability. Thus,

according to LØNØY (2006) and HOERLLE *et al.* (2018), the sample 1-20B has the majority of the pores represented by meso- and macropores;

ii) It is possible to note that the cumulative porosity curve, which shows that around 60% of the porosity of this sample is in the meso and macropore range;

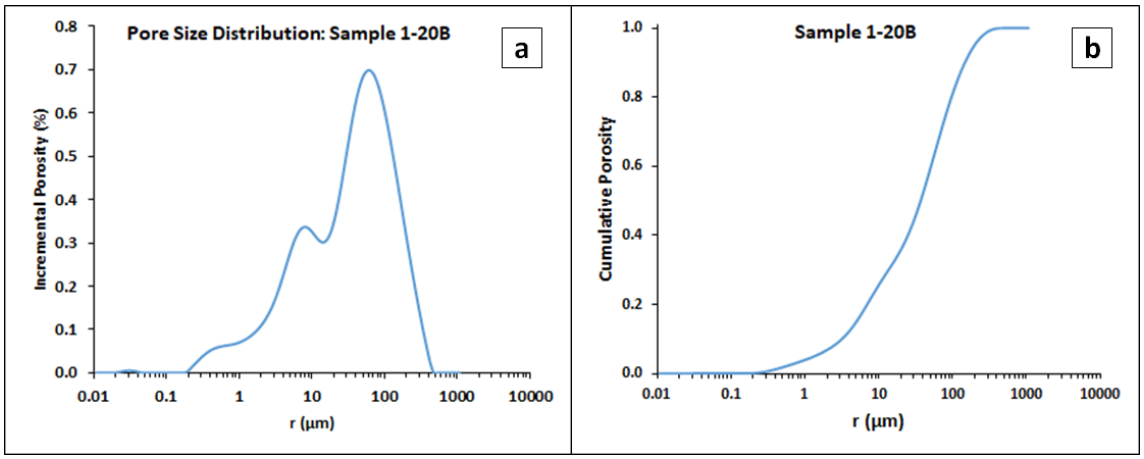


Figure 4-12 – (a) PSD curve obtained from NMR data, and (b) cumulative porosity for sample 1-20B.

Samples 1-19B and 1-20B, which were removed from closely related regions, have characteristics regarding the distribution of their very similar pore sizes. However, as shown in Table 4-1, the permeability difference is significant, around 300 mD, stating that although the PSD curves are quite analogous, the way these pores are connected and the geometries of the porous systems are not identical.

Finally, Figure 4-13 shows the PSD curves and accumulated porosity for sample 1-34A. From the analysis of the curves it can be verified that:

i) Sample 1-34A does not show the very characteristic peaks found in samples with higher porosity and Kabs. However, one can estimate the first peak in the range of 0.6 µm, while the second peak is in the range of 9 µm to 10 µm. The third and largest of them is in the 90 µm and 100 µm range. This sample was described, in the present work, having high porosity and high permeability. Thus, according to LØNØY (2006) and HOERLLE *et al.* (2018), sample 1-20B has the majority of the pores represented by meso and macropores;

ii) By observing the accumulated porosity curve, it can be seen that something around 60% to 65% of the porosity of this sample is in the range of meso and macropores;

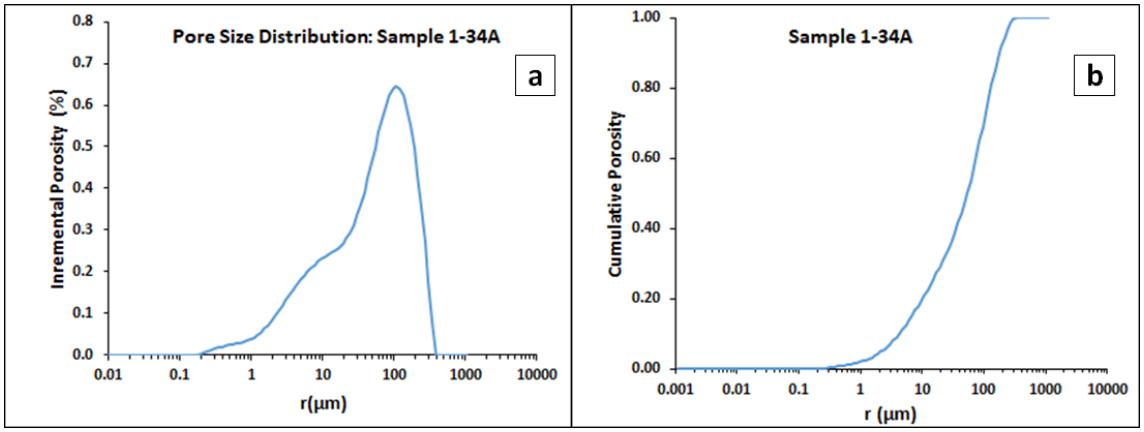


Figure 4-13 – (a) PSD curve obtained from NMR data, and (b) cumulative porosity for sample 1-34A.

4.1.6 Fluids Analysis

The step of analyzing the densities and viscosities of the fluids used in this work is extremely important for the purpose of characterizing the contact angle and interfacial tension between two fluids during the primary drainage simulations in the digital systems that are reconstructed from the microtography images of X ray.

From the information presented in Chapter 3, the fluid density measurements used to conduct the subsequent numerical tests were obtained. The obtained curves show the density values measured at different pressures, keeping the temperature constant and equal to 60ºC.

Figures 4-14 and 4-15 show the measured density values and the fitting equations as a function of the linear regression of the points obtained for Oil B and Brine B, respectively.

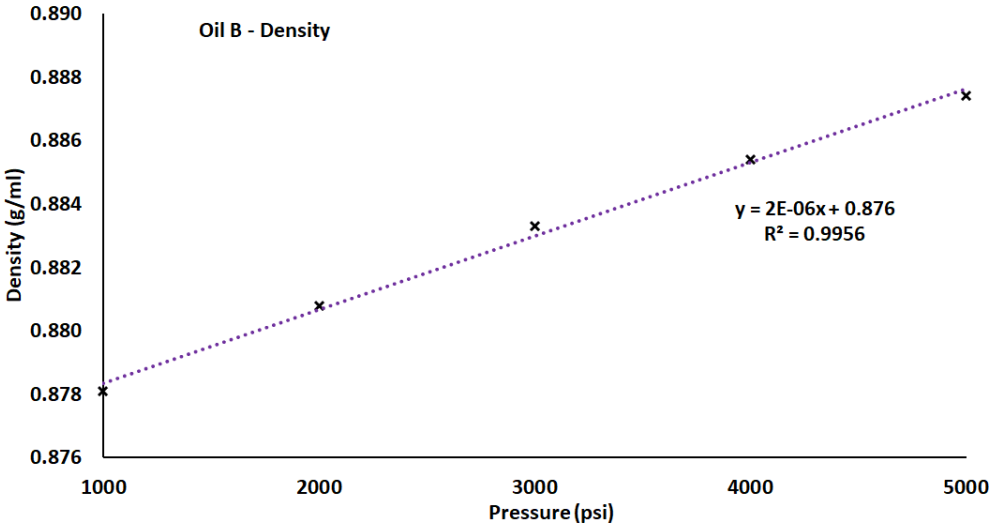


Figure 4-14 – Density measurements of Oil B at 60ºC using Anton Paar DMA HPM densitometer with a thermostatic bath at different pressures.

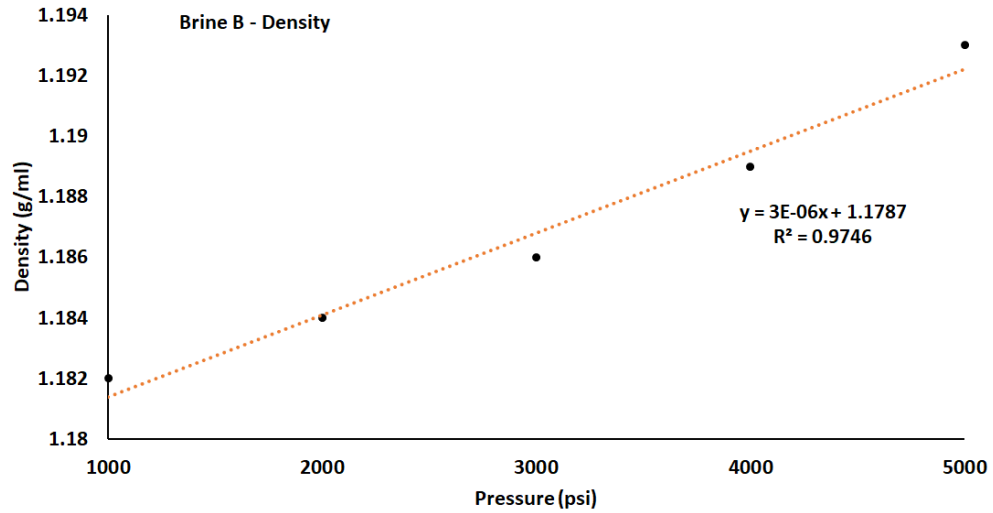


Figure 4-15 – Density measurements of Brine B at 60ºC using Anton Paar DMA HPM densitometer with a thermostatic bath at different pressures.

The viscosity values estimated through the *OLI Studio 9.6*® software for all the fluids mentioned above are shown in Table 4-7. Estimatives were made at 25 °C and 60 °C at 14.7 psi (atmospheric pressure) and 1000 psi were performed. This information is essential for the simulation of primary drainage with different scenarios: comparing with the data from the experiments performed in the centrifuge, and for studies involving the Pre-salt scenario. In the same Table 4-7 the estimated density values for Model Oil A and Model Brine are presented through the same software.

Table 4-7. Viscosity (cP) and density(g/cm^3) estimates for Model Brine, Model Oil A, Brine B, and Oil B from measurements and simulations using *OLI Studio 9.6*® software

Fluid	Model Brine	Model Oil A	Oil A	Brine B	Oil B
Vicosity (cP) at 21ºC / 14.7 psi	0.970	1.970	26.2	2.272	62.07
Vicosity (cP) at 60ºC / 14.7 psi	0.516	0.992	5.63	1.192	16.07
Vicosity (cP) at 60ºC / 1,000 psi	0.516	1.162	14.5	1.194	18.61
Density (g/cm^3) at 21ºC / 14.7 psi	1.027	0.785	0.844	1.209	0.862
Density (g/cm^3) at 60ºC / 14.7 psi	1.012	0.762		1.192	0.850
Density (g/cm^3) at 60ºC / 1,000 psi	1.015	0.771		1.193	0.854

4.1.7 Contact Angle Measurements

As previously stated in Chapter 3, Kruss/Eurotechnica DSA equipment was used for contact angles measurements. The procedure presented by DREXLER *et al.* (2019) states that measurements are performed every 30 seconds for the complete experiment time. In order to discuss the results, the ANDERSON (1986) criteria to classify wettability is considered:

i) CA < 60°: Water-wet

ii) 60° < CA < 75°: Weakly water-wet

iii) 75° < CA < 105°: Intermediate-wet

iv) 105° < CA < 120°: Weakly oil-wet

v) CA > 120 °: Oil-wet

Table 4-8 shows the contact angle measurements obtained after the experiments in the DSA. It is important to note that because of the number of rock slabs available for the CA tests, two samples were used for each Brine/Oil combination. Samples 1-19B and 1-34A were selected for the calibration of the simulations as a function of the data from the centrifuge tests, as well as the calibration of the digitally reconstructed porous systems as a function of the Kabs, as will be described later. Table 4-9 shows the CA measurements for the rock slab of sample 1-19B at different pressures and at the temperature of 60 °C.

The results obtained from SEM-EDS and XRD analysis show that all samples have more than 99% of calcite in their composition and therefore present similar behavior regarding the rock-fluid interaction, obviously, the same fluid-fluid combination.

Table 4-8. Contact Angle (CA) measurements involving the coquina rock slabs and the interaction between selected fluids at 60ºC and 1,000 psi.

Rock Slab	Model Brine / Model Oil A – CA	Brine B / Oil B – CA
1-4	-	131º
1-19B	42º	-
1-20B	-	127º
1-34A	44º	-

It can be stated that the CA difference between sample 1-19B and 1-34A could be related to the surface roughness and composition of each rock slab. Altough all samples were polished, minor alteration in measurements can occur. Coquina samples have considerable roughness in agreement with their greater porosity and wider pore distribution.

Discussion about the aging process can be found elsewhere, altough the procedure was similar to those found in the literature (DREXLER *et al.*, 2019; FACANHA *et al.*, 2016):

i) The samples were kept at constant reservoir (test) temperature: 60ºC;

ii) The rock slabs were aged in brine for 1 day: Model Brine for samples 1-19B and 1-34A, and Brine B for samples 1-4 and 1-20B;

iii) The rock slabs were aged in oil for 30 days: Model Oil A for samples 1-19B and 1-34A, and Oil B for samples 1-4 and 1-20B;

iv) The cleaning of bulk oil on the surface was done by centrifugation in a tube filled with the test brine at 3000 rpm for 20 minutes.

The last topic is also important: CA cannot be measured on the surface if it is covered by an excess bulk oil film, once it is not representative of the solid surface.

The obtained CA measurements indicate two different behaviors:

i) CA of the coquina samples (1-19B and 1-34A) aged and measured with the combination of Model Oil A and Model Brine indicate a water-wet behavior;

ii) CA of the coquina samples (1-4 and 1-20B) aged and measured with the combination of Oil B and Brine B indicate an oil-wet behavior.

These measurements indicate a clearly changing in wettablity from water-wet to oil-wet just changing the fluids composition and their interaction with the rock surface.

These measured CA can be used for drainage simulation purposes, using the results of samples 1-19B and 1-34A to check the *Pc-Sw* curves from the centrifuge method.

Table 4-9. Contact Angle (CA) measurements at different pressures involving the coquina rock slab from sample 1-19B and the interaction between selected fluids.

Pressure (psi)	Model Brine / Model Oil A – CA
1,000	43.7º
2,000	42.5º
3,000	41.8º
4,000	41.2º
5,000	40.2º

4.1.8 Interfacial Tension Measurements

Interfacial Tension (IFT) values were measured using DSS Kruss/Eurotechnica goniometer based on DSA technique, as previsously described (Chapter 3). The measurement were conducted using two different pressures: 1,000 psi and 5,000 psi. The combination of the fluids were the same as those defined during the CA measurements: the first fluid-fluid interaction between Model Brine and Model Oil A, and the second one between Brine B and Oil B.

Table 4-10 presents the results of IFT measurements according to each fluid-fluid interaction. Experiments were carried out at 60ºC. Pre-Salt crude, Oil B, contains high concentrations of surface-active components (i.e. resins and asphaltenes) which is not found at Model Oil A. The results show that Oil B have relatively low values of interfacial tension with Brine B in comparison with IFT measurements from the interaction of Model Oil A and Model Brine.

Table 4-10. Interfacial Tension (IFT) measurements involving the combination of selected fluids.

Presure (psi) / Temperature	IFT (mN/m): Model Brine / Model Oil A	IFT (mN/m) Model Brine / Oil A	IFT (mN/m) Brine B / Oil B
14.7 / 21ºC		27.2	
1,000 / 60ºC	30.2		10.5
5,000 / 60ºC	29.2		10.3

Although interfacial tension measurements were performed at relatively high pressures, it is seen that at a pressure variation of 4,000 psi there was no significant change in the measured values for IFT.

Some important observations should be made regarding the IFT measures carried out:

i) The effect of pressure is weak compared to that of temperature for similar fluids composition and rock lithology (DREXLER, 2018);

ii) The DSA measurement of the IFT is linearly dependent on the density difference between the phases for fluids with similar or equal composition (DREXLER *et al.*, 2018);

Although all IFT measurements for Brine B and Oil B interaction were performed at pressures ranging from 1,000 to 5,000 psi, the primary drainage simulations involving Oil A and Model Brine are conducted at 14.7 psi pressure. According to the obtained measurements, the IFT value for this interaction is presented in Table 4-10 can be used for simulation purposes. However, temperature may play a more significant role in IFT values.

4.2 Digital and Numerical Results

4.2.1 X-ray Computed Microtomography

The first topic to address for each μCT image package refers to the acquisition and reconstruction time, as well as the number of slices and file size. Table 4-11 presents all these information. The reconstruction of digital models is related to the file size, once it was used Avizo® 9.5 software for post-processing and data manipulation.

It can be verified that μCT images file sizes with higher resolution (9.97μm) have at least 60GB of data that should be loaded and treated using visualization software, such as Avizo® 9.5, using a large amount of RAM. A powerful GPU is also necessary for post-processing and visualization purposes. As previously described, all computational efforts from filtering to numerical simulation were performed using a robust workstation. Nevertheless, the computational cost for higher resolution images manipulation is extremely high and this topic willbe address throughout this chapter.

Table 4-11. Acquisition time (h), number of slices, reconstruction time (h), obtained pixel size (μm), and file size (GB) for the studied coquina samples μCT images

Sample	**Acquisition Time (h)**	**Number of slices**	**Reconstruction Time (h)**	**Pixel Size (μm)**	**File Size (GB)**
1-4	6.595	3,901	4.0272	9.97	64.8
1-19B	8.0969	4,304	9.9061	9.97	71.5
1-20B	3.6614	3,893	7.7655	9.97	64.6
1-34A	5.4883	4,161	8.9977	9.97	62.2
1-4	1.3119	2,197	1.5241	18.52	10.2
1-19B	1.3783	2,179	0.5881	18.87	8.25
1-20B	1.1605	2,196	1.2411	17.81	9.11
1-34A	1.6611	2,210	0.2803	18.16	10.3
1-4	1.3869	1,705	0.5394	24.95	4.59
1-19B	1.4232	1,807	0.2655	24.95	4.86
1-20B	1.3572	1,739	0.2703	24.95	4.08
1-34A	1.3665	1,999	0.3011	24.95	4.69

Based on the acquisiton and pre-processing parameters presented and discussed in Chapter 3, after μCT image acquisition is the application of specific filters to reduce noise from the images and to sharpen them. As already stated, it was used the non-local means filter to reduce the image noise, specially the salt-and-pepper effect after the reconstruction of the images. It was selected Avizo® 9.5 software to pass the non-local means filter (Figure 4-16 (b)) and to reconstruct the 3D model of the rock, as well as to segment the image.

There is a possibility to use different post-processing image filters, such as Median, Gaussian, Anisotropic diffusion etc. All filtering steps in this work were performed with Non-local means filter. This filter is capable to reduce dramastically the salt-and-pepper noise as well as to enhance the contrast between different phases, such as rock components and the rock-pore interfaces, make them sharper and distinguishable.

The image evaluation stage starts with loading the images themselves and then using the selected filter, in this case Non-local means. From these data are selected volumes of interest, through cutting tools and selection of the software itself. For the rock slabs, cuboids were selected that had the maximum volume of the samples (according to the red squares present in Figure 3-6). The superficial regions pain rock slabs were excluded due to two main points:

i) To avoid edge effects from acquisition and that generate greater interference and noise in the outermost regions of the reconstructions;

ii) Exclude regions that overlap the background causing more difficulties in the later segmentation stage.

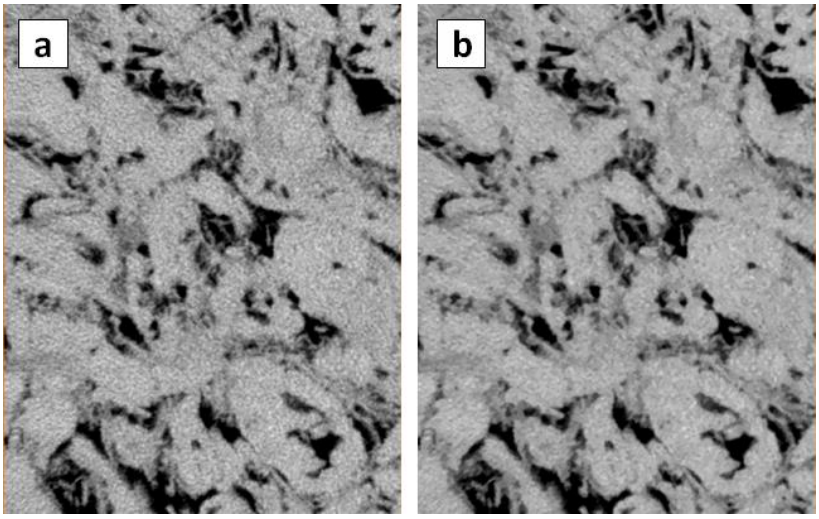


Figure 4-16 – Main step related to the noise reduction of (a) an original μCT image using (b) non-local filter from Avizo® 9.5. It is possible to verifiy that the image after the filter application is sharper and presents less salt-and-pepper noise.

For the plugs, the cylinders with the largest possible volumes were selected excluding the outermost regions that could lead to interference, as previously explained.

The steps related to the passage of the filter, selection of the volumes and their cuts are more computationally costly as the images with higher resolution are processed. The use of a more powerful GPU dramatically reduces the time required to apply the filter. The manipulation of volumes through specific display functions such as *Volume Rendering*, for example, are also influenced by the GPU, amount of RAM and CPU processing capacity.

4.2.2 Segmentation

This topic will address the results obtained through different segmentation methods: NMR-based segmentation and automated segmentation using developed algorithms based on well-known methods (Kittler & Illingworth, Ridler & Calvard, Otsu, Niblack e Bernsen). The results are expressed as a function of 8-bit images for study purposes, whose values in the gray scale range from 0 to 255.

4.2.2.1 NMR-based Segmentation

As described in Chapter 3, segmentation based on the NMR method is based on the idea that the porous system can be reconstructed by marking the porosity results from the NMR data analysis and the values obtained by digital petrophysics. Thus, by selecting the Threshold value (Th) that is necessary for the reconstruction of the calibrated three-dimensional model in function of the porosity estimates obtained from the μCT images.

As the porosity estimation is given as a function of the digital model generated from the μCT images, the pixel size plays a fundamental role in this selection. Based on Figure 3-13, the porosity values that can be obtained for the plugs of the selected samples are shown in Table 4-12. The last column refers to the porosity value found by analyzing the NMR data.

Table 4-12. Sub-resolution and detectable porosities from each reconstructed digital pore systems obtained from each coquina plug.

Sample	**Pixel Size (μm)**	**Sub-resolution Porosity (%)**	**Detectable Porosity (%)**	**NMR Porosity (%)**
1-4	9.97	3.51	10.75	14.26
1-19B	9.97	2.01	17.73	19.74
1-20B	9.97	2.53	15.83	18.36
1-34A	9.97	1.77	13.95	15.72
1-4	18.52	4.96	9.30	14.26
1-19B	18.87	3.91	15.83	19.74
1-20B	17.81	4.11	14.25	18.36
1-34A	18.16	2.81	12.91	15.72
1-4	24.95	5.49	8.77	14.26
1-19B	24.95	4.59	15.15	19.74
1-20B	24.95	5.08	13.28	18.36
1-34A	24.95	3.51	12.21	15.72

Based on the values of detectable porosity presented in Table 4-12, the segmentation based on the estimated digital porosity can be evaluated from the models generated with different resolutions. This method allows a calibration of the digital porosity and segmentation of concomitant form, using the detectable porosity as calibrator. Table 4-13 shows the porosities obtained from the segmentation based on the detectable NMR porosity and the porosity calculated from the digitally reconstructed networks.

Table 4-13. Calculated and detectable porosities from reconstructed digital pore systems obtained from each coquina plug.

Sample	**Pixel Size (µm)**	**Calculated Porosity (%)**	**Detectable Porosity (%)**	**Δϕ (%)**	**Relative Difference**
1-4	9.97	9.05	9.29	0.24	0.026
1-19B	9.97	15.73	15.83	0.10	0.006
1-20B	9.97	12.98	13.91	0.93	0.067
1-34A	9.97	12.45	12.68	0.23	0.018
1-4	18.52	7.37	7.64	0.27	0.035
1-19B	18.87	13.45	13.82	0.37	0.027
1-20B	17.81	11.60	12.36	0.76	0.061
1-34A	18.16	11.27	11.45	0.18	0.016
1-4	24.95	6.29	6.98	0.69	0.099
1-19B	24.95	12.71	13.00	0.29	0.022
1-20B	24.95	11.14	11.29	0.15	0.013
1-34A	24.95	9.98	10.61	0.63	0.059

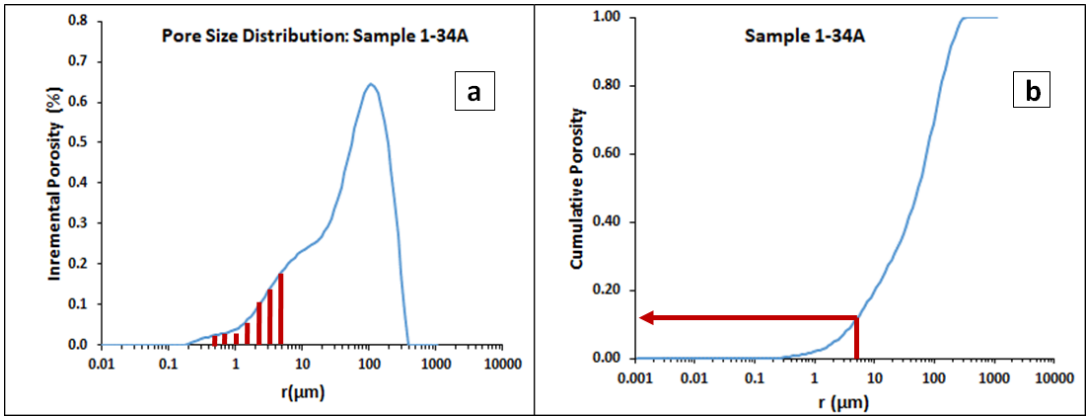


Figure 4-17 – (a) PSD curve of plug 1-34A obtained from NMR data showing the area under the curve that corresponds to the sub-resolution porosity which cannot be reconstructed from µCT images with 9.97 µm pixel size (in red); and (b) percentage of the porosity (identified by the red arrow) that is not detectable during the segmentation procedure.

Figure 4-17 shows schematically the procedure for calculating the sub-resolution as well as the detectable porosity from the PSD curve as well as the percentage of the porosity obtained by the NMR technique that can not be detected in the reconstruction of the digital model from µCT images of sample 1-34A with pixel size equal to 9.97 µm. In Figure 4-17 (a) it can be seen that the area under the PSD curve with radius less than 4.985 µm represents the sub-resolution porosity, which can not be digitally identified or reconstructed.

The red arrow in Figure 4-17 (b) identifies the percentage of the sub-resolution porosity. In this case, 12.7% of the porosity obtained by the NMR, equal to 15.72% for the sample 1-34A, can not be visualized in the digital model of the porous system obtained from the images of μCT with pixel size equal to 9.97 μm. For other models obtained from images with different pixel sizes, the procedure is the same. Table 4-13 shows that the smaller the pixel size, the greater the porosity detectable by this method.

4.2.2.2 Automated Segmentation – Algorithms

In order to obtain Th values and consequent segmentation of images from μCT, images of samples 1-4 and 1-34A obtained with different pixel sizes were selected. All the images used were on the 8-bit base to facilitate the use of computational codes. Table 4-14 presents the results obtained in the automated segmentation step. The corresponding value obtained by the NMR-based method is inserted for comparison between the results obtained. This value is considered, for all purposes, as the reference value. For each analyzed method, the minimum and maximum values obtained from the statistical analysis of the threshold values obtained from each image analyzed for each sample are inserted.

Table 4-14. Threshold values (Th) of 8-bit μCT images from the NMR-based segmentation and automated procedures according to the methods of Kittler & Illingworth, Otsu, Ridler & Calvard, Niblack, and Bernsen.

		NMR-based Th	Kittler & Illlingworth / Otsu – Th		Ridler & Calvard – Th		Niblack / Bernsen – Th	
Sample	Pixel size (μm)		Min	Max	Min	Max	Min	Max
1-4	9.97	55	69	71	65	67	65	67
1-4	18.52	53	52	64	72	76	73	77
1-34A	9.97	64	64	67	67	70	67	70
1-34A	18.16	63	83	85	70	71	70	72

The methods were grouped according to the results obtained, being Kittler & Illingworth and Otsu equivalents, as well as those of Niblack and Bernsen. Table 4-15 presents the information from the statistical analysis to obtain the threshold values from the automated methods of segmentation. A 95% confidence interval was used to obtain the minimum (Min) and maximum (Max) values.

Table 4-15. Statistical analysis for threshold values (Th) evaluation of 8-bit μCT images from automated procedures according to the methods of Kittler & Illingworth (K&I), Otsu (Ot), Ridler & Calvard (R&C), Niblack (Ni), and Bernsen (Be).

Method	Sample	N	Mean	SD	SE	Ci	Min	Max
K&I/Ot	1-4 (9.97μm)	13	70.0	1.077	0.299	0.651	69	71
	1-4 (18.52μm)	11	58.0	9.372	2.826	6.296	52	64
	1-34A (9.97μm)	13	65.5	2.722	0.755	1.645	64	67
	1-34A (18.16μm)	10	84.2	1.640	0.519	1.173	83	85
R&C	1-4 (9.97μm)	13	65.9	1.587	0.440	0.959	65	67
	1-4 (18.52μm)	11	74.3	3.113	0.939	2.091	72	76
	1-34A (9.97μm)	13	68.4	2.059	0.571	1.245	67	70
	1-34A (18.16μm)	10	70.6	1.162	0.367	0.831	70	71
Ni/Be	1-4 (9.97μm)	13	66.3	1.657	0.460	1.001	65	67
	1-4 (18.52μm)	11	75.0	3.125	0.942	2.099	73	77
	1-34A (9.97μm)	13	68.5	1.729	0.479	1.045	67	70
	1-34A (18.16μm)	10	70.8	1.040	0.329	0.744	70	72

* N – Number of images; SD – Standard Deviation; SE – Standard Error; Ci – Confidence interval.

From the results presented in Tables 4-14 and 4-15 it is possible to verify that for the threshold values obtained from the number of samples reported (N), all ranging from 10 to 13 sections, only two Th values based on the NMR are equivalent to the minimum value found for the Kittler & Illingworth/Otsu method, using a 95% confidence interval.

In general, all values obtained by automated methods were higher than those obtained by the reference method based on the NMR data. These results have a direct implication in the generation of models of the porous systems of the studied samples, since the higher the values of Th the larger the reconstructed porous system, having direct impacts on porosity and Kabs (Silva *et al.*, 2018). Although the analyzes were based on a small number of images, the results provide a clear indication of the upper boundaries that identify the region which is certainly composed only of rocky material. This limit is important when working with information from visualization techniques, such as petrographic slides analysis and SEM, besides guiding the selections of Th values from the NMR-based method.

4.2.3 Coquina Rock Slabs Modeling

Based on insight from the experimental data, it was possible to proceed with modeling of the selected rock slab regions. Initially, two specific regions of rocks slabs from samples 1-20B and 1-34A were selected. The use of two pixel sizes helps in the

visualization of the sub-resolution porosity, not detected in images with lower resolutions. Figure 4-18 shows the digital three-dimensional reconstruction of a rock slab ROI of sample 1-20B. This ROI has dimensions, as previously reported, of 10 mm x 10 mm with thickness around 5 mm, according to Figure 4-18 (b). After the digital reconstruction, the segmentation of these rock slabs was evaluated. Due to the size of these samples, it was not possible to use the NMR-based segmentation method, using a hybrid method: petrographic slide, SEM data and automated segmentation using the method of Kittler & Illingworth (K&I). Figures 4-18 (c) and (d) present reconstructions from μCT images with pixel sizes equal to 6.77 and 9.97 μm.

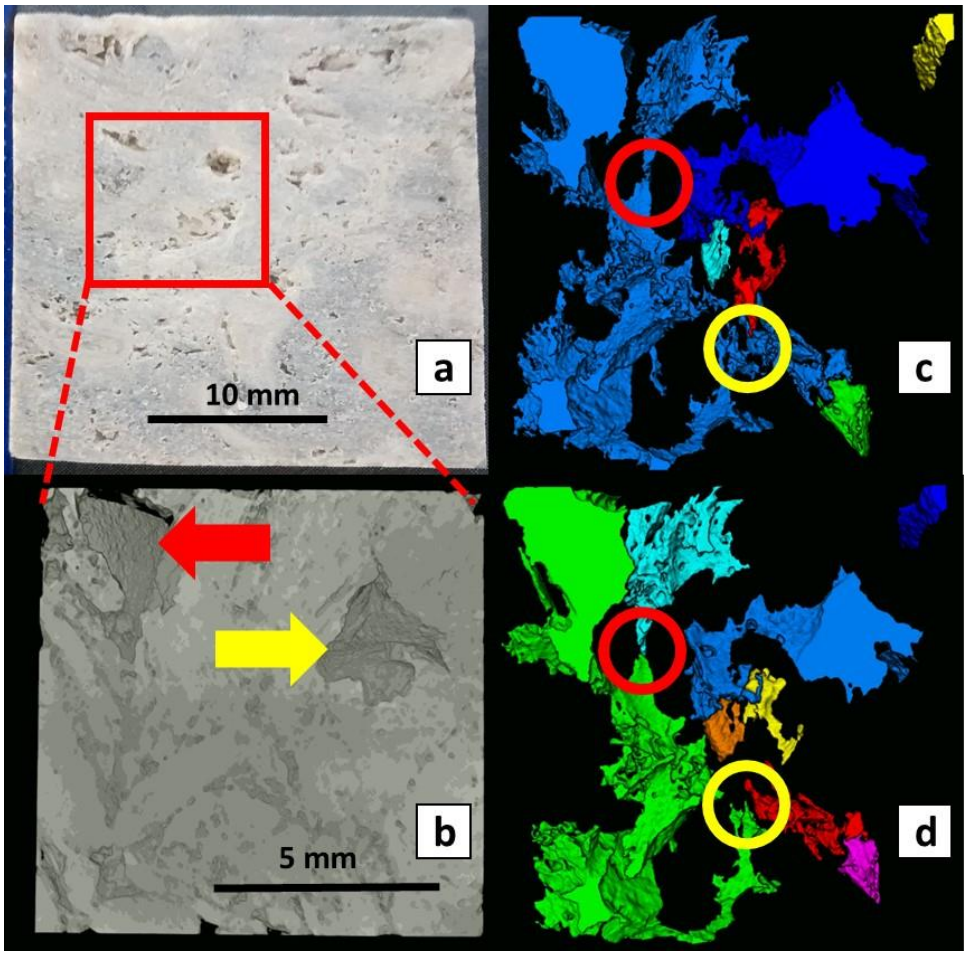


Figure 4-18 – (a) Image of the selected area for μCT, indicating with a red arrow the presence of vugular porosity; (b) 3D volume reconstruction of the region using 6.77μm pixel size μCT images, with the red and yellow arrows highlighting the same vugs as in (b); (c) 3D segmentation and reconstruction of the pore region of the sample, showing red and yellow circles identifying connected ROI from the 6.77μm pixel size μCT images; (d) same from the 9.97μm images, altough the circles do not show connected ROI due to the resolution limitation: pore diameters between 6.77 and 9.97μm are responsible for this connection.

In these reconstructions from images with different pixel sizes, one can clearly see in red and yellow circles the loss of connectivity in different ROI as a function of undetected pores in the images with pixel size equal to 9.97 μm. This loss of connectivity can be detected in PNM-based reconstruction, as shown in Figure 4-19. The red circles show the same ROI reconstructed from images with larger (Figure 4-19 (a)) and smaller (Figure 4-19 (b)) resolutions.

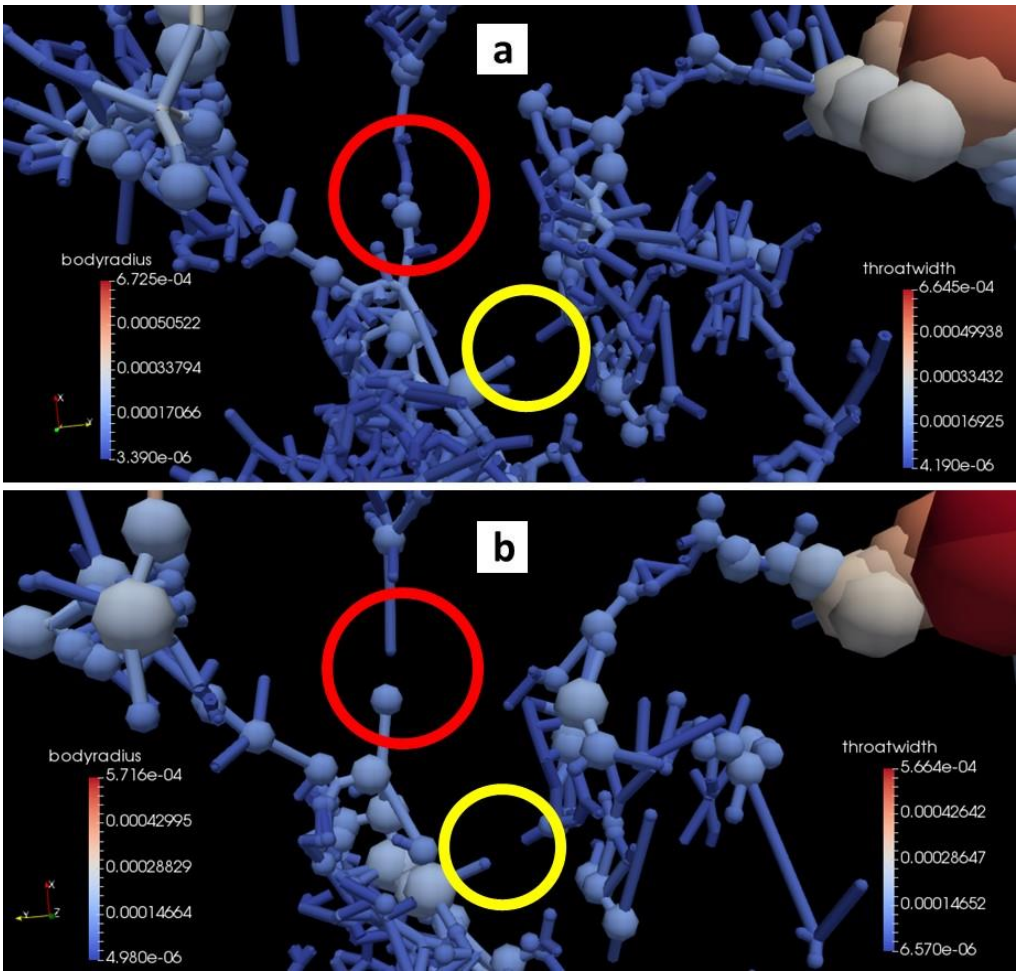


Figure 4-19 – PNMs of the reconstructed slab (a) from the 6.77μm pixel size μCT images, highlighting two ROI defined by the red and yellow circles, showing the distributions of pore body and pore throat radii, and (b) from the 9.97μm images. The red circles presents a ROI connected from higher resolution reconstructed model (a), which is not detectable from the lower resolution model (b). The yellow circles from both models show a not connected region, independently of the resolution. Scales are in m.

It can be verified the presence of pores that connect two neighboring regions, whose diameters vary between 6.77 and 9.97 μm, in the model generated from images with higher resolution. However, some regions remain disconnected regardless of the

selected pixel size. Two possible scenarios may explain this region bounded by yellow circles:

i) This region is formed by a region bounded by the rock itself;

ii) This region is also connected, however, by pores with diameters lower than 6.07 μm.

For the verification of the connection in the regions delimited by the yellow circles, it is necessary to obtain new images with pixel size less than 6.77 μm. In the present work, however, the limitation of X-ray microtomography equipment (distance between source, sample and detector) prevented an analysis with even smaller pixel sizes. The choice of pixel size of 9.97 μm was purposeful: this was the smallest pixel size selected for the reconstruction of the porous system of the entire plug of the samples studied. In addition, the manipulation of pore data is another important point: the number of pores obtained and reconstructed from images with higher resolutions is much higher than that obtained from images with lower resolution. Figure 4-20 shows two graphs that demonstrate the impact of pixel size on the number of pores (counting pore bodies and pore throats).

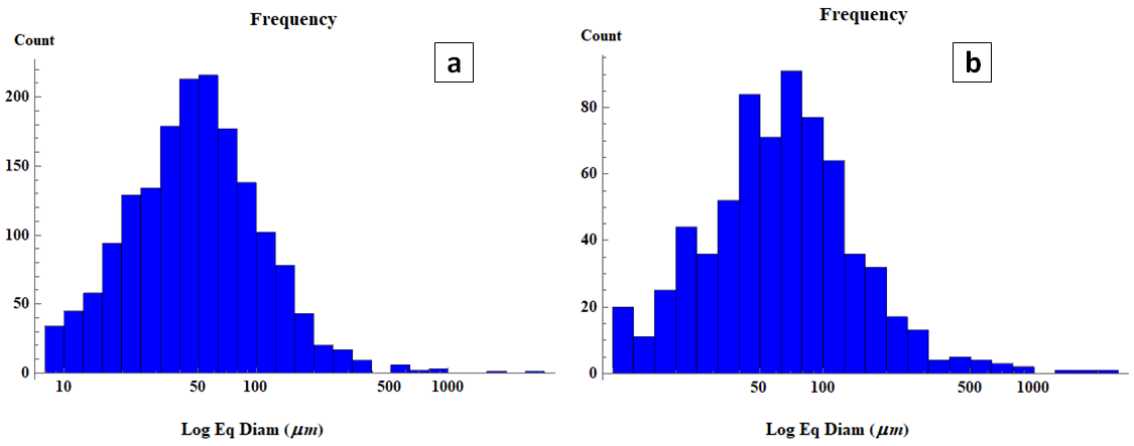


Figure 4-20 – Pore size frequency distributions (equivalent diameters) of the digital pore system of the rock slab 1-20B obtained using (a) 6.77 μm and (b) from 9.97 μm μCT images. Notice a much larger number of spherical elements in the reconstructed model using the higher resolution.

For simulation purposes, reconstructing the PNM of this rock slab of sample 1-20B through the images with different resolutions, one can first verify the modeling networks themselves: distribution of the radii of the pore bodies and pore throats. Figure

4-21 shows the PNM of the porous network obtained from images with smaller pixel size (6.77 μm). The different colors in the model present in Figure 4-21 (a) refer to the different disconnected clusters present in the porous network reconstruction. A pre-processing was performed prior to the generation of the models, disregarding clusters with very small dimensions. These clusters are agglomerations of voxels, and are considered a small size when the number of voxels is less than 100,000 voxels for the samples slabs models 1-20B and 1-34A. This value is variable depending on the sample size, pixel size selected, and segmentation performed. Figure 4-21 (b) presents the PNM of the porous network, being able to visualize the system formed by pore bodies and pore throats. The throats are reconstructed from three possible meanings between pores with different radius: harmonic, geometric and arithmetic. In this example, the pore radius and pore throat diameters obtained from the harmonic mean are presented.

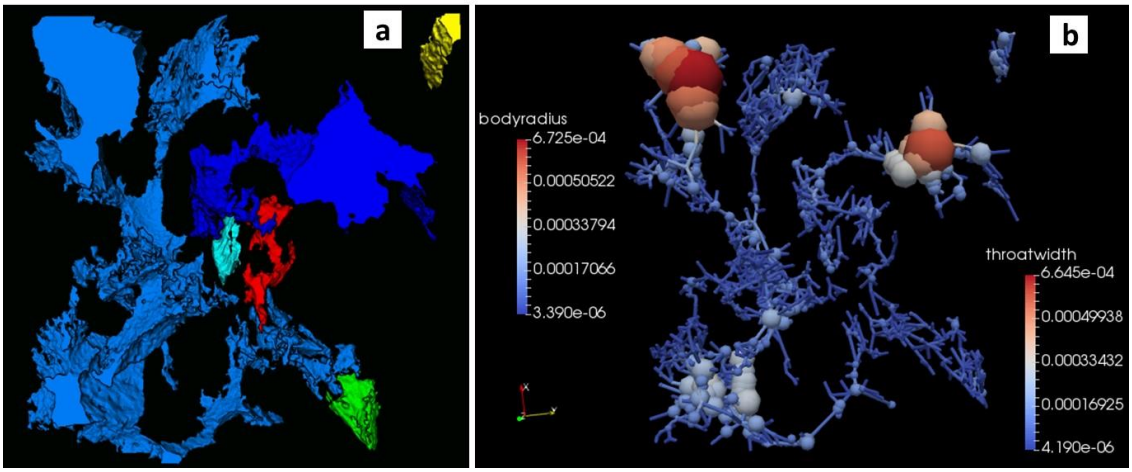


Figure 4-21 – (a) Digital reconstruction of the ROI from the rock slab 1-20B from the 6.77μm pixel size μCT images showing different clusters (different colors), and (b) the PNM showing the dimensions of pore bodies (radii) and pore throats (diameters). Scales are in m.

Figures 4-22 (a) and (b) present the information regarding the clusters and the PNM of the porous network generated from the images with lower resolution. It is possible to verify a smaller number of pore bodies and pore throats, when compared to the models generated with smaller pixel size. The pore throats were generated from the harmonic mean from the radii of the spherical elements that constitute them.

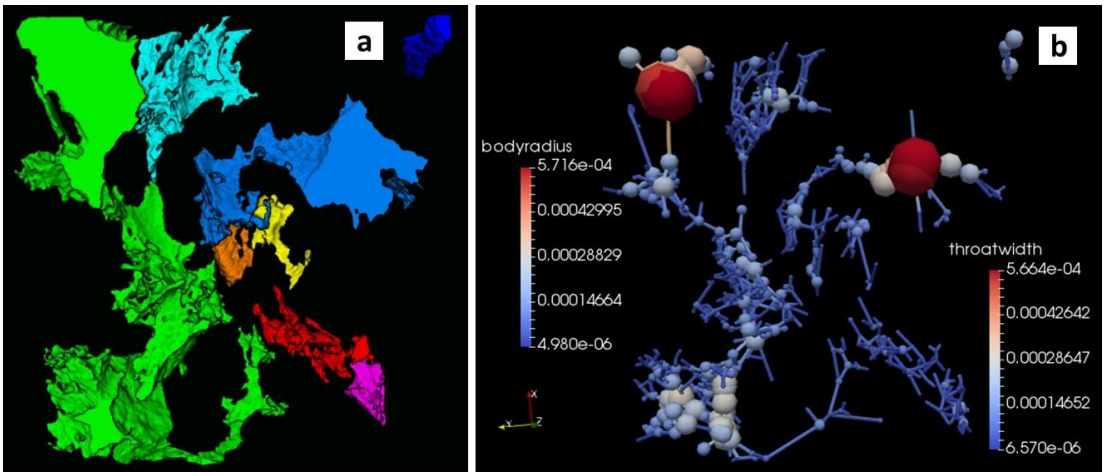


Figure 4-22 – (a) Digital reconstruction of the ROI from the rock slab 1-20B from the 9.97μm pixel size μCT images showing different clusters (different colors), and (b) the PNM showing the dimensions of pore bodies (radii) and pore throats (diameters). It is possible to verify a large number of disconnected clusters. Scales are in m.

These lost connections in the PNM obtained with images of smaller resolution, have direct impact in the estimates of Kabs. Table 4-16 presents the digital porosity and Kabs values for rock slabs 1-20B and 1-34A ROI.

Table 4-16. Porosity (ϕ) and absolute permeability (Kabs) estimated from the reconstructed coquina rock slab from samples 1-20B and 1-34A obtained with two different pixel sizes.

			Kabs (mD)		
Rock Slab	PNM – μCT Pixel size images (μm)	ϕ (%)	Harmonic	Geometric	Arithmetic
1-20B	6.07	9.86	3,859	6,348	8,343
1-20B	9.97	8.96	3,529	4,566	5,628
1-34A	6.77	8.43	2,568	2,755	2,984
1-34A	9.97	7.72	2,137	2,422	2,746

Some points can be discussed in function of these numerical results obtained from the modeling of these samples:

i) As expected, the digital porosities in the models obtained with smaller pixel sizes are higher than those calculated from the models obtained with larger pixel sizes: pores with diameters greater than 6.77 μm lower than 9.97 μm, considered sub-resolution in PNMs with 9.97 μm, can be identified and reconstructed in the higher resolution model;

ii) With the largest number of connections in the sample with smaller pixel size, it is observed that the estimates of Kabs are also larger, a behavior that was already predicted. The higher number of connections, in this case, allows greater flow of fluid in the porous system: the detection of a larger number of connected pores is a function of the adopted resolution and has a direct effect on Kabs estimates. Figure 4-23 shows detectable connections (red and yellow circles) only in the reconstructed model with images obtained with higher resolution;

iii) All Kabs estimates presented values higher than 2.0 D, which can be considered high as a function of the Kabs measurements of the plugs of these same samples. An important point to be presented refers to the fluid flow direction adopted in the simulation, Z axis, which has a very small dimension, 5mm. These volumes can not be considered REVs of the plugs, since the obtained digital porosities, as well as the calculated Kabs, are quite different from the measurements obtained experimentally for the total volume of the plugs;

iv) The values of Kabs are directly dependent on the average adopted for the calculation of the pore throats: values obtained for Kabs from the harmonic mean of the throats are inferior to those found from the geometric mean, all being lower than the arithmetic mean.

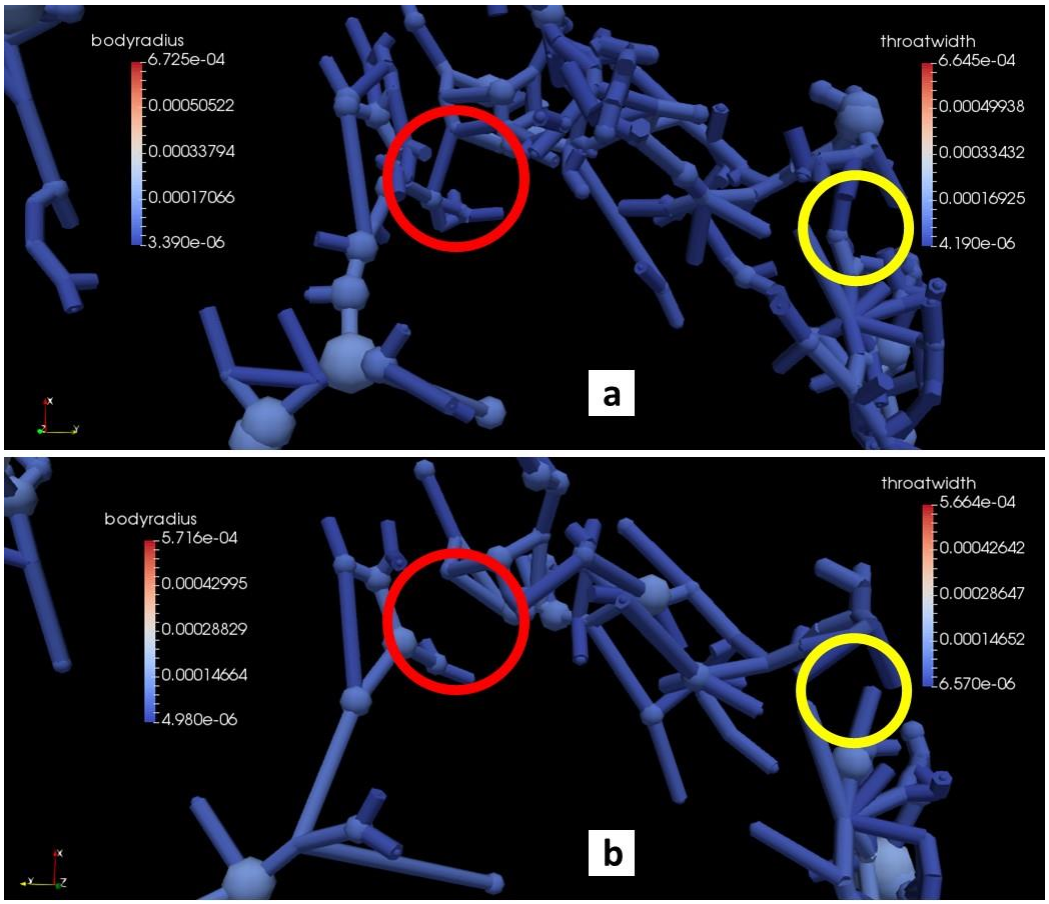


Figure 4-23 – PNMs of the reconstructed slab (a) from the 6.77µm pixel size µCT images, highlighting two ROI defined by the red and yellow circles, showing the distributions of pore body and pore throat radii, and (b) from the 9.97µm images. The red and yellow circles presents ROI connected from higher resolution reconstructed model (a), which are not detectable from the lower resolution model (b), leading to different Kabs estimates. Scales are in m.

Regarding the rock slab frpom sample 1-34A, the µCT images of the thin section showed the presence of clear vugular porosity, as well as some intraparticle porosity. Figure 4-24 shows the selected region (red square) that was used for the SEM, EDS and µCT images using two different pixel sizes, whose 3D reconstruction can be observed in Figure 4-24 (b). The 3D reconstructions of the pore systems from the 6.77µm, Figure 4-24 (c), and 9.97µm pixel size µCT images, Figure 4-24 (d), showed that the vug was part of the largest pore system within the rock slab, and close to a region whose contours delimited a bivalve shell. This region showed very little porosity, regardless of the pixel size used for µCT imaging. Digital porosities obtained with the two different pixel sizes are shown in Table 4-16.

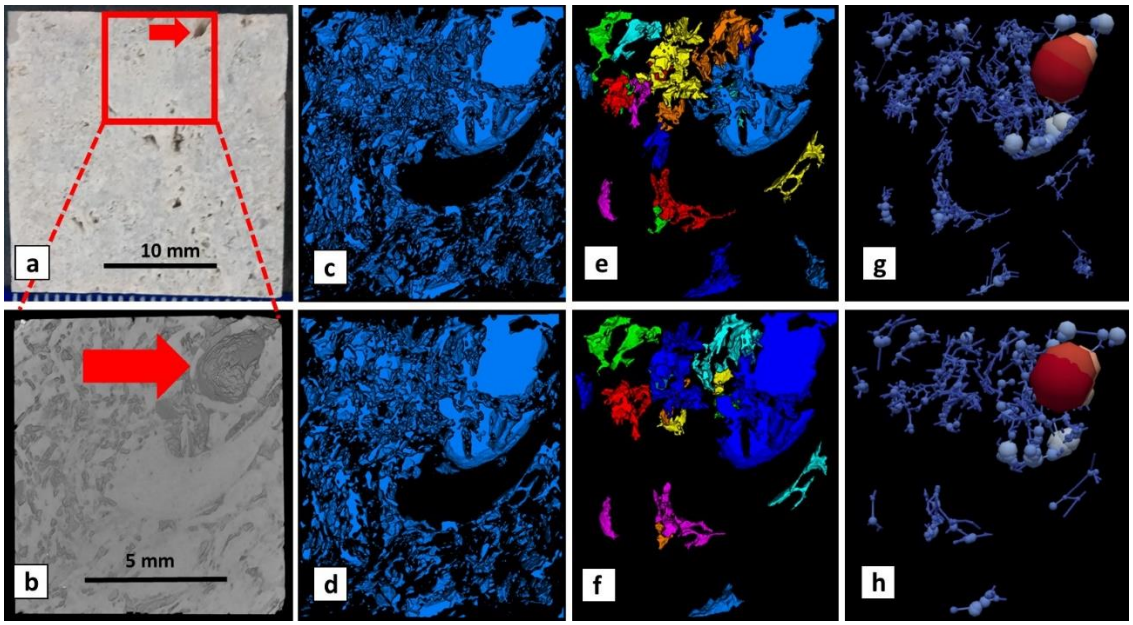


Figure 4-24 – (a) Image of the selected area for μCT, indicating with a red arrow the presence of vugular porosity; (b) 3D volume reconstruction of the region using 6.77μm pixel size μCT images, with the red arrow highlighting the same vug as in Fig.6a; (c) 3D segmentation and reconstruction of the pore region of the sample, with the right upper extremity being the assimilated vug and a central region with lower porosity showing well-defined bivalve contours from the 6.77μm pixel size μCT images; (d) same from the 9.97μm images (e) selection of the largest pores from the 6.77μm μCT images; (f) same from the 9.97μm images; (g) PNM generated with the largest pores from the 6.77μm pixel size μCT images; and (h) same from the 9.97μm images.

Next, it was performed PNM simulations for laminar fluid flow in two digitally reconstructed rock slabs, to obtain the absolute permeability. As shown in Table 4-16, estimated values were much higher than the measured value of 639 mD data for the entire plug (Table 4-1). The higher calculated values were to be expected because of the very small rock slab volume used in the μCT analysis. The volume presumably was much smaller than the minimum representative elementary volume (REV) needed for scale-independent permeability measurements (or calculations in this case). By comparison, the rock slab was large enough for the porosity calculations and measurements. We hence emphasize here that the PNM-based permeability estimates we obtained for the modeled rock slabs do not have an immediate direct relationship with the permeability measured using the entire coquina plug. To properly compare the measured absolute permeability of the plug, the PNM model should be applied to the entire plug.

We selected the largest pore systems from each reconstructed model, which are visualized in Figure 4-24 (e) (from the 6.77μm pixel size μCT images) and Figure 4-24 (f) (from the 9.97μm pixel size μCT images). The number of voxel-based clusters in

Figure 4-24 (e) was higher than that in Figure 4-24 (f), indicating that small clusters (represented by different colors) are only generated from higher-resolution images. Figures 4-24 (g) and (h) show the PNMs of the regions discussed previously. A first direct observation refers to the amount of pore bodies and pore throats generated for the construction of the PNMs. For construction of the model imaged with 9.97µm pixel size, we generated a much smaller number of points (Figures 8-24 (a) and (b)), although the topology of the system was maintained.

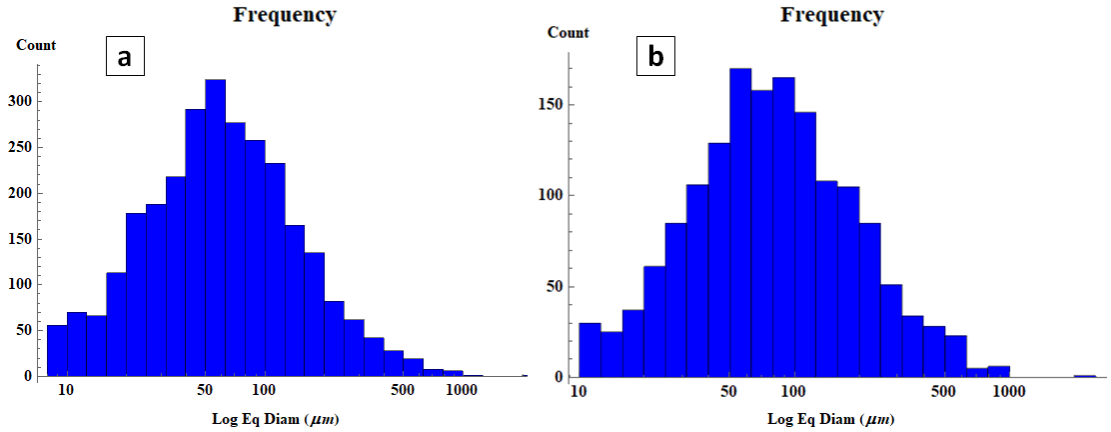


Figure 4-25 – Pore size frequency distributions (equivalent diameters) of the digital pore system of the rock slab obtained using (a) 6.77 µm and (b) from 9.97 µm µCT images. Notice a much larger number of spherical elements in the reconstructed model using the higher resolution.

Some important points can be drawn from the PNM simulations based on different pixel size µCT images. Most important, the results for porosity and absolute permeability were larger for the reconstructed model using higher resolution µCT images (6.77µm), thus suggesting that some pore bodies and pore throats were not included in the lower resolution µCT images (9.97µm), which must have influenced the numerical estimates. Differences between the absolute permeability values varied between 11.8% and 22.2%, considering the different averages for pore-throat construction in each model. The pore throat radii based on harmonic means of the spherical elements that composed them were physically coherent, since they accounted for regions of constriction prior to modeling the pore throats using the PNM.

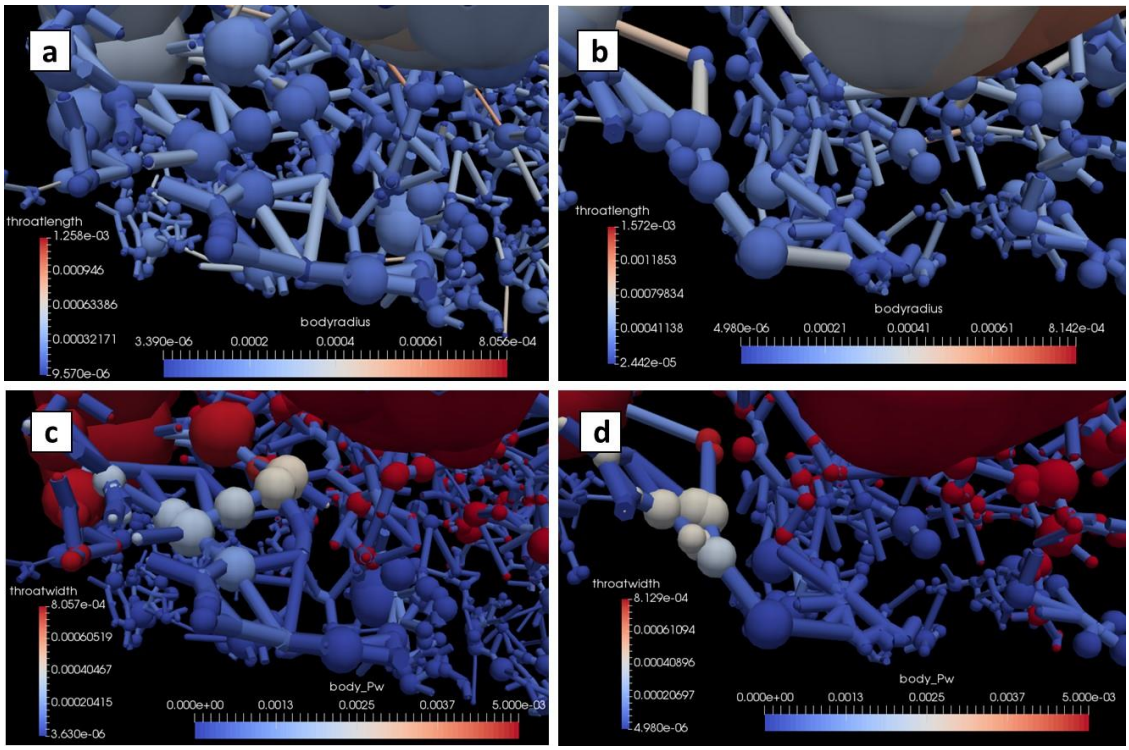


Figure 4-26 – PNMs of the reconstructed slab (a) from the 6.77μm pixel size μCT images, and (b) from the 9.97μm images, showing the distributions of pore radii and pore lengths. PNMs of the regions with greater pressure differentials between pore bodies following numerical simulation of fluid flow, as well as of the diameters of the pore throats in these regions, using (c) 6.77μm pixel size μCT images and (d) 9.97μm images. The length and pressure units are m and Pa, respectively.

An analysis of the region with the greatest pressure differential, which was responsible for most of the fluid flow, is shown in Figure 4-26. The plots visualize the length of the pore throats and the radii of the pore bodies for the slab reconstructed PNM using 6.77μm (Figure 4-26 (a)) and 9.97μm (Figure 4-26 (b)) pixel size μCT images as obtained with the Paraview® software (AYACHIT, 2015). A larger number of pore bodies and pore throats are apparent when using higher resolution μCT images, which leads to higher absolute permeability values. The images in Figure 4-25 were generated from the models whose pore throats were calculated using harmonic means of their constituent spherical elements. The smaller pore throat diameters for both models can be seen in Figures 4-26 (c) and (d), as well as the pressure (ranging from 0 to 5.0×10^{-3} Pa) in each pore body of this region. The simulation results indicate that fluid in this rock slab flows preferably through the mesopores and macropores.

4.2.4 Coquina Plug Modeling

After analysis of the rock slab, it was performed a analysis of the coquina plugs in its entirety. The main objective was to calibrate the PNM based on their estimates of Kabs, as well as to study PNM performance for a heterogeneous and complex pore system involving a large number of mesopores and macropores. It was selected for this purpose the μCT images generated using three different pixel sizes of 9.97, 18.16, and 24.95 μm, thus testing the effects of resolution on the calculated parameters. Table 4-17 presents results of the 3D modeling scenarios and the experimental data of the selected petrophysical properties. Regarding porosity, the pore network reconstructed with higher resolution μCT images clearly presented better results when comparing the digital estimates to the measured data in Table 4-1. The same is true for the absolute permeability estimates using PNM.

Table 4-17. Porosity (ϕ) and absolute permeability (Kabs) of the reconstructed coquina plugs 1-19B and 1-34A using PNM based on 2% input/output boundaries.

			Kabs (mD)		
Plug	PNM – μCT Pixel size images (μm)	ϕ (%)	Harmonic	Geometric	Arithmetic
1-19B	9.97	15.7	461.3	711.5	1,179
	18.87	13.5	372.6	615.7	955.4
	24.95	12.7	845.7	1386	2027
	Experimental	19.8		765.1	
1-34A	9.97	12.4	548.3	953.9	1,236
	18.16	11.3	480.5	911.5	1,419
	24.95	9.98	464.9	848.4	1,283
	Experimental	16.3		639.1	

It is possible to verify that the results of Kabs vary according to the pixel size of the images coming from μCT and with the average adopted for the reconstruction of the pore throats as a function of the spherical elements. By analyzing the results of sample 1-19B a gradual increase in Kabs values can be verified as the harmonic, geometric and arithmetic averages are used, regardless of the pixel size adopted. This result was already expected, since the results from the arithmetic mean are greater than or equal to those obtained by the geometric mean, which in turn are greater than or equal to those obtained through the harmonic mean. However, for sample 1-19B, the results of Kabs obtained through the reconstructed model from μCT images with a pixel size of 24.95μm are higher

than the results obtained from the reconstructed models with higher resolutions (pixel sizes equal to 9.97 and 18.87µm). Comparing to the results obtained from the PNM of sample 1-34A, there is an inconsistency, which can be explained by the very quality of the images originating from µCT. This is an extremely important point: the quality of the images can have a direct impact on the results from the numerical simulation to obtain Kabs. Reconstructed images after acquisition in µCT of sample 1-19B with a pixel size of 24.95um were considered low quality, and their negative impact on kabs, regardless of the calculated mean, can be easily identified.

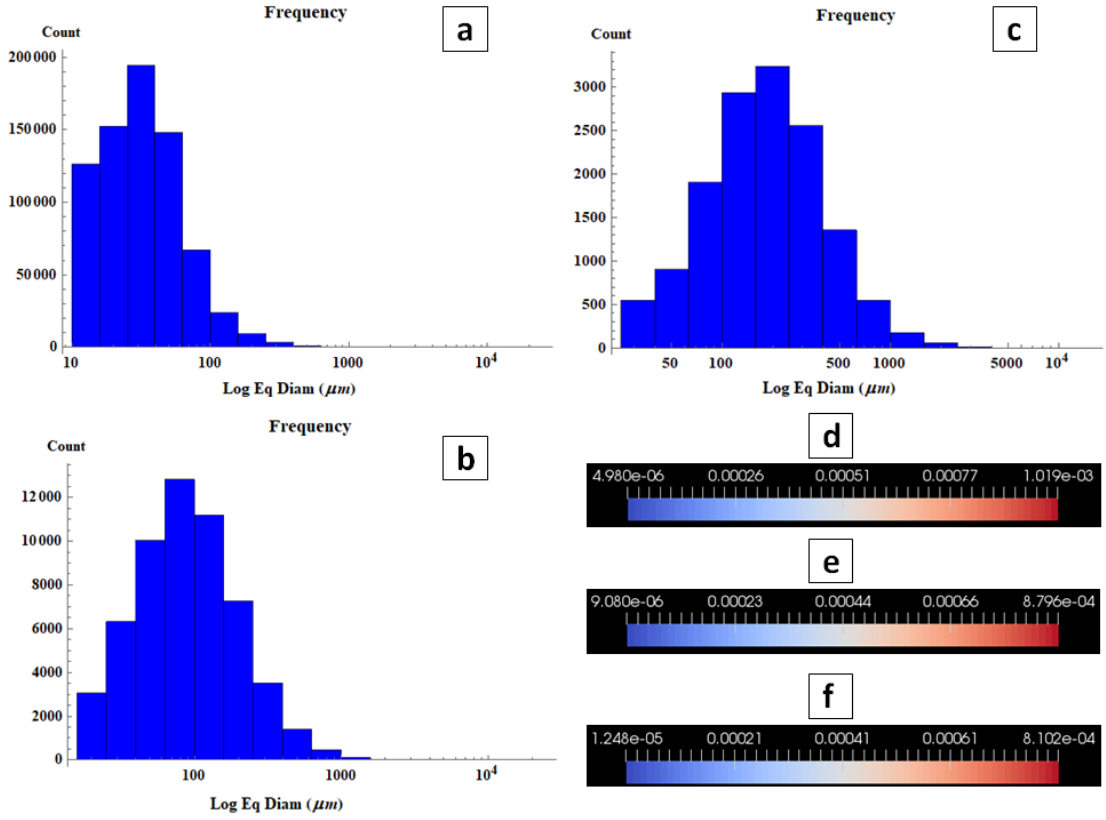


Figure 4-27 – Frequency distributions of the equivalent diameters (Eq Diam) of the pore bodies and pore throats of the digital pore system of the plug obtained using (a) 9.97µm, (b) 18.16µm, and (c) 24.95µm µCT images; and the range of pore throat radii (scale in m) found with the models generated using (d) 9.97µm, (e) 18.16µm, and (f) 24.95µm µCT images.

Another important point refers to the average used to calculate the pore throats, based on the spherical elements that do not represent pore bodies on the models. Regarding the sample 1-34A, harmonic averaging gave the best results compared to the measured data, presenting a percentual difference of 14.2%, 24.8%, and 27.3% for the

PNM based results using μCT images with 9.97μm, 18.16μm, and 24.95μm pixel size, respectively. It is important to note here that the comparison between the PNM and the measured data for the entire plug does not require some REV verification since the experimental results were measured also on the entire plug.

Figure 4-27 shows frequency distributions of the generated pore throats and pore bodies of sample 1-34A. The results indicate that the total number of pore bodies and pore throats for the model using higher resolution μCT images is more than 60 times larger than obtained with the lower resolution μCT images. This impressive increase relates to the capacity to recreate pore bodies and pore throats that are not detectable from lower resolution μCT images, as can be seen in Figures 4-27 (d), (e), and (f), which presents the range of pore throat radii (in m) for the models based on μCT images with 9.97μm, 18.16μm, and 24.95μm, respectively.

PNM results for plug 1-34A obtained with the intermediate resolution (18.16μm pixel size μCT images) and assuming the harmonic averages of the pore throats are shown in Figure 4-28. The input and output boundaries were implemented based on the selection of 2% of the plug length (from the number of μCT images slices), which leads to a well-defined layer for fluid entrance. As expected, some overlap occurred of the distributions of the pore bodies and pore throats, but with the largest pore throats being linked to the largest pore bodies, thus indicating good results regarding the PNM generation methodology. A selected few pore throats were several mm wide, which created regions for considerable fluid flow between the two linked pore bodies. However, the majority of pore throats remained within the μm range. The larger pore throats were important to preserve connections between vugs, thus creating preferential paths for fluid flow.

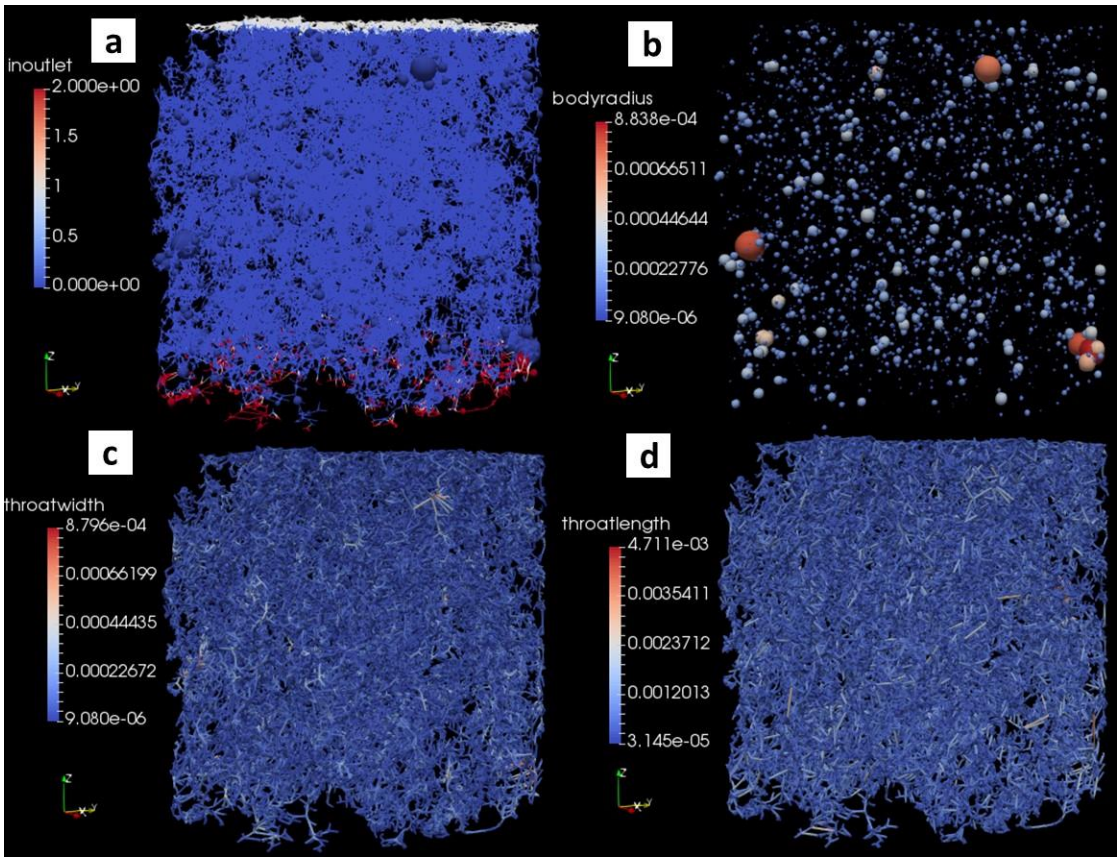


Figure 4-28 – PNM results for plug 1-34A based on 18.16μm μCT images presenting: (a) input (white region) and output (red region) boundaries for the fluid flow numerical simulations, and ranges of (b) pore body radii, (c) pore throat radii, and (d) pore throat lengths. Scales are in m.

PNM results for sample 1-34A (all using harmonic averages of the pore throat radii) obtained with the different resolutions were analyzed. Figure 4-29 shows the final generated pore network and the calculated pressure fields. Results indicated that part of the well-connected network could not be generated using lower resolution μCT images. Still, in terms of fluid flow, the PNM captured important connections between mesopores and macropores since the calculated absolute permeabilities values (as shown in Table 4-17) were close to the measured value. The three PNM simulations showed specific regions with higher pressure drops, which were preferably accessed by fluid during the flow experiment. Figure 4-29 further shows that the number of pore bodies and pore throats increases immensely as the μCT images resolution increased.

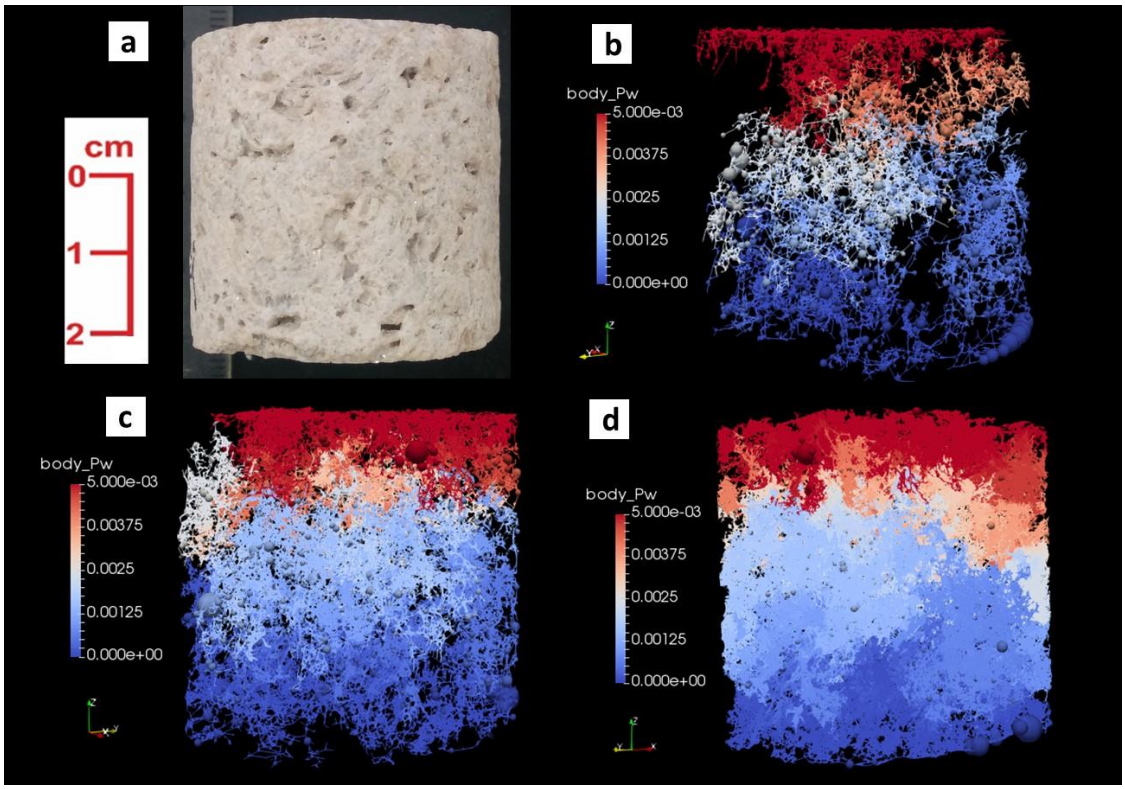


Figure 4-29 – (a) Image of plug 1-34A, and PNM results of the pressure field based on (b) 24.95 μm, (c) 18.16 μm, and (d) 9.97μm pixel size μCT images (pressure scales are in Pa).

Another important result relates to the possibility to conduct numerical experiments using relatively large sample volumes. It was showed that this is feasible despite the computational demand. The use of relatively large plugs avoids non-representative results, especially for the absolute permeability in view of the required REV. This characteristic is crucial when upscaling results from plugs to cores and beyond.

As mentioned, the input and output limits for sample 1-34A were defined as 2% of the total length of the plug from the number of slices of the μCT images, as a function of the z-axis coordinates of the outermost pores. This choice is arbitrary and can easily be changed in the PNM generation code. However, the results of Kabs are influenced by the choice of this parameter of input and output. Table 4-18 presents the results of Kabs for sample 1-19B as a function of different percentages for the definition of input/output boundaries. A small variation in this percentage can significantly influence the estimated Kabs result, being a parameter of extreme importance during the calibration stage of the PNM. The higher the percentage, the greater the value of Kabs obtained numerically. The definition of this value, although arbitrary, must respond to some basic premises adopted:

i) The results of Kabs dependent on the adopted means can not exceed the value obtained experimentally, since a percentage of the porosity (Table 4-13) can not be detected and measured by the μCT technique, due to the limitation imposed by the resolution adopted, such that its impact on the estimated Kabs can not be measured;

ii) Very low values for the input/output percentage (less than 2%) generate problems of numerical convergence during the simulation of the single-phase flow for network calibration;

iii) Values obtained for a given input percentage can not be higher than the values found for a PNM obtained from μCT images with smaller pixel size.

Figure 4-30 shows the results of the single-phase flow simulations for the PNM of the sample 1-19B reconstructed from the images of μCT with 18.87μm of pixel size, and geometric mean for the pore throats, as a function of the percentages of input/output equal to 2%, 5% and 8%. A gradual increase in the input (in white) and output (in red) regions is observed in Figures 4-30 (a), (b) and (c), being the blue region the one effectively used for the calculation of the pressures and velocities. Figures 4-30 (d), (e) and (f) show the pressure fields of these PNMs, whose entries are 2%, 5% and 8%, respectively. Although the Kabs values vary approximately 100mD, between the values obtained from the harmonic mean and the arithmetic, it is not possible to detect any visual changes in the pressure field.

Table 4-18. Absolute permeability (Kabs) of the reconstructed coquina plug 1-19B using PNM based on different input/output boundaries (%).

Sample 1-19B	Input/Output	Kabs (mD)		
Pixel Size (μm)	(%)	Harmonic	Geometric	Arithmetic
9.97	2.0	461.3	711.5	1,179
	5.0	505.4	778.9	1,274
	8.0	551.7	847.5	1,369
18.87	2.0	372.6	615.7	955.4
	5.0	386.3	654.8	986.5
	8.0	427.3	714.0	1,075
24.95	2.0	845.7	1,386	2,027
Experimental			765.1	

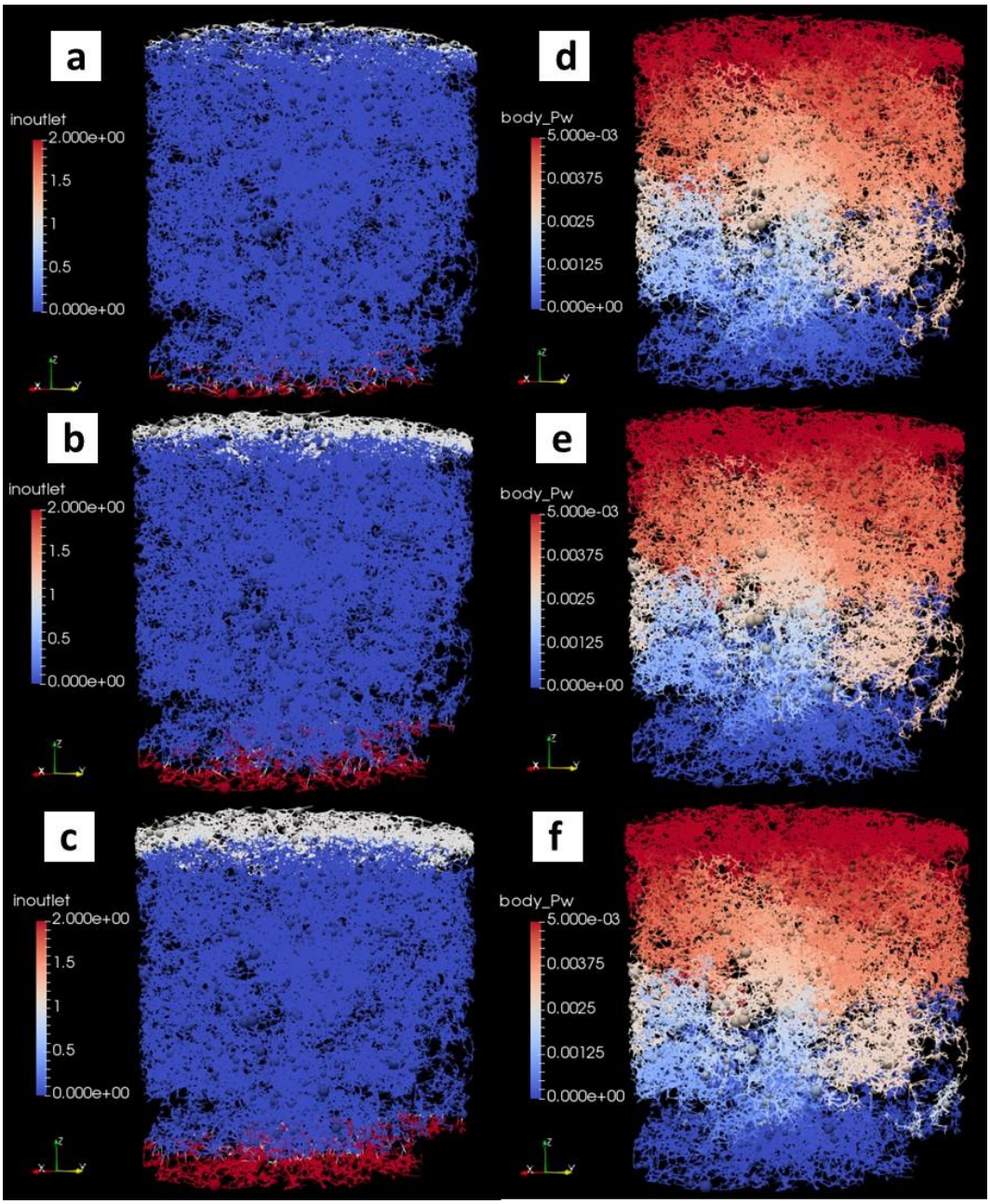


Figure 4-30 – (a) PNM of plug 1-19B based on 18.87μm pixel size images (pore throats based on geometric average) with 2% input and output boundaries (white and red zones, respectively), (b) 5%, and (c) 8%; (d) PNM results of the pressure field based on 2%, (e) 5%, and (f) 8% input/ouput boundaries. Pressure scales are in Pa.

The averages of the spherical elements that constitute the pore throats have a decisive impact on the results of Kabs, as already discussed. However, the maximum values of the pore throats radii do not present significant differences, as can be seen in Figure 4-31. This difference is also not significant if the values are compared to the smaller radii of the pore bodies, according to Figure 4-31 (a). The results indicate that small changes in pore throat radii over the PNM have a large impact on Kabs results. A

small increment (of the order of 1μm) in the radius of each pore throat leads to a significant increase in Kabs estimates, as shown in Table 4-18. Figures 4-31 (b), (c) and (d) show the pore throat radii obtained from the harmonic, geometric and arithmetic averages, respectively. Figure 4-31 (a) shows the radii of the pore bodies. All PNMs were obtained from μCT images with pixel size equal to 18.87μm.

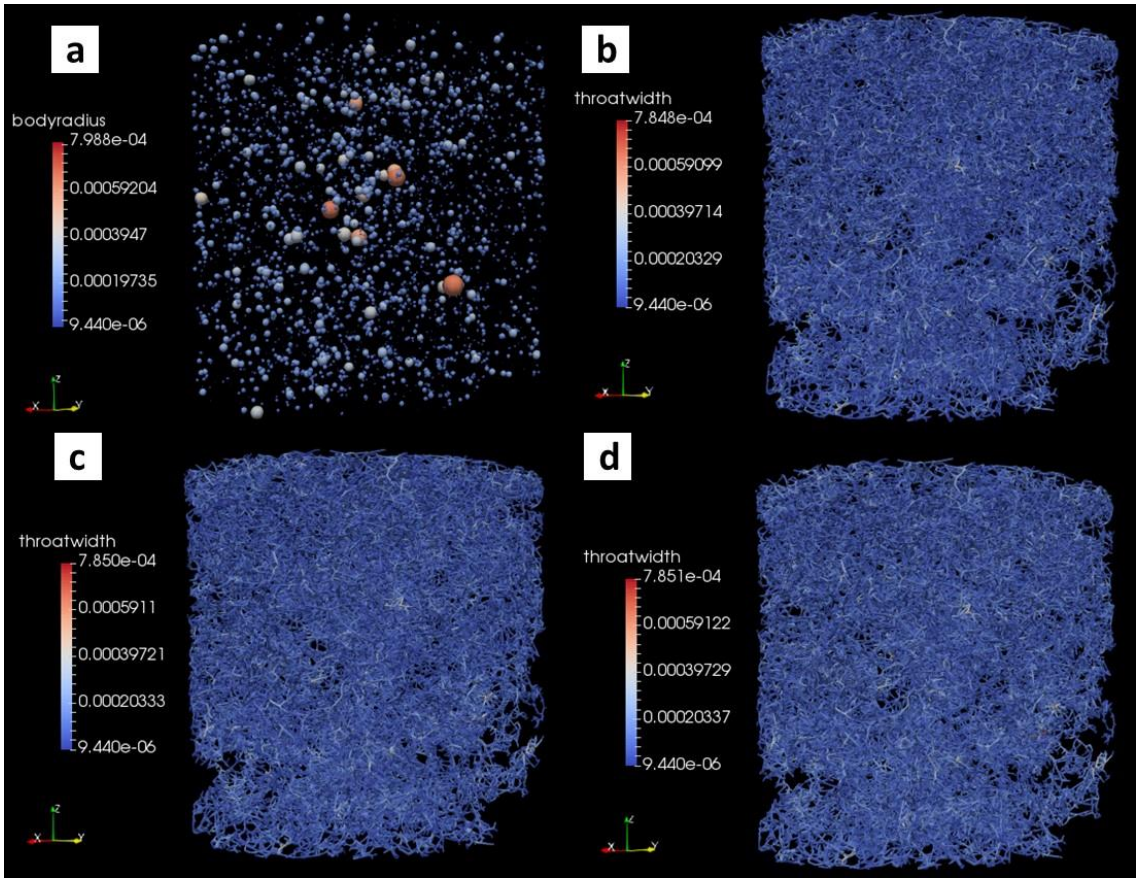


Figure 4-31 – (a) Pore body size distribution from the PNM of plug 1-19B based on 18.87μm pixel size images; (b) Pore throat size distribution based on harmonic average, (c) geometric average, and (c) arithmetic average. Scales in m.

Some important points may be highlighted because of the results presented in Tables 4-17 and 4-18, as well as the execution of this workflow stage itself:

i) PNMs reconstructed from μCT images with higher resolutions (smaller pixel sizes) lead to results closer to those obtained experimentally, since a larger number of smaller pores can be detected, and these may be responsible for a larger number of connections (as assessed in rock slab PNMs from different resolutions);

ii) Although the results of Kabs for the PNMs generated from images with higher resolutions approximate the experimental results, the

computational cost (time) for PNM generation and respective numerical simulation increases considerably (Table 4-19);

iii) The choice of the selected mean for the generation of pore throats will depend on the results of Kabs obtained from the simulation. The calibration of the network by the Kabs estimation goes through this choice: for sample 1-19B, the geometric mean returned better results, while for the sample 1-34A the harmonic mean brought results closer to the measured experimental value;

iv) The percentage of the layer that defines the input / output boundaries also plays an important role in the Kabs results, and it is possible to define which value brings better results: by the estimates obtained from the PNMs of samples 1-19B and 1-34A, the choice of a value equal to 2% brought satisfactory results;

v) To obtain a PNM that is representative of the actual porous system of the sample studied, some parameters must be used together with the network calibration by the estimated Kabs: PSD from the NMR data to identify the mean of the pore radius distribution, identifying whether the peak of the distribution can be detected in reconstructed PNM from images having well-defined pixel size;

vi) From this information, one can generate and choose the PNM that provides the value of Kabs closer to the experimental value, for purposes of two-phase simulation, this PNM being calibrated as a function of the porosity, through segmentation based on NMR data, and by Kabs obtained by numerical simulation.

Although the PNMs generated from the images of μCT with higher resolution bring results closer to the real ones when working with the same parameters, i.e., the average for the calculation of the radius of the pore throats and percentage for the definition of the input/output boundaries, the choice of the network can and should also be conditioned to the computational cost to generate the networks and subsequent numerical simulation, as already mentioned. It is possible to define a network generated from μCT images with larger pixel sizes, provided they are of good quality and that the PSD peak can be detected by NMR data. In this way, it is possible to work with PNM

with a much smaller number of pores and that present a kabs value calculated quite close to the experimental value, enough for both a correct definition of the average to be used to calculate the radii of the pore throats and the adequate input/output percentage. Figure 4-32 (c) presents a PNM that corresponds to a good option for performing the primary drainage simulations: Kabs value of 615.7 versus 765.1 mD measured experimentally (relative difference of 19.5%), with 2% input/output boundaries and geometric mean for the calculation of pore throats.

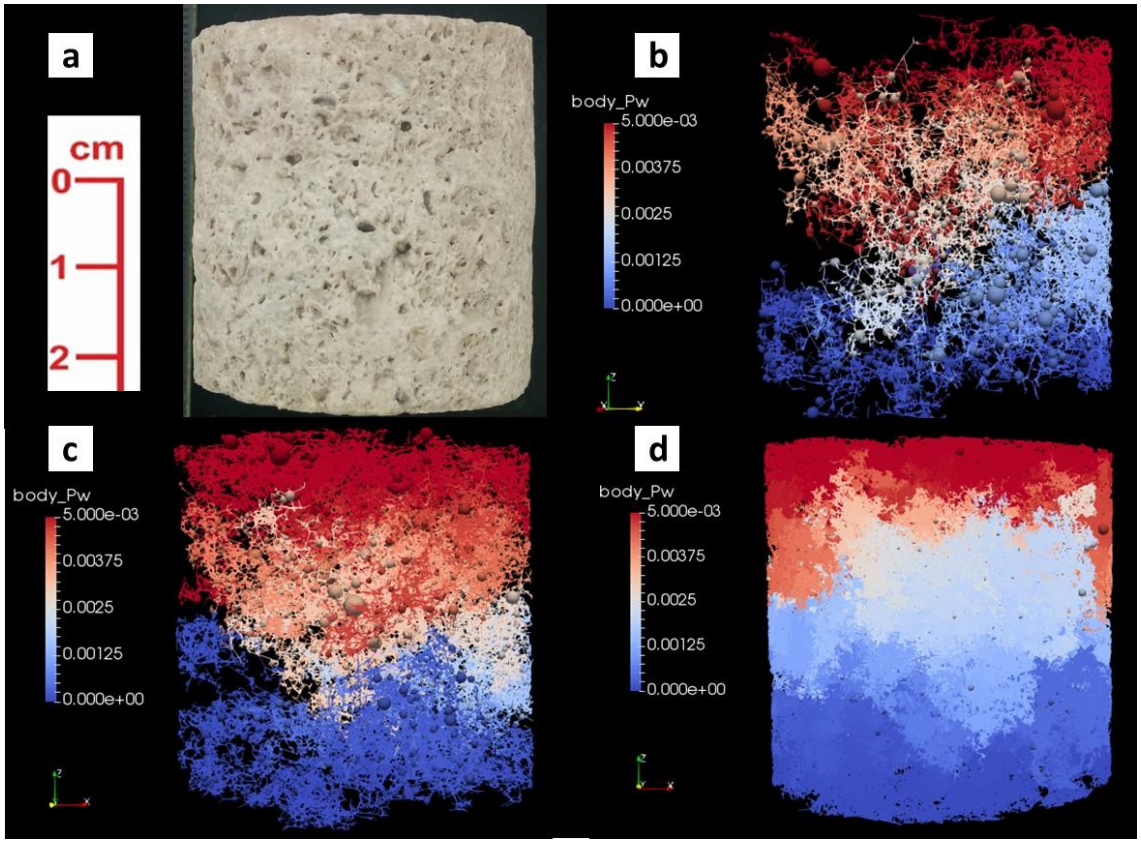


Figure 4-32 – (a) Image of plug 1-19B, and PNM results of the pressure field based on (b) 24.95µm, (c) 18.16µm, and (d) 9.97µm pixel size µCT images, considering 2% of input/output boundaries. Pressure scales are in Pa.

Table 4-19. Computational time for filtering, PNM generation, and numerical simulation to estimate Kabs based on different pixel size µCT images for sample 1-19B.

Sample 1-19B	Computational Time (min)		
Pixel Size (µm)	Filtering	PNM Generation	Kabs Numerical Simulation
9.97	36	4560	48
18.87	15	840	16
24.95	6	180	2

4.2.5 Sub-resolution Porosity Analysis

The studies involving sub-resolution porosity were conducted directly on the μCT images of the plug of sample 1-4, which presented the lowest value of Kabs among the samples studied, and it was not possible to observe the connection bewteen the largest clusters which represent the pore system in this plug. Figure 4-33 shows the reconstruction of the pore system of the sample 1-4 from μCT images with pixel sizes equal to 9.97, 18.53 and 24.95 μm, in the images (a), (b) and (c) respectively.

As previously specified in Chapter 3, the sub-resolution pore generation was obtained from the log-normal distribution by specifying the characteristic parameters of the distribution. In order to control the amount of pores in sub-resolution that are connected from this methodology, it were created three main parameters that regulate the maximum distance between the regions that can be connected, defined as Maximum Distance Factor (MDF), the number of neighborhoods that each neighbor can connect to, defined as Number of Closest Zones (NCZ), and finally, the number of connections that must exist between each neighbor, Number of Closest Connections (NCC). The definition of these parameters, as well as those related to the log-normal distribution, influences the size of the pore bodies and pore throats generated, the location of the new pores and their connections, influencing the Kabs estimates of the generated networks.

MDF is a factor that stipulates a maximum region in which a pore of sub-resolution can be generated, in addition to defining the area in which the connection between neighborhoods can occur. This parameter is a factor that multiplies the value obtained by the arithmetic mean of the lengths of the throats, generating a sphere of influence with that radius in microns. NCZ defines the number of neighboring regions that can connect within that region delimited by the MDF, while the NCC defines the number of connections between each neighborhood that can exist within this zone of interest.

Similar to the effects of the input/output boundary layer, the combination of the effect of these parameters can be measured in the Kabs estimates. The first direct result of the generation and connection of these new pores in sub-resolution is the connection of the previously disconnected clusters and the possibility of performing the numerical simulation of the fluid(s) flow, since in the networks originally obtained, due to the lack of connectivity, the estimates for Kabs were all equal to zero, although the experimental Kabs were equal to 33.19 mD.

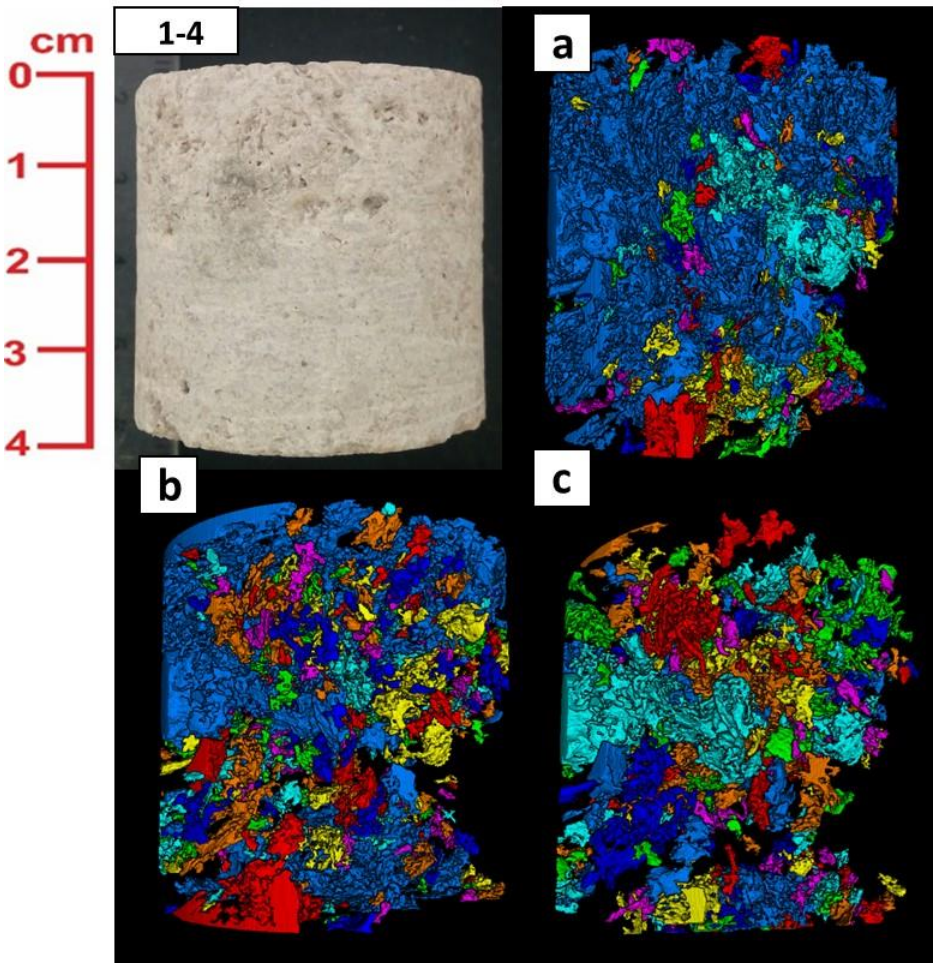


Figure 4-33 – (a) Image of plug 1-4, and digital reconstruction of the porosity system based on (b) 24.95μm, (c) 18.16μm, and (d) 9.97μm pixel size μCT images. It is possible to verify different number of connected clusters from each model.

Initially, the effects of changing the MDF, NCZ and NCC parameters on the networks obtained from PNM generated with μCT images with 18.53μm pixel size and input/output boundaries equivalent to 2% of the z - axis dimension were investigated. Table 4-20 presents the results of the Kabs estimates for the numerical simulation of the single-phase flow in the network previously specified. The parameters were altered keeping constant two of them, in order to analyze the direct impact of only one.

The values of MDF, NCZ and NCC were arbitrated according to some basic assumptions after the first simulations were performed, since the impact of these values could not have been initially predicted:

i) As previously mentioned, it was considered the geometric mean for the definition of pore throat dimensions, as well as an input/output boundary obtained with 2% of the value of the network dimension in the *z* axis;

ii) The network chosen had 18.53μm, because the computational time and cost for pore generation in sub-resolution, connection between neighborhoods and simulation to obtain Kabs are lower than the PNM obtained with 9.97μm;

iii) The initial value for the MDF was chosen eight times the arithmetic mean of the pore throats length, since, for values below these, there was not enough connectivity to obtain an estimate of Kabs in an order of magnitude close to the experimental value obtained for this sample;

iv) The choices of NCZ and NCC equal to three were made in order to obtain a number of connections capable of allowing the simulation of the fluid flow and respective estimation of the Kabs value: it was considered, initially, three neighborhoods and three connections for each one of these neighborhoods;

v) The initial baseline condition for evaluation refers to the rebuilt PNM with MDF combination equal to 8, NCZ equal to 3 and NCC also equal to 3;

vi) Kabs values can be compared to the experimental value obtained for this sample: 33.19 mD;

vii) The effects of pore throats that may intercept each other during the generation process were disregarded.

The results presented on Table 4-20 for the Kabs estimates show that the parameter of greatest influence is the NCZ, although all values are very close, they are about one order of magnitude below the measured experimental value.

Table 4-20. Kabs estimates based on PNM generated from 18.53μm pixel size μCT images for sample 1-4 considering 2% of input/output boundaries and geometric average for pore throats generation.

Sample 1-4 18.53μm	Parameters			Kabs Numerical Simulation
PNM	MDF	NCZ	NCC	mD
Case 1	8	3	3	0.395
Case 2	8	3	4	0.445
Case 3	8	4	3	0.605
Case 4	9	3	3	0.576
Case 5	9	4	3	0.407

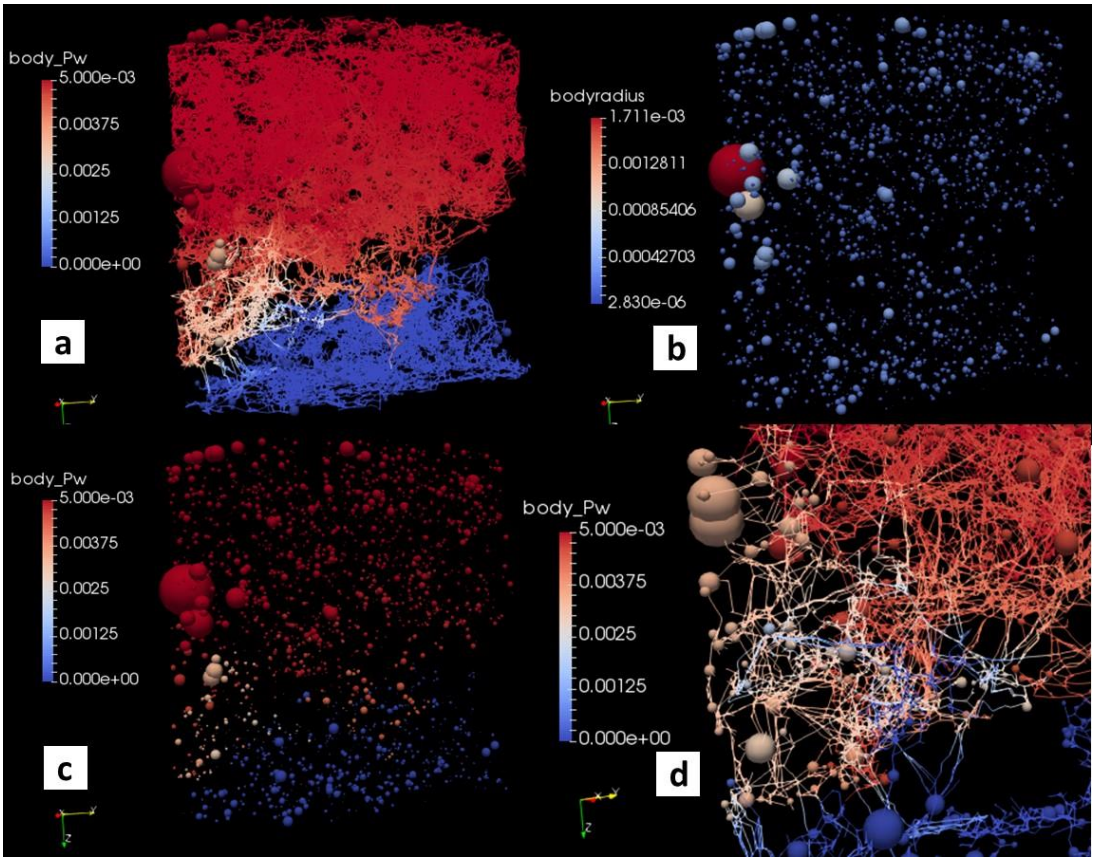


Figure 4-34 – (a) Result of the pressure field based on 18.53µm pixel size µCT images PNM for Case 3, (b) pore bodies radii, (c), pressure of pore bodies, showing in lighter colours the connected region, and (d) zoom in of this region. Pressure scales in Pa, dimension in m.

Table 4-21. Kabs estimates based on PNM generated from 18.53µm pixel size µCT images for sample 1-4 considering geometric average for pore throats generation for Case 3 using different input/output boundaries.

Sample 1-4 18.53µm	Input/Output Boundaries	Kabs Numerical Simulation
PNM	%	mD
Case 3	2	0.605
	10	3.85
	20	4.37

Figure 4-34 shows the results of the numerical simulation for convergence of the pressure field of Case 3, according to the parameters reported in Table 4-20. It is possible to observe that the radii of the pore bodies are much smaller than the radii obtained directly by the PNM from the images with 18.53µm of pixel size. Directly, the smallest radii are equal to 9.265µm, whereas after the generation and reconnection of the pores

under sub-resolution, it can be verified, according to Figure 4-34 (b), that the smallest radii are equal to 2,830μm.

From the Kabs estimates, as presented in Table 4-21, PNMs obtained from the images with pixel size equal to 9.97μm and input/output boundaries with a value of 10% were selected. In addition, the systems generated with the MDF combination of 9, NCZ equal to 4 and NCC of 3 were selected. Among the PNMs obtained, the Kabs with the different averages for the calculation of the pore throats were estimated. Table 4-22 shows the results obtaineds.

Table 4-22. Kabs estimates based on PNM generated from 9.97 μm and 18.53μm pixel size μCT images for sample 1-4 considering 10% of input/output boundaries and three average for pore throats generation.

Sample 1-4	Pore Throat	Numerical Simulation
Pixel Size (μm)	Average	Kabs (mD)
Experimental		33.19
9.97	Harmonic	15.68
9.97	Geometric	31.85
9.97	Arithmetic	51.20

It is possible to verify that the results found for PNMs generated with higher resolution and input/output boundaries defined as 10% of the number of sections in the z-direction are much closer to the measured experimental value, presenting the same order of magnitude (value measured in laboratory equal to 33.19 mD). The network, whose pore throats were generated from the harmonic mean, presented a Kabs value close to the reference value, with a relative error of 4.03%, calculated from the data presented on Table 4-22.

Figure 4-35 shows the PNM results of the sample 1-4 obtained with μCT images with pixel size equal to 9.97μm, and throats obtained from geometric mean, input/output boundaries with 10%, MDF of 9, NCZ equal to 4, NCC equal to 3 and a numerically imposed pressure differential equal to 5.0x10-3 Pa. The sub-resolution porosity was inserted from the log-normal distribution with parameters -4.71 and 0.0087 for μ and σ respectively, due to the fact that the sample network has a similar distribution for this characteristic among macro-throats.

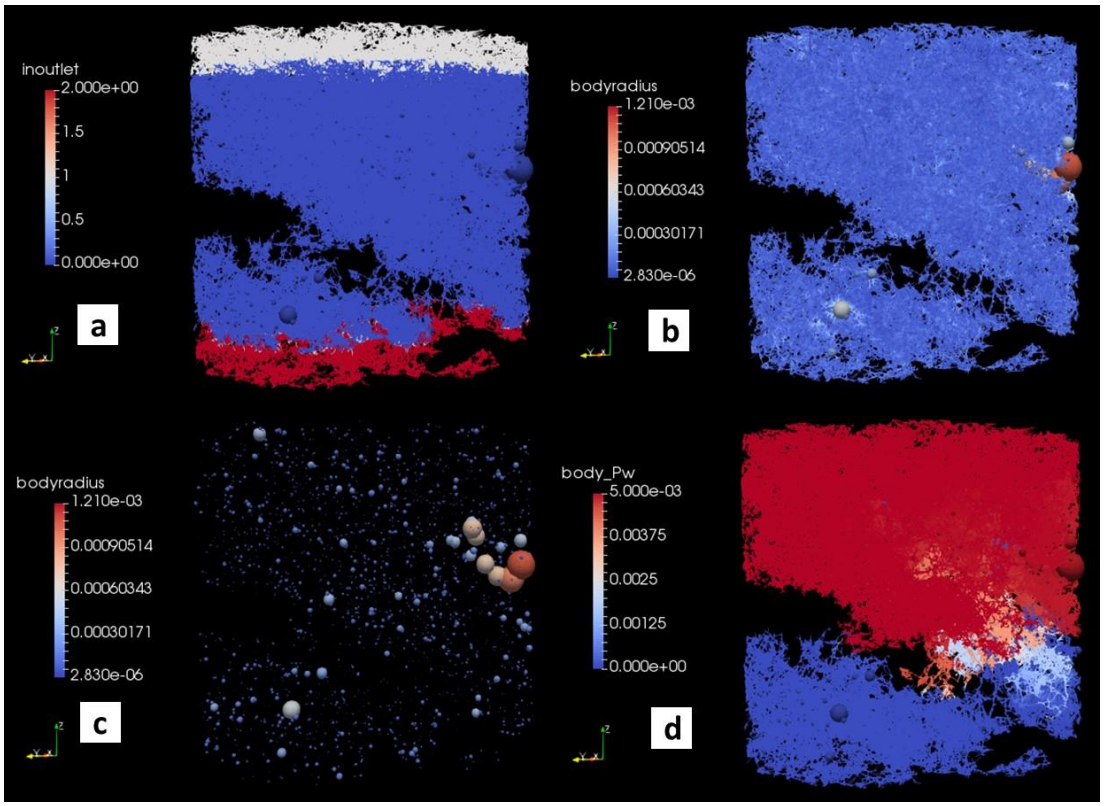


Figure 4-35 – PNM of sample 1-4 based on 9.97µm pixel size µCT images showing, (a) 10% input/output boundaries; (b) pore bodies and pore throat radii; (c), size of pore bodies; and (d) pressure field for the studied PNM. Pressure scales in Pa, dimension in m.

Concerning the insertion and reconnection of pores in sub-resolution for pore networks generated with lower resolutions, as in the case of PNMs generated with µCT images with pixel size equal to 18.53µm and 24.95µm, some considerations are presented:

i) For the networks obtained with µCT images with pixel size equal to 18.53µm, regardless of the average used to define the pore throats (arithmetic, geometric or harmonic), as well as the input/output boundaries (2%, 10% or 20%) and combinations of parameters MDF, NCZ and NCC, numerically estimated Kabs values were always one or two orders of magnitude below the reference value (value obtained experimentally);

ii) For networks obtained with µCT images with pixel size equal to 24.95µm, regardless of any parameters adopted in any of the steps inherent to the network generation and subsequent reconnection, there was no generation of connectivity between the neighborhoods.

For comparison, Figure 4-36 presents the results of the pressure fields for the PNMs obtained from different resolutions. It can be noticed that the sub-resolution pores generated allowed the reconnection of the neighborhoods in the vicinity of the same region (Figures 4-36 (b) and (d)). A great advantage of using this methodology for the generation and reconnection of porosity in sub-resolution is due to the fact that the algorithm seeks the connection through the topological proximity between the pore bodies and pore throats already existing and those that are generated during the execution of the process. This step intends to minimize the effect of the generation of new pores in regions that are not initially candidates to receive these new points, especially due to the gray scale of the μCT images that are not compatible with the existence of these pores.

Although the results are quite interesting, some improvements are still needed in the code and in the execution of the script, in order to improve some points:

i) Delimitation of specific regions where the sub-resolution pore bodies and throats can be inserted and connected: selection based on the gray scale of the μCT images of the regions with highest probability to have this porosity in sub-resolution;

ii) Possibility to correlate the pore size distribution obtained from the NMR technique to the distribution curve adopted during the execution of the script, in order to calibrate the adopted parameters;

iii) Possibility of using other experimental techniques for calibrating throat size distribution (TSD) curves, such as the use of data from the mercury injection capillary pressure (MICP) technique, or even the acquisition of μCT images of some regions with smaller pixel sizes (increased resolution).

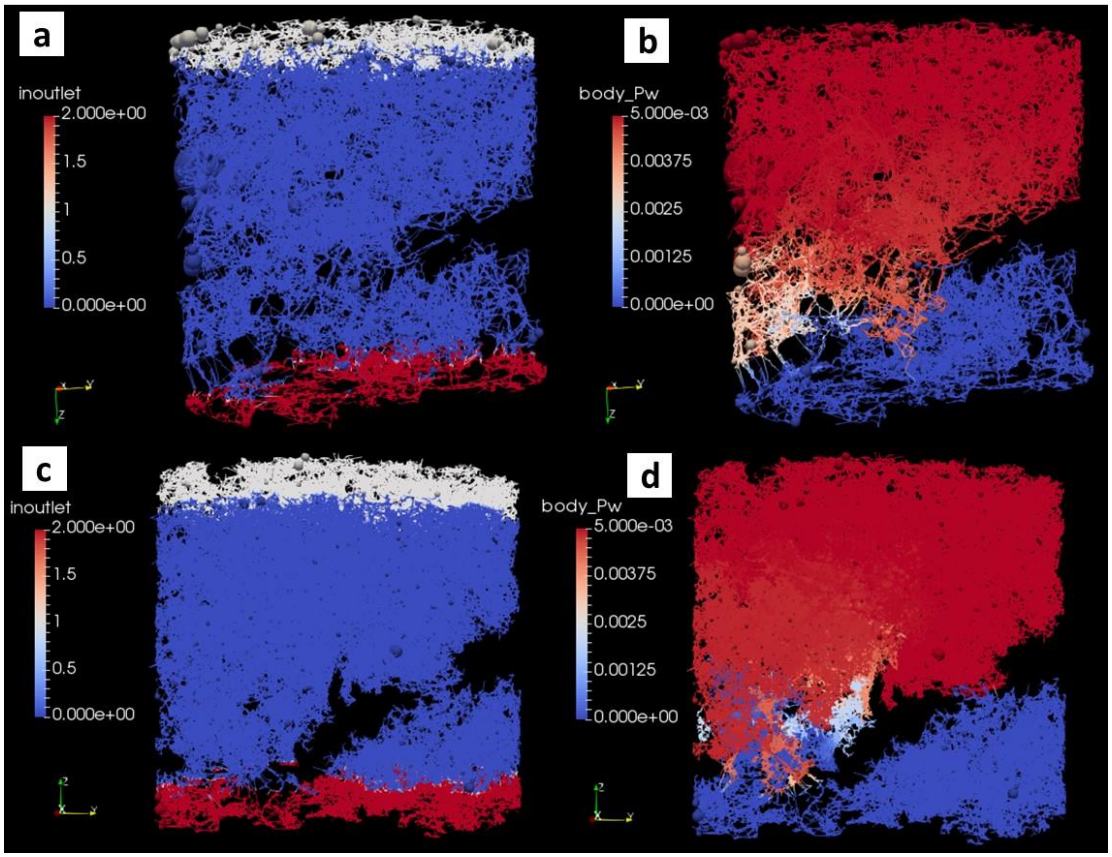


Figure 4-36 – (a) PNM of sample 1-4 based on 18.53µm pixel size µCT images with 10% input/output boundaries; (b) pressure field for this PNM; (c) PNM of sample 1-4 based on 9.97µm pixel size µCT images with 10% input/output boundaries; and (d) pressure field for this second studied PNM. Pressure scales in Pa.

4.2.6 Primary Drainage Studies

As described in Chapter 3, the tests were performed to obtain the *Pc-Sw* curves by the centrifuge method for samples 1-19B, 1-20B and 1-34A. Initially, the saturation indexes (SIs) of the selected samples were calculated, as a first quality control for subsequent two-phase flow simulations. Table 4-23 shows the SI values. One may verify that sample 1-34A has a SI lower than 95%, considered a first control to obtain results that are satisfactorily representative. Although the value for this sample did not reach the minimum control level, the Pc-Sw curve obtained for this sample was used also for comparisons with the numerical simulations.

Table 4-23 – Saturation Index (SI) for primary drainage studies.

Sample	SI (%)
1-19B	98.34
1-20B	98.22
1-34A	92.15

Figure 4-37 shows the Pc-Sw curves obtained for the aforementioned samples. From the experimental results obtained by the centrifuge method, some important observations may be highlighted:

i) All samples show curves that converge to Swir (irreducible water saturation) values below 0.1, except for two samples, 1-20B and 1-34A, which exhibit an unusual behavior regarding curve inflection;

ii) As previsously informed in Chapter 3, the estimated capillary pressure curves from centrifuge measurements were obtained using inverse non-linear regression based on Maximum Likelihood Estimation (MLE) using the homographic parameterization as presented by ALBUQUERQUE *et al*. (2018);

iii) All curves can have their Swir points identified between 10 and 20 psi, thus facilitating numerical simulations of the points whose capillary pressures approximate these values.

From the primary drainage simulation using experimental data from Model Oil and Model Brine, it is possible to estimate the capillary pressure curves of the samples. Initially, studies were performed involving PNMs generated from the μCT images with pixel size in the order of 18μm. The curves for three samples can be seen in Figures 4-38, 4-39 and 4-40. PNMs were selected that pore throats which were generated from the averages Kabs estimates, closer to the measured real values: for sample 1-19B, geometric mean, for 1-20B, arithmetic mean, and for 1- 34A, the harmonic mean.

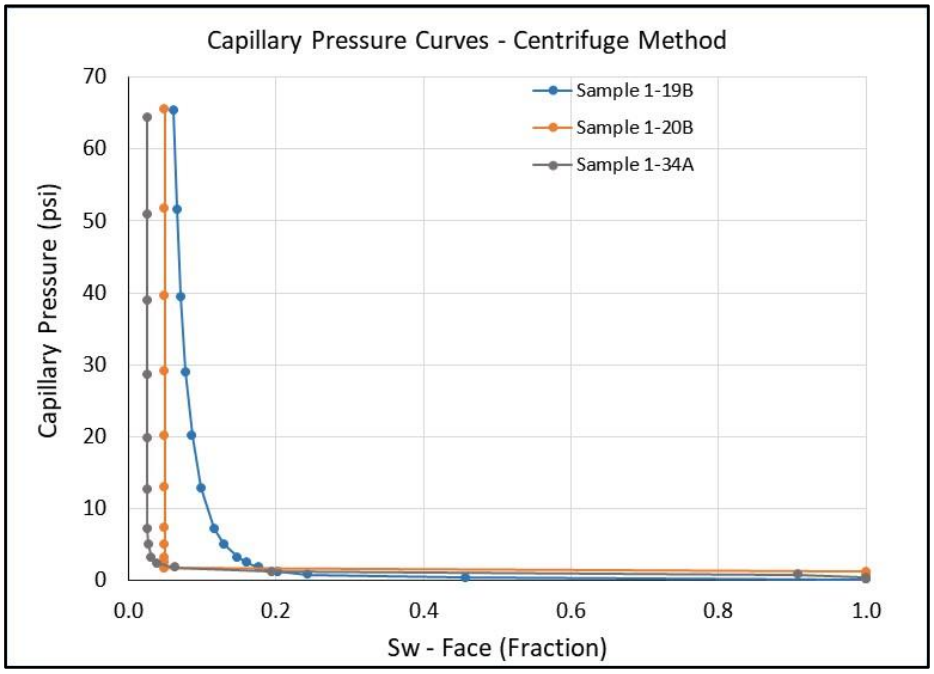


Figure 4-37 – Capillary pressure curves obtained from the centrifuge method for samples 1-19B, 1-20B, and 1-34A.

From the analysis of the curves for the selected samples, some aspects can be discussed:

i) All PNM simulations involving rock-fluid and fluid-fluid interaction properties showed Swir values below the values determined experimentally;

ii) The capillary pressures for samples 1-20B and 1-34A had a direct relation with the capillary pressures determined using the centrifuge; sample 1-19B showed the PNM-based Pc values higher than those obtained experimentally;

iii) Table 4-24 shows that all samples exhibited a sudden steep decrease in saturation (fraction) for relatively low rotation speeds (around 1,250 RPM), demonstrating that Model Oil was able to fill the pore system of the samples, expelling significantly the Model Brine;

iv) No problems are made to the integration of Eq. 4.14 as well as to the errors obtained as a function of which step.

Tabela 4-24 – Centrifuge Method results for samples 1-19B, 1-20B, and 1-34A.

Rotation	Capillary Pressure	Sample 1-19B	Sample 1-20B	Sample 1-34A
RPM	psi	Saturation	Saturation	Saturation
500	0.20	1.000	1.000	1.000
750	0.45	0.457	1.000	1.000
1,000	0.80	0.244	1.000	0.908
1,250	1.23	0.202	1.000	0.194
1,500	1.80	0.177	0.049	0.063
1,750	2.44	0.160	0.049	0.039
2,000	3.18	0.148	0.049	0.031
2,500	4.97	0.129	0.049	0.027
3,000	7.15	0.116	0.049	0.026
4,000	12.72	0.098	0.049	0.025
5,000	19.87	0.086	0.049	0.025
6,000	28.61	0.078	0.049	0.025
7,000	38.94	0.071	0.049	0.025
8,000	50.86	0.066	0.049	0.025
9,000	64.37	0.061	0.049	0.025

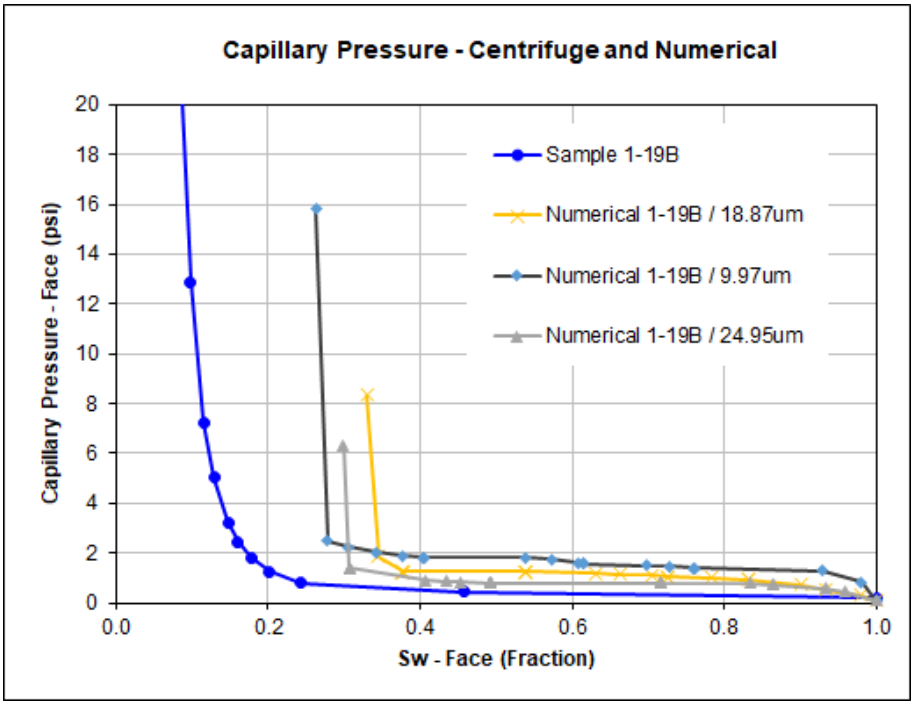


Figure 4-38 – Comparison of capillary pressure curves obtained with the centrifuge method and PNM numerical simulations for sample 1-19B at laboratory condition.

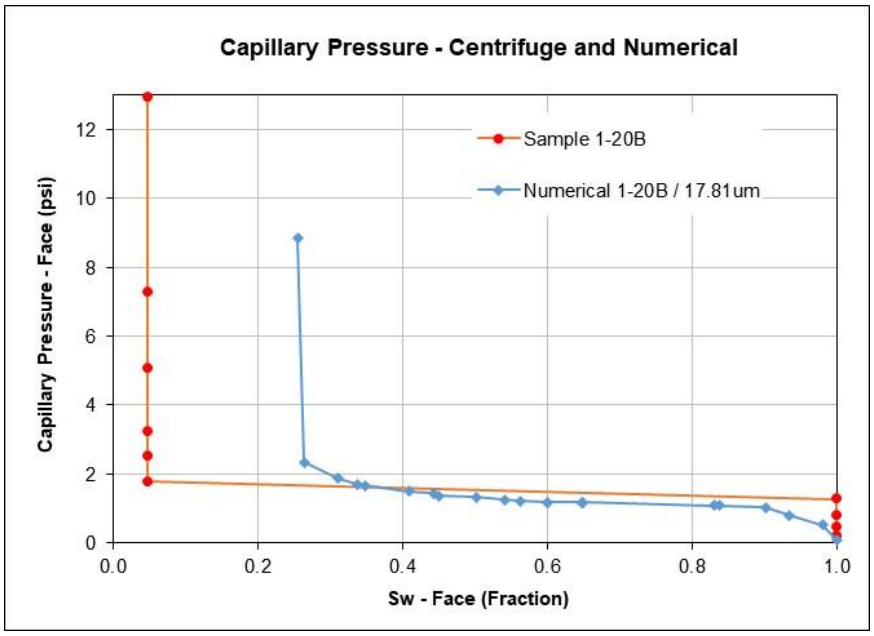


Figure 4-39 – Comparison of capillary pressure curves obtained from the centrifuge method and numerical simulation for sample 1-20B at laboratory condition.

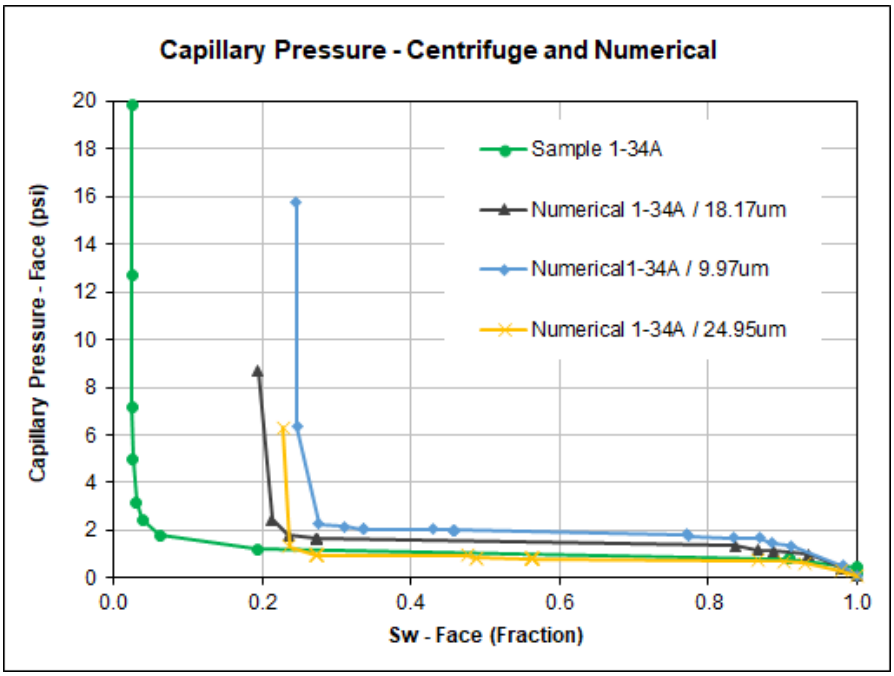


Figure 4-40 – Comparison of capillary pressure curves obtained from the centrifuge method and numerical simulations for sample 1-34A at laboratory condition.

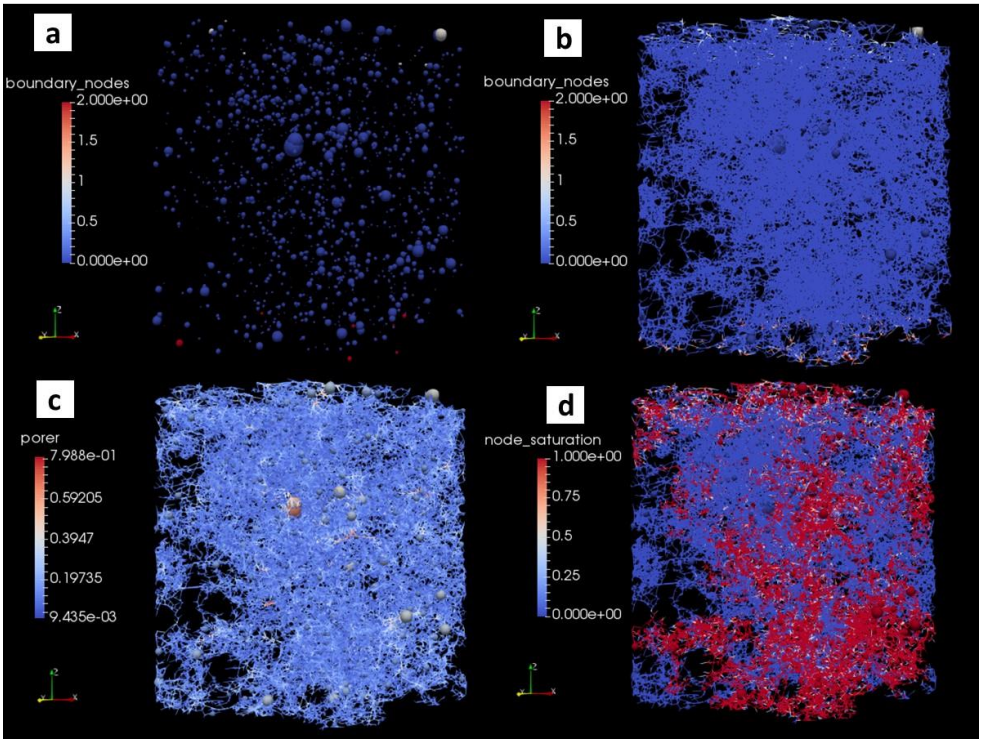


Figure 4-41 – (a) PNM of sample 1-19B based on 18.87μm pixel size μCT images with input/output boundaries selected by PoreFlow; (b) the input/output boundaries considered few points; (c) pore bodies and pore throats radii; and (d) saturation: blue is the wetting phase and red is the non-wetting phase.

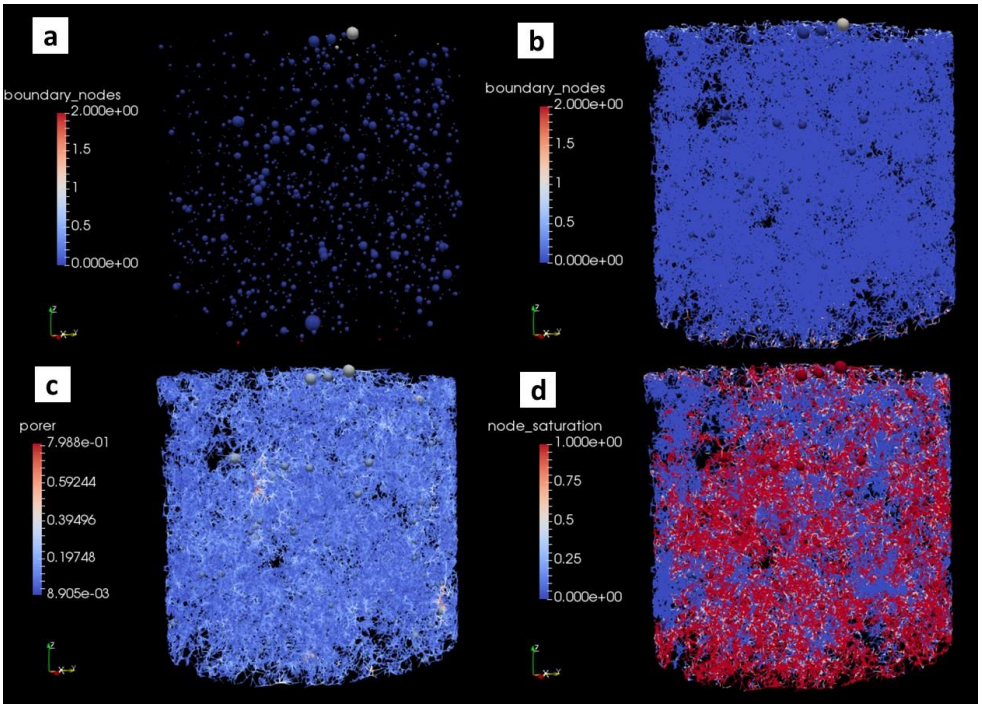


Figure 4-42 – (a) PNM of sample 1-20B based on 17.81μm pixel size μCT images with input/output boundaries selected by PoreFlow; (b) the input/output boundaries considered few points; (c) pore bodies and pore throats radii; and (d) saturation: blue is the wetting phase and red is the non-wetting phase.

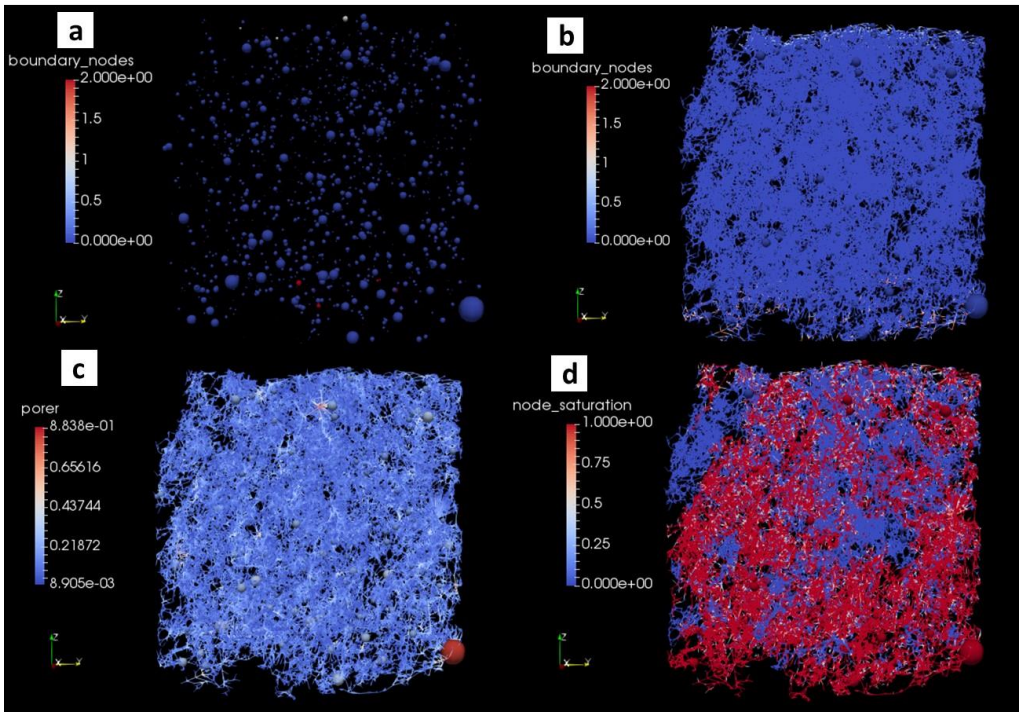


Figure 4-43 – (a) PNM of sample 1-34A based on 18.17μm pixel size μCT images with input/output boundaries selected by PoreFlow; (b) the input/output selection considered few points; (c) pore bodies and pore throats radii; and (d) saturation: blue is the wetting phase and red is the non-wetting phase.

Although the results of the Pc-Sw curves obtained from the PNMs generated with μCT images with different pixel sizes do not have a perfect correlation with the experimental centrifuge data, some important points support the understanding of possible numerical discrepancies:

i) The delimited input/output boundaries during the drainage simulations are changed by the PoreFlow code, as shown in Figures 4-41, 4-42, and 4-43. Recalculated values may have a more significant impact on results. The impact of these boundaries was discussed previously to obtain the Kabs estimates and during sub-resolution porosity analysis. For the primary drainage curves obtained, a possible change in these values constitutes a point of interest for other studies;

ii) As mentioned in item 3.1.10 of this work, it were considered circular cross sections for the pore throats. This definition, according to RAOOF & HASSANIZADEH (2012), has a significant impact on the results, since the effects of corner angles in relation to two-phase flow in all pore throats are disregarded. Only the pore bodies can have their geometry altered, considering cuboids with well-defined corner angles;

iii) Differences in saturation were found for the highest numerically calculated capillary pressure and its experimental equivalent of 0.21 for sample 1-19B (Pc close to 8 psi); 0.21 for sample 1-20B (Pc close to 8 psi, once more); and 0.17 for sample 1-34A (same Pc as above). These results indicate that there is a shift close to 0.2 in the saturation fraction, indicating a possible constant numerical inconsistency, at least for PNMs obtained from μCT images with pixel size in the order of 18μm.

Figure 4-44 shows the saturation maps obtained from the PNM of sample 1-19B reconstructed from different resolutions. It is possible to analize from the primary drainage curves (Figure 4-38) that the model based on higher resolution presents a closer behaviour with the experimental results regarding the Swir value. However, the initial points from the numerical curve do not have a consistent convergence with the laboratory data. The saturation maps present the non-wetting phase (in red) advancing through the pore system while the wetting phase (in blue) is the immobile brine, trapped in the smaller pore throats.

There is another important assumption regarding the wettability of the rock: in order to perform the centrifuge method, it is expected to have all samples with water-wet behaviour. The preparation of the rocks is an essential part of the experiment of primary drainage: cleaning and wettability tests. Although the cleaning process was considered satisfactory, all samples were previously in contact with Oil A, as one first attempt to generate the primary drainage curves was perfomerd earlier. Possible differences between experimental and numerical results could also be addressed to a changed wettability behaviour, once the curves apparently show two characteristics: samples with well connected pore systems and the possibility of an oil-wet behaviour after all preparation steps.

Figure 4-45 shows the results of primary drainage involving PNM from sample 1-19B at a semi-reservoir condition: 1,000 psi and 60ºC. The pre-salt reservoir condition is more extreme, 5,000 to 10,000 psi and 60ºC to 90ºC in different fields. However, the numerical results, from different resolution-based PNM, show an oil-wet behaviour, as expected from the laboratory measurements of contact angles at specified IFT, densities and viscosities. The previous paragraph introduced the idea of a changed wettability from the laboratory primary drainage experiments.

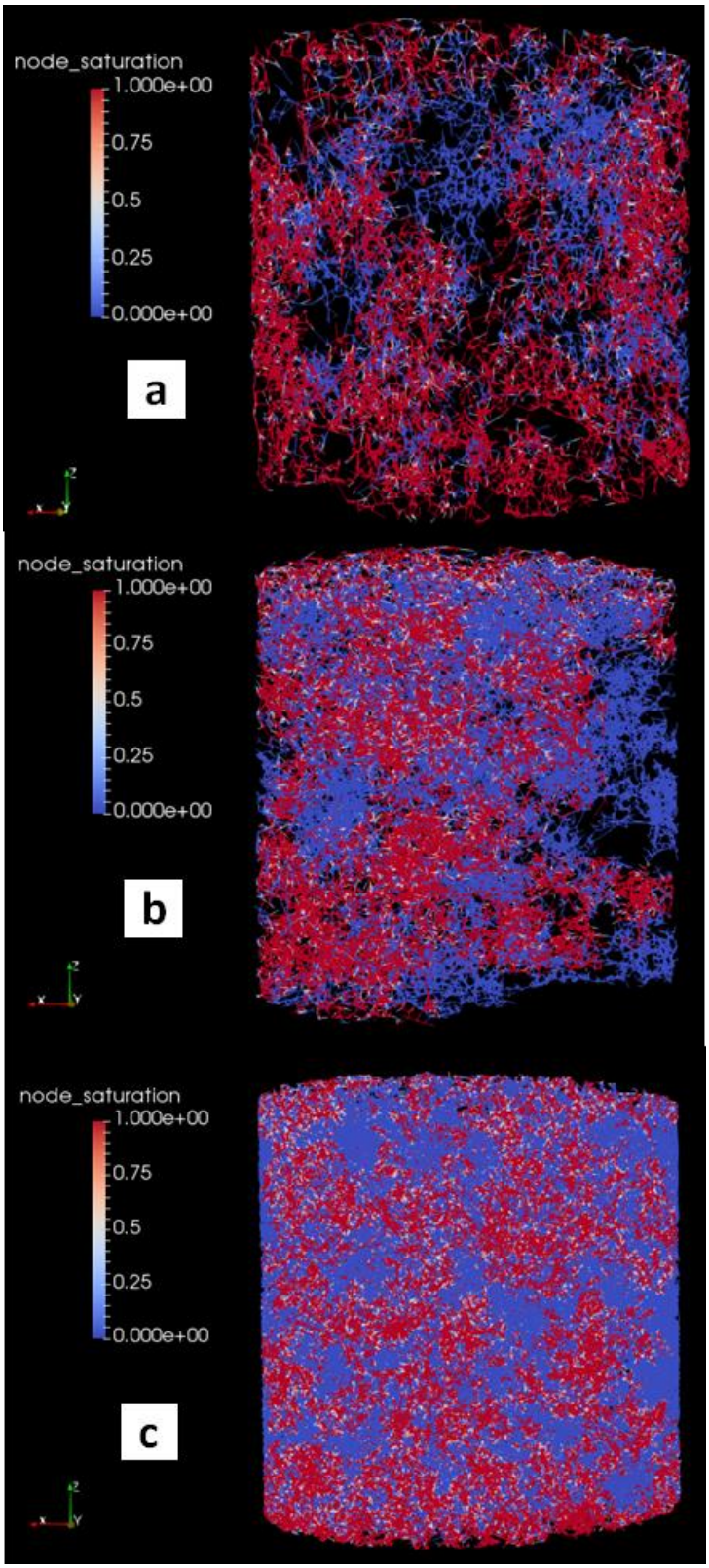


Figure 4-44 – (a) Saturation map of sample 1-19B based on 24.95μm pixel size μCT images; (b) 18.87μm; and (c) 9.97μm. Saturation map: blue is the wetting phase and red is the non-wetting phase.

The curves look similar to the laboratory results, even considering the differences of different parameters (as shown in Tables 4-7, 4-8, and 4-10). Although the differences of IFT, contact angles, densities, and viscosities, the first points, at low capillary pressures show a similar pattern to the centrifuge-based curve. The values of Swir are closer to the experiment measurements, even considering a changed wettability, which modifies the phases: oil represents the wet phase.

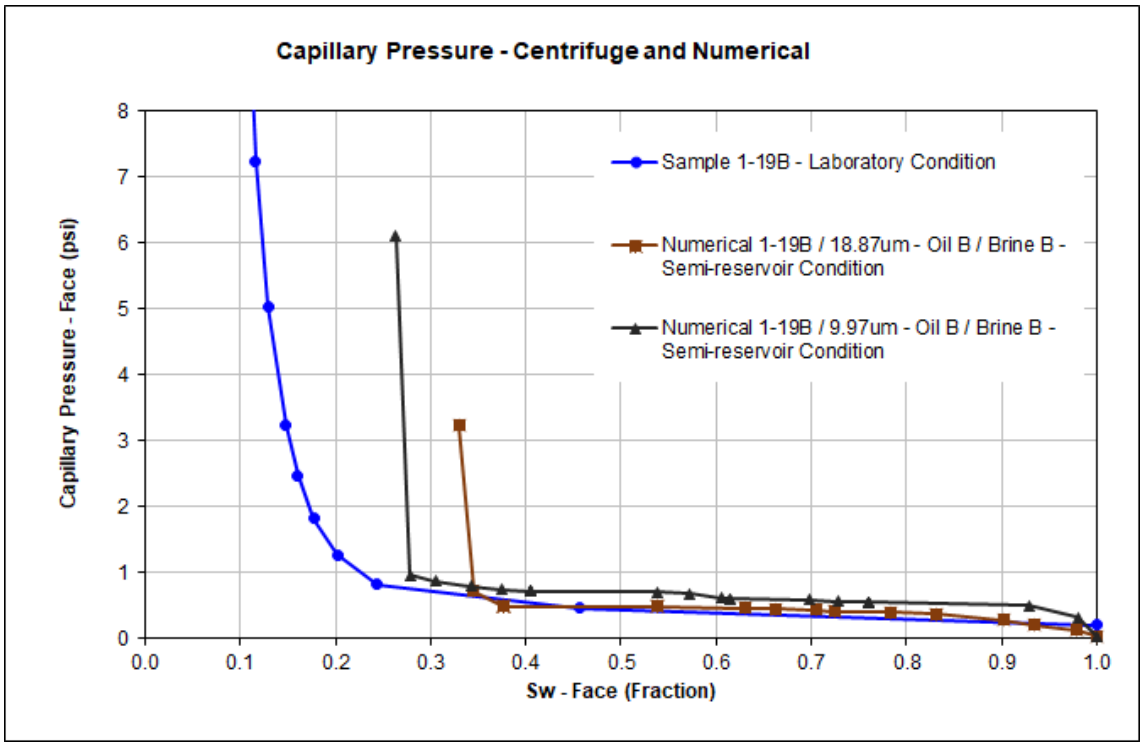


Figure 4-45 – Comparison of capillary pressure curves obtained from the centrifuge method and numerical simulations for sample 1-19B in a oil-wet semi-reservoir scenario of pre-salt.

The curve from a higher resolution-based PNM (pixel size equals to 9.97 μm) presents a closer Swir to the laboratory value, although the capillary pressures are higher than the pressures obtained from the lower resolution-based PNM. The last points show a Sw difference of 0.07. The smaller pore bodies and pore throats in the higher resolution-based PNM are responsible for this change.

It is important to present some results from the other two samples, 1-20B:

i) PNM of sample 1-20B generated with 9.97μm presented several challenges: the number of points (pore bodies and pore throats as well) are a challenge for the Kabs simulator, leading to some errors during

the single-phase and two-phase flow simulations. There were some numerical problems of convergence;

ii) PNM of sample 1-20B generated with 24.95μm presented other significant challenge: even presenting a experimental Kabs value of 1,075 mD, the NMR-based segmentation procedure was not enough to generate a well-connected pore system. The automated segmentation procedures could generate a better connectivity, but the pore system was not generated using the automated methods.

5 CONCLUSIONS

This work investigated experimentally and numerically several aspects of coquina carbonate rock samples, very close analogues to important pre-salt hydrocarbon reservoir rocks of Santos Basin (Brazil). A series of analyses were carried out on a thin section using optical microscopy, on a rock slab taken from a plug using SEM, EDS, XRD and μCT, and on a larger plug using both μCT images and direct measurements. These analyses together with 3D imaging was used to examine the rock matrix composition and to verify and digitally reconstruct the pore systems, which provided much insight about the matrix and macropore fluid flow processes in the naturally very heterogeneous rock sample. Using PNM numerical simulations, we could estimate the absolute permeability of the rock slab and the entire plug, which presented a proper REV relative to the measured value. The experimental results were important to stablish significant correlations for the entire plug, mostly to obtain reliable information about the pore structure required in the modeling step. In these studies it was possible to detect bivalve and ostracode shells within the coquina sample and identify mesopores and macropores providing the main pathways for fluid flow inside the almost pure calcite rock sample. Digital reconstruction of the pore system, along with detailed experimental analyses, allowed us to construct and use the PNM models with confidence. The models were also used to verify the main aspects related to fluid flow modeling: (*i*) rock slab models provided less accurate permeability values compared to the entire plug due to their volumes below the REV; (*ii*) pore throat radii calculated with harmonic averages gave the best results for the absolute permeability; and (*iii*) higher μCT resolution images provided the best result for the permeability according to the experimental data for the entire plug. In order to generate more realistic pore systems for the coquinas, it was used additional experimental techniques like nuclear magnetic resonance to verify prevailing pore distributions, and to further improve the segmentation procedures for additional PNM studies, especially for multiphase flow conditions. Studies involving sub-resolution porosity were conducted, showing that PNM is an excellent technique to address this important topic, presenting numerical results of Kabs very close to the laboratory measurement. Finally, two-phase flow simulations could be performed focused on primary drainage studies to evaluate Pc-Sw curves for three different coquina samples, from centrifuge method and generated from simulations involving PNMs generated from μCT images with different pixel sizes. The results showed that the simplifications selected

for drainage simulation should be evaluate carefully in order to estimate and generate curves of Pc-Sw with high confidence.

5.1.1 Further Studies

From the results and discussions presented throughout this work, some points for future work and research are presented:

i) Although the selected experimental techniques are extremely important for the understanding of the pore system, a technique that has not been addressed in this work refers to the Mercury Intrusion Capillary Pressure (MICP). Throat Size Distribution (TSD) curves can be obtained through this technique, and in a joint analysis with the NMR data, can provide more information on the studied pore systems, as well as give a clear indication of the capillary pressures submitted to the systems. It is important, therefore, the inclusion of this technique within the proposed workflow, this being an important future work;

ii) New techniques associated with the acquisition of μCT data, including digital zooming in of specific regions of the plugs studied, without the need to cut the samples, can provide even more useful information regarding the reconstruction of PNMs of different carbonate samples. In addition, a multi-resolution analysis of a single plug and the possibility of doing the same analysis experimentally, while obtaining the images of μCT, in a process currently called 4D acquisition, will certainly bring important information for the understanding of the flow dynamics in these porous systems;

iii) Automated segmentation techniques still present some restrictions and some experimental methods, such as the use of the NMR data, presented in this work, may help in this step. However, the utilization of new algorithms of identification and recognition (Machine Learning) and the increasing growth of the number of data regarding these carbonate samples (Big Data), play an important role in the new techniques of automated segmentation. The use of these techniques could bring an even greater gain in the reconstruction and modeling of the studied pore networks;

iv) Studies on sub-resolution porosity present many challenges. Some of them: (a) improvement of the code for generation and reconnection of the pores in specific regions of the samples; (b) better control of PSD curves using NMR and MICP data to calibrate the parameters of the distribution curves used for the generation of pore bodies and pore throats; and (c) possibility of using data obtained from the two-phase simulation for better calibration of the generated networks. All of these topics can be included in a larger study regarding sub-resolution porosity.

v) Improvement of the predictions of the numerically obtained Pc-Sw curves, using some changes in the generated networks themselves: alteration of the cross-sections of the pore throats (triangular sections, rectangular sections etc.), in such a way that there are corner angles, which will alter the results of the curves obtained from the primary drainage. In addition, the possibility of carrying out the complete primary drainage and forced imbibition tests (both with the centrifuge method), and the respective numerical simulations, would bring information and significant improvements to the methodology for obtaining and simulating the Swir and Sor (residual oil saturation) points;

vi) The proposed workflow can be used in a broader context as part of a set of methodologies that also involve different upscaling techniques, either through different Kriging techniques, the use of Flow Zone Indicators (FZI), porosity and permeability trends etc., in order to obtain data that can be used in reservoir simulation.

6 BIBLIOGRAPHY

AHMED, T. **Reservoir Engineering handbook**, 4th Ed. Burlington, MA: Gulf Professional Publishing. 2010

AHR, W. M. **Geology of Carbonate Reservoirs: The Identification, Description, and Characterization of Hydrocarbon in Carbonate Rocks**, First edition. Wiley, New Jersey, U.S.A., 2008.

AIRD, E. G. A. **Basic physics for medical imaging**. Butterworth-Heinemann. 1988.

AL-ANSI, N., GHARBI, O., RAEINI, A. Q., YANG, J., IGLAUER, S., BLUNT, M. J. "Influence of Micro-Computed Tomography Image Resolution on the Predictions of Petrophysical Properties". In: **International Petroleum Technology Conference 2013**, Beijing, China, 26–28 Março, 2013.

ALBERTS, L., BAKKE, S., BHATTAD, P., CARNERUP, A., KNACKSTEDT, M., ØREN, P., SOK, R., VARSLOT, T., YOUNG, B. "Characterization of Unconventional Reservoir Core at Multiple Scales". In: **Unconventional Resources Technology Conference**, Denver, Colorado – U.S.A., 12-14 agosto, 2013. SPE paper 168934 / URTeC paper 1619973.

ALBUQUERQUE, M. R., ELER, F. M., CAMARGO, H. V. R., COMPAN, A. L. M., CRUZ, D. A., PEDREIRA, C. E. 2018. "Estimation of Capillary Pressure Curves from Centrifuge Measurements Using Inverse Methods". In: **Rio Oil & Gas Expo and Conference**, Rio de Janeiro – Brasil, 24-27 setembro, 2018.

AL-RAOUSH, R. I., WILLSON, C. S. "A pore-scale investigation of a multiphase porous media system". In: **Journal of Contaminant Hydrology 77**, 67–89. Elsevier. 2005.

ALVES, R. A. B. R. **Desenvolvimento de um Algoritmo Computacional para Reconstrução da Microporosidade Utilizando a Técnica de Pore Network Model**. 79p. Monografia, Engenharia de Petróleo – Politécnica (POLI) – Universidade Federal do Rio de Janeiro.

ANDERSON, W.G.: "Wettability Literature Survey – Part 1: Rock/Oil/Brine Interactions and the Effects of Core Handling on Wettability", **Journal of Petroleum Technology 38**, pp. 1125–1144, Out. 1986.

ANP – Agência Nacional do Petróleo, Gás Natural e Biocombustíveis. 2018. **Anuário estatístico brasileiro do petróleo, gás natural e biocombustíveis: 2018**. Disponível em: <http://www.anp.gov.br/publicacoes/anuario-estatistico/anuario-estatistico-2018>. Acesso em Novembro de 2018.

ARNS, C. H., A. SAKELLARIOU, T. J. SENDEN, A. P. SHEPPARD, R. SOK, W. V. PINCZEWSKI, M. A. KNACKSTEDT. "Digital core laboratory: Reservoir core analysis from 3D images". **Petrophysics 46(4)**: 260-277. 2005.

ARNS, C.H. “A comparison of pore size distributions derived by NMR and X-ray-CT techniques”. **Phys A 339**:159–165. 2004.

ARNS, J., ARNS, C. H., SHEPPARD, A. P., SOK, R. M., KNACKSTEDT, M. A., PINCZEWSKI, W. V. “Relative permeability from tomographic images; effect of correlated heterogeneity”. In: **Journal of Petroleum Science and Engineering**, 39, pp. 247 – 259. 2003.

AVIZO. **Reference Manual**. Version 9.5. January 2018.

AYACHIT, U. **The ParaView Guide: A Parallel Visualization Application**. Kitware. 2015.

AZAMBUJA, N.C.; ARIENTI, L.M. “Guidebook to the Rift-Drift Sergipe-Alagoas, Passive Margin Basin, Brazil”. **The 1998 American Association of Petroleum Geologists International Conference and Exhibition**. p.113, 1998.

AZZAM, M. I. S., DULLIEN, F. A. L. “Flow in tubes with periodic step changes in diameter: a numerical solution”. **Chem. Eng. Sci**. 32, 1445–1455. 1977.

BEAR, J. **Dynamics of Fluid in Porous Media**, Dover Publications inc., pp. 151–173. 1972.

BEHROOZMAND, A. A., KEATING, K., AUKEN, E. “A Review of the Principles and Applications of the NMR Technique for Near-Surface Characterization”. In: **Surv Geophys**, Elsevier, 2014. DOI 10.1007/s10712-014-9304-0

BELTRÃO, R. L. C., SOMBRA, C. L., LAGE, A. C. V. M., FAGUNDES NETTO, J. R., HENRIQUES, C. C. D. “Challenges and New Technologies for the Development of the Pre-Salt Cluster, Santos Basin, Brazil”. In: **2009 Offshore Technology Conference**, Houston, Texas – USA, 4-7 May, 2009. OTC Paper 19880.

BERNSEN J. ‘‘Dynamic limiaring of gray level images’’ **ICPR 86: Proc. Intl. Conf. Patt. Recog.**, pp. 1251–1255. 1986.

BIENIECKI, W., GRABOWSKI, S. “Multi-pass approach to adaptive limiaring based image segmentation”. In: **CADSM’2005**, 23-26 fevereiro, Lviv-Slavske, Ucrânia. 2005.

BIRD, R. B., STEWART, W. E., LIGHTFOOT, E. N. **Transport Phenomena**, John Wiley & Sons, New York. 1960.

BLUNT, M. J. “Flow in porous media — pore-network models and multiphase flow”. **Curr. Opin. Colloid Interface Sci**. 6, 197–207. 2001

BLUNT, M. J., JACKSON, M. D., PIRI, M., VALVATNE, P. H. “Detailed physics, predictive capabilities and macroscopic consequences for pore-network models of multiphase flow”. In: **Advances in Water Resources, 25**, 1069–1089. 2002.

BOGGS Jr., S. **Principles of Sedimentology and Stratigraphy**, Fourth edition. Pearson Prentice Hall, New Jersey, U.S.A., 2006.

BOHLING, G. C. **Introduction to Geostatistics**. Kansas Geological Survey Open File Report no 26 (2007), 50. 2007.

BROWN, R.J.S., FATT, I.: "Measurements of Fractional Wettability of Oilfield Rocks by the Nuclear Magnetic Relaxation Method", **Transactions, AIME 207**: 262–264, 1956.

BUADES, A., COLL, B., MOREL, J. M. A non local algorithm for image denoising, in Proc. **Int. Conf. Computer Vision and Pattern Recognition** (CVPR) 2005, vol. 2, pp. 60-65. 2005.

BULTREYS, T., DE BOEVER, W., CNUDDE, V. "Imaging and image-based fluid transport modeling at the pore scale geological materials: A practical introduction to the current state-of-the-art". **Earth-Science Reviews** 155: 93-128. 2016.

BULTREYS, T., BOONE, M. A., BOONE, M. N., DE SCHRYVER, T., MASCHAELLE, B., VAN HOOREBEKE, L., CNUDDE, V. "Fast laboratory-based micro-computed tomography for pore-scale research: Illustrative experiments and perspectives on the future". **Advances in Water Resources** 95: 341–351. 2015.

BUSH, J. W. M. Surface Tension Module. Department of mathematics, Massachusetts Institute of Technology – MIT. Notas de aula. www.web.nit.edu. Acessado em Maio de 2017.

BUTT, H. J.; GRAF, K.; KAPPL, M. 2006. **Physics and Chemistry of Interfaces**. Berlin, Germany: WILEY-VCH Verlag GmbH & Co.

CÂMARA, R. N. 2013. **Caracterização Petrofísica de Coquinas da Formação Morro do Chaves (Barremiano/Aptiano), Intervalo Pré-sal da Bacia de Sergipe-Alagoas**. Dissertação de Mestrado, Programa de Pós-graduação em Geologia /UFRJ, Rio de Janeiro, Brasil.

R. G. CARBONELL, S. WHITAKER**.** Heat and Mass Transfer in Porous Media**. Fundamentals of Transport Phenomena in Porous Media**. Martinus Nijhoff Publishers, 1984.

CARMINATTI, M., DIAS, J. L., WOLFF, B. "From Turbidites to Carbonates: Breaking Paradigms in Deep Waters". In: **2009 Offshore Technology Conference**, Houston, Texas – USA, 4-7 May, OTC Paper 20124.

CHAN, T. F., VESE, L. A. "Active Contours Without Edges". In: **IEEE Transactions on Image Processing, Vol. 10, No. 2**. 2001.

CNUDDE, V., BOONE, M. N. "High-resolution X-ray computed tomography in geosciences: A review of the current technology and applications". In: **Earth-Science Reviews 123 (2013)**: 1–17. Elsevier. 2013.

CNUDDE, V., MASSCHAELE, B., DIERICK, M., VLASSENVROECK, J., HOOREBEKE, L.V., JACOBS, P. “Recent progress in X-ray CT as a geosciences tool”. In: **Applied Geochemistry**, 21: 826-832, 2006.

COATES, G.R., XIAO. L., PRAMMER, G. **NMR logging principles and applications**. Halliburton Energy Services, Houston. 1999.

COENEN, J., TCHOUPAROVA, E., JING, X. “Measurement Parameters and Resolution Aspects of Micro X-ray Tomogrraphy for Advanced Core Analysis”. In: **International Symposium of Society of Core Analysts**, Abu Dhabi, UAE. 2004.

CONSTANTINIDES, G.N., PAYATAKES, A.C. Network simulation of steady-state two-phase flow in consolidated porous media. **AIChE J**. 42, 369–382. 1996.

CORBETT, P. W. M. **Integration of static and dynamic models. Petroleum geoengineering**. SEG/EAGE Distinguished Instructor Series, vol. 12, pp. 100–190. 2009.

CORBETT, P. W. M., ANGGRAENI, S., BOWDEN, D. “The use of the probe permeameter in carbonates-addressing the problems of permeability support and stationarity”. In: **Log Anal. 40 (5)**, 316–326. 1999.

CORBETT, P. W. M., BORGHI, L. “Lacustrine Carbonates – for the purpose of reservoir characterisation are they different?”. In: **2013 Offshore Technology Conference Brasil**, Rio de Janeiro – Brazil, 29-31 October, 2013. OTC Paper 24482.

CRAIG, F.F. JR.: The Reservoir Engineering Aspects of Waterflooding, **Monograph series, SPE**, Richardson, TX, 1971.

DE VRIES, E. T., RAOOF, A., VAN GENUCHTEN, M. T. “Multiscale modelling of dual-porosity media: a computational pore-scale study flow and solute transport”. **Advances in Water Resources** 105: 82-95. 2017.

DEDAVID, B. A., GOMES, C. I., MACHADO, G. **Microscopia Eletrônica de Varredura: Aplicações e preparação de amostras: materiais poliméricos, metálicos e semicondutores**. Porto Alegre, RS. EDIPUCRS, 2007.

DEUTSCH, C. V. **Geostatistical reservoir modeling**. Oxford University Press. 2002.

DIGGLE, P. J. and RIBEIRO JR, P. J. **Model-based Geostatistics**. New York: Springer. 2007.

DONALDSON, E. C., ALAM, W. **Wettability**. Houston, TX: Gulf Publishing Company. 2008

DOS SANTOS, E., AYRES, H., PEREIRA, A., MACHÍN, J., TRITLLÁ, J., LEITE, K., SILVA, E. “Santos Microbial Carbonate Reservoirs: A Challenge”. In: **2013 Offshore Technology Conference Brasil**, Rio de Janeiro – Brazil, 29-31 October, 2013. OTC Paper 24446.

DREXLER, S**. Study of the fluid-fluid and rock-fluid interactions: Impact of dissolved CO_2 on interfacial tension and wettability for the Brazilian Pre-salt scenario**. 2018. 234f. Tese de doutorado, Programa de Pós- Graduação em Engenharia Civil – COPPE, Universidade Federal do Rio de Janeiro – UFRJ. Rio de Janeiro, RJ – Brasil.

DREXLER, S., SOUZA, F. P., CORREIA, E. L., SILVEIRA, T. M. G., COUTO, P. 2018. Statistical Analysis to Evaluate the key Parameters Affecting Wettability of a Brazilian Pre-Salt Crude and Brine on Different Mineral Rocks. **Rio Oil & Gas Conference 2018**. Rio de Janeiro, Brazil: IBP.

DUNN, K. J., BERGMAN, D. J., LATORRACA, G. A. **Nuclear magnetic resonance—petrophysical and logging applications**. Elsevier, Amsterdam. 2002a.

DUNN, K. J., BERGMAN, D. J., LATORRACA, G. A. **Nuclear magnetic resonance—petrophysical and logging applications**. Elsevier Science, Kidligton, pp 1–30. 2002b.

DUNSMUIR, J. H., FERGUSON, S. R., D'AMICO, K. L., STOKES, J. P. "X-ray Microtomography: a New Tool for the Characterization of Porous Media". In **SPE Annual Technical Conference and Exhibition**, 1991.

ENGELHARDT, M., BAUMANN, J. "Determination of size and intensity distribution of the focal spot of a microfocus X-ray tube using image processing". In: **Proc. ECNDT 2006**, Th 2.5.4., pp 1-13, Berlin, Set 2006.

ESTRELLA, R. R. 2015. **Variação da Porosidade e da Permeabilidade em Coquinas da Formação Morro do Chaves (Andar Jiquiá), Bacia Sergipe-Alagoas**. 84p. Monografia, Geologia – Instituto de Geologia (IGEO) – Universidade Federal do Rio de Janeiro.

FACANHA, J. M. F. 2017. **Fundamentals of Wettability Applied to Brazilian Pre-Salt Reservoirs and Wettability Alteration Evaluation in Low Salinity Water Injection**. [s.l.] Heriot-Watt University. Edinburgh – UK.

FAERSTEIN, M. **Impactos da Molhabilidade da Rocha na Produção e Recuperação de Petróleo**. 2010. 190f. Dissertação de mestrado, Programa de Pós-Graduação em Engenharia Civil – COPPE, Universidade Federal do Rio de Janeiro – UFRJ. Rio de Janeiro, RJ – Brasil.

FATT, I. "The network model of porous media". **Transactions of the American Institute of Mining Metallurgical Petroleum Engineers** 207,144–181. 1956.

FÄY-GOMORD, O., SOETE, J., DAVY, C. A., JANSSENS N., TROADEC, D., CAZAUX, F., CALINE, B., SWENNEN, R. "Tight chalk: Characterization of the 3D pore network by FIB-SEM, towards the understanding of fluid transport". **Journal of Petroleum Science and Engineering 156**: 67-74. 2017.

FEIJÓ, F.J.; PEREIRA, M.J. Bacia de Santos. **Boletim de Geociências da Petrobrás**, Rio de Janeiro, v.8, n.1, p.219-234, 1994.

FERNANDES J. S., APPOLONI C. R., MOREIRA A. C., FERNANDES C. P. "Porosity and pore size distribution determination of tumblagooda formation sandstone by X-Ray Microtomography". In: **International Nuclear Atlantic Conference INAC 2007**. 2007.

FERNANDES, J. S., APPOLONI, C. R., MARQUES, L. C., FERNANDES, C. P. "Microstructure Parameters Evaluation of Botucatu Formation Sandstone By X-Ray Microtomography". In: **2009 International Nuclear Atlantic Conference - INAC 2009**, Rio de Janeiro, Brasil, 27 setembro – 02 outubro, 2009.

FIORELLI, G. L. **Caracterização de coquinas e dolomitos integrando três metodologias distintas: resistividade elétrica, ressonância magnética nuclear (RMN) e porosimetria por intrusão de mercúrio (MICP)**. 2015 129f. Dissertação de Mestrado, Faculdade de Engenharia Mecânica e Instituto de Geociências da Universidade Estadual de Campinas.

FORBES, P. 1994. Simple and Accurate Methods for Converting Centrifuge Data Into Drainage and Imbibition Capillary Pressure Curves. **The Log Analyst**.

FORMIGLI, J. M., PINTO, A. C. C., ALMEIDA, A. S. "Santos Basin's Pre-Salt Reservoirs Development – The Way Ahead". In: **2009 Offshore Technology Conference**, Houston, Texas – USA, 4-7 May, OTC Paper 19953.

GHARAHBAGH, A. E., FAKHIMI, A. "Numerical Determination of Representative Volume Element of Rock". In: **44th US Rock Mechanics Symposium and 5th U.S.-Canada Rock Mechanics Symposium**, Salt Lake City, UT – U.S.A. Junho 27–30, 2010. ARMA paper 10-131. 2010.

GLOTIN, G.; GENET, J.; KLEIN, P. 1990. "Computation of Drainage and Imbibition Capillary Pressure Curves from Centrifuge Experiments". **Proceedings of SPE Annual Technical Conference and Exhibition**.

GOMES, O. F. M. **Microscopia co-localizada: novas possibilidades na caracterização de minérios**. 2007. 105f. Tese de Doutorado. Pontifícia Universidade Católica do Rio de Janeiro.

HASSLER, G. L., BRUNNER, E. 1945. Measurement of Capillary Pressures in Small Core Samples. **Petroleum Transactions of AIME**, v. 160, n. 1, p. 114–123.

HAYASHI. F. Y. D., 2014. **Avaliação do Volume Representativo Elementar (REV) em estromatólito de Lagoa Salgada**. Trabalho Final de Curso. Geologia/UFRJ. Rio de Janeiro, RJ – Brasil.

HOERLLE, F. O. 2018. **Estudo da Heterogeneidade, Anisotropia e Conectividade do Sistema Poroso das Coquinas da Formação Morro do Chaves (Bacia de Sergipe-Alagoas)**. Dissertação de Mestrado, COPPE/UFRJ, Rio de Janeiro, Brasil.

HOERLLE, F. O. L., RIOS, E. H., SILVA, W. G. A. L., PONTEDEIRO, E. M. B. D., LIMA, M. C. O., CORBETT, P. W. M., ALVES, J. L. D., COUTO, P. "Nuclear Magnetic Resonance to Characterize the Pore System of Coquinas from Morro do Chaves Formation, Sergipe-Alagoas Basin, Brazil.". **Brazilian Journal of Geophysics**. 36 (3): 1-8. 2018.

HOORFAR, M.; KURZ, M. A.; NEUMANN, A. W. 2005. Evaluation of the surface tension measurement of axisymmetric drop shape analysis (ADSA) using a shape parameter. **Colloids and Surfaces A: Physicochemical and Engineering Aspects**, v. 260, n. 1–3, p. 277–285.

HORNAPOUR, M., KOEDERITZ, L., HARVERY, A. H. **Relative Permeabilities of Petroleum Reservoirs**. Boca Raton, FL: CRC Press, Inc. 1990

HOUSTON, A. N., SCHMIDT, S., TARQUIS, A. M., OTTEN, W., BAVEYE, P. C., HAPCA, S. M. "Effect of scanning and image reconstruction settings in X-ray computed microtomography on quality and segmentation of 3D soil images". In: **Geoderma 207-208**: 154-165. Elsevier. 2013.

HUTTON, D. **Fundamentals of Finite Element Analysis**, New York: McGraw-Hill. 2004.

IZZO JR., J., JOSHI, A., GREW, K., CHIU, W., TKACHUK A., WANG, S., YUN, W. "Nondestructive Reconstruction and Analysis of SOFC Anodes Using X-ray Computed. Tomography at Sub-50 nm Resolution". In: J. **Electrochem. Soc. 155 (5)**, pp. B504-B508. 2008.

JOEKAR-NIASAR, V. **The Immiscibles Capillarity Effects in Porous Media: Pore-Network Modelling**. Utrecht University – Geosciences Faculty – Earth Sciences Department. 2010.

JOEKAR-NIASAR, V., HASSANIZADEH, S. J. "Effects of fluids properties on non-equilibrium capillarity effects: dynamic pore-network modeling". **International Journal of Multiphase Flow** 37: 198-214. 2011.

JOHNSON, C. **Numerical Solutions of Partial Differential Equations by the Finite Element method**, Cambridge University Press. 1987.

JONES, C. M., CHAVES, H. A. F. "Assessment of Yet-To-Find Oil in the Brazilian Pre-Salt Region". In: **2011 Brasil Offshore Conference**, Macaé – Brazil, 14-17 June. SPE paper 143911.

KACZMARCZYK, J., DOHNALIK, M., ZALEWSKA, J, CNUDDE, V. "The interpretation of X-ray Computed Microtomography images of rocks as an application of volume image processing and analysis". In: **WSCG 2010 Communication papers**. 2010.

KACZMARCZYK, J., DOHNALIK, M., ZALEWSKA, J. “Three-dimensional Pore Scale Fluid Flow Simulation Based on Computed Microtomography Carbonate Rocks’ Images”. In: **V European Conference on Computational Fluid Dynamic**, ECCOMAS CFD 2010, 14-17 junho, 2010.

KANIT, T., FOREST, S., GALLIET, I., MOUNOURY, V., JEULIN, D. “Determination of the size of the representative volume element for random composites: statistical and numerical approach”. In: **International Journal of Solids and Structures, Volume 40, Issues 13–14**, 3647–3679, Junho/Julho. 2003.

KEEHM, Y., MUKERJI, T. “Permeability and Relative Permeability from Digital Rocks: Issues on Grid Resolution and Representative Elementary Volume”. In: **SEG Int'l Exposition and 74th Annual Meeting**, Denver, Colorado – U.S.A. 10-15 October. 2004.

KITTLER, J., ILLINGWORTH, J. “Minimum Error Thresholding” In: **Pattern Recognition, Vol.19, No.1**, pp. 41-47, Great Britain. 1986.

KNACKSTEDT, M., GOLAB, A., RIEPE, L. “Petrophysical characterization of unconventional reservoir core at multiple scales”. In: **SPWLA 53rd Annual Logging Symposium**. Cartagena, Colômbia, 16-20 junho, 2012.

LEACH, R. O., WAGNER, O. R., WOOD, H. W., HARPLE, C. F. A laboratory study and field study of wettability adjustment in waterflooding. **Journal of Petroleum Technology, 14 (2)**, 206 – 212. SPE Paper 119-PA. 1962.

LEVITT, M. H. **Spin dynamics: basics of nuclear magnetic resonance**. Wiley, Chichester. 2006.

LINDQUIST, W., VENKATARANGAN, A., DUNSMUIR, J., WONG, T. 2000. Pore and throat size distributions measured from synchrotron x-ray tomographic images of fontainebleau sandstones. Journal of Geophysical Research – All Series – 105 (B9), 21. 2000.

LINDQUIST, W. B., VENKATARANGAN, A. “Investigating 3D geometry of porous media from high resolution images”. **Phys. Chem. Earth Solid Earth Geod**. 24, 593–599. 1999.

LINDQUIST, W. B., LEE, S., COKER, D. A., JONES, K. W., SPANNE, P. “Medial axis analysis of void structure in three-dimensional tomographic images of porous media”. **J. Geophys. Res.** 101, 8297. 1996.

LIU, J., PEREIRA, G. G., LIU, Q., LIEB-REGENAUER, K. “Computational challenges in the analyses of petrophysics using microtomography and upscaling: A review”. **Computers & Geosciences** 89, pp. 107-117, 2016.

LIU, J., PEREIRA, G. G., LIEB-REGENAUER, K. “From characterisation of pore-structures to simulations of pore-scale fluid flow and the upscaling of permeability using microtomography: A case study of heterogeneous carbonates”. In: **Journal of Geochemical Exploration 144**, pp. 84-96, 2014.

LIU, Y., HARDING, A., ABRIEL, W., STREBELLE, S. “Multiple-point simulation integrating wells, three-dimensional seismic data, and geology”. **AAPG bulletin**. 88 (7), 905–921. 2004.

LØNØY A. Making sense of carbonate pore systems. **AAPG bulletin**, 90(9): 1381–1405. 2006.

LUCIA, F. J. **Carbonate reservoir characterization: an integrated approach**. Springer Science & Business Media, 2007.

LUNA, J. L., PEROSI, F. A., RIBEIRO, M. G. S., SOUZA, A, BOYD, A., BORGHI, L. F., CORBETT, P. W. M. “Petrophysical Rock Typing of Coquinas from the Morro do Chaves Formation, Sergipe-Alagoas Basin (northeast brazil)”. **Brazilian Journal of Geophysics**. 34 (4). 2016.

ŁYDŻBA, D., RÓŻAŃSK, A. “On the minimum size of Representative Volume Element: An n-point probability approach”. In: **Harmonising Rock Engineering and the Environment – Qian & Zhou (eds)**, Taylor & Francis Group, London, ISBN 978-0-415-80444-8. 2012.

MA, S., MASON, G., MORROW, N. R. “Effect of contact angle on drainage and imbibition in regular polygonal tubes”. **Colloids Surfaces A** 117, 273–291. 1996.

MALISKA, A. M. **Microscopia Eletrônica de Varredura**. Notas de Aula. Universidade Federal de Santa Catarina – UFSC. 2013.

MALVERN, L. E. **Introduction to the Mechanics of a Continuous Media**, Prentice-Hall. 1969.

MARLE, C. M. “On macroscopic equations governing multiphase ow with dffusion and chemical reactions in porous media”**. Int. J. Engng. Sci**., 50: 643-662, 1982.

MEES, F., SWENNEN, R., GEET, M.V., JACOBS, P. “Aplications of x-ray computed tomography in geosciences”. In: **Geological Society Special Publications**, London, pp1-6, 2003.

MELLO, M. R., BENDER, A. A., AZAMBUJA FILHO, N. C., DE MIO, E. “Giant Sub-Salt Hydrocarbon Province of the Greater Campos Basin, Brazil”. In: **2011 Offshore Technology Conference Brasil**, Rio de Janeiro – Brazil, 4-6 October, 2011. OTC Paper 22818.

MUMFORD D., SHAH J. “Optimal approximation by piecewise smooth functions and associated variational problems”. In: **Commun. Pure Appl. Math, vol. 42**, pp. 577–685. 1989.

NARSILIO, G., BUZZI, O., FITYUS, S., YUN, T. S., SMITH, D. W. “Upscaling of Navier–Stokes equations in porous media: Theoretical, numerical and experimental approach”. In: **Computers and Geotechnics 36**, 7: 1200–1206. Elsevier. 2009.

NETO, J. M. R., FIORI, A. P., LOPES, A. P., MARCHESE, C., PINTO-COELHO, C. V., VASCONCELLOS, E. M. G., SILVA, G. F., SECCHI, R. "A microtomografia computadorizada de raios x integrada à petrografia no estudo tridimensional de porosidade em rochas". In: **Revista Brasileira de Geociências 41 (3)**: 498-508, Setembro, 2011.

NIBLACK W. **An Introduction to Image Processing**. Prentice-Hall, Englewood Cliffs, NJ – U.S.A. pp. 115–116. 1986.

NORDAHL, K., RINGROSE, P. S. "Identifying the Representative Elementary Volume for Permeability in Heterolithic Deposits Using Numerical Rock Models". In: **Math Geosci 40**: 753–771. International Association for Mathematical Geology. 2008.

OKABE, H., BLUNT, M. J. "Pore space reconstruction of vuggy carbonates using microtomography and multiple-point statistics". In: **Water Resources Research, Vol. 43**, W12S02. 2007.

OKABE, H., BLUNT, M. J. "Pore space reconstruction using multiple-point statistics". In: **Journal of Petroleum Science and Engineering, 46**, 121–137. 2005.

OKABE, H., BLUNT, M. J. "Prediction of permeability for porous media reconstructed using multiple-point statistics". In: **Phys. Rev. E., 70, 066135**. 2004.

OKASHA, T.M., FUNK, J.J., Al-RASHIDI, H.N.: "Fifty Years of Wettability Measurements in the Arab-D Carbonate Reservoir", SPE 105114, **15th SPE Middle East Oil & Gas Show and Conference**, Bahrain, Mar. 2007.

OLI Studio. **A Guide to Use OLI Studio**. Version 9.6. 2018.

OLIVEIRA R., PEPIN, A. H., CARVALHO, M. S. "Estimation for Representative Element Area of a Coquinas Analogue Using Statistical and Numerical Methods". In: **SPE Latin American and Caribbean Petroleum Engineering Conference**, Maracaibo, Venezuela, 21-23 Maio. 2014.

OREN, P., BAKKE, S., ARNTZEN, O. "Extending predictive capabilities to network models". **SPE Journal** 3 (4): 324–336. 1998.

OTSU, N. ''A Limiar Selection Method from Gray-Level Histograms". In: **IEEE Transactions on Systems, Man, and Cybernetics**, SMC-9, 62–66. 1979.

PADGETT, R., KOTRE, C. J. "Assessment of the effects of pixel loss on image quality in direct digital radiography". **Physics in Medicine and Biology**, v. 49, pp 977-986. 2004.

PETERS, E. J. **Advanced Petrophysics: Dispersion, interfacial phenomena, wettability, capillarity, capillary pressure, relative permeability**. Live Oak. 2012.

PÉNELOUX, A.; RAUZY, E.; FRÉZE, R. 1982. A consistent correction for Redlich-Kwong-Soave volumes. **Fluid Phase Equilibria**, v. 8, n. 1, p. 7–23, januray.

PINHEIRO, R.S., SANTOS, A. R, MARQUES, M., SCHNITZLER, E., SIGNORINI, D., TOMITA, R. A. "Well Construction Challenges In The Pre-Salt Development Projects". In: **2015 Offshore Technology Conference**, Houston, Texas – USA, 4-7 May, OTC Paper 25888.

PIZARRO, J. O. S., BRANCO, C. C. M. "Challenges in Implementing an EOR Project in the Pre-Salt Province in Deep Offshore Brasil" In: **2012 SPE EOR Conference at Oil and Gas West Asia**, Muscat – Oman, 16-18 April. 2012. SPE paper 155665.

RADKE, C.J., KOVSCEK, A.R., WONG, H.: "A Pore-Level Scenario for the Development of Mixed Wettability in Oil Reservoirs", **American Institute of Chemical Engineers Journal 39**, 6: 1072–1085, Jun. 1993.

RAMIASA, M., RALSTON, J., FETZER, R., SEDEV, R. "The influence of topography on dynamic wetting". **Advances in Colloid and Interface Science**, v.206, p. 275-293. 2014.

RANSOHOFF, T.C., RADKE, C.J. "Laminar flow of a wetting liquid along the corners of a predominantly gas-occupied noncircular pore". **J. Colloid Interface Sci**. 121, 392–401. 1988.

RAOOF, A. **Reactive/Adsorptive Transport in (Partially-) Saturated Porous Media: from pore scale to core scale**. Utrecht University – Geosciences Faculty – Earth Sciences Department. 2011.

RAOOF, A., HASSANIZADEH, S. M. "A new method for generating pore-network models of porous media". **Transport in Porous Media** 81 (3), 391–407. 2009.

RAOOF, A., NICK, H. M., HASSANIZADEH, S. M., SPIERS, C. J. "PoreFlow: A complex pore-network model for simulation of reactive transport in variably saturated porous media". **Computers & Geosciences** 61: 160-174. 2013.

RAZA, S.H., TREIBER, L.E., ARCHER, D.L.: "Wettability of Reservoir Rocks and its Evaluation", **Prod. Monthly 32**, No. 4, 2-7, Abr. 1968.

REKTORYS, K. **Variational Methods in Mathematics, Science and Engineering**, D. Reidel Publishing Company. 1977.

RIDLER, T. W., CALVARD, S. "Picture Limiaring Using an Iterative Selection Method". In: **IEEE Transactions on Systems, Man, and Cybernetics, Vol. sMC-8, No. 8**. 1978.

ROSA, A. J., CARVALHO, R. S., XAVIER, J. A. D. **Engenharia de Reservatórios de Petróleo**. Editora Interciência Ltda., Rio de Janeiro, RJ, Brasil, 2006.

RUDIN, W. **Principles of Mathematical Analysis**, McGraw-Hill. 1976.

SALATHIEL, R. A. Oil Recovery by Surface Film Drainage in Mixed-Wettability Rocks. **Journal of Petroleum Technology**, 25 (10), 1216 – 1224. SPE Paper 4104-PA. 1973.

SCANIP, +FE, +NURBS and +CAD. **Reference Guide**. Version 6.0. 2013. Simpleware Ltd. http://www.simpleware.com

SCHOLLE, P. A., ULMER-SCHOLLE, D. S. "A Color Guide to the Petrography of Carbonate Rocks: Grains, textures, porosity, diagenesis". **American Association of Petroleum Geologists Memoir 77**, 474 p. 2003.

SCHÄFER, W. **Ecology and Paleoecology of Marine Environments**. Chicago: The University of Chicago Press, 568p, 1972.

SEEVERS, D.O. "A nuclear magnetic method for determining the permeability of sandstones". In **33rd annual logging symposium**, society of professional well log analysts, transactions, paper L. 1966.

SEGERLIND, L. J. **Aplied Finite Element Analysis**, New York: John Wiley. 1984.
SELLEY, R. C. **Applied Sedimentology**, Second edition. Academic Press, California, U.S.A. 1984.

SERVIDONI, A. P. S. 2012. **Análise de Porosidade e o Potencial como Rocha Reservatório em Estromatólito do Recente da Lagoa Salgada, Litoral Fluminense – RJ** / Dissertação de Mestrado, Programa de Pós Graduação em Geologia, Setor de Ciências da Terra – UFPR. Curitiba, PR – Brasil.

SEZGIN, M., SANKUR, B. "Survey over image limiaring techniques and quantitative performance evaluation". In: **Journal of Electronic Imaging 13(1)**, 146–165. 2004.

SHEPPARD, A., LATHAM, S., MIDDLETON, J., KINGSTON, A., MYERS, G., VARSLOT, T., FOGDEN, A., SAWKINS, T., CRUIKSHANK, R., SAADATFAR, M., FRANCOIS, N., ARNS, C., SENDEN, T. "Techniques in helical scanning, dynamic imaging and image segmentation for improved quantitative analysis with X-ray micro-CT". In: **Nuclear Instruments and Methods in Physics Research B**. Elsevier, 2014. http://dx.doi.org/10.1016/j.nimb.2013.08.072

SILVA, W. G. A. L. 2015. **Análise do Espaço Poroso para Simulação Numérica do Escoamento de Fluidos em Estromatólitos Utilizando Microtomografia Computadorizada de Raios-X**. Dissertação de Mestrado, COPPE/UFRJ, Rio de Janeiro, Brasil.

SILVEIRA FILHO, O. T. 2003. **Dispersão Térmica em Meios Porosos Periódicos. Um Estudo Numérico**. 2003. 152f. Tese de doutorado, Modelagem Computacional, Universidade do Estado do Rio de Janeiro – UERJ, Rio de Janeiro.

SOARES, A. P. J. 2016. **Influência da molhabilidade da rocha na recuperação de petróleo de reservatórios carbonáticos**. 131f. Tese de doutorado, Programa de Pós-Graduação em Engenharia Química, Universidade Federal do Rio Grande do Norte – UFRN. Natal, RN – Brasil.

SOUZA, A., CARNEIRO, G., ZIELINSKI, L., POLINSKI, R., SCHWARTZ, L., H¨URLIMANN, M. D., BOYD, A., RIOS, E. H., SANTOS B. C. C., TREVIZAN W. A., MACHADO, V. F., AZEREDO, R. B. V. Permeability Prediction Improvement using 2D NMR Diffusion-T2 Maps. **SPWLA 54th Annual Logging Symposium**, New Orleans, Louisiana, June 22-26. 2013.

STRALEY, C., ROSSINI, D., VINEGAR, H., TUTUNJIAN, P., MORRISS, C. "Core analysis by low-field NMR". **Log Anal 38**:84–93. 1997.

STROEVEN, M., ASKES H., SLUYS L.J. "Numerical determination of representative volumes for granular materials". In: **Comput. Methods Appl. Mech. Engrg. 193**, 3221-3238. 2004.

TAVARES, A. C. G. **Fácies diagenéticas em coquinas da Formação Morro do Chaves (Barremiano-Aptiano, Bacia de Sergipe-Alagoas)**. 2014. 192f. Dissertação (Mestrado em Geologia)- Programa de Pós-graduação em Geologia, Instituto de Geociências, Universidade Federal do Rio de Janeiro, Rio de Janeiro.

TELES, A. P. **Aplicação da Microtomografia Computadorizada de Raios X por Dupla-Energia na Caracterização de Materiais Porosos.** 2016. 113f. Tese de Doutorado, Programa de Pós-Graduação em Engenharia Nuclear – COPPE/UFRJ. Rio de Janeiro, RJ – Brasil.

TIMUR, A. "Producible porosity and permeability of sandstones investigated through nuclear magnetic resonance principles". **Long Anal** 10:3-11. 1969.

THOMPSON, K.E. "Pore-scale modeling of fluid transport in disordered fibrous materials". **AIChE J.** 48, 1369–1389. 2002.

TOUATI, M., SUICMEZ, S., FUNK, J., CINAR, Y., KNACKSTEDT, M. "Pore Network Modeling of Saudi Aramco Rocks: A Comparative Study". **Society of Petroleum Engineers**. 2009.

TREIBER, L.E., ARCHER, D.L., OWENS. W. W.: "Laboratory Evaluation of the Wettability of Fifty Oil-Producing Reservoirs", **SPEJ**, 12, 531-40, Dez. 1971.

VIK, B., BASTESEN, E., SKAUGE, A. "Evaluation of representative elementary volume for a vuggy carbonate rock – Part I: Porosity, permeability, and dispersivity". In: **Journal of Petroleum Science and Engineering**, 112, pp. 36-47, 2013.

VIK, B., BASTESEN, E., SKAUGE, A. "Evaluation of representative elementary volume for a vuggy carbonate rock – Part II: Two-phase flow". In: **Journal of Petroleum Science and Engineering**, 112, pp. 48-60, 2013.

VIK, B., DJURHUUS, K., SPILDO, K., SKAUGE, A. “Characterisation of Vuggy Carbonates”. In: **2007 SPE/EAGE Reservoir Characterization and Simulation**, Abu Dhabi, U.A.E., 28–31 October, 2007. SPE paper 111434.

VILCÁEZ, J., MORAD, S., SHIKAZONO, N. “Pore-scale simulation of transport properties of carbonates rocks using FIB-SEM 3D microstructure: Implications for field scale solute transport simulations”. **Journal of Natural Gas and Engineering 42**, 13-22. 2017.

VIRGONE, A., BROUCKE, O., HELD, A., LOPEZ, B., SEARD, C., CAMOIN, G., SWENNEN, R., FOUBERT, A., ROUCHY, J., PABIAN-GOYHENECHE, C., GUO, L. “Continental Carbonates Reservoirs: The Importance of Analogues to Understand Presalt Discoveries”. In: **2013 International Petroleum Technology Conference**, Beijing – China, 26-28 March. IPTC paper 17013.

WITHJACK, E. M. “Computed Tomography for Rock-Property Determination and Fluid-Flow Visualization”. In: **SPE Formation Evaluation**, pp: 606-704, Dezembro, 1988. Paper original SPE 16951.

WILDENSCHILD, D., VAZ, C. M. P., RIVERS, M. L., RIKARD, D., CHRISTENSEN, B. S. B. “Using X-ray Computed Tomography in Hydrology: Systems, Resolutions, and Limitations”. In: **Journal of Hydrology 267(3)**: 285-297. 2002.

XIONG, Q., BAYCHEV, T. G., JIVKOV, A. P. “Review of pore network modelling of porous media: Experimental characterisations, network constructions and applications to reactive transport”. **Journal of Contaminant Hydrology** 192: 101-117. 2016.

YEONG, C. L. Y., TORQUATO, S. “Reconstructing random media”. In: **Phys. Rev. E., 57**, 495–506. 1998a.

YEONG, C. L. Y., TORQUATO, S. “Reconstructing random media. II. Three-dimensional media from two-dimensional cuts”. In: **Phys. Rev. E., 58**, 224–233. 1998b.

YAKHSHI-TAFTI, E.; KUMAR, R.; CHO, H. J. 2011. Measurement of Surface Interfacial Tension as a Function of Temperature Using Pendant Drop Images. **International Journal of Optomechatronics**, v. 5, n. 4, p. 393–403.

YIN, S., DE VRIES, E. T., RAOOF, A. Computational codes for solute transport in porous media. **Class notes**. Utrecht University – The Netherlands. May, 2017.

YOUSSEF, S., ROSENBERG, E., GLAND, N., KENTER, J. A. M., SKALINSKI, M., VIZIKA, O. “High Resolution CT and Pore-Network Models to Assess Petrophysical Properties of Homogeneous and Heterogeneous Carbonates”. In: **2007 SPE/EAGE Reservoir Characterization and Simulation Conference**, Abu Dhabi, UAE, 28-31 outubro, 2007.SPE paper 111427.

ZHAO, H. Q., MACDONALD, I. F., KWIECIEN, M. J. “Multi-orientation scanning: a necessity in the identification of pore necks in porous media by 3-D computer reconstruction from serial section data”. **J. Colloid Interface Sci**. 162, 390–401. 1994.

ZHOU, D., BLUNT, M. J., ORR, F. M. “Hydrocarbon drainage along corners of noncircular capillaries”. **J. Colloid Interface Sci**. 187, 11–21. 1997.

ZHOU, D., DILLARD L. A., BLUNT M. J. “A physically based model of dissolution of nonaqueous phase liquids in the saturated zone”. **Transp. Porous Media**, 39(2), 227–255. 2000.

APPENDIX A: EVALUATION AND CLASSIFICATION OF AUTOMATED SEGMENTATION METHODS ACCORDING TO SEZGIN & SANKUR (2004)

Evaluation and classification of 40 different techniques of segmentation for non-destructive tests (NDTs) according to the mean score and criteria established by SEZGIN & SANKUR (2004).

Rank	Method	Average score (AVE)	Rank	Method	Average score ($\bar{S}$)
1	Cluster_Kittler	0.256	21	Shape_Ramesh	0.460
2	Entropy_Kapur	0.261	22	Spatial_Cheng	0.481
3	Entropy_Sahoo	0.269	23	Attribute_Tsai	0.484
4	Entropy_Yen	0.289	24	Local_Bernsen	0.550
5	Cluster_Lloyd	0.292	25	Spatial_Pal_a	0.554
6	Cluster_Otsu	0.318	26	Local_Yasuda	0.573
7	Cluster_Yanni	0.328	27	Local_Palumbo	0.587
8	Local_Yanowitz	0.339	28	Entropy_Sun	0.588
9	Attribute_Hertz	0.351	29	Attribute_Leung	0.590
10	Entropy_Li	0.364	30	Entropy_Pun_a	0.591
11	Spatial_Abutaleb	0.370	31	Spatial_Beghdadi	0.619
12	Attribute_Pikaz	0.383	32	Local_Oh	0.619
13	Shape_Guo	0.391	33	Local_Niblack	0.638
14	Cluster_Ridler	0.401	34	Spatial_Pal_b	0.642
15	Cluster_Jawahar_b	0.423	35	Entropy_Pun_b	0.665
16	Attribute_Huang	0.427	36	Local_White	0.665
17	Shape_Sezan	0.431	37	Local_Kamel	0.697
18	Entropy_Shanbag	0.433	38	Local_Sauvola	0.707
19	Shape_Rosenfeld	0.442	39	Cluster_Jawahar_a	0.735
20	Shape_Olivio	0.458	40	Entropy_Brink	0.753

Source: SEZGIN & SANKUR (2004)